Development of a Multifluid Magnetohydrodynamic Model for Anisotropic, Partially Ionized Plasmas

by

Ken Miura

A thesis submitted in conformity with the requirements
for the degree of Doctor of Philosophy
Graduate Department of Aerospace Engineering
University of Toronto

Abstract

Development of a Multifluid Magnetohydrodynamic Model for Anisotropic, Partially Ionized Plasmas

Ken Miura

Doctor of Philosophy

Graduate Department of Aerospace Engineering

University of Toronto

2019

A multifluid magnetohydrodynamic (MHD) model based on an extended fluid dynamics description for each plasma species is proposed for the prediction of the flow and behaviour of fully and partially ionized non-equilibrium anisotropic plasmas. Two-(electrons and ions) and three-fluid (ions, electrons and neutrals) plasma models are described that both make use of a 10-moment or Gaussian anisotropic moment closure of the Boltzmann equation. The moment equations for each plasma species are fully coupled to the Maxwell's equations which govern electromagnetic wave propagation within the plasma and a Bhatnagar-Gross-Krook (BGK) relaxation time approximation is used to model non-equilibrium collisional processes between the plasma species. Chemical kinetic models are included to represent the partially ionized plasma processes. Unlike conventional MHD models, the proposed multi-species MHD model is capable of taking into account large temperature anisotropies and temperature differences between the electrons and ions, both of which can occur for low-density, high-temperature plasmas and/or strongly magnetized plasmas. A second-order Godunov-type finite-volume method is developed for the solution of the one- and two-dimensional forms of the multifluid plasma models, which includes temporal limiting in one-dimension and a parallel scheme utilizing a Newton-Krylov-Schwarz (NKS) implicit algorithm for the two-dimensional solution procedure. The numerical fluxes in the Godunov-type scheme are solved using HLLE and Godunov numerical flux functions. The two-dimensional solution procedure includes Generalized Lagrange Multiplier (GLM) and diffusive error correction schemes for the treatment of divergence errors associated with the electromagnetic field. An accuracy assessment is performed for the two-dimensional numerical solution procedure, demonstrating good convergence of solutions for a range of problems. The

validated two-dimensional solution procedure for the multifluid MHD model is then applied to the solution of the well-known Geospace Environmental Modelling (GEM) challenge problem involving magnetic field reconnection and numerical results are compared to established solutions in the literature. Results of grid refinement and parametric studies for the GEM case are also described. The proposed multifluid MHD model is shown to recover known published results with relatively small computational effort and the potential of the proposed treatment for describing a range of non-equilibrium anisotropic plasma flows is demonstrated.

Acknowledgements

I would like to thank Professor Clinton P. T. Groth for his support, patience and guidance in helping me develop this thesis. I would also like to thank my thesis committee members, Professor David Zingg and Professor James Gottlieb, for their help, feedback and support.

The friendship of the people and the environment at the University of Toronto Institute for Aerospace Studies, made my stay here enjoyable and productive. I would like to particularly thank Scott Northrup, Lucian Ivan, James McDonald, Boone Tensuda, and Professor Craig Steeves for their discussions and assistance.

To my wife, Winnie Tong, who has been beyond patient and understanding with my studies. I truly could not have accomplished my thesis without her love and support, and I do not know if there is any way I could ever thank her enough for that. I would also like to thank my parents for their support over the years. Finally, I would like to thank my children, David and Catherine, for making my life an even greater adventure.

I am grateful to the University of Toronto, the Ontario Government, and the National Science and Engineering Research Council for their financial support which allowed me to pursue my thesis.

Computational resources provided by the SciNet High Performance Consortium at the University of Toronto and Compute/Calcul Canada and funded from the Canadian Foundation for Innovation (CFI) and the Province of Ontario, Canada, was used for most of the simulations in this thesis.

Ken Miura
University of Toronto Institute for Aerospace Studies
2017

Contents

List of Figures

List of Symbols

P_s	Pressure tensor of species s
T_s	Average bulk temperature of species s
R_s	Universal gas constant for species s
a_{ref}	Reference speed of sound
c	Speed of light
e	Fundamental electric charge
m_s	Mass of species s
n_s	Number density of species s
q_s	Charge of species s
t	Time scalar
$\mathbf{F}$	Flux diad
$\mathbf{S}$	Source state vector
$\mathbf{U}$	Conservative solution state vector
$\mathbf{W}$	Primitive solution state vector
$\mathbf{v}_s$	Individual velocity for species s
$\mathbf{w}_s$	Diffusion velocity for species s
$\mathbf{u}_s$	Average velocity for species s

Alphanumeric Symbols

$\mathbf{j}$	Current density vector
$\hat{c}$	Non-Dimensional Speed of Light
λ_E	Electric Diffusion Coefficient
λ_D	Debye length

$\mathcal{F}_s$ Maxwell-Boltzmann distribution function for species s

$\mathcal{G}_s$ Gaussian distribution function for species s

c_s random velocity for species s

E total energy

$e\mathcal{E}_{iz}$ Ionization energy in SI units

$e_\circ$ elementary charge constant in cgs units

E_{hd} hydrodynamic energy

h Planck's constant

k Boltzmann constant

L Characteristic length

$r_{\mathrm{c,i}}$ Ion cyclotron radius or Larmour radius

10TFMHD 10 moment two-fluid magnetohydrodynamics

BGK Bhatnagar-Gross-Krook

BILU Block Incomplete Lower-Upper

FGLM Full magnetic and electric GLM error correction

FGLM Multifluid magnetohydrodynamic model with GLM divergance cleaning

GEM Geospace Environmental Modeling challenge

GLM Generalized Lagrange Multiplier

IVP Initial Value Problem

MGLM Magnetic GLM error correction, no electric error correction

MGLM Multifluid magnetohydrodynamic magnetic GLM model

MGLMED Magnetic GLM and electric diffusive error correction

MHD Magnetohydrodynamics

MMHD Multifluid magnetohydrodynamics

NGLM No error correction applied on the Maxwell's equations

NKS Newton-Krylov-Schwarz implicit scheme

PIC Particle-In-Cell

SER Switched Evolution/Relaxation startup

TSCF Time Step Control Factor

$\mathbf{B}$ Magnetic flux density vector

$\mathbf{D}$ Electric displacement vector

$\mathbf{E}$ Electric field intensity vector

$\mathbf{H}$ Magnetic field intensity vector

Greek Symbols

α Ionization reaction rate constant

β Recombination reaction rate constant

ϵ_0 Electrical permitivity of vacuum

μ_0 Magnetic permeability of vacuum

ν Collision frequency

ω_{ce} Electron cyclotron frequency

ω_{ci} Ion cyclotron frequency

ω_{pe} Electron plasma frequency

ρ_q Charge density

$\sigma_\circ$ Electrical conductivity

γ Specific heat ratio

ν_s Self collision frequency of species s

$\nu_{s,t}$ Collision frequency of interparticle collisions between species s and t

σ_a Collision Cross-Section for process or interaction a

Superscripts

T Transpose

Subscripts

c Collision terms

e Electron species

ion Ion species

Chapter 1

Introduction

1.1 Overview

The theoretical study and numerical modelling of plasmas have many applications in the fields of physics and aerospace engineering. Current applications of numerical plasma modelling include problems in flow control [9–12], hypersonics [13–17], space electric propulsion (EP) systems [18–26] and space plasmas [4, 27, 28]. A particular area of interest for this thesis is the behaviour of space plasmas associated with the Earth's magnetosphere [29] as depicted in the schematic diagram of Figure 1.1. The magnetosphere is a magnetic field that encloses the planet earth and exists as close as 40,000 km and extends as far as several million kilometres at the magnetotail. Understanding plasma dynamics in the magnetosphere is important to reducing the interference of communications and satellite operations in the environment of space as well as understanding how the magnetosphere protects the earth from high energy solar winds, radiation and electromagnetic disruptions [30, 31].

Collectively, the study of flows and interactions of plasmas with electromagnetic forces is referred to as magnetohydrodynamics (MHD) [32–34]. The modelling of plasmas can be considerably more complicated than regular fluid dynamic flows as there is the added complexity of the electro-magnetic interactions (such as the Lorentz force) combined with the widely varying physical characteristics of the plasma species (i.e., the electrons and ions). One of the many unique properties of charged particles in plasmas is the ability to be influenced by, and to influence, the electric and magnetic fields. This property also gives rise to plasma anisotropies as ion and electron temperatures along magnetic field lines can differ from temperatures perpendicular to the field lines. This is key in understanding the behaviour of plasmas when the magnetic fields are strong or in rarefied conditions, such as those found in space. Further, control of

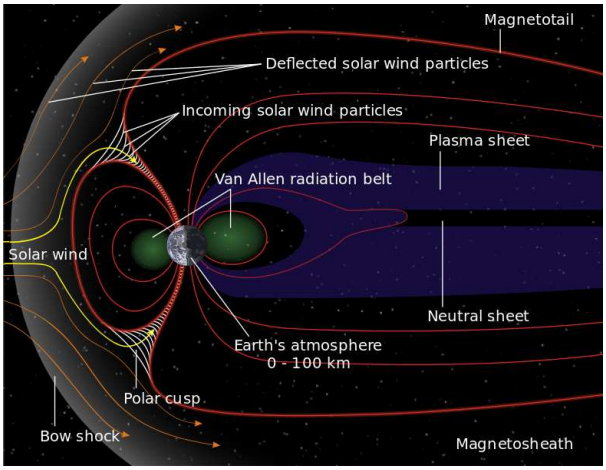

Figure 1.1: Schematic of Magnetosphere by Crochot [1].

the plasma particles can be achieved by taking advantage of these unique properties and is the source of interest from the flow control and hypersonics communities, where applications in these fields often involve partially, as opposed to fully, ionized plasmas. Harnessing the unique anisotropic properties of plasmas can also aid in the design of innovative propulsion systems, as plasmas can be heated and controlled in ways that isotropic fluids and gases cannot [35].

1.2 Motivation

A common model used in the simulation of plasmas [36,37] is traditional MHD, which includes three variants: ideal, Hall, and resistive MHD [32–34, 38–43]. These are essentially single-fluid, 5-moment, formulations of the plasma, assuming isotropic temperatures and pressures and do not differentiate between the electron and ion temperatures. They also do not directly solve the full set of Maxwell's equations governing the electro-magnetic fields. Instead, the electro-magnetic fields are often incorporated by assuming a strong magnetic field or by taking the magnetic flux frozen in with the fluid. The electric field is often not explicitly solved for and represented by a generalized Ohm's law [15], whose validity and applicability can be a concern [13, 44]. Lastly, the single fluid description of the plasma adopted in traditional MHD descriptions is unable to model partially ionized and non-quasi-neutral plasmas, or the associated chemistry. These characteristics of traditional MHD gives rise to limitations which have been recognized repeatedly in the literature [13, 16, 25, 45] where in many instances the approach has been applied to situations and/or regimes beyond its true applicability [46]. In fact, the regime in which ideal MHD is formally valid is rather non-physical [47, 48].

On the other extreme end of the plasma modelling spectrum from ideal MHD descriptions are the so-called particle simulation methods [49–52]. In particle simulations, individual particles and/or groupings of particles are tracked and their collisions/interactions can be directly simulated, as required, using Monte Carlo based approaches [52]. Although particle simulations can provide the full solution information that is desired in terms of anisotropic and non-equilibrium effects, tracking and simulating the individual interactions of particles can be extremely computationally expensive and can be difficult to apply to large-scale or complicated problems. Near-equilibrium or high-density regimes are also very challenging to treat accurately if particle simulations are used for the entire or even portions of the problem [53]. For example, when applied to the simulation of space plasmas and the GEM challenge described in the next section, many simplifications are made to the governing set of equations as well as to the problem definition and how particles are distributed. Spatial and particle count resolutions for such simulations are also quite low for many of these applications so that the computations remain tractable [3, 54].

In order to overcome the deficiencies of traditional MHD without resorting to full particle simulations, many extensions to traditional MHD have been proposed. Recognizing the need for a tensorial treatment of the temperature and pressures, the most common extension of the MHD model is to use a Navier Stokes-type fluid dynamics model in conjunction with a treatment of Maxwell's equations which includes the electric field, where coupling between the two sets of equations occurs in the diffusive source terms [13, 16, 23, 55]. A charge conservation equation is also added. This modelling approach is sometimes called the full magnetofluid dynamics equations (FMFD) or real magnetogasdynamics equations. However, the anisotropic pressure effects are only possible in the presence of gradients with such models. A large range of plasma models fall into a range lying somewhere between the FMFD equations and ideal MHD descriptions [10, 12, 56, 57]. It should also be noted that the FMFD models are still not a fully anisotropic description of the plasma and do not include a full treatment of Maxwell's equations.

Particle simulations can be combined with traditional MHD descriptions to recover the non-equilibrium and anisotropic kinetic collision behaviour [21, 22, 58]. Hybrid methods which include fluid equations to simplify certain computational regions of the flow [5] or parts of the system of equations, such as the electron fluid, have also been proposed [2, 25, 54]. However, once again this can dramatically increase the costs of the simulation. Note that a good overview of the range of models discussed up to this point in the introduction can be found in the reviews by Shang [59, 60].

From the preceding discussion, it would seem that accurate modelling of space plasmas is not

possible using traditional MHD models due to the presence of plasma anisotropies, the requirement for a full modelling of Maxwell's equations, and the ability to handle non-quasi-neutral and multi-temperature plasmas. On the other hand, as noted above, particle simulations, while dealing with these issues, are very expensive. Models that can predict such plasma flows with more modest computational costs could potentially allow significant advancement of plasma modelling in all areas and, in particular, help in the understanding of magnetosphere and solar wind interactions [30,31], as well as fill the need in the simulation and design of efficient, reliable and cheap space propulsion systems [23, 25, 26, 60, 61] and other practical plasma applications.

Comprehensive and computationally tractable models for realistic anisotropic plasmas are not readily available in the literature, however several recent studies have made notable attempts to arrive at suitable descriptions. An example of how the multi-temperature problem has been addressed in previous studies is provided by the Shumlak and Loverich two-fluid model [62,63], which treats the electron and ion species as well as the Maxwell's equations separately, coupled only through source terms. However, this model is based on an isotropic fluid model, and therefore cannot model anisotropic plasmas. An updated version of this two-fluid model was more recently proposed by Hakim *et al.* [64, 65], which includes some anisotropic pressures through a 10-moment formulation of the fluid equations. However, the latter does not take into account collisional effects, which is important for high density equilibrium conditions, as well as for rarefied gas conditions such as those encountered in the modelling of space plasmas. The model of Hakim *et al.* therefore also suffers from oscillations and the requirement of very high grid resolutions to resolve these oscillations. To address these issues, during the course of this thesis, a fully 10-moment, anisotropic two-fluid plasma model with a full modelling of Maxwell's equations, with particle collisions that is capable of describing non-quasi-neutral plasmas ranging from the equilibrium to the collisionless regimes [47] was developed. This was developed in parallel to the subsequent work by Hakim and Loverich *et al.* [66] and prior to the recent model of Johnson *et al.* [7], which can be viewed as the most comprehensive of the multi-fluid models to date.

There is one further property of plasmas absent from most traditional MHD descriptions, which is the fact that plasmas are not always fully ionized, and that neutral particles exist in the plasma as well. Taking into account the influences of the neutral particles, and the consequent interparticle reactions, is important for the modelling of flow control devices and EP devices, such as ion thrusters, which require a neutralizer in order to operate efficiently [58]. Though partially ionized plasmas have been often simulated using traditional MHD [67] and direct numerical simulation, a model with the capabilities of particle simulations, but based on fluid equations is thus far absent. It is clear that, due to the complexity of the problem, there

are many open issues that need to be addressed going forward for the accurate modelling of plasmas.

1.3 Geospace Environmental Modelling (GEM) Magnetic Reconnection Challenge

A standard representative problem very often considered in the numerical modelling of space plasmas is the Geospace Environmental Modelling (GEM) magnetic reconnection challenge. Although examined for some time, more recent observations from studies of the ESA Cluster mission data [68] and the successfully launched NASA MMS [69] has renewed interest in the modelling and exploration of this problem.

In this thesis, the GEM magnetic reconnection challenge is used in the evaluation and validation of a proposed new multifluid MHD model and companion solution method developed herein. The original problem was posed by Birn *et al.* [27] to investigate the role of magnetic reconnection in the dynamics of energy and particle transfers in the magnetosphere, particularly the magnetotail region during high solar activity. The problem has since been investigated by a large number of researchers using a variety of models and numerical methods [2–4, 7, 27, 38, 54, 63, 65, 66, 70–73]. The GEM challenge exists in a regime which is virtually collisionless [74], giving rise to large temperature and pressure anisotropies [4], as well as two-fluid currents. Traditional MHD models are not strictly valid for this regime due to the simplifying assumptions. Accurate, fast, reconnection has also been shown to require electric and magnetic fields that are not frozen to the fluid [3]. The simulation results that are thought to be most accurate for the GEM problem are obtained using hybrid particle and collisionless, kinetic, particle-in-cell (PIC) simulation methods [2,3,54,70]; however, significant inroads have been made in simulating this problem using extended fluid models [7,65,66]. Though significant research has been carried out related to the GEM problem, a very high resolution simulation using multiple species, both electron and ion, utilizing fully anisotropic fluid models, along with a full simulation of Maxwell's equations with divergence error cleaning formulated in a Godunov-type finite-volume scheme has not been performed to this date. Furthermore, a grid convergence resolution study is rare, particularly for the GEM problem. This is due to computational and stability considerations which usually require a modification of the GEM problem such as a reduction, or simplification, in the governing system of equations compromising the largely decoupled, anisotropic nature of the system.

Often, the GEM challenge problem has been solved using ideal, resistive and Hall MHD mod-

els [27,38,71,72]. The problems with these plasma descriptions is that they treat the plasma as a single fluid with combinations of infinite conductivity, an artificial resistivity and a generalized or simplified Ohm's law, which does not reflect the true behaviour of an electro-magnetic plasma system. These MHD models couple, to a degree, the fluid with the electric and magnetic fields as intrinsic to the fluid instead of as a standalone field. This is the so called frozen-in magnetic flux condition of traditional MHD methods [27]. Further, the fluids are usually isotropic as opposed to truly collisionless plasmas, as specified in the GEM challenge, which as a consequence have anisotropic features. As such, results with traditional, frozen-in magnetic flux condition, MHD models have been inconsistent and very dependent on the tuning parameters and changes in models and numerical solution methods. For instance, Otto [38] compared MHD and Hall MHD with resistivity models and found that the reconnection rates doubled when moving from ideal MHD to the Hall MHD model, but found the reconnection changed greatly with the resistivity parameters used. The reconnection rate was, however, significantly lower than that expected from particle codes unless a non-physical value for the resistivity was used. Ma and Bhattacharjee [72] utilized a Hall MHD code with a more accurate Ohm's law, but still utilized an isotropic single fluid description of the plasma with no discrete electric field. Ma and Bhattacharjee state that the ion pressure gradient can be neglected, which is counter to the findings discussed by Schmitz and Grauer [4]. They go on to say that while the electron pressure gradient should not be neglected, it is a common assumption in the literature and also neglect it anyway. The results of Ma and Bhattacharjee do not align with any other results, except qualitatively, with times and reconnection rates differing from those predicted by other simulation results. Birn and Hesse [71] brought anisotropic effects into the resistive MHD equations. Like all other traditional MHD results, the reconnection takes much longer (hundreds of non-dimensionalized time), but it was noted in their study that with added anisotropies, the reconnection rate was reduced, and as the rate of isotropization increased, the reconnection rate increased. As will be shown, these findings are also observed in the present study.

As mentioned previously, the perceived benchmark methods for the solution of the GEM problem are the PIC and hybrid codes. Shay *et al.* [2] have compared a PIC and hybrid code with Hall MHD. The hybrid model treats ions as particles, but treats the electrons as an isotropic fluid, an assumption that is not valid as stated before [4]. Further, the PIC and hybrid code uses a restricted form of the governing equations, with additional constraints and assumptions which eliminates several variables and also assumes that equilibrium quantities are only a function of z while perturbed variables have no x component. The differences between the various schemes, including changing the mass ratio by orders of magnitude, was found not to greatly affect reconnection, but did affect the fluid dynamics. Hesse *et al.* [70] explored the PIC model

further and Kuznetsova *et al.* [54] explored the differences between PIC and hybrid models, where the hybrid model is found to be more stable with no magnetic island forming due to the isotropic nature of the electron fluid equations. Note that in all of the simulations listed above, not all of the particles are simulated. Instead, a background distribution of particles is created that have different properties than the simulating particles and which are not affected by the fluid and electromagnetic forces.

More recently, other advanced non-PIC schemes allowing non-equilibrium treatment of the plasma have been used to simulate the GEM problem. The most successful of these has been those based on the Darwin-Vlasov model and various two-fluid formulations. Schmitz *et al.* [4, 75] presents a fully anisotropic two-fluid plasma model in which the particle distribution functions are directly computed. However the major deficiency in this formulation is that it is still quite computationally expensive, does not incorporate plasma particle collisions and does not provide a full modelling of Maxwell's equations. In the Darwin-Vlasov model, the 'vacuum' wave modes are eliminated, which is to say all speed of light waves of Maxwell's equations are not considered by splitting the electric field into longitudinal and tangential components, where the tangential components are not evolved. Further, not all electric and magnetic field components are considered for the charge displacement correction. A more recent Vlasov-BGK model has been proposed by Liu *et al.* [73], which incorporates BGK particle collision modelling to the Darwin-Vlasov system. However, the Vlasov-BGK model comes with its own complications in the solution procedure and an extremely high computational cost, requiring the use of simplified problems and low mesh resolution simulations. Hakim [65] and Loverich *et al.* [63, 66] have tackled the GEM problem with a two-fluid approach using various levels of modelling for collisional effects and temperature anisotropies. However, a fully anisotropic code is not used, with either 5-moment fluid descriptions used for both plasma components, or having a 5-moment formulation for the electrons. Further, the actual reconnection problem studied by Hakim was not the same as the original GEM problem. Johnson *et al.* [6, 7] presents a fully anisotropic two-fluid simulation for the GEM problem using the original GEM challenge definition in his thesis. The results of the latter are however of relatively lower spatial resolution to those considered herein and required a constant collision 'isotropization' pressure equation to remain stable for the duration of the simulations. Hybrid models which include both the Darwin-Vlasov model and the two-fluid model have also been proposed to address the computational difficulty of the Darwin-Vlasov model while providing fully anisotropic simulation capabilities [5]. Despite these advancements, the two-fluid Darwin-Vlasov model still remains computationally expensive and is limited to tailor-made problems such as the GEM challenge where the domain can be split into regions where the respective plasma models can be reasonably applied.

1.4 Research Goals of Thesis

The goal of this thesis is then to develop a practical multifluid MHD (MMHD) model, which is capable of resolving non-equilibrium, anisotropic, multi-temperature, partially ionized plasma effects without resorting to the complexity and numerical difficulty of direct particle simulations. A set of transport equations are sought that include temperature and pressure anisotropies, as well as a full modelling of Maxwell's equations, eliminating the need for a generalized Ohm's law constitutive relation, with multispecies capabilities taking into account neutral particles as well as the ions and electrons, along with interspecies reactions such as ionization, recombination and charge exchange. The MMHD formulation follows what was developed previously in the thesis research of Ohsawa [48], which includes the key elements of anisotropic plasma modelling, as well as capabilities for modelling rarefied, near equilibrium, partially ionized plasmas. An effective numerical solution strategy for the solution of the MMHD model in two space dimensions is then developed. The proposed MMHD model is thus equipped to simulate a range of non-equilibrium, multispecies, anisotropic, partially ionized, plasmas as well as near equilibrium plasmas in two dimensions (2D), and be computationally tractable for performing space plasma simulations. In order to demonstrate the potential of the proposed MMHD model and companion solution method, they are applied here to the GEM magnetic reconnection problem as described above and the results of this application are discussed.

1.5 Outline of Thesis

Following this introduction, the remainder of the thesis continues first with a brief review of relevant gaskinetic theory, which provides the basis of the proposed MMHD model. The proposed MMHD model is then described, which is based on the 10-moment Gaussian moment closure with BGK collision terms, with various formulations for the Maxwell's equations. The models for the collisions and reactions are presented as well. A dispersion analysis is then presented for the linearized system of equations in which the behaviour of the MMHD eigen system is explored and the hyperbolicity for the moment system is demonstrated. A one-dimensional (1D), temporally limited, dual-time implicit, second-order finite-volume Godunov upwind numerical solution procedure with a Harten-Lax-van Leer-Einfeldt (HLLE) numerical flux function is then developed and studied for the 1D form of the proposed MMHD model. The recovery of the ideal MHD limit is demonstrated and explored, along with the computational advantages of the implicit dual-time scheme. The proposed solution method is then extended to the two-dimensional case in which a parallel scheme with a Newton Krylov Schwarz (NKS)

implicit algorithm is developed and validated through a rigorous accuracy assessment study showing robust convergence. The two-dimensional solution method is also validated through direct comparison with a Gaussian moment closure solution method for various flow regimes. Finally, the numerical results for the GEM challenge are presented as obtained using the proposed MMHD solution procedure. The numerical results are compared to established solutions in the literature. Numerical predictions for more realistic plasma cases are also considered. The last chapter of the thesis provides a summary of the thesis achievements and conclusions as well as a discussion of directions for future research.

Chapter 2

Gaskinetic Theory

2.1 Overview

A brief overview of gaskinetic theory, which is used as a basis for the development of the proposed transport equations for the MMHD model, is presented in this chapter. The underlying kinetic equations for the charged and neutral particles are presented, beginning with a definition of the velocity distribution function. Moment closure techniques for obtaining approximate solutions to the governing kinetic equations are also briefly reviewed. In particular, a 10-moment or Gaussian moment closure based on the Gaussian distribution function is presented that is essential for representing the anisotropic behaviour of plasmas. The basic form of the 10-moment equations for plasmas is then presented, along with the corresponding BGK approximations for relevant elastic collisional processes.

2.2 Kinetic Theory and the Velocity Distribution Function

Kinetic theory seeks to describe the time evolution of a system of often numerous discrete objects via a statistical or probabilistic approach. The objects and system being modelled can be anything from vehicles and traffic [76, 77], to stellar bodies and galaxies [78]. Partial integro-differential equations, known as kinetic equations, can be developed for the study of these systems and used to predict their behaviour. The behaviour of gases and plasmas is one such system that can be described using the statistical description provided by kinetic theory and is known collectively as gaskinetic theory [79]. Gaskinetic theory seeks to represent the probabilistic behaviour of gases and plasmas by making use of a distribution function for the

motion of the individual particles. The velocity distribution function, $\mathrm{F}_s(\mathbf{x}, \mathbf{v}_s, t)$, is related to the probability density of the particles in a 6-dimensional phase space where $\mathbf{x}$ is the position vector, $\mathbf{v}_s$ is the velocity vector for species s, and t is the time. By definition, integrating the distribution function over all velocity space for a given volume or position will result in the number density for the given volume or position given by[1]

$$n_s(\mathbf{x}, t) = \int_{-\infty}^{\infty} \mathrm{d}v_{s,x} \int_{-\infty}^{\infty} \mathrm{d}v_{s,y} \int_{-\infty}^{\infty} \mathrm{d}v_{s,z}\, \mathrm{F}_s(v_{s,x}, v_{s,y}, v_{s,z}, \mathbf{x}, t) = \langle \mathrm{F}_s(\mathbf{x}, \mathbf{v}_s, t) \rangle \,, \tag{2.1}$$

where n_s is the number density of species s. Put another way, for any infinitesimal volume in space defined by $\mathrm{d}\mathbf{x}$, there are $\mathrm{d}n_s$ particles that have a velocity contained within the infinitesimal velocity space defined by $\mathrm{d}\mathbf{v}_s$ such that

$$\mathrm{d}n_s = \mathrm{F}_s(\mathbf{x}, \mathbf{v}_s, t)\, \mathrm{d}\mathbf{x}\, \mathrm{d}\mathbf{v}_s. \tag{2.2}$$

The integral operator on the right of Equation (2.1), $\langle \cdot \rangle$, is used here to represent integration over the entire velocity space and in the general case can be expressed as

$$\langle M(\mathbf{v}_s) \mathrm{F}_s(\mathbf{x}, \mathbf{v}_s, t) \rangle = \int_{-\infty}^{\infty} \mathrm{d}v_{s,x} \int_{-\infty}^{\infty} \mathrm{d}v_{s,y} \int_{-\infty}^{\infty} \mathrm{d}v_{s,z}\, M(\mathbf{v}_s) \mathrm{F}_s(v_{s,x}, v_{s,y}, v_{s,z}, \mathbf{x}, t) \tag{2.3}$$

where $M(\mathbf{v}_s)$ is the moment function. Taking various velocity dependent moment functions for $M(\mathbf{v}_s)$ and integrating over all velocity space is known as taking velocity moments of a distribution function and is a way of determining relevant macroscopic properties of gases which are then functions of regular three-dimensional physical space, a subset of the six-dimensional phase space of the distribution functions. The integral of Equation (2.1) is in fact known as taking the zeroth-degree velocity moment as the moment function, $M(\mathbf{v}_s)$, is of order 0 in $\mathbf{v}_s$. Further details of the macroscopic properties of a gas are to follow.

2.3 Boltzmann Kinetic Equation for Plasmas

The Boltzmann equation [79] is a non-linear integro-partial differential equation that is capable of describing the evolution of a non-equilibrium velocity distribution function in space and time, as well as velocity space. It is an approximation to the Liouville equation [80] and is part of the Bogoliubov-Born-Green-Kirkwood-Yvon (BBGKY) hierarchy [81, 82] and is given by

$$\frac{\partial \mathrm{F}_s(\mathbf{x}, \mathbf{v}_s, t)}{\partial t} + v_{s,k} \frac{\partial \mathrm{F}_s(\mathbf{x}, \mathbf{v}_s, t)}{\partial x_k} + a_{s,k} \frac{\partial \mathrm{F}_s(\mathbf{x}, \mathbf{v}_s, t)}{\partial v_{s,k}} = \frac{\delta \mathrm{F}_s(\mathbf{x}, \mathbf{v}_s, t)}{\delta t}. \tag{2.4}$$

The term on the right hand side, $\delta \mathrm{F}_s(\mathbf{x}, \mathbf{v}_s, t)/\delta t$, is the collision term (or collision integral) that accounts for the influence of interparticle collisions on the time rate of change of the

[1] In this work, vector notation is used where ever possible, however, tensor notation is used when required and when expression in tensor notation is easier to interpret.

distribution function and in general requires the evaluation of a five-dimensional integral. The acceleration term, a_{sk}, takes into account external forces that may act on the gas and is taken to be divergence free with respect to velocity [79]. For plasmas, the external force is the Lorentz force, which represents the influence of electromagnetic fields on the charged particles and is given by

$$a_{s,k} = \frac{q_s}{m_s} \left(E_k + \epsilon_{klm} v_{s,l} B_m \right). \tag{2.5}$$

Here, q_s and m_s is the charge and mass of species s, and $\mathbf{E}$ and $\mathbf{B}$ are the electric and magnetic field density vectors, respectively. With the Lorentz force, Equation (2.5), substituted into Equation (2.4), the resulting equation is known as the Boltzmann equation for plasmas.

2.4 Maxwell's Equation of Change

In order to move from the phase space of the Boltzmann equation to transport equations for the macroscopic fluid dynamics quantities in physical space, Maxwell's equations of change can be derived by taking the Boltzmann equation, Equation (2.4), and multiplying by a moment function of $\mathbf{v_s}$, $M(\mathbf{v}_s)$, as appearing in Equation (2.3). The result is

$$\frac{\partial}{\partial t} \langle M_s \, F_s \rangle + \frac{\partial}{\partial x_i} \langle v_{s,i} M_s \, F_s \rangle + \left\langle a_{s,i} \frac{\partial M_s \, F_s}{\partial v_{s,i}} \right\rangle = \left\langle M_s \, \frac{\delta F_s}{\delta t} \right\rangle, \tag{2.6}$$

which is regarded as Maxwell's equation of change in conservative form [79] and describes the transport of the macroscopic quantity or moment, $\langle M_s \, F_s \rangle$.

2.5 Velocity Moments and Moment Closures

By taking Maxwell's equation of change, Equation (2.6), and selecting a suitable representation for the distribution function, it is possible to derive various macroscopic descriptions for systems of fluids and gases. Many such distributions can exist, but a common and useful distribution is the Maxwell-Boltzmann distribution or Maxwellian describing equilibrium solutions of the Boltzmann equation above given by

$$\mathcal{M}_s = n_s \left(\frac{m_s}{2\pi k T_s} \right)^{3/2} \exp \left[- \frac{m_s (\mathbf{v}_s - \mathbf{u}_s)^2}{2 k T_s} \right], \tag{2.7}$$

where k is the Boltzmann's constant, T_s is the temperature for species s, and $\mathbf{u_s}$ is the bulk velocity vector for species s. It is also useful to introduce the random velocity here given by

$$\mathbf{c}_s = \mathbf{v}_s - \mathbf{u}_s, \tag{2.8}$$

which is the velocity of a particle minus the bulk velocity, meaning that the statistical average of such a velocity vector for all particles is zero. The Maxwellian is a particularly useful distribution function as it represents a normal statistical, local thermodynamic equilibrium distribution. Any real world monatomic gas tends to evolve towards a Maxwellian distribution under the action of collisional processes [79].

The moment function, M_s, in Equation (2.6) is commonly a monomial in some degree of the total velocity, $\mathbf{v_s}$, or random velocity, $\mathbf{c_s}$. One problem encountered when taking the velocity moments of Equation (2.6) is that the resulting equations always introduce an additional term in the flux of the macroscopic quantity requiring the evaluation of the next higher velocity moment. One solution to this is to select the distribution function in a way that results in the higher order moment being defined entirely in terms of only the lower order moments or macroscopic quantities of interest. This is the basic idea behind most moment closure techniques.

The closure of moment equations has been studied for some time with classic closures being defined by taking perturbative expansions around the Maxwellian first described by Grad [80,83]. Modern closures include the popular hierarchy of maximum entropy closures of Levermore [84]. The most straight forward and lowest order member of both the Grad and Levermore closures is represented by taking the Maxwellian distribution of Equation (2.7) for the distribution function, F_s, in Equation (2.6) and taking the subsequent velocity moments for the set of moment functions given by

$$M_s\left(\mathbf{v}_s\right) = \left\{m_s, m_s\mathbf{v}_s, m_s v_s^2\right\}, \tag{2.9}$$

which are associated with the zeroth, first and second velocity moments of Maxwell's equation of change. When performing the integration, it is useful to make the substitution for the velocity and bulk velocity vector in Equations (2.7), (2.6) and (2.9) with the random velocity vector of Equation (2.8). The high-order moments are closed with the second-order moment being a function the lower order moments and with the third order moment being zero:

$$p_s(\mathbf{x},t) = \frac{1}{3}\left\langle m_s c_s^2\, F_s(\mathbf{x},\mathbf{c}_s t)\right\rangle = n_s k T_s, \tag{2.10}$$

$$\mathbf{h}_s(\mathbf{x},t) = \left\langle \frac{1}{2} m_s c_s^2 \mathbf{c}_s\, F_s(\mathbf{x},\mathbf{c}_s,t)\right\rangle = \mathbf{0}, \tag{2.11}$$

meaning there is no heat flux. One characteristic for most moment closures is that under equilibrium conditions, the moment equations reduce to the well-established Euler equations describing flows in local thermodynamic equilibrium. Performing the velocity moment integration using the equilibrium Maxwellian distribution function, and setting $\mathbf{a}_s = 0$, it can be

shown that the Euler equations are recovered as given by

$$\begin{aligned}
\frac{\partial \rho_s}{\partial t} + \frac{\partial}{\partial x_i}(\rho_s u_{s,i}) &= \left(\frac{\delta \rho_s}{\delta t}\right)_{\mathrm{C}}, \\
\frac{\partial}{\partial t}(\rho_s u_{s,k}) + \frac{\partial}{\partial x_i}\left(\rho_s u_{s,i} u_{s,k} + p_s\, \delta_{ik}\right) &= \left(\frac{\delta(\rho_s u_{s,k})}{\delta t}\right)_{\mathrm{C}}, \\
\frac{\partial}{\partial t}\left(\frac{3}{2}p_s + \frac{1}{2}\rho_s u_s^2\right) + \frac{\partial}{\partial x_i}\left[\left(\frac{3}{2}p_s + \frac{1}{2}\rho_s u_s^2\right) u_{s,i} + p_s u_i\right] &= \left(\frac{\delta \mathcal{E}_s}{\delta t}\right)_{\mathrm{C}}.
\end{aligned} \tag{2.12}$$

which govern the transport of mass, momentum and energy for the gas. This is also known as the 5-moment equations in the Levermore hierarchy [84]. Please refer to the textbook by Gombosi [79] for more details Maxwell's equation of change and derivation of the Euler equations. Other references for velocity moments of higher order closures and the derivation of governing equations for fluid dynamics can be found in the papers by Groth [85], Brown *et al.* [86] and Levermore [84]. The evaluation of the collision terms appearing in the preceding equations is addressed later in Section 2.7 of this chapter.

2.6 10-moment Gaussian Closure

An important property of charged particles, is the ability to have different, anisotropic, temperatures in different directions that result from plasmas coupling with Maxwell's equations through the Lorentz force of Equation (2.5). As can be seen from the Lorentz force, charged particles can be directly influenced by the electric field in a preferred direction and will also spiral around magnetic field lines. This results in movement, energy, and pressures in directions parallel and perpendicular to magnetic field lines. This occurs in both equilibrium and non-equilibrium conditions. The local Maxwellian distribution, Equation (2.7), is incapable of capturing this behaviour, so a different distribution function is sought.

A distribution function that results in a hyperbolic set of closed moment equations and is capable of allowing for anisotropic pressures and temperatures would be desired for many plasma applications. One such closure is the so-called Gaussian distribution of the 10-moment Gaussian closure. In the Gaussian closure, the species phase space distribution function is approximated as follows:

$$\mathcal{G}_s(\mathbf{x}, \mathbf{v}_s, t) = \frac{n_s(\mathbf{x}, t)}{(2\pi)^{3/2}(\det\Theta_s)^{1/2}} \exp\left(-\frac{1}{2}\Theta^{-1}_{s,ij} c_{s,i} c_{s,j}\right) \tag{2.13}$$

where $\Theta_{sij} = P_{sij}/\rho_s$. The 10-moment Gaussian closure was studied by Levermore [84] and is a second-order member of the Levermore maximum entropy hierarchy. It was however first considered by others such as Maxwell [87] and Holway [88–90]. As a member of the Levermore

maximum entropy hierarchy, it represents the most likely distribution function that maximizes the entropy generated by the Maxwell's equation of change for the given finite set of moments associated with the Gaussian distribution [91]. It is not a perturbative function like Grad closures making it elegantly simple. It is strictly positive and closes the moment in the same way as the Maxwellian distribution function; with the third-order moment vanishing. The Gaussian closure has been extensively studied and has been applied successfully to the numerical prediction of a range of non-magnetized gaseous flows by Levermore [92], McDonald *et al.* [93–97] and Groth *et al.* [91].

The transport equations of the 10-moment Gaussian closure can be derived by approximating the distribution function $\mathrm{F}_s(\mathbf{x}, \mathbf{v}_s, t)$ with the Gaussian distribution function, Equation (2.13), and then taking appropriate velocity moments of the Boltzmann equation, Equation (2.4) as defined by Maxwell's equation of change [84–86]. For the plasma applications of interest here, the Lorentz force of Equation (2.5) is considered when evaluating the velocity moments for Maxwell's equation of change, Equation (2.6), using the following moment functions:

$$M_s = [m_s, m_s v_{s,i}, m_s v_{s,j} v_{s,k}] \tag{2.14}$$

the following 10-moment multispecies transport equations for plasmas can be derived and expressed in weak conservative form as:

Multispecies Conservative Continuity Equation

$$\frac{\partial m_s n_s}{\partial t} + \frac{\partial m_s n_s u_{s,i}}{\partial x_i} = \left(\frac{\delta(m_s n_s)}{\delta t}\right)_{\mathrm{C}}, \tag{2.15}$$

Multispecies Conservative Momentum Equation

$$\begin{aligned} \frac{\partial m_s n_s u_{s,k}}{\partial t} + \frac{\partial m_s n_s u_{s,i} u_{s,k}}{\partial x_i} + \frac{\partial P_{s,ik}}{\partial x_i} - n_s(G_k + q_s E_k) \\ -n_s q_s \varepsilon_{k\alpha\gamma} u_{s,\alpha} B_\gamma = \left(\frac{\delta(m_s n_s v_{s,k})}{\delta t}\right)_{\mathrm{C}}, \end{aligned} \tag{2.16}$$

Multispecies Conservative Energy Equation

$$\begin{aligned} &\frac{\partial}{\partial t}\left(m_s n_s u_{s,j} u_{s,k} + P_{s,jk}\right) + \frac{\partial}{\partial x_i}\left(m_s n_s u_{s,i} u_{s,j} u_{s,k} + P_{s,jk} u_{s,i} + P_{s,ik} u_{s,j} + P_{s,ij} u_{s,k}\right) \\ &-n_s u_{s,j}(G_k + q_s E_k) - n_s u_{s,k}(G_j + q_s E_j) - n_s q_s(\varepsilon_{j\alpha\gamma} u_{s,\alpha} u_{s,k} + \varepsilon_{k\alpha\gamma} u_{s,\alpha} u_{s,j}) B_\gamma \\ &-\frac{q_s}{m_s}(\varepsilon_{j\alpha\gamma} P_{s,\alpha k} + \varepsilon_{k\alpha\gamma} P_{s,\alpha j}) B_\gamma = \left(\frac{\delta(m_s n_s v_{s,j} v_{s,k})}{\delta t}\right)_{\mathrm{C}}. \end{aligned} \tag{2.17}$$

It should be noted that when taking the velocity moments to arrive at the species transport equations, the third-order velocity moments of $\mathcal{G}_s$ are all identically equal to zero corresponding to the situation where the heat flux for each species is zero. Besides the ability to model anisotropic pressures and energies, the above set of equations is desirable because it is hyperbolic

and is suitable for numerical solution using well-established Godunov-type upwind finite-volume methods [83, 98].

For completeness, to obtain the primitive form of the equations, the moment functions,

$$M_s = [m_s, m_s c_{s,i}, m_s c_{s,j} c_{s,k}], \tag{2.18}$$

and the random velocity definition, Equation (2.8), are substituted into Equation (2.6) to obtain the following set of moment equations:

Multispecies Primitive Continuity Equation

$$\frac{\partial m_s n_s}{\partial t} + u_{s,i}\frac{\partial m_s n_s}{\partial x_i} + m_s n_s \frac{\partial u_{s,i}}{\partial x_i} = \left(\frac{\delta(m_s n_s)}{\delta t}\right)_{\mathrm{C}}, \tag{2.19}$$

Multispecies Primitive Velocity Equation

$$\frac{\partial u_{s,k}}{\partial t} + u_{s,i}\frac{\partial u_{s,k}}{\partial x_i} + \frac{1}{m_s n_s}\frac{\partial P_{s,ki}}{\partial x_i} - \frac{q_s}{m_s}(E_k + \epsilon_{k\alpha\gamma} u_{s,\alpha} B_\gamma) = \left(\frac{\delta u_{s,k}}{\delta t}\right)_{\mathrm{C}}, \tag{2.20}$$

Multispecies Primitive Pressure Equation

$$\begin{aligned}\frac{\partial P_{s,jk}}{\partial t} + u_{s,i}\frac{\partial P_{s,jk}}{\partial x_i} + P_{s,jk}\frac{\partial u_{s,i}}{\partial x_i} + P_{s,ij}\frac{\partial u_{s,k}}{\partial x_i} + P_{s,ik}\frac{\partial u_{s,j}}{\partial x_i} \\ -\frac{q_s}{m_s}(\epsilon_{j\alpha\gamma} P_{s,\alpha k} + \epsilon_{k\alpha\gamma} P_{s,\alpha j}) B_\gamma = \left(\frac{\delta P_{s,jk}}{\delta t}\right)_{\mathrm{C}}.\end{aligned} \tag{2.21}$$

2.7 Bhatnagar-Gross-Krook Collision Operators

The right hand side collision integrals appearing in Equation (2.4) are now considered. Modelling exactly the behaviour of the particles undergoing collisions can be both theoretically challenging and computationally expensive, so an often-used and convenient mathematical approximation for the effects of inter-particle collisions, the Bhatnagar-Gross-Krook (BGK) collision model [99], is deemed to be sufficient for the present study and is adopted here. The BGK model uses a relaxation time approximation of the form

$$\left(\frac{\delta F_s}{\delta t}\right)_c = \left(\frac{\delta F_s}{\delta t}\right)_{el} \equiv \sum_t \frac{\mathcal{M}_{s(st)} - F_s}{\theta_{st}} \tag{2.22}$$

where

$$\mathcal{M}_{s(st)} = n_s \left(\frac{m_s}{2\pi k T_{s(st)}}\right)^{3/2} \exp\left(-\frac{m_s(\mathbf{v}_s - \mathbf{u}_{s(st)})^2}{2kT_{s(st)}}\right), \tag{2.23}$$

$$\mathbf{u}_{s(st)} = \frac{m_s \mathbf{u}_s + m_t \mathbf{u}_t}{m_s + m_t}, \tag{2.24}$$

$$T_{s(st)} = T_s + 2\frac{m_s m_t}{(m_s + m_t)^2}(T_t - T_s) + \frac{m_t}{3k}\frac{m_s m_t}{(m_s + m_t)^2}(\mathbf{u}_t - \mathbf{u}_s)^2, \tag{2.25}$$

and where the subscript $s(st)$ refers to the species s for the interaction between s and t. Therefore, $\mathcal{M}_{s(st)}$ is the Maxwellian distribution function for species s about the mass weighted average bulk velocity, $\mathbf{u}_{s(st)}$, and $1/\theta_{st} = \nu_{st}$ is the collision frequency of the interaction between species s and t. The BGK collision operator is used to model elastic collisions herein.

2.8 Elastic Collisions

In order to derive the elastic collision terms utilizing the BGK approximation above, a few relations must be discussed. First, the random velocity can be written so that

$$\mathbf{c}_{s(st)} = \mathbf{v}_s - \mathbf{u}_{s(st)} = \mathbf{c}_s + \frac{m_t}{m_s + m_t}\left(\mathbf{u}_s - \mathbf{u}_t\right). \tag{2.26}$$

This implies that

$$\left\langle m_s \left(\frac{\delta F_s}{\delta t}\right)_{\mathrm{C}} \right\rangle = 0 \tag{2.27}$$

for the continuity collision term and

$$\left\langle m_s \mathbf{v}_s \left(\frac{\delta F_s}{\delta t}\right)_{\mathrm{C}} \right\rangle = \sum_t n_s m_s \tilde{\nu}_{st}(\mathbf{u}_t - \mathbf{u}_s) \tag{2.28}$$

for the momentum collision terms. Also note that

$$\begin{gathered} \left\langle m_s c_{s(st)k} c_{s(st)l} F_{s(st)} \right\rangle = n_s k_B T_{s(st)} \delta_{kl} \\ = p_s \delta_{kl} + 2\tfrac{n_s m_s m_t}{(m_s+m_t)^2}(T_t - T_s)\delta_{kl} + \tfrac{n_s m_t}{3k}\tfrac{m_s m_t}{(m_s+m_t)^2}(\mathbf{u}_t - \mathbf{u}_s)^2 \delta_{kl} \end{gathered} \tag{2.29}$$

and

$$\tilde{\nu}_{st} = \frac{m_t}{m_s + m_t}\nu_{st}. \tag{2.30}$$

Therefore the second-order random velocity moment is given by

$$\begin{gathered} \left\langle m_s c_{sk} c_{sl} F_{s(st)} \right\rangle = n_s k_B T_{s(st)} \delta_{kl} + n_s m_s \left(\tfrac{m_t}{m_s m_t}\right)^2 \left(u_{sk} - u_{tk}\right)\left(u_{sl} - u_{tl}\right) \\ = p_s \delta_{kl} + 2\tfrac{n_s m_s m_t}{(m_s+m_t)^2}(T_t - T_s)\delta_{kl} + \tfrac{n_s m_t}{3k}\tfrac{m_s m_t}{(m_s+m_t)^2}(\mathbf{u}_t - \mathbf{u}_s)^2 \delta_{kl} \\ + n_s m_s \left(\tfrac{m_t}{m_s m_t}\right)^2 \left(u_{sk} - u_{tk}\right)\left(u_{sl} - u_{tl}\right) \end{gathered} \tag{2.31}$$

such that

$$\begin{gathered} \left\langle \left(\frac{\delta\left(m_s c_{sj} c_{sk} F_s\right)}{\delta t}\right)_{\mathrm{C}} \right\rangle = \nu_s\left(p_s \delta_{jk} - P_{sjk}\right) + \sum_t 2\frac{m_s n_s \tilde{\nu}_{st}}{(m_s + m_t)} k_B (T_t - T_s)\delta_{jk} \\ + \sum_t \frac{m_s m_t n_s \tilde{\nu}_{st}}{m_s + m_t}\left[\frac{1}{3}\delta_{jk}(\mathbf{u}_t - \mathbf{u}_s)^2 + (u_{tj} - u_{sj})(u_{tk} - u_{sk})\right] \end{gathered} \tag{2.32}$$

and

$$\begin{gathered} \left\langle \left(\frac{\delta(m_s n_s v_{sj} v_{sk} F_s)}{\delta t}\right) \right\rangle = \nu_s\left(p_s \delta_{jk} - P_{sjk}\right) + \sum_t 2\frac{m_s n_s \tilde{\nu}_{st}}{(m_s + m_t)} k_B (T_t - T_s)\delta_{jk} \\ + \sum_t \frac{m_s m_t n_s \tilde{\nu}_{st}}{m_s + m_t}\left[\frac{1}{3}\delta_{jk}(\mathbf{u}_t - \mathbf{u}_s)^2 + (u_{t,j}u_{t,k} - u_{s,j}u_{s,k}) + \frac{m_s}{m_t}\left((u_{t,j} - u_{s,j})u_{s,k} + (u_{t,k} - u_{s,k})u_{s,j}\right)\right] \end{gathered} \tag{2.33}$$

are the collision terms for the macroscopic quantities representing energy.

With the BGK elastic collision terms, the basic form of the 10-moment fluid dynamics equations for plasma modelling is complete. In the next chapter, these equations are utilized to form the MMHD model which will include multiple species of gases, reactive and non-reactive collisions, and the Maxwell's equations with divergence cleaning.

Chapter 3

Multifluid Magnetohydrodynamics Model

3.1 Overview

This chapter presents the proposed MMHD model along with Generalized Lagrange Multiplier (GLM) method used here for divergence cleaning. Included in the chapter is the full MMHD model description, with elastic and inelastic collision terms involving charge exchange and ionization-recombination for the ions and electrons. Several subsets of the model are also presented including the 10-moment two-fluid magnetohydrodynamics (10TFMHD) model and different proposed divergence cleaning methods for the numerical treatment of Maxwell's equations.

3.2 Maxwell's Equations

In order to have a complete description of a plasma, the electro-magnetic fields must be described in addition to the fluid properties of each component of the plasma. This is done through the solution of Maxwell's equations [100], presented here in vector notation as reformulated by Heaviside [101] as follows:

$$\frac{\partial \mathbf{B}}{\partial t} + \nabla \times \mathbf{E} = \mathbf{0}, \tag{3.1}$$

$$\frac{\partial \mathbf{D}}{\partial t} - \nabla \times \mathbf{H} = -\mathbf{j}, \tag{3.2}$$

$$\nabla \cdot \mathbf{B} = 0, \tag{3.3}$$

$$\nabla \cdot \mathbf{E} = \frac{\rho_q}{\epsilon_0}, \tag{3.4}$$

which in turn represent Faraday's law, Ampère's law, Gauss's law for magnetism (also known as the solenoidal condition) and Gauss's law, respectively. In the above equations, $\mathbf{B}$ is the magnetic flux density vector, $\mathbf{E}$ is the electric field intensity vector, $\mathbf{H}$ is the magnetic field intensity vector, $\mathbf{D}$ is the electric displacement vector, $\mathbf{j}$ is the current density vector, ρ_q is the charge density, and ϵ_0 is the electrical permittivity of free space. The vectors $\mathbf{B}$ and $\mathbf{H}$, and $\mathbf{E}$ and $\mathbf{D}$ are related by

$$\mathbf{B} = \mu_0 \mathbf{H}, \tag{3.5}$$

$$\epsilon_0 \mathbf{E} = \mathbf{D}, \tag{3.6}$$

where μ_0 is the magnetic permeability of vacuum. The charge density for the plasma is given by

$$\rho_q = \sum_s q_s n_s, \tag{3.7}$$

which involves a sum over all species in the plasma. In the MMHD model described in the section to follow, only Equations (3.1), and (3.2) are solved through numerical methods and the solenoidal condition, and Gauss's law, Equations (3.3) and (3.4), which are in fact constraints on the solutions of the other two equations, are not directly enforced. The treatment of these equations is addressed in Section 3.8.

3.3 Multifluid MHD Governing Equations

The MMHD model with no divergence cleaning is presented first. This model is used extensively for analysis, especially for 1D problems an analyses, as there is no need to correct for $\nabla \cdot \mathbf{B} = \mathbf{0}$ when only the evaluation of one-dimensional fluxes is required and initial jumps in the normal component of the magnetic field are not admissible. The governing equations for the MMHD model presented here are a follow on to the two-fluid model of Shumlak and Loverich [62]. The model is extended to include the 10-moment fluid dynamics equations from Chapter 2 in a similar fashion to Hakim *et al.* [64–66]. It is generalized to include a neutral third species with elastic and inelastic collision effects between the three species.

When the 10-moment fluid dynamics equations for plasmas, Equations (2.15)-(2.17), are taken to represent each component of a three-species plasma consisting of neutrals, ions and electrons, and coupled with Faraday's law, Equation (3.1), and Ampère's law, Equation (3.2), to prescribe the electromagnetic forces, the resulting coupled set of governing equations can be expressed in

weak conservation form as

$$\frac{\partial \mathbf{U}}{\partial t} + \nabla \cdot \overrightarrow{\mathbf{F}} = \frac{\partial \mathbf{U}}{\partial t} + \frac{\partial \mathbf{F}_i}{\partial x_i} = \mathbf{S} + \mathbf{S}^{col} \tag{3.8}$$

with

$$\mathbf{U} = \begin{pmatrix} \mathbf{U}_{ion} \\ \mathbf{U}_e \\ \mathbf{U}_n \\ \mathbf{U}_M \end{pmatrix}, \quad \mathbf{F}_i = \begin{pmatrix} \mathbf{F}_{ion,i} \\ \mathbf{F}_{e,i} \\ \mathbf{F}_{n,i} \\ \mathbf{F}_{M,i} \end{pmatrix}, \quad \mathbf{S} = \begin{pmatrix} \mathbf{S}_{ion} \\ \mathbf{S}_e \\ \mathbf{S}_n \\ \mathbf{S}_M \end{pmatrix}, \quad \mathbf{S}^{col} = \begin{pmatrix} \mathbf{S}_{ion}^{col} \\ \mathbf{S}_e^{col} \\ \mathbf{S}_n^{col} \\ \mathbf{S}_M^{col} \end{pmatrix}, \tag{3.9}$$

where

$$\mathbf{U}_s = \begin{pmatrix} \rho_s \\ \rho_s u_{s,k} \\ \rho_s u_{s,j} u_{s,k} + P_{s,jk} \end{pmatrix}, \quad \mathbf{F}_{s,i} = \begin{pmatrix} \rho_s u_{s,i} \\ \rho_s u_{s,i} u_{s,k} + P_{s,ik} \\ \rho_s u_{s,i} u_{s,j} u_{s,k} + P_{s,jk} u_{s,i} \\ + P_{s,ik} u_{s,j} + P_{s,ij} u_{s,k} \end{pmatrix}, \tag{3.10}$$

$$\mathbf{S}_s = \begin{pmatrix} 0 \\ q_s \frac{\rho_s}{m_s} \left(E_k + \epsilon_{k\alpha\gamma} u_{s\alpha} B_\gamma \right) \\ q_s \frac{\rho_s}{m_s} \left(u_{s,j} E_k + u_{s,k} E_j \right) + q_s \frac{\rho_s}{m_s} \left(\epsilon_{j\alpha\gamma} u_{s,\alpha} u_{s,k} + \epsilon_{k\alpha\gamma} u_{s,\alpha} u_{s,j} \right) B_\gamma \\ + \frac{q_s}{m_s} \left(\epsilon_{j\alpha\gamma} P_{s,\alpha k} + \epsilon_{k\alpha\gamma} P_{s,\alpha j} \right) B_\gamma \end{pmatrix}, \tag{3.11}$$

and where $s \in \{ion, e, n\}$. Maxwell's equations are represented as

$$\mathbf{U}_M = \begin{pmatrix} B_j \\ \varepsilon_0 E_j \end{pmatrix}, \quad \mathbf{F}_{M,i} = \begin{pmatrix} \epsilon_{ji\alpha} E_\alpha \\ -\varepsilon_0 c^2 \epsilon_{ji\alpha} B_\alpha \end{pmatrix}, \quad \mathbf{S}_M = \begin{pmatrix} 0 \\ e \left(\frac{\rho_e}{m_e} u_{e,j} - \frac{\rho_{ion}}{m_{ion}} u_{ion,j} \right) \end{pmatrix}. \tag{3.12}$$

The individual species solution, flux and source vectors of Equations (3.10) and (3.11) are ordered starting with the continuity equation, then the momentum equations, and finally the energy equations, where ρ_s is the density, $\mathbf{u}_s$ is the bulk velocity, $P_{s,jk}$ is the three dimensional pressure tensor, q_s is the charge, and m_s is the mass for species s. Going from the vector notation in Equation (3.8) to the tensor representations in Equations (3.10) and (3.11), it should be noted that the index i is associated with the derivative with respect to x in the flux terms.

Maxwell's equations given in Equation (3.12) include both Faraday's and Ampére's laws for the electric field $\mathbf{E}$, and the magnetic field $\mathbf{B}$, respectively, ε_0 is the permittivity of free space and c

is the speed of light. As mentioned previously, the solenoidal condition, Equation (3.3), and the charge displacement, Equation (3.4) are not strictly enforced. In 1D simulations, the solenoidal condition is automatically satisfied, however there can be charge displacement errors, but for the 1D simulations considered here they are assumed to be negligible. The solenoidal condition, however, does play a role when extending the model to the 2D case and the treatments of both constraints, Equations (3.3) and (3.4), are discussed in Section 3.8 to follow. The source vector of Equation (3.11) only includes the non-collision source terms with the collision source terms, $\mathbf{S}_s^{col}$, defined and addressed in the next section.

3.4 Collision Source Terms

The collision source terms of Equations (3.8) and (3.9) are comprised of several individual collision terms representing different particle interactions and can be expanded as follows:

$$\begin{aligned}
\mathbf{S}_e^{col} &= \left(\frac{\delta F_e}{\delta t}\right)^{\text{col}} = \sum_{\sigma\in\{ion,e,n\}} \left(\frac{\delta F_e}{\delta t}\right)_{e\sigma}^{\text{el}} + \left(\frac{\delta F_e}{\delta t}\right)^{\text{iz-rc}}, \\
\mathbf{S}_{ion}^{col} &= \left(\frac{\delta F_{ion}}{\delta t}\right)^{\text{col}} = \sum_{\sigma\in\{ion,e,n\}} \left(\frac{\delta F_{ion}}{\delta t}\right)_{ion\sigma}^{\text{el}} + \left(\frac{\delta F_{ion}}{\delta t}\right)^{\text{iz-rc}} + \left(\frac{\delta F_{ion}}{\delta t}\right)^{\text{cx}}, \\
\mathbf{S}_n^{col} &= \left(\frac{\delta F_n}{\delta t}\right)^{\text{col}} = \sum_{\sigma\in\{ion,e,n\}} \left(\frac{\delta F_n}{\delta t}\right)_{n\sigma}^{\text{el}} + \left(\frac{\delta F_n}{\delta t}\right)^{\text{iz-rc}} + \left(\frac{\delta F_n}{\delta t}\right)^{\text{cx}},
\end{aligned} \tag{3.13}$$

where the superscripts el, iz-rc, and cx represent elastic, ionization-recombination, and charge exchange collisions, respectively. Note that the electron collision terms do not include a charge exchange term since only ions and neutrals are involved in charge exchange. There are obviously no collision terms related to Maxwell's equations in the MMHD model and therefore

$$\mathbf{S}_M^{col} = 0. \tag{3.14}$$

The following sections summarize and provide expressions for each of the collision source terms appearing in Equation (3.13) above. For terms where the collision or reaction models require specific gas species, singly ionized argon and monatomic hydrogen gases are considered in this thesis.

3.5 Elastic Collision Source Terms

Non-equilibrium elastic collisional processes between the plasma species are represented using the BGK relaxation time approximation as presented in Section 2.7. The various terms are summarized below:

Continuity Collision Term

$$\sum_{t\in\{ion,e,n\}} \left(\frac{\delta\rho_s}{\delta t}\right)^{\text{el}}_{st} = 0, \tag{3.15}$$

Momentum Collision Terms

$$\sum_{t\in\{ion,e,n\}} \left(\frac{\delta\rho_s v_{s,k}}{\delta t}\right)^{\text{el}}_{st} = \left\langle \left(\frac{\delta(\rho_s v_{s,k})}{\delta t}\right)^{\text{el}} \right\rangle = \sum_t \rho_s \tilde{\nu}_{st}(u_{t,k} - u_{s,k}), \tag{3.16}$$

Energy Collision Terms

$$\sum_{t\in\{ion,e,n\}} \left(\frac{\delta\rho_s v_{s,j}v_{s,k}}{\delta t}\right)^{\text{el}}_{st} = \left\langle \left(\frac{\delta(\rho_s v_{s,j}v_{s,k})}{\delta t}\right)^{\text{el}} \right\rangle =$$
$$\nu_s\left(p_s\delta_{jk} - P_{s,jk}\right) + \textstyle\sum_t 2\frac{\rho_s\tilde{\nu}_{st}}{(m_s+m_t)}k_B(T_t - T_s)\delta_{jk}$$
$$+\sum_t \frac{m_t\rho_s\tilde{\nu}_{st}}{m_s+m_t}\left[\frac{1}{3}\delta_{jk}(\mathbf{u}_t-\mathbf{u}_s)^2 + (u_{t,j}u_{t,k} - u_{s,j}u_{s,k}) + \frac{m_s}{m_t}\left((u_{t,j}-u_{s,j})u_{s,k} + (u_{t,k}-u_{s,k})u_{s,j}\right)\right] \tag{3.17}$$

where $\tilde{\nu}_{st}$ and temperature $T_s$is given by

$$\tilde{\nu}_{st} = \frac{m_t}{m_s+m_t}\nu_{st}, \qquad T_s = \frac{P_s}{\rho_s \mathrm{R}_s}, \tag{3.18}$$

ν_{st} is the collision frequency for collisions between species s and t [79], and where ν_s is the self-collision frequency. Mathematical expressions are required to determine the collision frequencies for the elastic collisions and are discussed next.

3.5.1 Coulomb Collisions

The collisions between charged particles are governed by Coulomb forces, $\mathbf{F}_{st}$, which can be expressed as

$$\mathbf{F}_{st}(\mathbf{r}_{ts}) = k_e\frac{q_s q_t}{r_{ts}^2}\hat{\mathbf{r}}_{ts}, \tag{3.19}$$

where k_e is Coulomb's constant and $\mathbf{r}_{ts}$ is the vectorial distance going from particle t to s. It can be shown that the Coulomb collision frequency [102, 103] in this case is given by

$$\nu_{st} = \frac{n_t q_s^2 q_t^2}{3\pi^{3/2}\,\varepsilon_0^2 m_{st}^2\,\bar{g}_{st}}\ln\Lambda_{st}, \tag{3.20}$$

with

$$\Lambda_{st} = \frac{12\pi\varepsilon_0\,kT_{st}\lambda_{\mathrm{D}}}{|q_s\,q_t|}. \tag{3.21}$$

The weighted average for mass and temperature and the average velocity are

$$m_{st} = \tfrac{m_s m_t}{m_s+m_t}, \qquad T_{st} = \tfrac{m_t T_s + m_s T_t}{m_s+m_t}, \qquad \bar{g}_{st} = \sqrt{\tfrac{2kT_{st}}{m_{st}}}. \tag{3.22}$$

The Debye length is given by

$$\lambda_{\mathrm{D}} = \frac{1}{\sqrt{\frac{1}{\varepsilon_0}\sum_{\sigma\in\{ion,e,n\}}\frac{n_\sigma\, q_\sigma^2}{kT_\sigma}}}. \tag{3.23}$$

These expressions govern the interactions between electrons and ions only, and include self collisions.

3.5.2 Non-Coulomb Elastic Collisions

For partially ionized plasmas, a neutral species may be present in addition to the charged ions and electrons, and an appropriate non-Coulomb collision model is required to determine the collision frequencies for each of the possible interactions with the different gas types (argon and monatomic hydrogen). This is accomplished by examining the definition of the collision frequency in the BGK model which can be written formally as

$$\nu_{st} = n_t \int_{\mathbf{v}_s\in\mathbf{R}^3} d\mathbf{v}_s \int_{\mathbf{v}_t\in\mathbf{R}^3} d\mathbf{v}_t\, g_{st}\sigma_{st}(g_{st})\, f_s(\mathbf{v}_s)\, f_t(\mathbf{v}_t), \tag{3.24}$$

with $g_{st} = |\mathbf{v}_s - \mathbf{v}_t|$ and f_s is the normalized form of the distribution function, F_s/n_s. The collision cross-section σ_{st} is a function of the relative velocity of the two interacting particles s and t, where $s = t$ for self collisions. The collision cross-section is what is needed or must be defined for the various particle interactions; however, performing the integration over phase space is often not done for most practical applications. The integral is simplified by defining an average relative speed and this value is used to determine the collision cross-section and ultimately the collision frequency [104, 105]. Therefore Equation (3.24) can be simplified and approximated as

$$\nu_{st} \simeq n_t\, \bar{g}_{st}\, \sigma_{st}(\bar{g}_{st}), \tag{3.25}$$

where the average velocity is defined as

$$\bar{g}_{st} = \left(\int_{\mathbf{v}_s\in\mathbf{R}^3} d\mathbf{v}_s \int_{\mathbf{v}_t\in\mathbf{R}^3} d\mathbf{v}_t\ |\mathbf{v}_s - \mathbf{v}_t|^2\ f_s(\mathbf{v}_s) f_t(\mathbf{v}_t)\right)^{\frac{1}{2}}. \tag{3.26}$$

After performing the integration using local Maxwellian distribution functions for f_s and f_t, it can be shown that

$$\bar{g}_{st} = \sqrt{3k\left(\frac{T_s}{m_s} + \frac{T_t}{m_t}\right) + |\mathbf{u}_s - \mathbf{u}_t|^2}. \tag{3.27}$$

Please refer to the previous thesis by Ohsawa [106] for more details. What follows are the various collision cross-section models and formula utilized in the MMHD model to simulate non-reactive

elastic collisions that do not involve pure charged particle interactions. As mentioned, for this study, the plasma species considered are singly ionized, monatomic, argon and hydrogen.

Neutral Hydrogen Elastic Collisions

For the electron-hydrogen collision frequency, a linear interpolation of experimental data obtained by de Heer *et al.* [107] is used while for proton-hydrogen collisions, a curve fit to experimental data is used from Franco and Thomas [108] given by

$$\sigma_{\mathsf{H}^+\text{–}\mathsf{H}}(\mathcal{E}_{\mathrm{eV}}) = \frac{5.80 \times 10^4}{\mathcal{E}_{\mathrm{eV}}} \pi {a_0}^2 \ [\mathrm{m}^2], \tag{3.28}$$

with $\mathcal{E}_{\mathrm{eV}}$ being the thermal energy of the proton in eV, and $a_0 = 5.2918 \times 10^{-11}$ [m] is the Bohr radius. The hydrogen self collision is modelled simply as a hard sphere collision given by:

$$\sigma_{\mathsf{H}\text{–}\mathsf{H}} = 4\pi {a_0}^2, \tag{3.29}$$

where $\pi a_0^2 = 8.7974 \times 10^{-21}\,\mathrm{m}^2$ is the atomic collision cross-section.

Neutral Argon Elastic Collisions

For all neutral argon collisions, experimental tabulated data is linearly interpolated. Specifically, the electron-argon cross-sections are obtained from de Heer *et al.* [109], and ion-argon collision cross-sections are obtained from data from Cramer [110]. Finally, for neutral argon-argon self collision cross-sections, the data is obtained from Phelps *et al.* [111].

3.6 Inelastic Collision Source Terms

Though there are several different inelastic collision reactions, for this work, only the electron impact collision reactions will be considered. These are commonly single ion ionization-recombination and charge exchange reactions. For detailed derivations of the inelastic collision terms, please refer to Chapter 3 of Ohsawa's thesis [48].

3.6.1 Baum-Fang Ionization-Recombination Kinetic Reaction Equations

The Baum-Fang [112] kinetic reaction equations can be used to model the plasma reaction

$$A + e^- \underset{\beta}{\overset{\alpha}{\rightleftharpoons}} A^+ + 2e^- \tag{3.30}$$

which represents electron collision ionization where A represents the singly ionizable plasma species considered (argon or monatomic hydrogen). This is the dominant reaction for ionization-recombination when the plasmas are not weakly ionized. The rate constants α and β are for

ionization and recombination, respectively, and are determined from curve fit models or analytic models presented in Section 3.6.2.

Examining the reaction, the basic rate equations have the form

$$\begin{aligned}\left(\frac{\delta n_{ion}}{\delta t}\right)_{iz-rc} &= \alpha n_e n_n - \beta n_{ion} n_e^2, \\ \left(\frac{\delta n_e}{\delta t}\right)_{iz-rc} &= \alpha n_e n_n - \beta n_{ion} n_e^2, \\ \left(\frac{\delta n_n}{\delta t}\right)_{iz-rc} &= \beta n_{ion} n_e^2 - \alpha n_e n_n.\end{aligned} \tag{3.31}$$

It follows that,

$$\frac{\delta n_{ion}}{\delta t} = \frac{\delta n_e}{\delta t}, \qquad \frac{\delta n_n}{\delta t} = -\frac{\delta n_e}{\delta t}, \tag{3.32}$$

which means that for every ion that is created, an electron must be created, and when a neutral disappears, an ion and electron will be created. The model adopted here assumes a collision term of the form

$$\left(\frac{\delta F_s}{\delta t}\right)_{iz-rc} \equiv a_s(\Phi_s^{iz-rc} - F_s), \tag{3.33}$$

where Φ_s^{iz-rc} has the form

$$\Phi_s^{iz-rc} = n_s' \left(\frac{m_s}{2\pi k T'}\right)^{3/2} \exp\left[-\frac{m_s(\mathbf{v}_s - \mathbf{u}')^2}{2kT'}\right]. \tag{3.34}$$

This is very similar to the BGK collision term and corresponds to a local Maxwellian with new post reaction equilibrium temperatures, T', bulk velocity, $\mathbf{u}'$, and number densities, n_s', with collision coefficient a_s. These quantities are determined as described by Baum *et al.* [112].

Taking the zeroth-order velocity moment with the Gaussian distribution, Equation (2.13), for F_s, the model results in the species collisions integrals

$$\left(\frac{\delta n_s}{t}\right)^{\text{iz-rc}} = \nu_s^{\text{iz-rc}} \left(n_s' - n_s\right) \qquad s \in \{e, ion, n\}. \tag{3.35}$$

The collision frequencies are

$$\nu_{ion}^{\text{iz-rc}} = \beta n_e^2, \qquad \nu_e^{\text{iz-rc}} = \beta n_{ion} n_e, \qquad \nu_n^{\text{iz-rc}} = \alpha n_e. \tag{3.36}$$

By comparing the rate equations, Equation (3.31), to the collision term above, along with basic conservation laws for plasmas, and using the definition of the Saha's equation for the equilibrium temperature T' which is

$$\begin{aligned}\kappa(T') &= \frac{n_e' n_i'}{n_a'} \\ &= \frac{2g_{ion}}{g_n} \frac{[2\pi(m_e m_i/m_n)kT']^{3/2}}{h^3} \exp\left(-\frac{e\mathcal{E}_{iz}}{kT'}\right),\end{aligned} \tag{3.37}$$

where h is Planck's constant and $e\mathcal{E}_{iz}$ is the ionization potential energy, the equilibrium number densities are

$$n_e' = \frac{\kappa(T')n_e}{2\alpha n_{ion}} \left\{ -\beta n_{ion} + \left[\left(\beta n_{ion} + \frac{2\alpha n_{ion}}{\kappa(T')} \right)^2 + 4\frac{\alpha^2 n_{ion}}{\kappa(T')} \left(\frac{n_n}{n_e} - \frac{n_{ion}}{\kappa(T')} \right) \right]^{1/2} \right\}, \tag{3.38}$$

$$n_{ion}' = \frac{n_{ion}}{n_e} n_e', \tag{3.39}$$

$$n_n' = n_n - \left(\frac{\beta n_{ion} n_e}{\alpha} \right) \left[\frac{n_e'}{n_e} - 1 \right]. \tag{3.40}$$

The factors g_{ion} and g_n are the quantum degeneracy of the ions and neutral atoms, respectively. In equilibrium, the relationship

$$\kappa(T') = \frac{\alpha}{\beta} \tag{3.41}$$

also holds.

For the total equilibrium velocity vector, $\mathbf{u}'$, the collision integrals for the conservation of momentum were solved by taking the first-order velocity moment of Equation (3.33) to give

$$\mathbf{u}' = \frac{\beta n_e^2 n_{ion}(m_{ion}\mathbf{u}_{ion} + m_e\mathbf{u}_e) + \alpha n_e n_n m_n \mathbf{u}_n}{m_n(\alpha n_e n_n + \beta n_e^2 n_{ion})}. \tag{3.42}$$

To determine the equilibrium temperature, T', the ionization energy must be included along with the sum of the second-order velocity moments of Equation (3.33) to enforce the conservation of energy as this energy is stored within the binding energy of the electron's orbit. Therefore,

$$\sum_s \left\langle \left(\frac{\delta \frac{1}{2} m_s v^2 F_s}{\delta t} \right)_{iz-rc} \right\rangle + E_{iz} \left\langle \left(\frac{\delta F_i}{\delta t} \right)_{iz-rc} \right\rangle_i = 0. \tag{3.43}$$

The result of the integration is

$$\begin{aligned} (\alpha n_e n_n + \beta n_e^2 n_{ion} + \beta n_{ion} n_e n_e') \tfrac{3}{2} k T' + \tfrac{1}{2} m_n (\alpha n_e n_n + \beta n_{ion} n_e^2) u'^2 + e\mathcal{E}_{iz} \beta n_e^2 (n_{ion}' - n_{ion}) \\ = \beta n_e^2 \left(\tfrac{3}{2} n_{ion} k T_i + \tfrac{1}{2} n_{ion} m_{ion} u_{ion}^2 \right) + \beta n_{ion} n_e \left(\tfrac{3}{2} n_e k T_e + \tfrac{1}{2} n_e m_e u_e^2 \right) \\ + \alpha n_e \left(\tfrac{3}{2} n_n k T_n + \tfrac{1}{2} n_n m_n u_n^2 \right). \end{aligned} \tag{3.44}$$

It should be noted that in the work by Baum *et al.* [112], the n' term on the LHS is incorrectly written to be the neutral species but is in fact supposed to be the electron species as verified by doing the conservation of energy integrals. Although $\kappa(T')$ uses the equilibrium temperature, it was shown by Hoffert and Lien [113] that it is possible to substitute the current electron temperature T_e for the total equilibrium temperature T' for when the ionization is non-negligible.

Taking the preceding model and using the 10-moment Gaussian to approximate the distribution function, the appropriate velocity moments are taken to arrive at the ionization-recombination collision terms in conservative form:

$$\left(\frac{\delta F_s}{\delta t}\right)^{\text{iz-rc}} = \left[\begin{array}{lcl} \left\langle \left(\frac{\delta F_s}{\delta t}\right)^{iz-rc} \right\rangle & = & \nu_s^{\text{iz-rc}} \left(n_s' - n_s\right) \\ \left\langle \left(\frac{\delta \left(m_s \mathbf{v}_s F_s\right)}{\delta t}\right)^{iz-rc} \right\rangle & = & m_s \nu_s^{\text{iz-rc}} \left(n_s' \mathbf{u}' - n_s \mathbf{u}_s\right) \\ \left\langle \left(\frac{\delta \left(m_s v_{s,i} v_{s,j} F_s\right)}{\delta t}\right)^{iz-rc} \right\rangle & = & \nu_s^{\text{iz-rc}} \left[\left(n_s' k T' \delta_{ij} - P_{s,ij}\right)\right. \\ & & \left. + m_s \left(n_s' u_i' u_j' - n_s u_{s,i} u_{s,j}\right)\right] \end{array}\right]. \quad (3.45)$$

The above model was used for the one-dimensional solution procedure. However, it was found with the extension of the model to two-dimensions, a strict enforcement of Equation (3.32) was required to maintain conservation of mass. To enforce Equation (3.32), only the value of n_e' from Equation (3.38) is calculated, and then the source term from Equation (3.35) is determined for the electrons. Using the Equation (3.32) and Equation (3.39), all other reaction source terms were determined without calculating n_n', or other reaction source term from Equation (3.35).

3.6.2 Ionization Reaction Rates

To fully determine the ionization-reaction collision terms, either the ionization or recombination rate of Equation (3.41) requires the evaluation. This is accomplished here through either a curve fit to experimental data, or an analytic model depending on the plasma species. For this thesis a model is used to determine the ionization rate, α, and then the value of β is computed directly.

Hydrogen Ionization Reaction Rate

For monatomic hydrogen, a curve fit to the experimental data of Scholz and Walters [114] is used and is given by

$$\alpha = \kappa_{\text{iz}}(T) = 10^{-6} \exp\left(\sum_{k=0}^{6} a_k \ln(T)^k\right) \; [\frac{\text{m}^3}{\text{s}}], \quad (3.46)$$

where T is the plasma temperature defined by

$$T = \frac{m_e T_n + m_n T_e}{m_e + m_n}. \quad (3.47)$$

The coefficients are:

$$\begin{aligned} a_0 &= -9.61443 \times 10^1, \\ a_1 &= 3.79523 \times 10^1, \\ a_2 &= -7.96885, \\ a_3 &= 8.83922 \times 10^{-1}, \\ a_4 &= -5.34513 \times 10^{-2}, \\ a_5 &= 1.66344 \times 10^{-3}, \\ a_6 &= -2.08888 \times 10^{-5}. \end{aligned} \tag{3.48}$$

Argon Ionization Reaction Rate

For argon, an analytic model proposed by Hoffert and Lien [113] is used of the form

$$\alpha = \kappa_{\text{iz}}(T_e) = 3.75 \times 10^{-22} T_e^{3/2} \left(\frac{\Theta^*_{\text{A},1}}{T_e} + 2 \right) \exp\left(-\frac{\Theta^*_{\text{A},1}}{T_e} \right) \; [\frac{\text{m}^3}{\text{s}}]. \tag{3.49}$$

The characteristic temperature for excitation to the first excited state, $\Theta^*_{\text{A},1}$, for argon is $135,300$ [K].

3.7 Charge Exchange Collision Source Terms

Lastly, for the treatment of the charge exchange collision terms and for simplicity, it is assumed that the following process dominates:

$$A(\mathbf{v}_1) + A^+(\mathbf{v}_2) \rightarrow A^+(\mathbf{v}_1) + A(\mathbf{v}_2). \tag{3.50}$$

The above reaction represents an exchange of charge for the plasma species, A. The pre-collision velocities and states are preserved. Further, it is assumed these collisions are elastic in energy and velocity in that no energy is lost to particle excitation [102].

As proposed by Ripken and Fahr [105, 115], the collision terms are assumed to be made up of gain and loss terms as follows:

$$\left(\frac{\delta F_{ion}}{\delta t} \right)_{cx} = \left(\frac{\delta F_{ion}}{\delta t} \right)^{(+)} - \left(\frac{\delta F_{ion}}{\delta t} \right)^{(-)} \tag{3.51}$$

$$\begin{aligned} &= \left\langle |\mathbf{v} - \mathbf{v}_{ion}| \, \sigma_{cx} \left(|\mathbf{v} - \mathbf{v}_{ion}| \right) \right\rangle_{ion} F_n(\mathbf{v}) \\ &\quad - \left\langle |\mathbf{v} - \mathbf{v}_n| \, \sigma_{cx} \left(|\mathbf{v} - \mathbf{v}_n| \right) \right\rangle_n F_{ion}(\mathbf{v}), \end{aligned} \tag{3.52}$$

$$\left(\frac{\delta F_n}{\delta t} \right)_{cx} = \left(\frac{\delta F_n}{\delta t} \right)^{(+)} - \left(\frac{\delta F_n}{\delta t} \right)^{(-)} \tag{3.53}$$

$$\begin{aligned} &= \left\langle |\mathbf{v} - \mathbf{v}_n| \, \sigma_{cx} \left(|\mathbf{v} - \mathbf{v}_n| \right) \right\rangle_n F_{ion}(\mathbf{v}) \\ &\quad - \left\langle |\mathbf{v} - \mathbf{v}_{ion}| \, \sigma_{cx} \left(|\mathbf{v} - \mathbf{v}_{ion}| \right) \right\rangle_{ion} F_n(\mathbf{v}), \end{aligned} \tag{3.54}$$

where (+) and (−) superscripts represent gain and loss terms, respectively. The collision integrals $\langle |\mathbf{v}-\mathbf{v}_s|\,\sigma_{cx}\,(|\mathbf{v}-\mathbf{v}_s|)\rangle_s$ are very complicated and challenging to integrate directly, so several approximations and assumptions are made. The velocity dependence of the collision cross-section, σ_{cx}, is removed and the approximate collision frequency is defined as in Section 3.5.2 with the average relative velocity equation, Equation (3.27), so that

$$\langle |\mathbf{v}-\mathbf{v}_s|\,\sigma_{cx}\,(|\mathbf{v}-\mathbf{v}_s|)\rangle_s \simeq n_t \bar{g}_{st}\sigma_{cx}(\bar{g}_{st}) \equiv \nu_{st}^{cx}, \tag{3.55}$$

which results from the averaging of velocity

$$\begin{aligned} & n_t \int_{\mathbf{v}_t\in\mathbf{R}^3} d\mathbf{v}_t\,|\mathbf{v}_s-\mathbf{v}_t|\,\sigma_{cx}(|\mathbf{v}_s-\mathbf{v}_t|)\,f_t(\mathbf{v}_t) \\ \simeq\; & n_t \int_{\mathbf{v}_s\in\mathbf{R}^3} d\mathbf{v}_s \int_{\mathbf{v}_t\in\mathbf{R}^3} d\mathbf{v}_t\,|\mathbf{v}_s-\mathbf{v}_t|\,\sigma_{cx}(|\mathbf{v}_s-\mathbf{v}_t|)\,f_t(\mathbf{v}_t)\,f_s(\mathbf{v}_s). \end{aligned} \tag{3.56}$$

Refer to the textbook by Gombosi [79]. Only one collision cross-section, σ_{cx}, is required since there are only two species which can collide.

It therefore follows that the approximate collision terms for charge exchange [104, 105, 115] are approximated as

$$\left(\frac{\delta F_i}{\delta t}\right)_{cx}(\mathbf{v}_i) \equiv \nu_{cx}^{i}(n_n,\bar{v}_i)\left[\frac{n_i}{n_n}F_n(\mathbf{v}_i)-F_i(\mathbf{v}_i)\right], \tag{3.57}$$

$$\left(\frac{\delta F_n}{\delta t}\right)_{cx}(\mathbf{v}_n) \equiv \nu_{cx}^{n}(n_i,\bar{v}_i)\left[\frac{n_n}{n_i}F_i(\mathbf{v}_n)-F_n(\mathbf{v}_n)\right], \tag{3.58}$$

where

$$\nu_{cx}^{i}(n_n,\bar{v}_i) \equiv n_n \bar{g}_{in}\sigma_{cx}(\bar{v}_i), \tag{3.59}$$

$$\nu_{cx}^{n}(n_i,\bar{v}_i) \equiv n_i \bar{g}_{ni}\sigma_{cx}(\bar{v}_i), \tag{3.60}$$

with

$$\bar{g}_{in} = \bar{g}_{ni} = \left[3k_B\left(\frac{T_s}{m_s}+\frac{T_t}{m_t}\right)+(\mathbf{u}_s-\mathbf{u}_t)^2\right]. \tag{3.61}$$

Again taking velocity moments with the Gaussian approximation for the distribution function, the charge exchange collision terms are as follows:

$$\left(\frac{\delta F_{ion}}{\delta t}\right)^{\text{CX}} = \left[\begin{array}{lcl} \left\langle\left(\frac{\delta F_{ion}}{\delta t}\right)^{\text{CX}}\right\rangle & = & 0 \\ \left\langle\left(\frac{\delta\left(m_{ion}\mathbf{v}_{ion}F_{ion}\right)}{\delta t}\right)^{\text{CX}}\right\rangle & = & n_{ion}m_{ion}\nu_{ion}^{\text{CX}}\left(\mathbf{u}_n-\mathbf{u}_{ion}\right) \\ \left\langle\left(\frac{\delta\left(m_{ion}v_{ion,j}v_{ion,k}F_{ion}\right)}{\delta t}\right)^{\text{CX}}\right\rangle & = & \nu_{ion}^{\text{CX}}m_{ion}n_{ion}\left[\left(\frac{P_{n,jk}}{m_n n_n}-\frac{P_{ion,jk}}{m_{ion}n_{ion}}\right)\right. \\ & & \left.+\left(u_{n,j}u_{n,k}-u_{ion,j}u_{ion,k}\right)\right] \end{array}\right] \tag{3.62}$$

and

$$\left(\frac{\delta F_n}{\delta t}\right)^{\text{cx}} = \left[\begin{array}{lcl} \left\langle \left(\frac{\delta F_n}{\delta t}\right)^{\text{cx}} \right\rangle & = & 0 \\ \left\langle \left(\frac{\delta \left(m_n \mathbf{v}_n F_n\right)}{\delta t}\right)^{\text{cx}} \right\rangle & = & n_n m_n \nu_n^{\text{cx}} \left(\mathbf{u}_{ion} - \mathbf{u}_n\right) \\ \left\langle \left(\frac{\delta \left(m_n v_{n,j} v_{n,k} F_n\right)}{\delta t}\right)^{\text{cx}} \right\rangle & = & \nu_{ion}^{\text{cx}} m_n n_n \left[\left(\frac{P_{ion,jk}}{m_{ion} n_{ion}} - \frac{P_{n,jk}}{m_n n_n}\right)\right. \\ & & \left. + \left(u_{ion,j} u_{ion,k} - u_{n,j} u_{n,k}\right)\right] \end{array}\right]. \quad (3.63)$$

3.7.1 Collision Cross-Sections for Charge Exchange Interaction

To determine the collision cross-sections in Equations (3.59) and (3.60), experimental results are used here. The sources and form for the data are presented briefly below for both the monatomic hydrogen and argon plasmas.

Hydrogen Charge Exchange Collision Cross-Section

A curve fit to experimental data by Fite *et al.* [116] is used for the collision cross-section for monatomic hydrogen charge exchange. It has the form of a common collision cross-section with

$$\sigma_{\mathsf{H}^+-\mathsf{H}}^{\text{cx}} = \left(c_1 - c_2 \ln \mathcal{E}_{\text{eV}}\right)^{1/2} \ [\text{m}^2], \quad (3.64)$$

where $c_1 = 7.6 \times 10^{-10}$, $c_2 = 4.60 \times 10^{-11}$, and $\mathcal{E}_{\text{eV}}$ is the proton energy in eV.

Argon Charge Exchange Collision Cross-Section

For argon charge exchange, experimental data entered into a table obtained from Cramer [110] is employed. As with the ionization recombination cross-section tables, linear interpolation is used to obtain values from the table.

3.8 Divergence Cleaning Strategies for Maxwell's Equations

When the Maxwell's equations from the MMHD model, Equation (3.12), are discretized and solved numerically in two dimensions, depending on the spatial discretion procedure the divergence conditions associated with the electric and magnetic fields can no longer be guaranteed to hold. Among these are the $\nabla \cdot \mathbf{B} = 0$, solenoidal condition, Equation (3.3) and also the charge displacement condition of Equation (3.4). In order to correct for these possible errors, a divergence correction technique known as the Generalized Lagrange Multiplier (GLM) method is adopted [117, 118]. GLM treatments for both the magnetic field equations and electric field

equations are presented to effectively convect and disperse the errors associated with the non-satisfaction of these constraints away. The GLM technique was proposed and described by Munz *et al.* [117] and Dedner *et al.* [118]. A second technique is also considered for correcting errors associated with the electric field and is an adaptation of the error diffusion technique considered by Langdon and Marder [119, 120].

3.8.1 GLM Equations for the Electric Field

The basic procedure proposed by Munz *et al.* [117] is followed to modify the electric field equations of Maxwell's equations. These equations are Ampère's law, Equation (3.2), and Gauss's law, Equation (3.4). A generalized Lagrange multiplier is added to both equations to arrive at the following modified expressions:

$$\frac{\partial \mathbf{D}}{\partial t} - \nabla \times \mathbf{H} + \nabla \frac{\Phi}{\mu_0} = -\mathbf{j}, \tag{3.65}$$

$$\mathcal{D}(\Phi) + \nabla \cdot \mathbf{E} = \frac{\rho_q}{\epsilon_0}. \tag{3.66}$$

A hyperbolic set of differential equations can be formulated by defining

$$\mathcal{D}(\Phi) = \frac{1}{\chi^2} \frac{\partial \Phi}{\partial t}, \tag{3.67}$$

where Φ is the Lagrange multiplier for the electric field and χ is a non-dimensional parameter that controls the advection velocity of Φ. It is desirable for χ to have a value that is at least as large the speed of light which is the fastest propagation speed for Maxwell's equations. However, it can also be seen that as $\chi \to \infty$ the equations becomes elliptic. The final form of the GLM-corrected equations for the electric field are given by

$$\frac{\partial \mathbf{D}}{\partial t} - \nabla \times \mathbf{H} + \nabla \frac{\Phi}{\mu_0} = -\mathbf{j}, \tag{3.68}$$

$$\frac{\partial \Phi}{\partial t} + \chi^2 \nabla \cdot \mathbf{E} = \chi^2 \frac{\rho_q}{\epsilon_0}. \tag{3.69}$$

3.8.2 GLM Equations for the Magnetic Field

The magnetic field equations (Faraday's law and the solenoidal condition, Equations (3.1) and (3.3), respectively) are also modified to include GLM divergence cleaning. Following the same procedure as for the electric field and as proposed by Dedner *et al.* [118], the following GLM equations result:

$$\frac{\partial \mathbf{B}}{\partial t} + \nabla \times \mathbf{E} + \nabla \Psi = \mathbf{0}, \tag{3.70}$$

$$\mathcal{D}(\Psi) + \nabla \cdot \mathbf{B} = 0. \tag{3.71}$$

A mixed correction is chosen this time which has a hyperbolic and parabolic component, and is given by

$$\mathcal{D}(\Psi) = \frac{1}{c_h^2}\frac{\partial \Psi}{\partial t} + \frac{1}{c_p^2}\Psi, \tag{3.72}$$

where Ψ is the Lagrange multiplier for the magnetic field equations and the constants c_h and c_p are the advection speed and dissipation speed for Ψ. These choices of $\mathcal{D}(\Psi)$ result in

$$\frac{\partial \mathbf{B}}{\partial t} + \nabla \times \mathbf{E} + \nabla \Psi = \mathbf{0}, \tag{3.73}$$

$$\frac{\partial \Psi}{\partial t} + c_h^2 \nabla \cdot \mathbf{B} = -\frac{c_h^2}{c_p^2}\Psi, \tag{3.74}$$

where there is now a new source term for dissipation of Ψ in the modified solenoidal condition for $\mathbf{B}$.

3.8.3 Telegraph Equations

It is possible to reduce the GLM equations to two telegraph equations by taking the derivative of Equations (3.69) and (3.74) with respect to time and substituting the respective equations, Equations (3.68) and (3.73). Using the fact that the divergence of a curl is always 0, it can be shown that

$$\frac{\partial^2 \Psi}{\partial t^2} - c_h^2 \nabla^2 \Psi = -\frac{c_h^2}{c_p^2}\frac{\partial \Psi}{\partial t} \tag{3.75}$$

and

$$\frac{\partial^2 \Phi}{\partial t^2} - (\chi c)^2 \nabla^2 \Phi = \frac{\chi^2}{\epsilon_0}\left(\frac{\partial \rho_q}{\partial t} + \nabla \cdot \mathbf{j}\right). \tag{3.76}$$

This shows that the two GLM equation sets developed for $\mathbf{E}$ and $\mathbf{B}$ are not in fact coupled.

3.8.4 Maxwell's Equations with GLM Divergence Cleaning

By adopting the GLM approach outlined above in this work, what is referred to as the full GLM (FGLM) Maxwell's equations can then be summarized as follows:

$$\frac{\partial \mathbf{B}}{\partial t} + \nabla \times \mathbf{E} + \nabla \Psi = \mathbf{0}, \tag{3.73}$$

$$\frac{\partial \mathbf{D}}{\partial t} - \nabla \times \mathbf{H} + \nabla \frac{\Phi}{\mu_0} = -\mathbf{j}, \tag{3.68}$$

$$\frac{\partial \Psi}{\partial t} + c_h^2 \nabla \cdot \mathbf{B} = -\frac{c_h^2}{c_p^2}\Psi, \tag{3.74}$$

$$\frac{\partial \Phi}{\partial t} + \chi^2 \nabla \cdot \mathbf{E} = \chi^2 \frac{\rho_q}{\epsilon_0}. \tag{3.69}$$

These equations replace Maxwell's equations in the MMHD model, Equation (3.12), and are referred to as the multifluid magnetohydrodynamic model with GLM divergence cleaning. Another variation of Maxwell's equations, where only the divergence cleaning for the magnetic field is also considered throughout this thesis. This second approach is referred to as Maxwell's equations with magnetic field divergence cleaning (MGLM) and does not include the evolution of the electric field Lagrange variable Φ.

3.8.5 Divergence Cleaning via Diffusion for the Electric Field

Finally, alternate methods for correcting the electric field and charge separation errors that are commonly used in Particle In Cell (PIC) simulations are the Marder and Langdon-Marder schemes [119, 120]. The correction to the electric field is accomplished by adding a term that diffuses the errors associated with charge separation. In the implicit Langdon-Marder scheme, this correction takes the form

$$\mathbf{E}^{n+1}_{\text{corrected}} = \mathbf{E}^{n+1} + \Delta t \nabla \left[d \left(\nabla \cdot \mathbf{E}^{n+1} - \frac{\rho_q^{n+1}}{\epsilon_0} \right) \right]. \tag{3.77}$$

In the original Marder scheme, the variables in the diffusion term used values from the previous update instead of the current values (lagged update), namely

$$\mathbf{E}^{n+1}_{\text{corrected}} = \mathbf{E}^{n+1} + \Delta t \nabla \left[d \left(\nabla \cdot \mathbf{E}^{n} - \frac{\rho_q^{n}}{\epsilon_0} \right) \right]. \tag{3.78}$$

The diffusion coefficient d is chosen to be a function of a time scale and grid resolution specified according to

$$d \leq \frac{1}{2\Delta t} \left[\frac{\Delta x \Delta y}{\Delta x^2 + \Delta y^2} \right] \tag{3.79}$$

for 2D problems. This choice ensures that the von Neumann stability condition for diffusion is satisfied. As investigated in Langdon's paper [119], a lagged update results in less of a correction and a larger charge separation error.

The error diffusion is extended to the finite-volume schemes considered herein by simply adding a diffusion term on the left of Equation (3.78) for the electric field equations as a diffusive source term as suggested by Loverich *et al.* [66] so that the transport equation for $\mathbf{E}$ becomes

$$\frac{\partial \mathbf{E}}{\partial t} - c^2 \nabla \times \mathbf{B} = -\frac{1}{\epsilon_0}\mathbf{j} + \lambda_E \nabla \left(\nabla \cdot \mathbf{E} - \frac{\rho_q}{\epsilon_0} \right). \tag{3.80}$$

The new term on the left is non-zero when there are errors in the electric field and the resulting error is then diffused away at the rate governed by the electric diffusion coefficient λ_E. As

recommended by Loverich *et al.* [66], the diffusion coefficient is specified using

$$\lambda_E = c\Delta x \tag{3.81}$$

where Δx is chosen to be either the average, or the smallest grid spacing of the mesh. This results in a time scale of the same order as the speed of light. Solutions obtained using this method of error cleaning for the electric field are referred to as MGLMED solutions and include a GLM treatment for divergence cleaning of the magnetic field.

3.8.6 MMHD Summary

The preceding set of coupled partial differential equations describes the time evolution of partially ionized non-equilibrium anisotropic plasmas, consisting of a single ion species, in the absence of heat flux. It is important to note that the coupling of the four sets of equations for the ions, electrons, neutrals and electromagnetic fields occurs only through the source terms. Otherwise, each equation set may be treated in isolation.

3.9 The 10-Moment Two-Fluid MHD Model

In order to develop an efficient and accurate numerical solution procedure, it is useful to have a simpler subset of the MMHD equations to test. For this purpose, the 10-moment two-fluid MHD (10TFMHD) model was also formulated. The 10TFMHD model was used for many of the 1D analyses and simulations presented herein and is based on the MMHD model with no Maxwell's equations divergence cleaning.

In order to obtain the 10TFMHD model, a fully ionized plasma is assumed, eliminating the neutral species in the MMHD equations. This reduces the fluid dynamics equations to include only ions and electrons. Further, the interparticle collision terms reduce to include only the elastic collision terms of Section 3.5 (superscript el), since there are no longer any ionization or charge exchange reactions.

The above simplifications applied to the MMHD governing equations results in the following set of governing equations known as the 10-moment two-fluid MHD model (10TFMHD) in the weak conservative form, Equation (3.8) with

$$\mathbf{U} = \begin{pmatrix} \mathbf{U}_{ion} \\ \mathbf{U}_e \\ \mathbf{U}_M \end{pmatrix}, \quad \mathbf{F}_i = \begin{pmatrix} \mathbf{F}_{ion,i} \\ \mathbf{F}_{e,i} \\ \mathbf{F}_{M,i} \end{pmatrix}, \quad \mathbf{S} = \begin{pmatrix} \mathbf{S}_{ion} \\ \mathbf{S}_e \\ \mathbf{S}_M \end{pmatrix}, \quad \mathbf{S}^{col} = \begin{pmatrix} \mathbf{S}_{ion}^{col} \\ \mathbf{S}_e^{col} \\ \mathbf{S}_M^{col} \end{pmatrix}, \tag{3.82}$$

where

$$\mathbf{U}_s = \begin{pmatrix} \rho_s \\ \rho_s u_{s,k} \\ \rho_s u_{s,j} u_{s,k} + P_{s,jk} \end{pmatrix}, \quad \mathbf{F}_{s,i} = \begin{pmatrix} \rho_s u_{s,i} \\ \rho_s u_{s,i} u_{s,k} + P_{s,ik} \\ \rho_s u_{s,i} u_{s,j} u_{s,k} + P_{s,jk} u_{s,i} \\ + P_{s,ik} u_{s,j} + P_{s,ij} u_{s,k} \end{pmatrix}, \tag{3.83}$$

$$\mathbf{S}_s = \begin{pmatrix} 0 \\ q_s \frac{\rho_s}{m_s} \left(E_k + \epsilon_{k\alpha\gamma} u_{s\alpha} B_\gamma \right) \\ q_s \frac{\rho_s}{m_s} \left(u_{s,j} E_k + u_{s,k} E_j \right) + q_s \frac{\rho_s}{m_s} \left(\epsilon_{j\alpha\gamma} u_{s,\alpha} u_{s,k} + \epsilon_{k\alpha\gamma} u_{s,\alpha} u_{s,j} \right) B_\gamma \\ + \frac{q_s}{m_s} \left(\epsilon_{j\alpha\gamma} P_{s,\alpha k} + \epsilon_{k\alpha\gamma} P_{s,\alpha j} \right) B_\gamma \end{pmatrix}, \tag{3.84}$$

and where $s \in \{ion, e\}$. Maxwell's equations are represented as

$$\mathbf{U}_M = \begin{pmatrix} B_j \\ \varepsilon_0 E_j \end{pmatrix}, \quad \mathbf{F}_{M,i} = \begin{pmatrix} \epsilon_{ji\alpha} E_\alpha \\ -\varepsilon_0 c^2 \epsilon_{ji\alpha} B_\alpha \end{pmatrix}, \quad \mathbf{S}_M = \begin{pmatrix} 0 \\ e \left(\frac{\rho_e}{m_e} u_{e,j} - \frac{\rho_{ion}}{m_{ion}} u_{ion,j} \right) \end{pmatrix}. \tag{3.85}$$

The collision terms simplify to

$$\mathbf{S}_s^{col} = \begin{pmatrix} 0 \\ \rho_s \tilde{\nu}_{st} \left(u_{t,k} - u_{s,k} \right) \\ \nu_s \left(p_s \delta_{jk} - P_{s,jk} \right) + 2 \frac{\rho_s \tilde{\nu}_{st}}{(m_s + m_t)} k_B (T_t - T_s) \delta_{jk} \\ + \frac{m_t \rho_s \tilde{\nu}_{st}}{m_s + m_t} \left[\frac{1}{3} \delta_{jk} (\mathbf{u}_t - \mathbf{u}_s)^2 + (u_{t,j} - u_{s,j})(u_{t,k} - u_{s,k}) \right] \\ + \rho_s \tilde{\nu}_{st} \left[u_{s,k} (u_{t,j} - u_{s,j}) + u_{s,j} (u_{t,k} - u_{s,k}) \right] \end{pmatrix}, \quad (s,t) \in \{(e, ion),\ (ion, e)\}. \tag{3.86}$$

It is remembered that

$$\mathbf{S}_M^{col} = 0. \tag{3.87}$$

Chapter 4

Dispersion Analysis of Multifluid MHD Models

4.1 Overview

Contained in this chapter are dispersion analyses performed on the subset of the MMHD model, the 10TFMHD model described in the previous chapter. Various analyses have also been performed on the 5-moment two-fluid model of Shumlak and Loverich which includes an analytical and a numerical analysis of the non-discrete and discrete equations. The full dispersion analyses of the Shumlak and Loverich two-fluid model can be found in Appendix A. The results of the dispersion analysis on the 10TFMHD model indicate that the system of equations, while hyperbolic, also contain a wide range of disparate wave speeds and time scales. A numerical solution framework is proposed based on the results of the dispersion analysis and a discrete dispersion analysis is then applied to the resulting one-dimensional linearized equations of the framework. The results of the discrete dispersion analysis indicate that the system is compatible for solution by an appropriately selected combination of upwind finite-volume and implicit time marching methods.

4.2 Dispersion Analysis of the Two-Fluid MHD Model

In order to better understand the physical and mathematical behaviour represented by the system of equations given by Equations (3.8)–(3.13), and to aid in the development of an appropriate numerical solution procedure, a dispersion analysis of the MMHD subset, 10TFMHD,

was first carried out as part of this thesis. The dispersion analysis proceeded along the same lines as the 5-moment dispersion analysis that is included in the Appendix A for completeness; however, notable deviations included the 10-moment fluid description and inclusion of the influences of interparticle collision terms. Similar dispersion analyses have been carried out by Brown *et al.* [86], Groth *et al.* [121], and Hittinger [122] for the 10- and 35-moment closures of neutral, non-magnetized, gases. A description of the results of this dispersion analysis are now summarized below.

4.2.1 Non-Dimensional Linearized Transport Equations

The dispersion analysis is applied to the linearized form of the equations. In order to linearize the equations of the two-fluid MHD model of Section 3.9, it is first rearranged into a non-conservative form given by

$$\frac{\partial \mathbf{W}}{\partial t} + \mathcal{A}\frac{\partial \mathbf{W}}{\partial x} + \mathcal{B}\frac{\partial \mathbf{W}}{\partial y} + \mathcal{C}\frac{\partial \mathbf{W}}{\partial z} = \mathcal{S}\mathbf{W} \tag{4.1}$$

where the primitive solution vector is

$$\mathbf{W} = \begin{pmatrix} \mathbf{W}_{ion} \\ \mathbf{W}_{e} \\ \mathbf{W}_{M} \end{pmatrix}, \qquad \mathbf{W}_s = \begin{pmatrix} \rho_s \\ u_{s,x} \\ u_{s,y} \\ u_{s,z} \\ P_{s,xx} \\ P_{s,xy} \\ P_{s,xz} \\ P_{s,yy} \\ P_{s,yz} \\ P_{s,zz} \end{pmatrix}, \qquad \mathbf{W}_M = \begin{pmatrix} B_x \\ B_y \\ B_z \\ E_x \\ E_y \\ E_z \end{pmatrix}, \tag{4.2}$$

and $s \in \{ion, e\}$. The equations are then non-dimensionalized with respect to the following quantities:

$$\nu, \quad \rho_{ref}, \quad p_{ref}, \quad m_{ref}, \quad \mu_0, \tag{4.3}$$

which correspond to the interspecies collision frequency, the reference density, the reference isotropic pressure, the reference mass, and the magnetic permeability of free space, respectively. A reference sound speed can also be defined as $a_{ref} = \sqrt{\gamma p_{ref}/(\rho_{ref})}$. Using the preceding

quantities, the following transformations to non-dimensional variables is adopted:

$$\begin{gathered} t = \bar{t}\frac{1}{\nu}, \quad x = \bar{x}\frac{a_{ref}}{\nu}, \\ m_{ion} = \bar{m}_{ion} m_{ref}, \quad m_e = \bar{m}_e m_{ref}, \quad \rho_{ion} = \bar{\rho}_{ion}\rho_{ref}, \quad \rho_e = \bar{\rho}_e \rho_{ref}, \\ \mathbf{u}_{ion} = \bar{\mathbf{u}}_{ion} a_{ref}, \quad \mathbf{u}_e = \bar{\mathbf{u}}_e a_{ref}, \quad p_{ion} = \bar{p}_{ion}\gamma p_{ref}, \quad p_e = \bar{p}_e \gamma p_{ref}, \\ \mathbf{E} = \bar{\mathbf{E}}\gamma p_{ref}\sqrt{\frac{\mu_0}{\rho_{ref}}}, \quad \mathbf{B} = \bar{\mathbf{B}}\sqrt{\mu_0 \gamma p_{ref}}, \quad T = \bar{T}\frac{\gamma p_{ref}}{\rho_{ref}\mathrm{R}_{ion}}, \end{gathered} \tag{4.4}$$

where the bar indicates the appropriate non-dimensional quantity. Please note that in the remainder of this section, the bars have been dropped for simplicity.

The corresponding non-dimensional and non-conservative form of the governing equations are then linearized about an equilibrium solution state, $\mathbf{W}_0$, defined by

$$\mathbf{W}_0 = \begin{pmatrix} \mathbf{W}_{0,ion} \\ \mathbf{W}_{0,e} \\ \mathbf{W}_{0,M} \end{pmatrix}, \qquad \mathbf{W}_{0,s} = \begin{pmatrix} \rho_{0,s} \\ 0 \\ 0 \\ 0 \\ p_{0,s} \\ 0 \\ 0 \\ p_{0,s} \\ 0 \\ p_{0,s} \end{pmatrix}, \qquad \mathbf{W}_{0,M} = \begin{pmatrix} B_{0,x} \\ B_{0,y} \\ B_{0,z} \\ 0 \\ 0 \\ 0 \end{pmatrix}, \tag{4.5}$$

for which the average velocity, off diagonal pressure terms, and background electric field are assumed to be zero, which are all valid assumptions for quiescent plasmas under equilibrium conditions. The linearization is then achieved by assuming that the solution vector can be approximated by the perturbed solution vector defined by

$$\mathbf{W}^* = \mathbf{W}_0 + \tilde{\mathbf{W}}, \tag{4.6}$$

with

$$\tilde{\mathbf{W}} = \begin{pmatrix} \tilde{\mathbf{W}}_{ion} \\ \tilde{\mathbf{W}}_e \\ \tilde{\mathbf{W}}_M \end{pmatrix}, \quad \tilde{\mathbf{W}}_s = \begin{pmatrix} \tilde{\rho}_s \\ \tilde{u}_{s,k} \\ \tilde{P}_{s,jk} \end{pmatrix}, \quad \tilde{\mathbf{W}}_M = \begin{pmatrix} \tilde{B}_k \\ \tilde{E}_k \end{pmatrix}, \tag{4.7}$$

and where $\tilde{\mathbf{W}}$ is the perturbation of the solution from the equilibrium state. The resulting linearized non-conservative equations for $\tilde{\mathbf{W}}$ are then as follows:

Non-Dimensional Linearized Multispecies Non-Conservative Continuity

$$\frac{\partial \tilde{\rho}_s}{\partial t} + \rho_{0,s}\frac{\partial \tilde{u}_{si}}{\partial x_i} = 0 \qquad s \in \{e, ion\}, \tag{4.8}$$

Non-Dimensional Linearized Multispecies Non-Conservative Momentum

$$\frac{\partial \tilde{u}_{sk}}{\partial t} + \frac{1}{\rho_{0,s}} \frac{\partial \tilde{P}_{sik}}{\partial x_i} = \mathrm{Ke}\, \frac{q_s}{m_s} \left(\tilde{E}_k + \varepsilon_{k\alpha\gamma} \tilde{u}_{s\alpha} B_{0,\gamma} \right) + \tilde{\nu}_{st} \left(\tilde{u}_{tk} - \tilde{u}_{sk} \right), \qquad (s,t) \in \{(e,ion),\ (ion,e)\}, \tag{4.9}$$

Non-Dimensional Linearized Multispecies Non-Conservative Energy

$$\begin{aligned} &\frac{\partial \tilde{P}_{sjk}}{\partial t} + \delta_{jk} p_{0,s} \frac{\partial \tilde{u}_{si}}{\partial x_i} + \delta_{ij} p_{0,s} \frac{\partial \tilde{u}_{sk}}{\partial x_i} + \delta_{ik} p_{0,s} \frac{\partial \tilde{u}_{sj}}{\partial x_i} = \mathrm{Ke}\, \frac{q_s}{m_s} (\varepsilon_{j\alpha\gamma} \tilde{P}_{s\alpha k} + \varepsilon_{k\alpha\gamma} \tilde{P}_{s\alpha j}) B_{0,\gamma} \\ &\quad + \nu_s \left(\frac{1}{3} \left(\tilde{P}_{s,xx} + \tilde{P}_{s,yy} + \tilde{P}_{s,zz} \right) \delta_{jk} - \tilde{P}_{sjk} \right) + 2 \left(\frac{1}{\gamma m_{ref} \mathrm{R}_{ref}} \right) \\ &\quad + 2 \left(\frac{1}{m_{ref} \mathrm{R}_{ref}} \right) \frac{\rho_{0,s} \tilde{\nu}_{st}}{(m_s + m_t)} k_B \left[-\frac{p_{0,t}}{\rho_{0,t}^2 R_t} \tilde{\rho}_t + \frac{1}{3 \rho_{0,t} R_t} \left(\tilde{P}_{t,xx} + \tilde{P}_{t,yy} + \tilde{P}_{t,zz} \right) \right. \\ &\quad \left. + \frac{p_{0,s}}{\rho_{0,s}^2 R_s} \tilde{\rho}_s - \frac{1}{3 \rho_{0,s} R_s} \left(\tilde{P}_{s,xx} + \tilde{P}_{s,yy} + \tilde{P}_{s,zz} \right) \right] \delta_{jk}, \qquad (s,t) \in \{(e,ion),\ (ion,e)\}, \end{aligned} \tag{4.10}$$

where the non-dimensional quantity Ke is defined by

$$\mathrm{Ke} = \frac{e}{\nu m_{ref}} \sqrt{\gamma \mu_0 p_{ref}}. \tag{4.11}$$

Maxwell's equations become:

Faraday's Law

$$\frac{\partial \tilde{\mathbf{B}}}{\partial t} + \left(\frac{\partial \tilde{E}_z}{\partial y} - \frac{\partial \tilde{E}_y}{\partial z} \right)_x - \left(\frac{\partial \tilde{E}_z}{\partial x} - \frac{\partial \tilde{E}_x}{\partial z} \right)_y + \left(\frac{\partial \tilde{E}_y}{\partial x} - \frac{\partial \tilde{E}_x}{\partial y} \right)_z = 0, \tag{4.12}$$

Ampére's Law

$$\begin{aligned} &\frac{\partial \tilde{\mathbf{E}}}{\partial t} - \frac{c^2}{a_{ref}^2} \left(\left(\frac{\partial \tilde{B}_z}{\partial y} - \frac{\partial \tilde{B}_y}{\partial z} \right)_x - \left(\frac{\partial \tilde{B}_z}{\partial x} - \frac{\partial \tilde{B}_x}{\partial z} \right)_y + \left(\frac{\partial \tilde{B}_y}{\partial x} - \frac{\partial \tilde{B}_x}{\partial y} \right)_z \right) \\ &\qquad = -\frac{c^2}{a_{ref}^2} \mathrm{Ke}\, n_{ion} \tilde{\mathbf{u}}_{ion} + \frac{c^2}{a_{ref}^2} \mathrm{Ke}\, n_e \tilde{\mathbf{u}}_e. \end{aligned} \tag{4.13}$$

For the dispersion analysis, the following physical values were used to determine the various constants and reference values:

$$\begin{aligned} e &= 1.602189246 \times 10^{-19}\,\mathrm{C} & \gamma &= \tfrac{5}{3} \\ c &= 299792458\,\tfrac{\mathrm{m}}{\mathrm{s}} & m_{ref} &= m_{ion} = 1.6736 \times 10^{-27}\,\mathrm{kg} \\ \mu_0 &= 0.000001256637\,\tfrac{\mathrm{m\ kg}}{\mathrm{s^2 A^2}} & n_{ref} &= n_0 = 7.31955 \times 10^{23}\,\tfrac{1}{\mathrm{m^3}} \\ & & p_{ref} &= p_0 = 101325\,\mathrm{Pa} \end{aligned} \tag{4.14}$$

and the reference collision frequency was calculated from the ion-electron collision frequency based on the Coulomb collision model so that [103, 123]

$$\nu_{s,t} = \frac{4\sqrt{2\pi}e_\circ^4}{3k^{\frac{3}{2}}} n_{ion} Z_s^2 Z_t^2 \ln\Lambda \left(\frac{m_s + m_t}{m_s m_t}\right)^{\frac{1}{2}} \left(\frac{m_s + m_t}{m_s T_t + m_t T_s}\right)^{\frac{3}{2}} \tag{4.15}$$

where $e_\circ$ is the elementary charge constant and Z_s, Z_t is the charge number for the species s and t, respectively, and where the Coulomb logarithm is given by

$$\ln\Lambda = 23 + \frac{3}{2}\ln\left(\frac{T_e}{10^6}\right) - \frac{1}{2}\ln\left(\frac{n_e}{10^{12}}\right). \tag{4.16}$$

The collision frequency is determined by using the following conversions to CGS from SI units:

$$\begin{array}{rcl|rcl} & \textbf{CGS} & & & \textbf{SI} & \\ e_0 &=& e_{0,SI} * 2.9979 \times 10^9 \,\frac{\text{statC}}{\text{C}} & e_{0,SI} &=& 1.602189246 \times 10^{-19}\,\text{C} \\ k &=& k_{SI} * 1.0 \times 10^7 \,\frac{\text{erg}}{\text{J}} & k_{SI} &=& 1.380658 \times 10^{-23}\,\frac{\text{J}}{\text{K}} \\ n_0 &=& n_{0,SI} * 1.0 \times 10^{-6}\,\frac{\text{m}^3}{\text{cm}^3} & n_{0,SI} &=& 7.31955 \times 10^{23}\,\frac{1}{\text{m}^3} \\ m_e &=& m_{e,SI} * 1.0 \times 10^3\,\frac{\text{g}}{\text{kg}} & m_{e,SI} &=& 9.1093897 \times 10^{-31}\,\text{kg} \\ m_I &=& m_{I,SI} * 1.0 \times 10^3\,\frac{\text{g}}{\text{kg}} & m_{I,SI} &=& 1.6736 \times 10^{-27}\,\text{kg} \end{array} \tag{4.17}$$

4.2.2 Eigenvalue Analysis

For initial value problems (IVP) with planar wave propagation in the x-direction only, the perturbative solution vector, $\tilde{\mathbf{W}}$, in Equations (4.8)–(4.13) can be assumed to have the form

$$\tilde{\mathbf{W}} = \hat{\mathbf{W}} \exp\left[i\left(\omega \bar{t}^* - k\bar{x}^*\right)\right], \tag{4.18}$$

where ω is the temporal frequency, and k is the spatial wavenumber. For the initial value problem, ω is generally complex and k is strictly real valued. This results in the following eigenvalue problem:

$$\left(i\omega\mathbf{I} - ik\mathcal{A}^* - \mathcal{S}^*\right)\tilde{\mathbf{W}} = \mathbf{0}. \tag{4.19}$$

The form of the matricies are large and are not included here, but the procedure is outlined in more detail in Appendix A for the 5-moment model. A number of simplifications are now made which include assuming equal pressures, $p_{0,ion} = p_{0,e}$, that the plasma is a fully ionized quasi neutral plasma so that $n_0 = n_{0,ion} = n_{0,e}$ or $\rho_{0,e} = (m_e/m_{ion})\rho_{0,ion}$, and that the background magnetic field is aligned with the x-direction, $\mathbf{B}_0 = (B_0, 0, 0)$. The standard right eigenvalue problem can then be formed such that

$$\mathbf{H}\hat{\mathbf{W}} = \omega\hat{\mathbf{W}}, \tag{4.20}$$

where ω corresponds to the eigenvalue of the eigenvector $\hat{\mathbf{W}}$ and

$$\mathbf{H} = k\mathcal{A}^* - i\mathcal{S}^*, \tag{4.21}$$

and $k\mathcal{A}^*$ and $\mathcal{S}^*$ are the linearized, non-dimensional x-direction coefficient and source term matrices, respectively.

4.3 Results of the Dispersion Analysis

4.3.1 Wavespeeds of Fundamental Solution Modes

The eigenvalue problem of Equation (4.20) is solved numerically for ω for a range of values of k. The wave phase speeds are given by the real part of ω divided by the spatial wavenumber k, and the figures in this section provide the phase speed, ω_R/k, as a function of k. In what follows, the various characteristics of the two-fluid MHD model are shown in the Figures 4.2–4.11, where the fastest waves will be depicted first, and more of the eigenstructure will be revealed as we telescope or zoom in to investigate the slower wave modes. In addition, the computed wave structure is compared to the dispersive wave behaviour calculated for an isotropic 5-moment version of the two-fluid MHD model. The latter is equivalent to the two-fluid model of Shumlak and Loverich with the addition of modelling for interspecies collisions. The comparison with the 5-moment version of the two-fluid MHD equations is instructive as the high frequency wavespeeds of the 5-moment model correspond to accepted wavespeeds for the various modes present in ideal MHD descriptions [33, 62].

Figure 4.1 depicts the dispersive wave nature of the 10-moment two-fluid model showing the full range of wave modes including those with the fastest wavespeeds. Unfortunately, the only waves that can be really seen for this range of velocities and wavenumber are the L- and R-waves, which are the left and right circularly polarized plasma waves, respectively [33]. The fast L- and R-mode waves are composed of a total of four waves at order 10^4 for non-equilibrium conditions or for large values of k, which is equivalent to the speed of light following the non-dimensionalization. For small k, equilibrium conditions, these waves approach infinite wavespeeds. These waves also agree with the phase speeds of the L- and R-modes of the 5-moment analysis. The infinite wavespeeds may appear to pose some problems; however, the infinite wavespeeds encountered in this analysis all originate from the electron plasma frequency, which is associated with the plasma cut off frequency. For changes in charge density less than the plasma cut off frequency, the charges will realign to cause Debye shielding. The Debye shielding will stop the propagation of these infinite wavespeeds at equilibrium conditions. Moreover, it

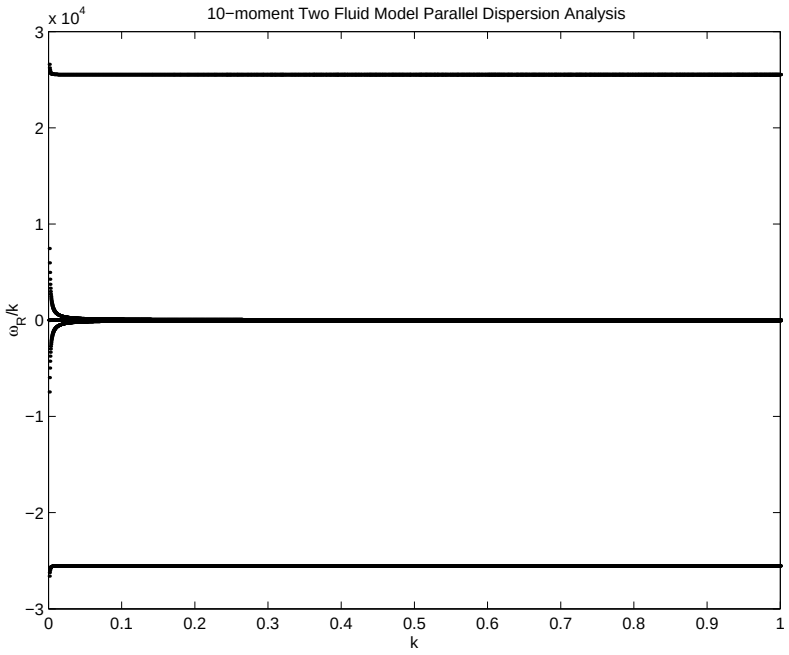

Figure 4.1: Phase speed as a function of non-dimensional wavenumber for the parallel direction, indicating behaviour of the L- and R-mode waves.

should also be noted that it is permissible for an unterminated wave phase speed to exceed c and, despite an infinite phase speed, the group velocity of these waves are in fact zero [33].

Figures 4.2 and 4.3 depict the dispersive behaviour for the next lower magnitude waves. These waves are the electron plasma waves which are the same magnitude as those in the 5-moment dispersion analysis. However, the dispersive wave behaviour of the 10-moment solution is not the same as that of the 5-moment case as can be seen in Figure 4.2. The phase speeds of the electron plasma waves are of order 10 for large values of k, which is about a thousand times slower than the L- and R-mode waves.

The next wave at about the same magnitude that can be seen in Figure 4.2 is the electron shear wave. A closer view of the high k behaviour of this wave can be seen in Figure 4.3. The behaviour of these waves for very small values of k are shown in Figure 4.4 and it can be seen that there is a pair of waves that, at this resolution, appear to be abruptly cut off. This is in fact the equilibrium behaviour of the electron shear waves, which can be seen in greater detail in Figures 4.5 and 4.7. The electron shear waves have two positive and two negatives waves that have the same phase speeds at high k as in Figure 4.3. As k decreases for conditions nearing equilibrium, the two sets of waves (one positive pair and one negative pair) approach the $\omega_R/k = 0$ axis, as seen in Figure 4.5. The waves then diverge from each other where one positive and one negative wave mode changes direction and cuts across the zero axis, while

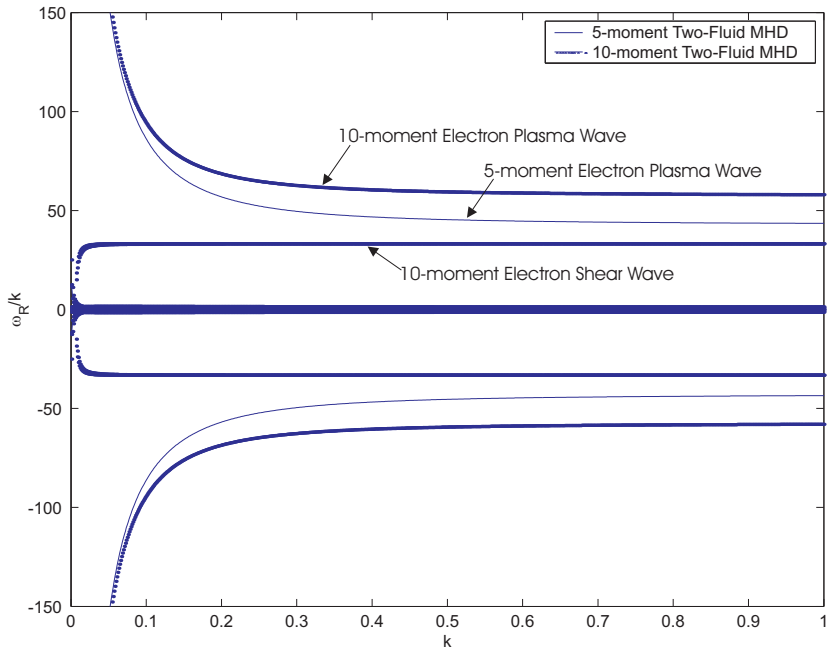

Figure 4.2: Phase speed as a function of non-dimensional wavenumber for the parallel direction showing electron plasma waves.

the other waves do not change direction, as seen in Figure 4.7. The resulting behavior of the electron shear waves can be seen in Figure 4.5 for equilibrium conditions when k is small.

For very small values of k, some interesting behaviour can be seen from the eight shear waves present in the two-fluid 10-moment solutions, which include not only the electron waves, but also the ion waves which are discussed later in this section. As can be seen in Figure 4.6, for very small values of k, some of the shear wave modes approach a phase speed of unity. There is some fairly complex structure that can be seen in the behaviour of the shear waves. Looking to the non-equilibrium region at high k, the waves that do not reverse direction when k decreases, diverge to infinity for very small values of k. This behaviour is the same for both the electron and ion plasma shear waves. The other wave, the one that cuts across the $\omega_R/k = 0$ axis then does an arc that returns towards the $\omega_R/k = 0$ axis as k becomes small, as seen in Figure 4.5, approaches plus or minus unity for equilibrium conditions. Once again, this is true for both electron and ion plasma waves, even though their phase speeds greatly differ in magnitude in the non-equilibrium regime. One positive and one negative wave from the electron and ion shear waves approaches ± 1 for very small values of k as illustrated in Figure 4.6. It shows a strong coupling between the ions and electrons since unity here corresponds to the ion acoustic speed.

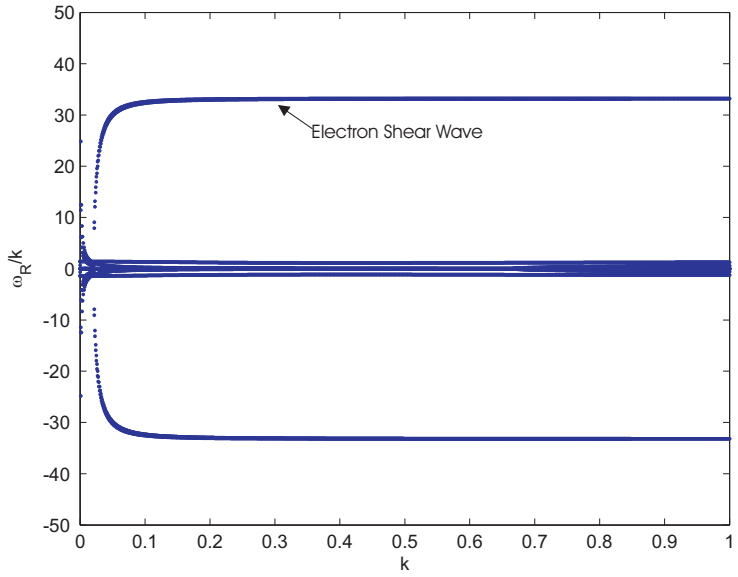

Figure 4.3: Phase speed as a function of non-dimensional wavenumber for the parallel direction showing electron shear waves.

In Figures 4.8 and 4.9, the dispersive behaviour of the Alfvén waves, which are one set of waves that do not have infinite speeds for very small values of k, can be seen. Figure 4.9 shows only the positive moving Alfvén wave compared to the 5-moment solution. At larger values of k, the behaviours of these waves depart. Remember that a value of unity here implies a value equal to the ion acoustic velocities, however, we approach ion acoustic velocities due to the non-dimensionalization which defined the magnetic field such that the Alfvén velocity $v_{al} = (cB_0\sqrt{\epsilon_0})/(\sqrt{\rho_{ref}})$ is equal to the ion acoustic velocity. In the 10-moment formulation, perturbations actually propagate faster than the Alfvén velocity, unlike in the isotropic formulation. This is perhaps due to the fact that the Alfvén phase speed is coupled to perpendicular plasma oscillations and the plasma is freer to vary in the 10-moment description as opposed to the ideal MHD limit where pressures are coupled in all directions. This is especially true for non-equilibrium conditions, which is why the Alfvén wavespeed diverges rapidly from the 5-moment isotropic result as k increases from zero, and then remains faster, and continues to diverge from the isotropic, near-equilibrium values.

There are two other major waves of interest that can be seen in Figure 4.8. One set is the ion shear waves which have been observed in previous figures. In Figure 4.10, the behaviour of the four ion shear waves can be seen bracketed within the lower hybrid wave in the small k regime. As was seen in the case of the electron shear waves, the ion shear waves exhibit complex behaviour at about $k = 0.02$. This is because the phase speeds shown in Figure 4.8 decrease

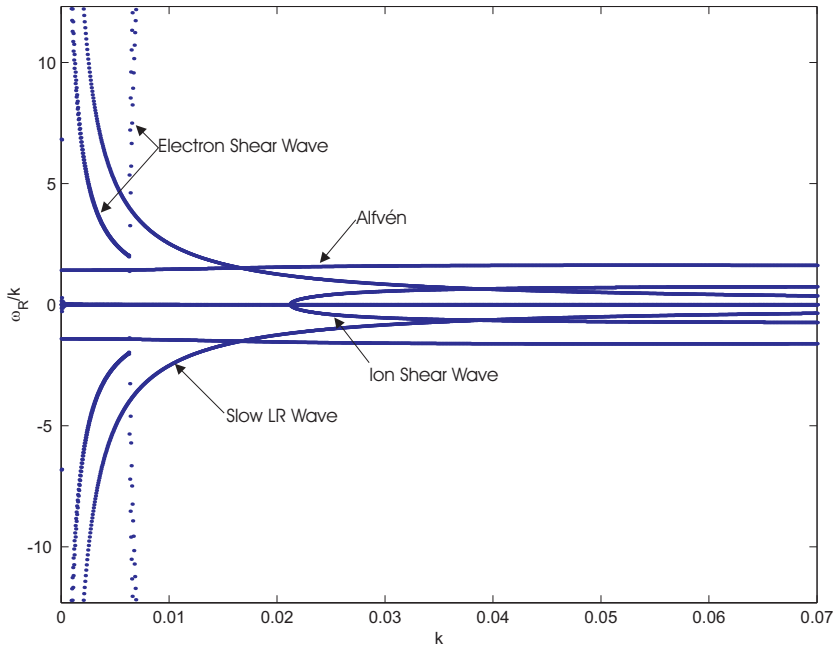

Figure 4.4: Phase speed as a function of non-dimensional wavenumber showing the dispersive wave behavior of the electron shear waves for small k.

and approach the $\omega_R/k = 0$ axis, where one pair of waves reverse direction and cross the zero axis as the electron shear waves did between $k = 0.006$ and $k = 0.007$. Note that the electron shear waves are much faster than the ion shear waves and asymptote to a constant value at smaller k than the ion shear waves. This means that electrons are much more sensitive to perturbations, and propagate for a wider range of k than the ion shear wave. This makes sense due to their relative mass differences. As in the case of the electron shear waves, the ion shear wave that reverses direction will go through a small arc, that passes very close to the $\omega_R/k = 0$ axis before approaching a phase speed of unity for very small values of k. The ion shear wave that does not reverse direction going from non-equilibrium conditions to equilibrium conditions will approach infinity for very small values of k. The ion shear waves are generally much slower than the electron shear waves for the entire domain being about two orders of magnitude slower than the electron shear waves for non-equilibrium conditions. This can be attributed to the fact that characteristic speeds tied to movement of particles are usually proportional to $1/\sqrt{m}$ and the ions are four orders of magnitude heavier than electrons.

The next waves encountered are the slow L- and R-mode waves (LR waves), which can both be seen in Figure 4.11. These waves can be seen along with the ion shear waves and are also compared to the 5-moment isotropic result. The two sets of slow LR waves do not agree exactly, however, this can be partially attributed to the fact that the LR waves for the 10-

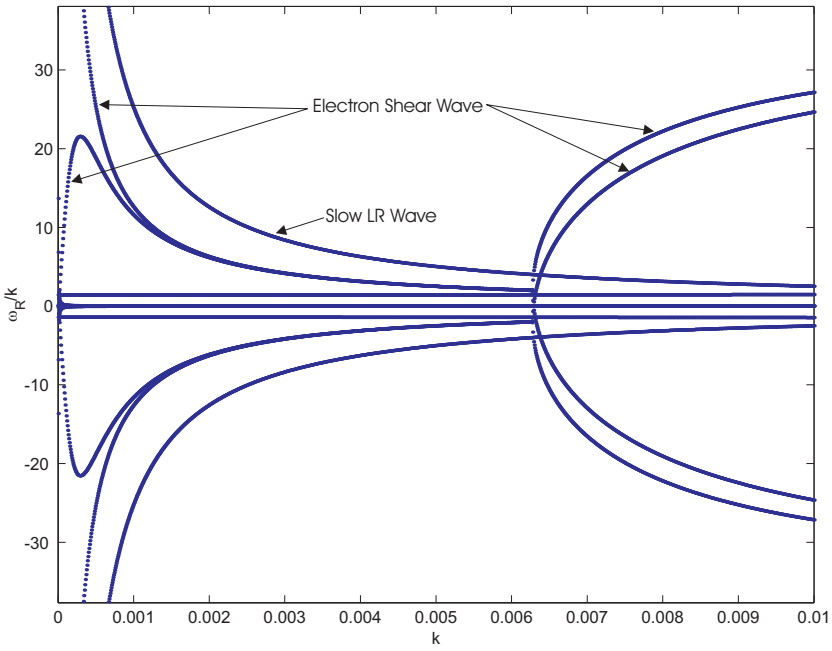

Figure 4.5: Phase speed as a function of non-dimensional wavenumber showing the dispersive wave behavior of the electron shear waves for very small k.

moment formulation now have a large imaginary component to them. The damping behaviour of these waves will be discussed in the next section. The temporal frequency of the slow LR waves are constant and not a function of k and hence the wavespeed will approach zero for very large values of k.

The last non-zero wave discussed is the lower hybrid wave. The variation of the phase speed of this wave can be seen in Figure 4.10. It is the wave that brackets the small k behaviour of the ion shear waves. The waves are relatively slow and it should be noted that the temporal frequency is constant and not a function of the spatial wavenumber, the phase speed goes to zero for very large values of k.

There are several zero magnitude waves (eight to be exact). These are waves that simply advect with the flow. These waves include electron and ion entropy, electron and ion transverse pressure waves, and magnetic and electric flux waves.

As can be seen in the dispersion analysis, the range of speeds over which the various wave modes propagate is very wide. There are large differences in phase speeds between the EM waves and the fluid dynamics waves, as well as between the propagation speeds of the ion and electron waves. These disparate speeds will present some numerical stiffness issues which need to be resolved or mitigated in any solution scheme developed for the MMHD model

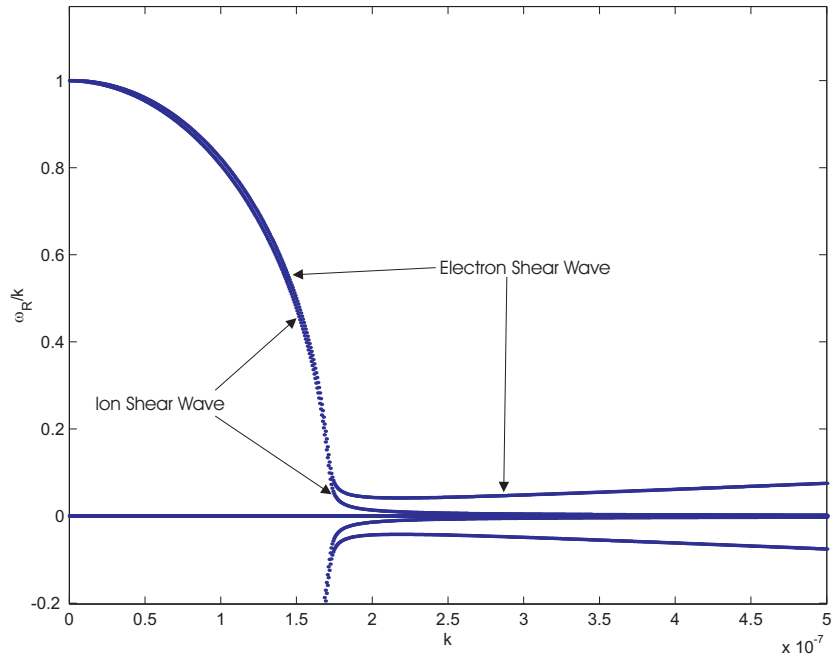

Figure 4.6: Phase speed as a function of non-dimensional wavenumber showing very small k behaviour for electron and ion shear waves for the parallel direction.

equations. Possible techniques for dealing with the stiffness would include local preconditioning methods [124–128] and the use of implicit time marching schemes [129–131].

4.3.2 Damping of Fundamental Solution Modes

In order to explore the damping behaviour of the system, the imaginary part of the eigenvalue, ω, has been analyzed. The damping behaviour is dictated by the imaginary part of Equation (4.18). Figures 4.12 and 4.13 illustrates the variation of the wave damping as a function of the wavenumber for wavenumbers in the range of 0 to 1. Figure 4.13 provides a closer look at the wave modes with lower damping rates. The number in the brackets indicate the number of waves represented by each line.

The high-speed LR waves appear to have no damping for this range. In actual fact, for very small values of k, or equilibrium conditions, when the LR wavespeeds approach infinity, there is very large damping of the waves as can be seen in Figure 4.15. This behaviour helps explain why we do not observe infinite waves in physical plasmas.

The Alfvén waves are less damped at near equilibrium conditions. At very small values of k it is not damped at all. Similarly, the electron plasma waves are also less damped nearer to

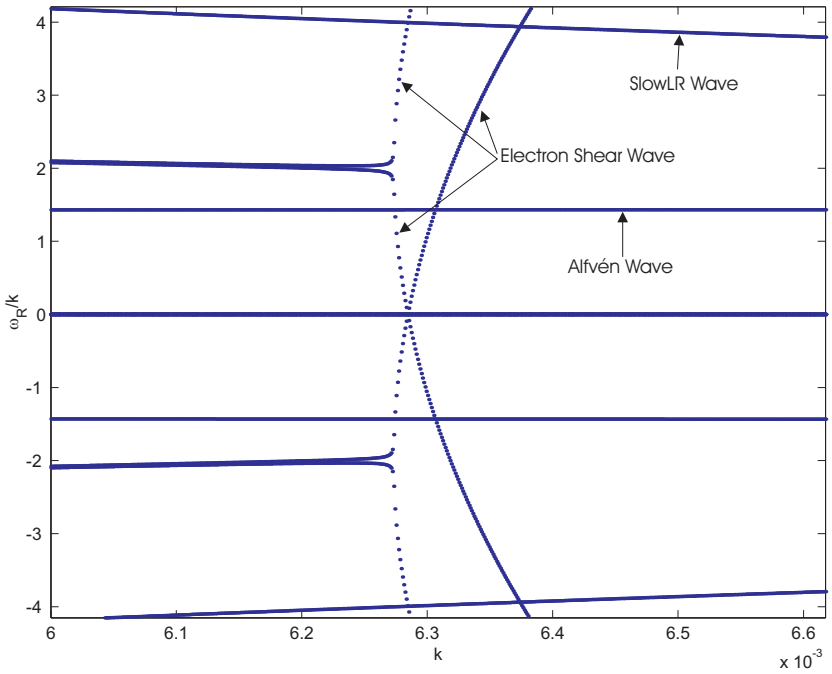

Figure 4.7: Phase speed as a function of non-dimensional wavenumber showing the dispersive wave behaviour of the electron shear waves near the $\omega_R/k = 0$ axis for small k.

equilibrium, but still remains damped for small values of k. This means perturbations and non-equilibrium disturbances are more strongly damped than equilibrium waves as can be expected of magneto-acoustic phenomenon.

There is an interesting phenomenon associated with both the ion and electron shear waves. For non-equilibrium values at large k, both sets of waves have a constant damping, where the electron shear waves have a much higher damping than the ions. This is likely due to the fact that electrons are much faster and lighter than the ions and thus, travel faster and exhibit higher damping when encountering other particles. For near equilibrium conditions, i.e., small k, both sets of the four shear waves split-off into two sets of two waves which can be seen in Figure 4.14. The split-off point for the electron shear waves coincides with the phenomenon observed in Figure 4.4. The ion shear waves exhibit a similar divergence which occurs at higher wavenumbers. This is the same point at which one set diverges to infinite phase speeds while the other set of waves cross the zero axis and eventually approaches a phase speed of unity. The labels "ESW uni" and "ISW uni" indicate the two waves that approach unity and "ESW inf" and "ISW inf" indicate the waves that approach infinity. The modes that approach unity actually end up as undamped waves for very small values of k. The "ESW uni" waves become undamped in Figure 4.15. This indicates that these ion acoustic speed waves (both electrons

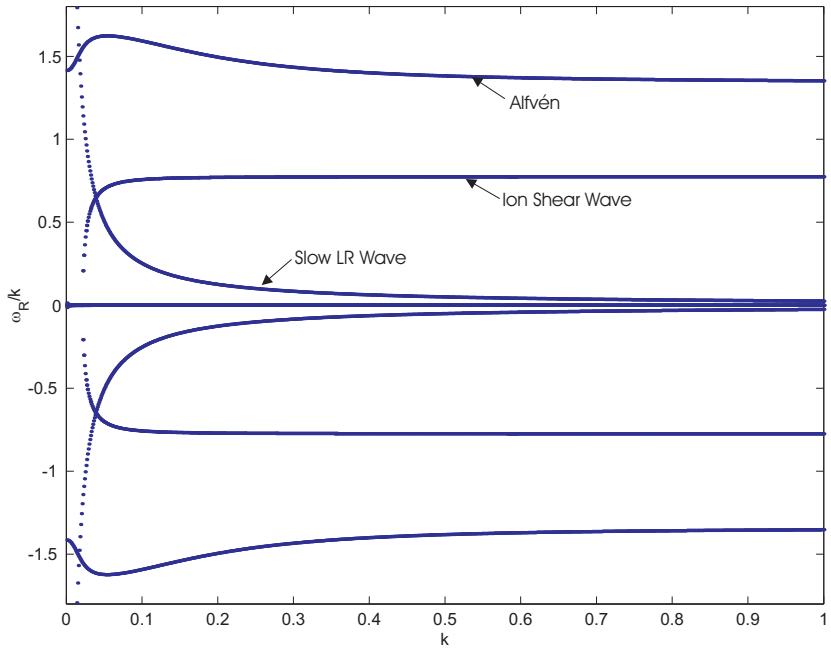

Figure 4.8: Phase speed as a function of non-dimensional wavenumber showing Alfvén and ion shear waves for the parallel direction.

and ions travelling at this speed) that propagate pressure shears are undamped at equilibrium. As mentioned before, at equilibrium conditions, there is a strong coupling between the ions and electrons, through the electric fields, causing them to propagate together at the ion acoustic velocity. The ion behaviour predominates because the larger mass of the ions over the electrons. Conversely, at non-equilibrium conditions, there is no coupling between the ions and electrons because there is insufficient time to compensate for local perturbations. For the waves that approach infinite wavespeeds, it can be seen that they are heavily damped. Once again, this helps mitigate the very fast wave speeds encountered. For the waves that approach infinity for small values of k, the electron waves are much more damped compared to the ions. Again, this is probably due to their relative masses. It should be noted that the shear waves for the ions and electrons have a similar structure to the shear waves of the 10-moment analysis for non-magnetized non-equilibrium gases [122]. The differences come from the non-dimensionalization used as well as the presence of two fluids coupled through electromagnetic forces.

The electron plasma waves exhibit less damping at equilibrium than at high k. Since the electron plasma waves are associated with thermal movements of electrons transmitting electron cyclotron information, the electron shielding at equilibrium masks strong charges while at high frequency spatial wave numbers there is less shielding resulting in strong charges and thus large damping due to coulomb collisions with other particles including the large ions impeding the

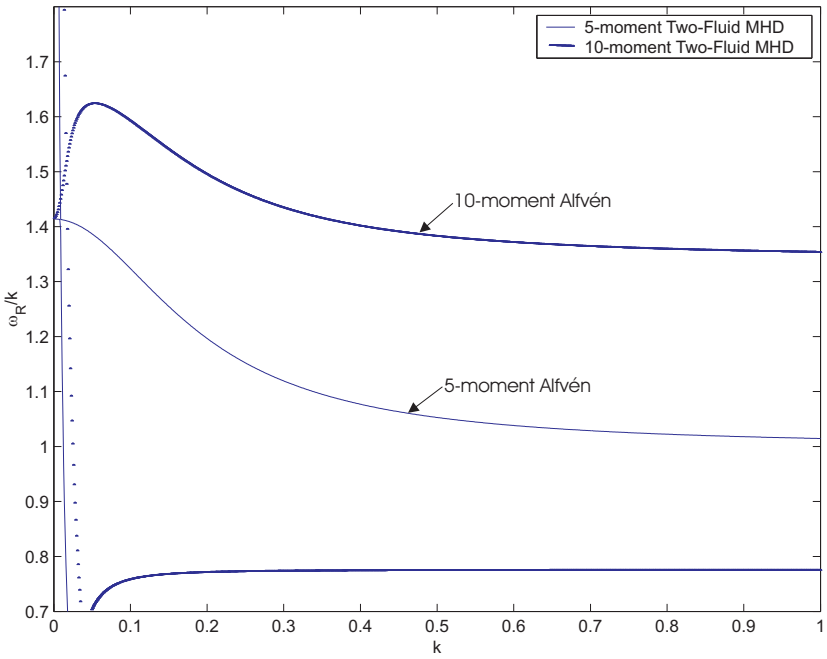

Figure 4.9: Phase speed as a function of non-dimensional wavenumber showing Alfvén waves for the parallel direction compared to the 5-moment dispersion analysis.

motion of thermal electrons. On the other hand, the lower hybrid waves, which are ion waves related to the ion plasma frequency, exhibits a constant damping rate for the full range of k considered.

The slow LR waves have the highest damping of all waves for the entire range of k. Some other waves that are present are the ion and electron transverse pressure waves which are zero velocity waves. Again the electron waves are more highly damped than the ions. There are also three undamped zero waves and one slightly damped wave. They appear to be linear combinations of transverse pressure, entropy, and parallel E and B flux waves, as determined from numerical evaluation of the corresponding eigenvectors.

4.4 Discrete Dispersion Analysis Based on Godunov Finite-Volume Scheme

In order to gain a better understanding of what sort of numerical solution scheme would be appropriate for solution of the 10TFMHD and ultimately the MMHD model, a dispersion analysis of the discretized form of the 10TFMHD equations was performed. A basic framework for the proposed numerical scheme was used to discretize the one-dimensional form of the

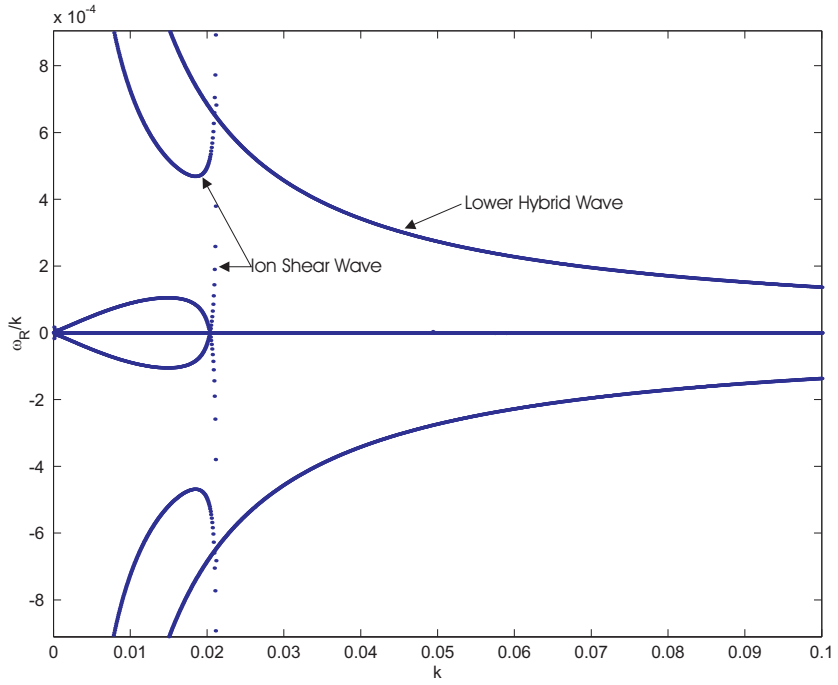

Figure 4.10: Phase speed as a function of non-dimensional wavenumber showing the lower hybrid and ion shear waves for the parallel direction.

10TFMHD equations. The proposed numerical scheme is a Godunov type finite-volume upwind scheme and is detailed in Section 5.2.1 of Chapter 5 to follow. Godunov type finite-volume schemes require a solution to a Riemann problem, and the proposed framework uses a Harten-Lax-van Leer-Einfeldt (HLLE) numerical flux function [132] and a piecewise constant spatial reconstruction. The proposed scheme considered here is a very basic first-order scheme from which a higher-order multi-dimensional numerical scheme can be developed. A summary of the results of the discrete dispersion analysis now follows.

4.4.1 Linearized Solution Scheme

Following the procedure outlined in the preceding dispersion analysis, a linearized non-dimensional form of the conservative transport equations, Equation (3.8), can be written as

$$\frac{\partial \mathbf{U}^*}{\partial t} + \frac{\partial \mathbf{F}_x^*}{\partial x} = \mathbf{S}^*, \tag{4.22}$$

where the equilibrium state used in the linearization process, $\mathbf{U}_0$, is the conservative version of Equation (4.5). The source term vector remains the same as for the non-discrete dispersion

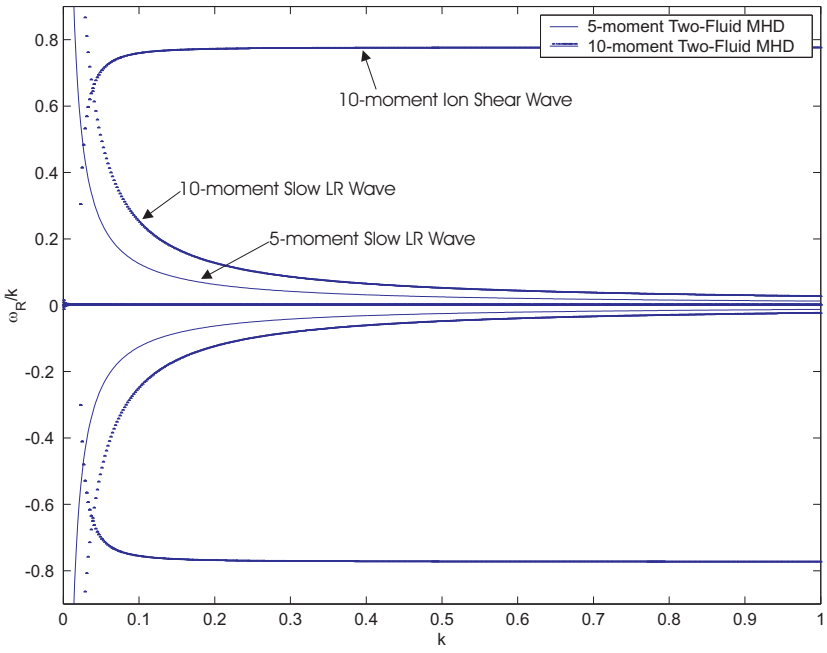

Figure 4.11: Phase speed as a function of non-dimensional wavenumber showing the slow LR waves for the parallel direction.

analysis. Therefore $\mathbf{U}^*$ and $\mathbf{F}_x^*$ is now

$$\mathbf{U}^* = \begin{pmatrix} \mathbf{U}^*_{ion} \\ \mathbf{U}^*_e \\ \mathbf{U}^*_M \end{pmatrix}, \qquad \mathbf{U}^*_s = \begin{pmatrix} \rho_{0,s} + \tilde{\rho}_s \\ \tilde{u}_{s,x} \\ \tilde{u}_{s,y} \\ \tilde{u}_{s,z} \\ p_{0,s} + \tilde{P}_{s,xx} \\ \tilde{P}_{s,xy} \\ \tilde{P}_{s,xz} \\ p_{0,s} + \tilde{P}_{s,yy} \\ \tilde{P}_{s,yz} \\ p_{0,s} + \tilde{P}_{s,zz} \end{pmatrix}, \qquad \mathbf{U}^*_M = \begin{pmatrix} \tilde{E}_x \\ \tilde{E}_y \\ \tilde{E}_z \\ B_{0,x} + \tilde{B}_x \\ B_{0,y} + \tilde{B}_y \\ B_{0,z} + \tilde{B}_z \end{pmatrix}, \tag{4.23}$$

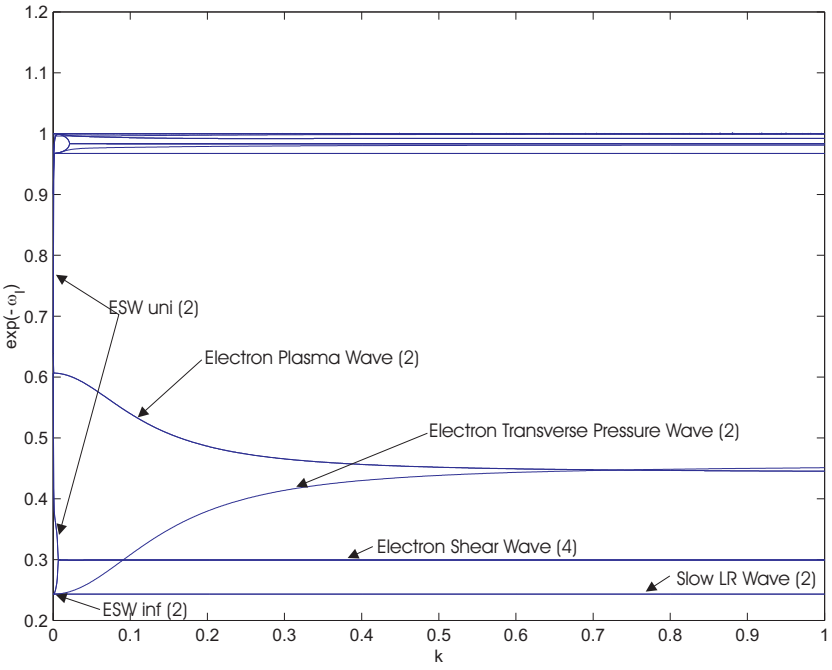

Figure 4.12: Damping factor as a function of non-dimensional wavenumber for each wave mode for the parallel direction.

$$\mathbf{F}^*_x = \begin{pmatrix} \mathbf{F}^*_{ion,x} \\ \mathbf{F}^*_{e,x} \\ \mathbf{F}^*_{M,x} \end{pmatrix}, \qquad \mathbf{F}^*_{s,x} = \begin{pmatrix} \rho_{0,s}\tilde{u}_{s,x} \\ \frac{1}{\rho_{0,s}}\left(p_{0,s} + \tilde{P}_{s,xx}\right) \\ \frac{1}{\rho_{0,s}}\tilde{P}_{s,xy} \\ \frac{1}{\rho_{0,s}}\tilde{P}_{s,xz} \\ 3p_{0,s}\tilde{u}_{s,x} \\ p_{0,s}\tilde{u}_{s,y} \\ p_{0,s}\tilde{u}_{s,z} \\ p_{0,s}\tilde{u}_{s,x} \\ 0 \\ p_{0,s}\tilde{u}_{s,x} \end{pmatrix}, \qquad \mathbf{F}^*_{M,x} = \begin{pmatrix} 0 \\ \frac{c^2}{a^2_{ref}}\tilde{B}_z \\ -\frac{c^2}{a^2_{ref}}\tilde{B}_y \\ 0 \\ -\tilde{E}_z \\ \tilde{E}_y \end{pmatrix}, \quad (4.24)$$

4.4.2 Finite-Volume Spatial Discretization and HLLE Flux Function

The proposed numerical scheme (see Chapter 5) is a Godunov-type upwind finite-volume scheme which requires a Riemann solver. The Riemann solver applied here is the HLLE approximate Riemann solver (see Chapter 5 for the rational for this choice and Appendix B.2 for a detailed description). The intermediate state $\mathbf{F}_*$ (Equation (5.12)) is used since for current purposes $(x/t) = 0$ and also because the slowest and fastest signal velocities are $\pm c$ with the equilibrium

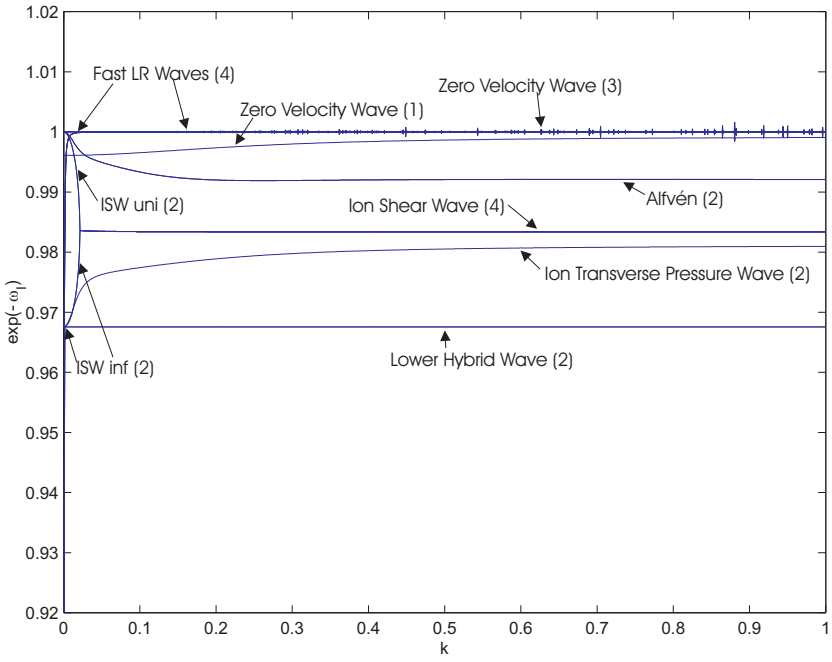

Figure 4.13: Damping factor as a function of non-dimensional wavenumber for the parallel direction showing those modes that exhibit reduced damping.

velocity being zero. The finite-volume solution of the linearized equation is considered for a uniform mesh with $x_j = x_0 + j\Delta x$ and $\Delta x = x_{j+1} - \Delta x_j = \text{constant}$. For the current analysis a piecewise constant spatial reconstruction was used as the values for the left and right states used to calculate the flux function. Therefore, for the $j+1/2$ cell division, $L = j$, and $R = j+1$, while for $j-1/2$, $L = j-1$, and $R = j$ where j is the cell index. Therefore, Equation (5.12) is taken and noting $\lambda^+\mathbf{I} = \mathbf{A}$ and $\lambda^-\mathbf{I} = -\mathbf{A}$, where $\mathbf{A}$ is a diagonal matrix with the characteristic velocities of each set of equations such that

$$\mathbf{A} = \begin{bmatrix} \mathbf{A}_{ion} & \cdots & \mathbf{0} \\ \vdots & \mathbf{A}_e & \vdots \\ \mathbf{0} & \cdots & \mathbf{A}_{Maxwell} \end{bmatrix} \quad \text{and} \quad \begin{aligned} \mathbf{A}_{ion} &= \sqrt{3}a_{ion}\mathbf{I} \\ \mathbf{A}_e &= \sqrt{3}a_e\mathbf{I} \\ \mathbf{A}_{Maxwell} &= c\,\mathbf{I} \end{aligned} \tag{4.25}$$

where

$$a_{ion} = a_{ref} = \sqrt{\frac{\gamma p_{ion}}{n_{ion} m_{ion}}}, \qquad a_e = \sqrt{\frac{\gamma p_e}{n_e m_e}}, \tag{4.26}$$

and c is the speed of light, the following sets of equations for the two fluxes involved in this formulation are finally obtained:

$$\mathbf{F}_{j+\frac{1}{2}} = \frac{1}{2}\left(\mathbf{F}_j + \mathbf{F}_{j+1} - \mathbf{A}^T\left(\mathbf{U}_{j+1} - \mathbf{U}_j\right)\right), \tag{4.27}$$

$$\mathbf{F}_{j-\frac{1}{2}} = \frac{1}{2}\left(\mathbf{F}_{j-1} + \mathbf{F}_j - \mathbf{A}^T\left(\mathbf{U}_j - \mathbf{U}_{j-1}\right)\right). \tag{4.28}$$

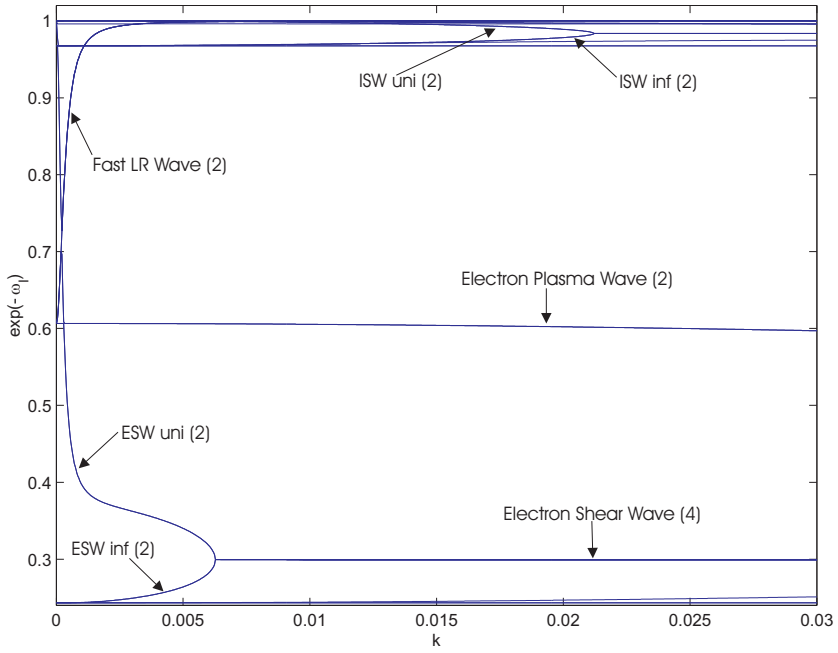

Figure 4.14: Damping factor as a function of non-dimensional wavenumber for small values of k for the parallel direction.

4.4.3 Time Marching Discretization

Two representative time marching schemes are used in order to discretize the equations. These are the rather simple first-order explicit and implicit Euler time marching schemes, respectively, which take the forms

$$\mathbf{U}_j^{n+1} = \mathbf{U}_j^n - \frac{\Delta t}{\Delta x_j}\left(\mathcal{F}_{j+\frac{1}{2}}^n - \mathcal{F}_{j-\frac{1}{2}}^n\right) + \Delta t \mathbf{S}_j^n, \tag{4.29}$$

and

$$\mathbf{U}_j^{n+1} = \mathbf{U}_j^n - \frac{\Delta t}{\Delta x_j}\left(\mathcal{F}_{j+\frac{1}{2}}^{n+1} - \mathcal{F}_{j-\frac{1}{2}}^{n+1}\right) + \Delta t \mathbf{S}_j^{n+1}. \tag{4.30}$$

Using the reconstructed flux functions of Equations (4.27) and (4.28) and substituting them into Equations (4.29) and (4.30), the following fully discrete update schemes for the solution, $\mathbf{U}$, are obtained:

$$\mathbf{U}_j^{n+1} - \mathbf{U}_j^n = \frac{\Delta t}{\Delta x_j}\left(\frac{1}{2}\right)\left[\mathbf{F}_{j-1}^n - \mathbf{F}_{j+1}^n + \mathbf{A}^T\left(\mathbf{U}_{j-1}^n - 2\mathbf{U}_j^n + \mathbf{U}_{j+1}^n\right)\right] + \Delta t \mathbf{S}_j^n, \tag{4.31}$$

and

$$\mathbf{U}_j^{n+1} - \mathbf{U}_j^n = \frac{\Delta t}{\Delta x_j}\left(\frac{1}{2}\right)\left[\mathbf{F}_{j-1}^{n+1} - \mathbf{F}_{j+1}^{n+1} + \mathbf{A}^T\left(\mathbf{U}_{j-1}^{n+1} - 2\mathbf{U}_j^{n+1} + \mathbf{U}_{j+1}^{n+1}\right)\right] + \Delta t \mathbf{S}_j^{n+1}, \tag{4.32}$$

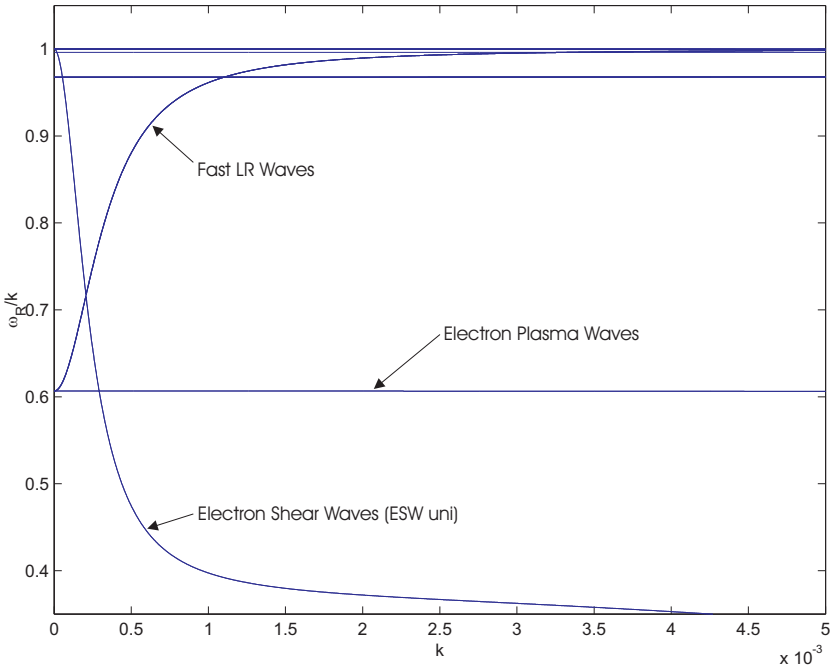

Figure 4.15: Damping factor as a function of non-dimensional wavenumber for very small values of k for the parallel direction.

for both the explicit and implicit Euler schemes, respectively. Following substitution of $\mathbf{U} = \mathbf{U}^*, \mathbf{F} = \mathbf{F}^*{}_x$, and $\mathbf{S} = \mathbf{S}^*$, the equilibrium values cancel, leaving only the perturbative terms involving equilibrium constants. The linearized non-dimensional form of the two-fluid MHD model equations results in the following fully discrete solution update scheme

$$\left(\tilde{\mathbf{W}}_j^{n+1} - \tilde{\mathbf{W}}_j^n\right) = \frac{\Delta t}{2\Delta x}\left[\mathbf{F}_{co}\left(\tilde{\mathbf{W}}_{j-1}^n - \tilde{\mathbf{W}}_{j+1}^n\right) + \mathbf{A}\left(\tilde{\mathbf{W}}_{j-1}^n - 2\tilde{\mathbf{W}}_j^n + \tilde{\mathbf{W}}_{j+1}^n\right)\right] + \Delta t \mathbf{S}_{co}\tilde{\mathbf{W}}_j^n \tag{4.33}$$

for the explicit Euler and

$$\left(\tilde{\mathbf{W}}_j^{n+1} - \tilde{\mathbf{W}}_j^n\right) = \frac{\Delta t}{2\Delta x}\left[\mathbf{F}_{co}\left(\tilde{\mathbf{W}}_{j-1}^{n+1} - \tilde{\mathbf{W}}_{j+1}^{n+1}\right) + \mathbf{A}\left(\tilde{\mathbf{W}}_{j-1}^{n+1} - 2\tilde{\mathbf{W}}_j^{n+1} + \tilde{\mathbf{W}}_{j+1}^{n+1}\right)\right] + \Delta t \mathbf{S}_{co}\tilde{\mathbf{W}}_j^{n+1} \tag{4.34}$$

for the implicit Euler where $\tilde{\mathbf{W}}_j^n$ is simply the perturbative primitive solution state vector Equation (4.6) for time level n and cell j, $\mathbf{F}^* = \mathbf{F}_{co}\tilde{\mathbf{W}}$ and $\mathbf{S}^* = \mathbf{S}_{co}\tilde{\mathbf{W}}$ which relate the flux and source terms to the perturbative solution vector through coefficient matrices. The time step is Δt. The diagonal matrix $\mathbf{A}$ contains the local numerical maximum wavespeeds of the system as a result of the HLLE Riemann flux function.

4.4.4 Discrete Eigenvalue Analysis

For the discrete eigenstructure, the trial solution for $\tilde{\mathbf{W}}$ in Equations (4.33) and (4.34) is

$$\tilde{\mathbf{W}}_j^n = Z^n \exp\left(i\left(jk\Delta x\right)\right)\hat{\mathbf{W}}. \tag{4.35}$$

Also,

$$Z = \left(\exp\left[i\,\omega\Delta t\right]\right) = e^{-\omega_I \Delta t}\left(\cos\omega_R\Delta t + i\sin\omega_R\Delta t\right) \tag{4.36}$$

where ω_R and ω_I are the real and imaginary parts of ω, respectively. Substitution of Equation (4.35) into Equations (4.33) and (4.34) results in a set of linear equations that can be expressed as an eigenvalue problem of the form

$$\mathbf{H}\hat{\mathbf{W}} = Z\hat{\mathbf{W}} \tag{4.37}$$

where

$$\mathbf{H} = \mathbf{I} + \frac{\Delta t}{\Delta x}\frac{1}{2}\left[\mathbf{F}_{co}\left(\mathrm{e}^{-ik\Delta x} - \mathrm{e}^{ik\Delta x}\right) + \mathbf{A}\left(\mathrm{e}^{-ik\Delta x} - 2 + \mathrm{e}^{ik\Delta x}\right)\right] + \Delta t\mathbf{S}_{co}, \tag{4.38}$$

and

$$\mathbf{H} = \left[\mathbf{I} - \frac{\Delta t}{\Delta x}\frac{1}{2}\left[\mathbf{F}_{co}\left(\mathrm{e}^{-ik\Delta x} - \mathrm{e}^{ik\Delta x}\right) + \mathbf{A}\left(\mathrm{e}^{-ik\Delta x} - 2 + \mathrm{e}^{ik\Delta x}\right)\right] - \Delta t\mathbf{S}_{co}\right]^{-1}, \tag{4.39}$$

for the explicit and implicit Euler time marching schemes, respectively. The time step, Δt, is determined in the same manner as the physical time step defined by Equation (5.25) through the TSCF parameter. The implicit scheme is unconditionally stable, at least for the linearized problem of interest here.

4.5 Results of Discrete Dispersion Analysis

The eigenvalue problems of Equation (4.38) and (4.39) were solved numerically for Z for a range of k values. Results for both the explicit and implicit schemes now will be presented, and the recovery of the analytic dispersive behaviour and the stability of the discrete system of equations are both examined.

4.5.1 Dispersion of the Finite-Volume Discretization with Explicit Time Marching Scheme

The dispersion of the discrete system with explicit time marching has been explored by plotting the eigenvalues of the eigen problem for four separate values of Δx ranging from $\Delta x = 1.0$ to

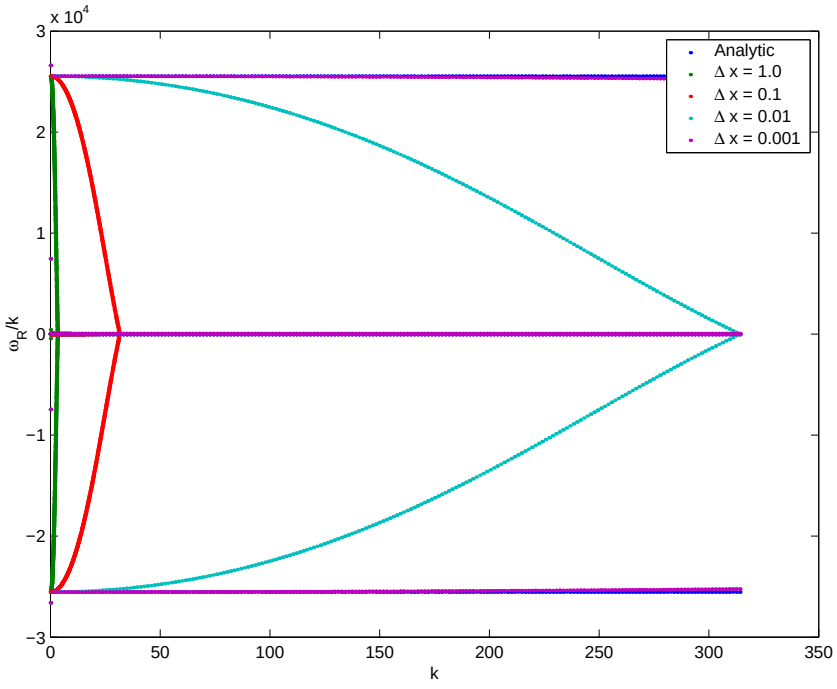

Figure 4.16: Phase speed as a function of non-dimensional wavenumber for various Δx for the parallel direction (L- and R-mode waves visible).

$\Delta x = 0.001$. The value of the TSCF parameter in all cases is 0.1. The discretized scheme is valid for k values up to $k_{\max} = \pi/\Delta x$, and a range of k up to 314 is shown to give a better illustration of the phase speed behaviour showing the full range of validity for the $\Delta x = 0.01$ case with the other cases for comparison. It should be noted that all of the following figures were stable in the imaginary plane as Δt satisfies the stability criteria of Equation (5.26). The results of the eigensystem analysis are shown in Figures 4.16 and 4.17.

As can be seen in the figures, as the Δx value becomes smaller, the wavespeeds approach the expected analytical wavespeeds described and discussed earlier in this chapter. Figure 4.16 shows the fastest L- and R-mode waves. In Figure 4.17, the scale of k is reduced to something closer to the previous analysis and the behaviour of the Alfvén waves can be seen as well as those of the ion shear wave and the slow L- and R-mode waves. Once again, the phase speeds approach the analytical values as Δx becomes small.

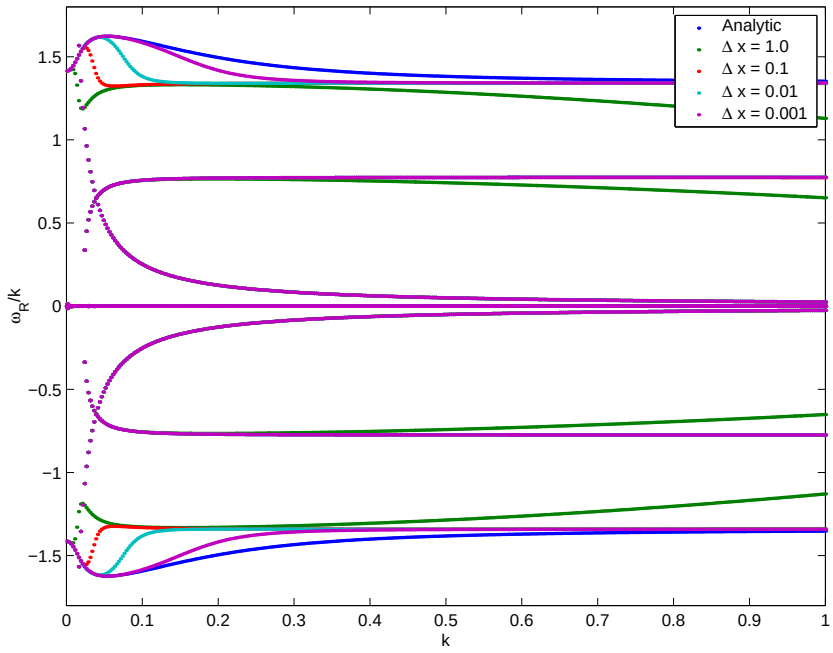

Figure 4.17: Phase speed as a function of non-dimensional wavenumber for various Δx for the parallel direction.

4.5.2 Stability of the Finite-Volume Discretization with Explicit Time Marching Scheme

Next, the stability of the finite-volume discretization with the explicit time marching scheme is examined. The stability of the solution scheme is dictated by the imaginary component of the eigenvalues. To view the unstable regions with greater ease, $-\omega_I$ as a function of non-dimensional wavenumber k is considered.

Figure 4.18 depicts the stability of the proposed solution method for when the condition of Equation (5.26) is not satisfied. A value of unity is used for Δx. and the analysis is performed for various TSCF values ranging from 100.0 to 0.1. As can be seen in Figure 4.18, the discrete equations become unstable when the TSCF is greater than unity, for which the time steps violate the stability condition of Equation (5.26). As the TSCF number becomes smaller, bringing the time step into the stable region, the imaginary component of ω moves to the stable region (i.e., $-\omega_I \leq 0$). The time step used for a TSCF of 1.0 is $\Delta t = 3.9 \times 10^{-5}$. Note that the time is non-dimensionalized according to $t = \bar{t}/\nu$ where ν is of order 10^{12} s^{-1}. This would require Δt of order 10^{-17} s to be stable. This is much smaller than other time scales associated with convection, acoustical propagation and collisional processes. This is where the stiffness arises. The electron plasma frequency dictates the numerical time step that can be taken, which is

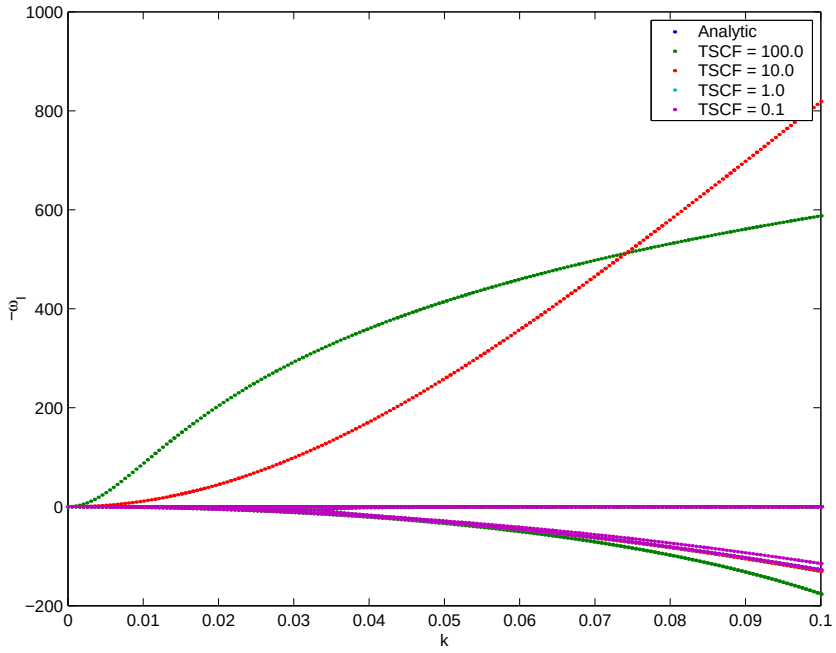

Figure 4.18: Stability of the explicit scheme for various TSCF for the parallel direction

usually much smaller than the time scales of the phenomenon that are often of primary interest.

In summary, it has been shown that an accurate numerical solution procedure for the 10TFMHD model can be achieved as Δx becomes small. This result has been found by other researchers such as Hakim *et al.* [64,65] for the two-fluid model and by Loverich *et al.* [63,133] and others [39, 43,134] for traditional MHD models. However, stability of the explicit time marching scheme is subject to the stability condition of Equation (5.26). This stability condition can result in a very stiff solution scheme if one is interested in only accurately resolving solution content associated with plasma convection, acoustical, and particle collisional processes, as is commonly the case.

4.5.3 Stability of the Finite-Volume Discretization with Implicit Time Marching Scheme

For the implicit time marching scheme, as in the explicit discrete dispersion analysis, Figure 4.19 depicts $-\omega_I$ as a function of non-dimensional wavenumber k using a Δx of unity for various values of TSCF ranging from 100.0 to 0.1. All eigenvalues in Figure 4.19 are now in the stable region ($-\omega_I \leq 0$) whereas in Figure 4.18 many of the waves were unstable when using the explicit method. It is clear that a stable and accurate solution scheme can be constructed for the 10TFMHD model using an implicit time marching scheme. The wavespeeds for the dispersion analysis of the discrete system with implicit time marching also approach the wavespeeds of

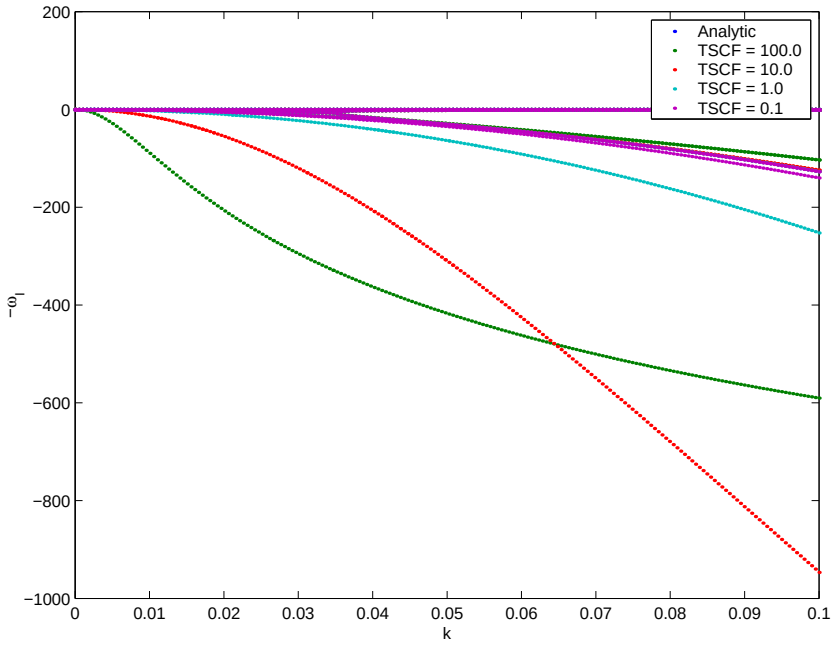

Figure 4.19: Stability of the implicit scheme for various TSCF for the parallel direction

the analytic dispersion analysis as Δx approaches zero.

4.5.4 Summary of the Results of the Discrete Dispersion Analysis

A first-order Godunov-type upwind finite-volume scheme with HLLE numerical flux functions, applied to a 10-moment description of a plasma with charged particles and a full modelling of Maxwell's equations, will produce realizable and stable, hyperbolic numerical solutions. The system has a large number of very disparate waves and time scales which must be considered and dealt with. An implicit method for the 10TFMHD system of equations can produce a stable and accurate solution. The results of the discrete dispersion analysis shows that the proposed numerical scheme produces a somewhat desirable eigensystem and suggests how to develop a full numerical scheme for the non-linear equations. The latter is the subject of the next chapter.

Chapter 5

Application of MMHD Models to One-Dimensional Plasma Flow Problems

5.1 Overview

This chapter is concerned with the development of a one-dimensional (1D) numerical scheme for the MMHD model, which was the forerunner to the fully two-dimensional (2D) scheme also developed herein. The one-dimensional study was first carried out to aid in understanding the behaviour of the MMHD system and inform the development of the proposed two-dimensional solution method. The proposed numerical scheme for the 1D case is a Godunov-type upwind finite-volume scheme using temporal limited, implicit dual-time stepping time marching. The first section of the chapter outlines the numerical solution procedure applied herein, while the second deals with results obtained from the developed numerical solution procedure for several 1D plasma flow IVPs.

5.2 Temporal Limited Implicit Dual-Time Stepping High-Order Time Marching Godunov Finite-Volume Scheme

Based on the results of the dispersion analysis of Chapter 4, a Godunov-type finite-volume upwind scheme [135] is proposed here for the solution of the MMHD equations in one space dimension, with the numerical fluxes evaluated using the HLLE approximate Riemann solver [132].

Schemes of this type are appropriate for hyperbolic systems of equations. The proposed scheme is extended to second-order spatial accuracy by way of a piecewise linear reconstruction for second-order accuracy in conjunction with a Barth-Jespersen slope limiter [136] to aid in the control of numerical oscillations. A second-order backwards difference (BDF) time marching scheme with a dual-time stepping procedure [137] along with additional temporal limiting [130] is used to compute second-order unsteady solutions. The fully implicit time marching scheme is used to integrate the resulting coupled system of ordinary differential equations that results from the finite-volume spatial discretization procedure. The combined scheme is used to solve the 10TFMHD equations for several one-dimensional problems.

5.2.1 Godunov Finite-Volume Scheme

The Godunov finite-volume upwind scheme is a monotonicity preserving scheme which is capable of capturing solution discontinuities without introducing oscillations. Originally proposed by Godunov in 1959 [135], the scheme can be derived by applying Green's theorem to Equation (3.8) to express the equations in integral form. For the one-dimensional case, Equation (3.8) reduces to

$$\frac{\partial \mathbf{U}}{\partial t} + \frac{\partial \mathbf{F}}{\partial x} = \mathbf{S} \tag{5.1}$$

where $\mathbf{U}$ is the conservative solution vector, $\mathbf{F}$ is the conservative flux vector in the x-coordinate, and $\mathbf{S}$ is the non-conservative source terms. The integral form of this equation can be written as

$$\iint \left(\frac{\partial \mathbf{U}}{\partial t} + \frac{\partial \mathbf{F}}{\partial x} \right) dxdt = \oint (\mathbf{U}dx - \mathbf{F}dt) = \iint \mathbf{S}dxdt. \tag{5.2}$$

A discrete finite-volume scheme is created by evaluating the above integral around the surface of a control volume representing a computational cell such as the one depicted in Figure 5.1. Integrating along the boundaries of the control surface in a counter-clockwise direction results in

$$\begin{gathered} \int_{x_i-\frac{\Delta x}{2}}^{x_i+\frac{\Delta x}{2}} \mathbf{U}\left(x, t_n\right) dx - \int_{t_n}^{t_n+\Delta t} \mathbf{F}\left(x_i+\frac{\Delta x}{2}, t\right) dt \\ - \int_{x_i+\frac{\Delta x}{2}}^{x_i-\frac{\Delta x}{2}} \mathbf{U}\left(x, t_n+\Delta t\right) dx + \int_{t_n+\Delta t}^{t_n} \mathbf{F}\left(x_i-\frac{\Delta x}{2}, t\right) dt = \int_{t_n}^{t_n+\Delta t} \int_{x_i-\frac{\Delta x}{2}}^{x_i+\frac{\Delta x}{2}} \mathbf{S}(x,t) dxdt \end{gathered} \tag{5.3}$$

noting that the cell average for $\mathbf{U}$ is

$$\mathbf{U}_i^n = \frac{1}{\Delta x} \int_{x_i-\frac{\Delta x}{2}}^{x_i+\frac{\Delta x}{2}} \mathbf{U}\left(x, t_n\right) dx \tag{5.4}$$

and for $\mathbf{S}$ is

$$\mathbf{S}_i^n \approx \frac{1}{\Delta t} \int_{t_n}^{t_n+\Delta t} \mathbf{S}_i(t) dt, \qquad \text{with} \qquad \mathbf{S}_i(t) = \frac{1}{\Delta x} \int_{x_i-\frac{\Delta x}{2}}^{x_i+\frac{\Delta x}{2}} \mathbf{S}(x,t) dx. \tag{5.5}$$

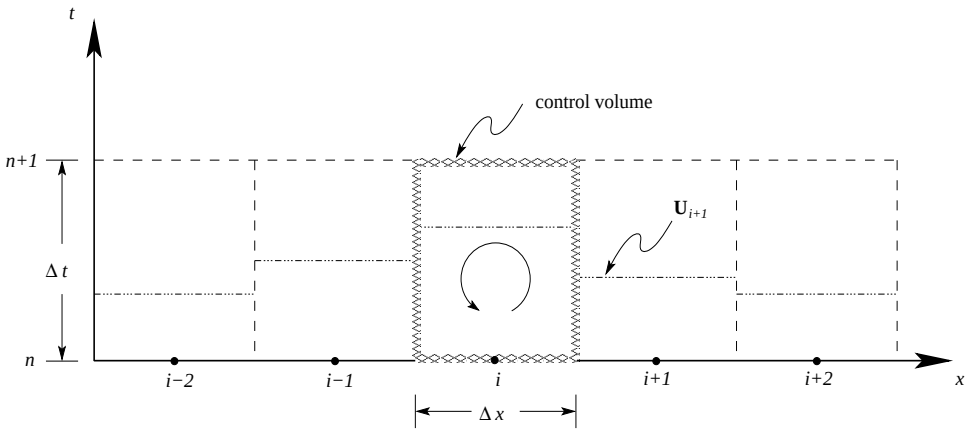

Figure 5.1: 1-D Finite-Volume Godunov's Method

The solution fluxes can be written as

$$\mathcal{F}^n_{i\pm\frac{1}{2}} = \frac{1}{\Delta t}\int_{t_n}^{t_n+\Delta t} \mathbf{F}\left(x_i \pm \frac{\Delta x}{2}, t\right) dt = \mathbf{F}\left(\mathcal{R}\left(\mathbf{U}^n_{L,i\pm\frac{1}{2}}, \mathbf{U}^n_{R,i\pm\frac{1}{2}}\right)\right) \tag{5.6}$$

where the right hand side of the above equation can be thought of as the flux function which requires the solution of a Riemann IVP whose arguments are the states to the left and right of the interface located at $i \pm \frac{1}{2}$, which is $\mathbf{U}^n_{L,i\pm\frac{1}{2}}$ and $\mathbf{U}^n_{R,i\pm\frac{1}{2}}$, respectively. These solution values are obtained using a spatial reconstruction discussed in the next section. It therefore follows that Equation (5.3) can be re-expressed as

$$\mathbf{U}^{n+1}_i = \mathbf{U}^n_i - \frac{\Delta t}{\Delta x}\left(\mathcal{F}^n_{i+\frac{1}{2}} - \mathcal{F}^n_{i-\frac{1}{2}}\right) + \Delta t \mathbf{S}^n_i \tag{5.7}$$

which is the original form of Godunov's finite-volume scheme with a first-order explicit Euler time-marching scheme. The spatial accuracy of the scheme depends on the order of the reconstruction used to evaluate the left and right solution states in Equation (5.6).

5.2.2 Spatial Reconstruction

In order to achieve second-order spatial accuracy, the cell-averaged state, along with a cell averaged gradient calculated using a least squares approach similar to that proposed by Barth [138], is used to determine the left and right states, $\mathbf{U}^n_{L,i+\frac{1}{2}}$ and $\mathbf{U}^n_{R,i+\frac{1}{2}}$, where the $i + \frac{1}{2}$ interface is considered. In the one-dimensional case, the least-squares computation of the cell gradient reduces to the solution slope based on the cell centered values of the two adjacent cells given by

$$\left.\frac{\partial \mathbf{U}^n}{\partial x}\right|_i = \frac{\mathbf{U}^n_{i+1} - \mathbf{U}^n_{i-1}}{2\Delta x}. \tag{5.8}$$

The piecewise linear spatial reconstruction is then given by

$$\mathbf{U}^n_{L,i+\frac{1}{2}} = \mathbf{U}^n_i + \frac{\Delta x}{2}\phi \left.\frac{\partial \mathbf{U}^n}{\partial x}\right|_i , \tag{5.9}$$

$$\mathbf{U}^n_{R,i+\frac{1}{2}} = \mathbf{U}^n_{i+1} - \frac{\Delta x}{2}\phi \left.\frac{\partial \mathbf{U}^n}{\partial x}\right|_{i+1} . \tag{5.10}$$

A monotonicity preserving scheme is sought; however, the second-order scheme with linear reconstruction above does not guarantee monotonicity, only first-order schemes are strictly monotonic (See Hirsch [98]). To ensure a monotonic solution using piecewise linear reconstruction, the slope limiter, ϕ, is introduced, which switches the influence of the solution gradient on or off, giving linear, or piecewise constant reconstruction where needed. To evaluate ϕ, the limiter functions suggested by Barth-Jespersen [136] is considered:

$$\phi_k = \begin{cases} \min\left(1, \dfrac{\mu_{max} - \bar{\mu}}{\mu_k - \bar{\mu}}\right) & \text{for } \mu_k - \bar{\mu} > 0, \\ \min\left(1, \dfrac{\mu_{min} - \bar{\mu}}{\mu_k - \bar{\mu}}\right) & \text{for } \mu_k - \bar{\mu} < 0, \\ 1 \text{ otherwise} & , \end{cases} \tag{5.11}$$

where $\bar{\mu}$ is the cell centered value of a component of the solution vector of interest for each cell, and μ_{max} and μ_{min} are the maximum and minimum values of the solution component being reconstructed of the cell centered values of the cell in question and all of its neighbours. Finally, μ_k is the unlimited spatially reconstructed value of $\mu(x_k)$ at the interface position k, which in this case is $\mu_{i\pm\frac{1}{2}}$.

5.2.3 Harten-Lax-van Leer-Einfeldt (HLLE) Flux Function

In order to evaluate the numerical flux in Equations (5.6), the interface between the two adjacent computational cells is treated as a one-dimensional Riemann IVP assuming a short time interval allowing the source terms to be neglected. The approximate HLLE Riemann solver [132] is adopted due to its relative simplicity, low computational cost and number of operations, and the ability to be implemented in a straightforward way for the MMHD system. It was also found to be very robust for most of the systems of equations and problems considered in this thesis. A simple general derivation of this flux function can be found in the Appendix B. The HLLE flux function results in the intermediate flux state

$$\mathbf{F}_* = \frac{\lambda^+ \mathbf{F_L} - \lambda^- \mathbf{F_R}}{\lambda^+ - \lambda^-} + \frac{\lambda^+ \lambda^-}{\lambda^+ - \lambda^-}\left(\mathbf{U_R} - \mathbf{U_L}\right), \tag{5.12}$$

where $\mathbf{U_L}$ and $\mathbf{U_R}$ are the left and right solution states, $\mathbf{F_L}$ and $\mathbf{F_R}$ are the left and right fluxes. The largest and smallest signal velocities are λ^+ and λ^-, respectively. The final form

of the approximate flux function for the right hand side of Equation (5.6) is

$$\mathbf{F} = \begin{cases} \mathbf{F_L} & \text{for } \left(\frac{x}{t}\right) < \lambda^-, \\ \mathbf{F}_* & \text{for } \lambda^- \leq \left(\frac{x}{t}\right) \leq \lambda^+, \\ \mathbf{F_R} & \text{for } \left(\frac{x}{t}\right) > \lambda^+. \end{cases} \tag{5.13}$$

For the MMHD model, λ^+ and λ^- are different for each species and for the Maxwell's equations. This is to prevent a very dissipative scheme which would come about from using the slowest and fastest wavespeed for the whole system, which includes the speed of light.

5.2.4 Temporal Limited Second Order Backwards Time Marching

Unconditionally stable implicit schemes were considered to allow large time steps and possibly reduce computational costs. Temporal limiting was required in this case to ensure monotonicity of the proposed fully-discrete TVD scheme. A temporal limited implicit second-order backwards differencing discretization (TLBDF) scheme is described by Wuilbaut *et al.* [130]. The BDF scheme is modified with a blending coefficient, θ, which can change the order from a second- to first-order in time scheme depending on the value of θ:

$$\left(1 + \frac{1}{2}\theta\right) \mathbf{U}^{n+1} - (1+\theta)\,\mathbf{U}^n + \frac{1}{2}\theta \mathbf{U}^{n-1} = \Delta t \left[\mathbf{R}^{n+1}\right]. \tag{5.14}$$

When $\theta = 1$, the BDF scheme is recovered while when $\theta = 0$ the first-order implicit Euler time integration scheme is recovered.

In order to determine θ, the minmod limiter of Roe [139] is used here given by

$$\text{minmod}(r) = \begin{cases} 1 & \text{if } 1 < |r| \text{ and } r > 0, \\ r & \text{if } |r| < 1 \text{ and } r > 0, \\ 0 & \text{if } r < 0, \end{cases} \tag{5.15}$$

where r in this case is defined by

$$r = \frac{\frac{\mathrm{U}_i^{n+1} - \mathrm{U}_i^n}{\Delta t^{n+\frac{1}{2}}}}{\frac{\mathrm{U}_i^n - \mathrm{U}_i^{n-1}}{\Delta t^{n-\frac{1}{2}}}}. \tag{5.16}$$

The blending coefficient described by Wuilbaut *et al.* [130] is thus

$$\theta_i = \sqrt{\frac{\text{minmod}(r_i)}{\max(1, |r_i|)}}. \tag{5.17}$$

Another blending parameter that will be used is the square of the above parameter. Namely,

$$\theta_i = \frac{\text{minmod}(r_i)}{\max(1, |r_i|)}, \tag{5.18}$$

which is a stronger, more sensitive blending parameter.

5.2.5 Dual-Time Stepping

In order to solve the semi-discrete form of the governing equations, a dual-time stepping formulation was adopted here of the form

$$\frac{\mathrm{d}\mathbf{U}}{\mathrm{d}t} + \frac{\mathrm{d}\mathbf{U}}{\mathrm{d}\tau} = \mathbf{R}\left(\mathbf{U}\right), \tag{5.19}$$

where t is the physical time, τ is a pseudo-time, $\mathbf{U}$ is the conservative solution state vector and $\mathbf{R}\left(\mathbf{U}\right)$ is the solution residual. The equation is arranged so that

$$\frac{\mathrm{d}\mathbf{U}}{\mathrm{d}\tau} = \mathbf{R}\left(\mathbf{U}\right) - \frac{\mathrm{d}\mathbf{U}}{\mathrm{d}t} = \mathbf{R}^*\left(\mathbf{U}\right) = \mathbf{0}. \tag{5.20}$$

The TLBDF scheme above is adapted to the dual time formulation with a few slight modifications. The TLBDF scheme is used for the derivative with respect to t, and an implicit Euler discretization is used for τ. Linearizing the right side implicit terms, it can be shown that

$$\begin{aligned} &\left[\left(1 + \frac{2+\theta}{2}\frac{\Delta\tau}{\Delta t}\right)\mathbf{I} - \Delta\tau\frac{\partial\mathbf{R}(\mathbf{U}^{n+k})}{\partial\mathbf{U}^{n+k}}\right]\frac{\Delta\mathbf{U}^{n+k}}{\Delta\tau} \\ &= \mathbf{R}(\mathbf{U}^{n+k}) - \left[\frac{(2+\theta)\,\mathbf{U}^{n+k} - (2+2\theta)\,\mathbf{U}^{n} + \theta\mathbf{U}^{n-1}}{2\Delta t}\right] \end{aligned} \tag{5.21}$$

for time level n with $\Delta\mathbf{U}^{n+k} = \mathbf{U}^{n+k+1} - \mathbf{U}^{n+k}$, and Δt and $\Delta\tau$ are the physical and pseudo time steps respectively. The blending coefficient is calculated for each cell at each subiteration using the transition $\mathbf{U}^{n+k}$ solution state. The solution residual $\mathbf{R}\left(\mathbf{U}^n\right)$ is obtained by using a discrete finite-volume scheme on a uniform spatial mesh with $x_i = x_0 + i\Delta x$ and $\Delta x = x_{i+1} - \Delta x_i = \text{constant}$, resulting in

$$\mathbf{R}\left(\mathbf{U}_i^n\right) = \left(-\frac{1}{\Delta x}\left(\mathcal{F}^n_{i+\frac{1}{2}} - \mathcal{F}^n_{i-\frac{1}{2}}\right) + \Delta t\mathbf{S}_i^n\right), \tag{5.22}$$

and $\partial\mathbf{R}\left(\mathbf{U}^n\right)/\partial\mathbf{U}^n$ is a banded block tridiagonal matrix of the form

$$\frac{\partial\mathbf{R}\left(\mathbf{U}_i^n\right)}{\partial\mathbf{U}_i^n} = \mathbf{B}\left(\frac{1}{\Delta x}\frac{\partial\mathcal{F}^n_{i-\frac{1}{2}}}{\partial\mathbf{U}_{i-1}}, \left(\frac{1}{\Delta x}\frac{\partial\mathcal{F}^n_{i-\frac{1}{2}}}{\partial\mathbf{U}_i} - \frac{1}{\Delta x}\frac{\partial\mathcal{F}^n_{i+\frac{1}{2}}}{\partial\mathbf{U}_i} + \frac{\partial\mathbf{S}_i^n}{\partial\mathbf{U}_i}\right), -\frac{1}{\Delta x}\frac{\partial\mathcal{F}^n_{i+\frac{1}{2}}}{\partial\mathbf{U}_{i+1}}\right), \tag{5.23}$$

for cell i. The term $\mathcal{F}^n_{i\pm\frac{1}{2}}$ is the interface flux at time level n and at interface $i \pm \frac{1}{2}$, and $\mathbf{S}_i^n$ is the source term. The banded tridiagonal matrix is a result of a first-order linearization for the implicit terms of the numerical scheme. The details of this derivation can be found in Appendix B.

Although the left side of Equation (5.23) is first-order, the dual-time formulation allows one to iterate and converge to a higher-order solution. Convergence is determined by comparing the norms of the residuals when

$$\left\|\mathbf{R}^*(\mathbf{U}^{n+k+1})\right\|_1 < \varepsilon\left\|\mathbf{R}^*(\mathbf{U}^n)\right\|_1 \tag{5.24}$$

where ε is chosen to be 0.001.

5.2.6 Time Step Control Factor (TSCF)

The time step, Δt, is determined through a Time Step Control Factor (TSCF) relation where the TSCF number is a non-dimensional parameter that controls the size of the time step as follows:

$$\text{TSCF} = \frac{\Delta t}{\min\left(\frac{\Delta x}{c}, \frac{1}{\omega_{pe}}\right)}, \tag{5.25}$$

where c is the speed of light and ω_{pe} is the electron plasma frequency, $\omega_{pe} = \sqrt{(n_e e^2)/(m_e \epsilon_\circ)}$. The inclusion of the plasma frequency in the definition of the TSCF parameter is a common limiting time scale in the numerical simulation of plasmas [140], which was verified in the dispersion analysis of Chapter 4 as one of the higher frequencies. For a typical conditionally stable explicit scheme, the stability condition,

$$\Delta t \leq \min\left(\frac{\Delta x}{c}, \frac{1}{\omega_{pe}}\right), \tag{5.26}$$

should be satisfied. This means a TSCF of unity represents the boundary between a typical unstable (TSCF > 1.0) and stable (TSCF ≤ 1.0) explicit scheme. The pseudo-time step, $\Delta\tau$, is determined using a pseudo or sub iteration TSCF which is defined by the same relation, but for the pseudo time step. For the BDF scheme, the pseudo TSCF is set two orders of magnitude higher than the physical TSCF.

5.3 Numerical Results for One-Dimensional MMHD Model

The numerical scheme outlined in Section 5.2 above was applied to the solution of the 10TFMHD model described in Section 3.9. The method of manufactured solutions (MMS) was first used to verify the implementation of the numerical solution scheme in 1D. Numerical results for a one-dimensional plasma flow were then considered and discussed in what follows. A validation of the 10TFMHD model was sought by considering its application to a well-known one-dimensional problem: the IVP of the Brio-Wu test case [141]. Computational time and the requirements for converged solutions for this test case are also examined.

5.3.1 Verification Using the Method of Manufactured Solutions

The method of manufactured solutions, or MMS [142,143], was used here as a way to verify the order of accuracy of the spatial discretization scheme developed above. MMS is a mathematical approach useful for verifying that the numerical method, as implemented, produces the expected

theoretical spatial accuracy. It uses an analytical continuum solution which is of high enough degree in all variables to exercise all the terms and derivatives in the code. This analytical solution is independent of the numerical code and does not necessarily have to resemble an actual physical solution. The method works by adding a new source term along with boundary conditions, which forces the code to converge to a known steady state function. The modified governing equations in the MMS for the case of the 10TFMHD model are

$$\frac{\partial \mathbf{U}}{\partial t} + \frac{\partial \mathbf{F}}{\partial x} = \mathbf{S} + \mathbf{S}^{col} + \mathbf{Q}_{MMS}. \tag{5.27}$$

The new term $\mathbf{Q}_{MMS}$ is the source term associated with the MMS.

Two functions were examined, where all primitive variables were equal to the spatial variable x and $1/x$ (The linear and inverse case, respectively) so that

$$\rho, u, v, w, P_{xx}, P_{xy}, P_{xz}, P_{yy}, P_{yz}, P_{zz}, B_x, B_y, B_z, E_x, E_y, E_z = x \text{ or } \frac{1}{x}. \tag{5.28}$$

Substituting the functions into the governing equations results in the $\mathbf{Q}_{MMS}$ for the MMS,

$$\frac{\partial \mathbf{U}_{MMS}}{\partial t} + \frac{\partial \mathbf{F}_{MMS}}{\partial x_i} - \mathbf{S}_{MMS} - \mathbf{S}^{col}_{MMS} = \mathbf{Q}_{MMS}, \tag{5.29}$$

which was determined using a symbolic math program.

The resulting numerical simulations were performed for various TSCF and also on different numerical solution procedures versus grid resolution. The error to the exact solution was calculated. In Figure 5.2, the errors obtained for the linear case is plotted against the number of points. Note this case is non-linear since the fluxes and source terms are non-linear in the primitive variables. Looking at this figure, it can be seen that the asymptotic regime is achieved almost immediately. The results are the same for several TSCF as well as for several different schemes showing second-order accuracy.

The numerical results for the inverse case were examined next due to the non-linear nature of the function which can be illustrated by the infinite number of terms that are contained in a Taylor expansion of the function. Figure 5.3 shows the solution error for various variables, grid resolutions and schemes. For smaller N, there can be seen a non-asymptotic region before 200 points, which is likely due to the now more complex function. After 200 points the method converges to second-order as expected. The different variables have different profiles, and all eventually converge to the expected second-order error. The profiles for each variable in the non-asymptotic region agree for all numerical schemes and TSCF.

In summary, it has been shown that the 1D numerical solution procedure converges to the expected second-order accuracy for smooth continuous solution content. Although the MMS

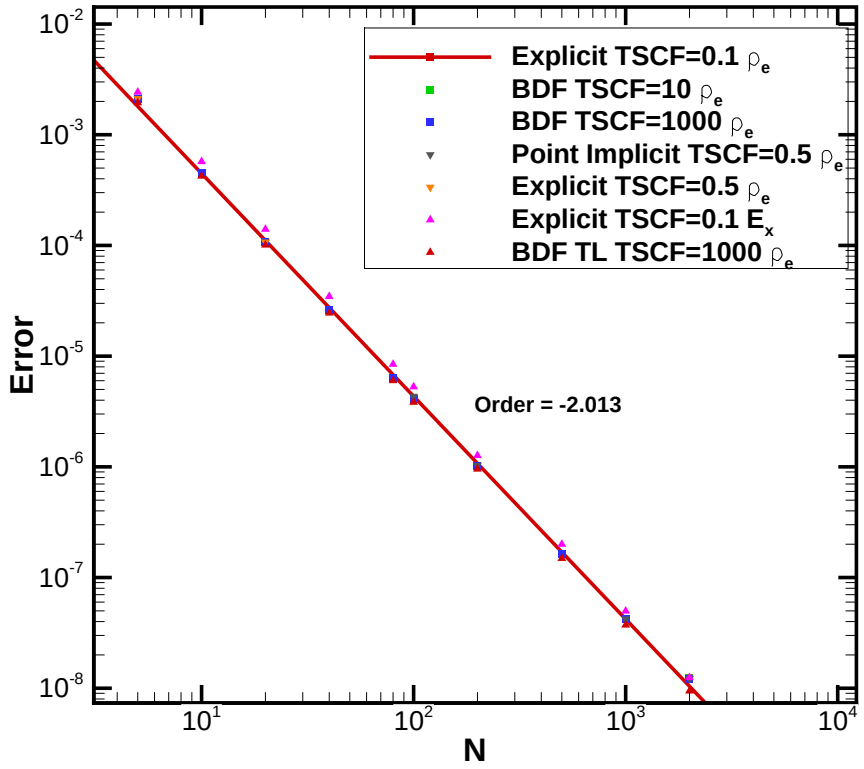

Figure 5.2: Spatial solution error as a function of N grid resolution points for various TSCF and numerical solution schemes for the linear test case.

procedure does not provide any information on the validity of the equations being solved, it does prove that the equations thus presented and developed are integrated correctly into a working and accurate solution procedure. As was shown in the work by Salari and Knupp on the MMS [144], even the smallest error would produce drastically reduced order of accuracy and the procedure was found to be extremely sensitive to any errors or tolerances.

5.3.2 Brio-Wu Shock-Tube Initial Value Problem

The Brio-Wu test case is a MHD shock-tube problem that gives rise to some rather complex unsteady wave structure due to the interaction of the plasma with the electromagnetic fields [141]. The simple discontinuous initial conditions for this problem are

$$\mathbf{W} = \begin{cases} \mathbf{W}^{\mathrm{L}} & \text{for} \quad 0 \leq x < L/2, \\ \mathbf{W}^{\mathrm{R}} & \text{for} \quad L/2 < x \leq L, \end{cases} \tag{5.30}$$

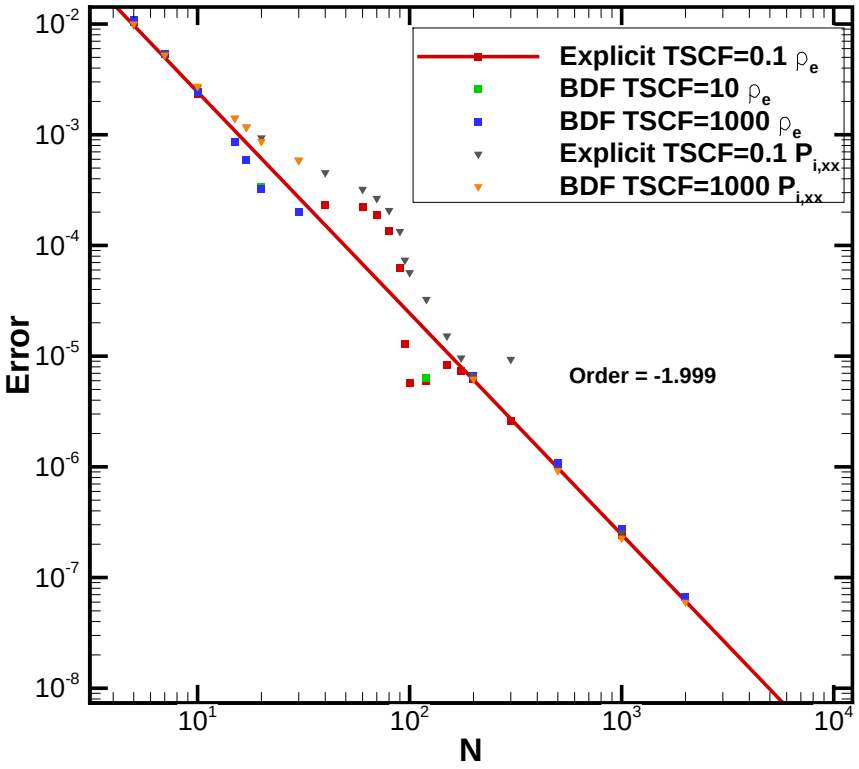

Figure 5.3: Spatial solution error as a function of N grid resolution points for various TSCF and numerical solution schemes for the inverse test case.

for $\{x \,|\, x \in [0, L]\}$, and where, in the case of the 10TFMHD equations

$$\mathbf{W}^{\mathrm{L}} = \begin{pmatrix} \mathbf{W}_e^{\mathrm{L}} \\ \mathbf{W}_{ion}^{\mathrm{L}} \\ \mathbf{W}_M^{\mathrm{L}} \end{pmatrix}, \qquad \mathbf{W}^{\mathrm{R}} = \begin{pmatrix} \mathbf{W}_e^{\mathrm{R}} \\ \mathbf{W}_{ion}^{\mathrm{R}} \\ \mathbf{W}_M^{\mathrm{R}} \end{pmatrix}, \tag{5.31}$$

with

$$\mathbf{W}_e^{\mathrm{L}} = \begin{pmatrix} m_e n_0 \\ \mathbf{0} \\ \frac{p_0}{2}\delta_{jk} \end{pmatrix}, \qquad \mathbf{W}_{ion}^{\mathrm{L}} = \begin{pmatrix} m_{ion} n_0 \\ \mathbf{0} \\ \frac{p_0}{2}\delta_{jk} \end{pmatrix}, \qquad \mathbf{W}_M^{\mathrm{L}} = \begin{pmatrix} \frac{3}{4}B_0 \\ B_0 \\ 0 \\ 0 \\ 0 \\ 0 \end{pmatrix}, \tag{5.32}$$

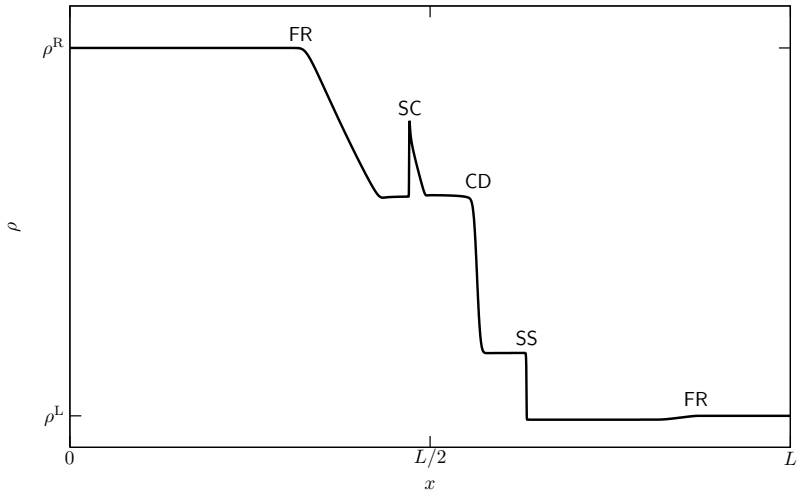

Figure 5.4: Density profile of the ideal MHD Brio-Wu solution.

$$\mathbf{W}_e^{\mathrm{R}} = \begin{pmatrix} \frac{m_e n_0}{8} \\ \mathbf{0} \\ \frac{p_0}{20}\delta_{jk} \end{pmatrix}, \qquad \mathbf{W}_{ion}^{\mathrm{R}} = \begin{pmatrix} \frac{m_{ion} n_0}{8} \\ \mathbf{0} \\ \frac{p_0}{20}\delta_{jk} \end{pmatrix}, \qquad \mathbf{W}_M^{\mathrm{R}} = \begin{pmatrix} \frac{3}{4}B_0 \\ -B_0 \\ 0 \\ 0 \\ 0 \\ 0 \end{pmatrix}, \tag{5.33}$$

and

$$\mathbf{W}_s = \begin{pmatrix} \rho_s \\ \mathbf{u}_s \\ P_{s,jk} \end{pmatrix}, \qquad s \in \{ion, e\} \qquad \text{and} \qquad \mathbf{W}_M = \begin{pmatrix} B_x \\ B_y \\ B_z \\ E_x \\ E_y \\ E_z \end{pmatrix}. \tag{5.34}$$

The quantities n_0, p_0, and B_0 are the reference number density, pressure, and magnetic field, respectively. The termination time for the Brio-Wu test case is defined by:

$$\tau = \frac{1}{10}\frac{L}{a_{ref}}. \tag{5.35}$$

The ideal MHD solution to the Brio-Wu IVP is illustrated in Figure 5.4 and has received considerable study [39–43, 63, 145]. The plasma waves that are present in the ideal MHD solution are a left moving fast rarefaction wave (FR), the slow compound (SC) wave, a contact discontinuity (CD), a slow shock (SS), and a right moving fast rarefaction wave (FR) as indicated in the figure.

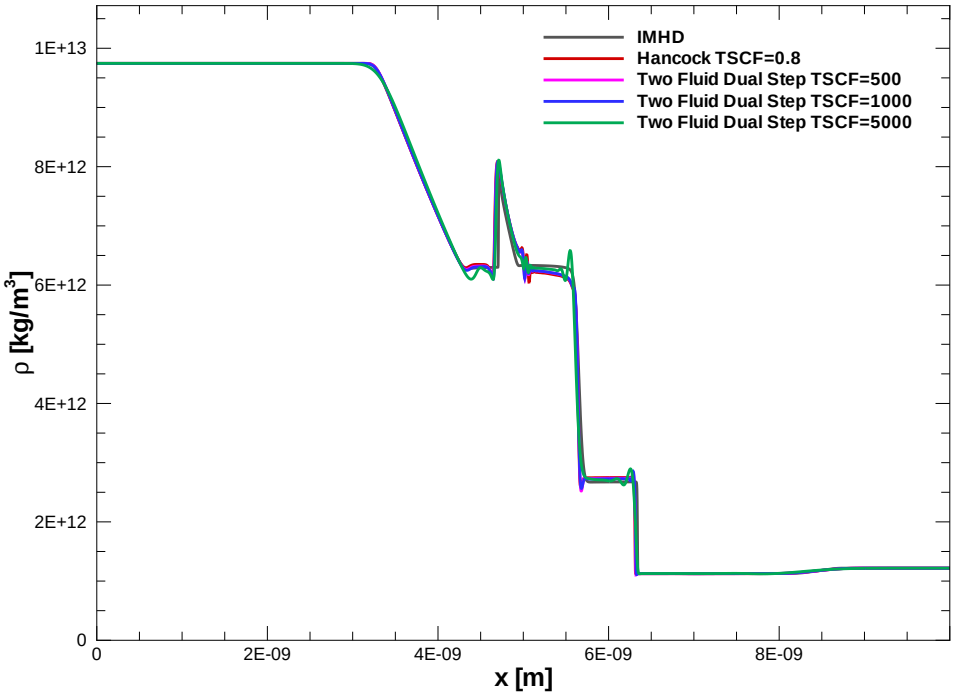

Figure 5.5: Density, ρ, as a function of x in the MHD limit.

5.3.3 Ideal MHD Limit Parameters for 10-moment Two Fluid MHD Model

In order to explore the recovery of the equilibrium ideal MHD limit by the 10TFMHD model, the Brio-Wu IVP was considered with the following parameters:

$$n_0 = 5.76 \times 10^{39}\,\mathrm{m}^{-3}, \qquad B_0 = 10^{10}\,\mathrm{T}, \qquad a_{ref} = 3.0 \times 10^{6}\,\frac{\mathrm{m}}{\mathrm{s}}, \qquad t = 3.33 \times 10^{-16}\,\mathrm{s}. \quad (5.36)$$

A modified electron to ion mass ratio of 0.01 was adopted to reduce the computational cost of the simulation by making the two plasma species wave speeds less disparate. It should be noted that the ideal MHD solution to the Brio-Wu test case is not strictly physical and arises from mathematical peculiarities inherent in the ideal MHD equations and assumptions. This is the reason why the parameters chosen are not physically common. They were chosen to approximate the conditions that satisfy the assumptions of ideal MHD. See Chapter 5 of Ohsawa's Thesis [48] for more details. See also Torrilhon [134] for discussion of intermediate, non physical waves in the ideal MHD equations.

5.3.4 Non-Temporal Limited Dual-Time Stepping BDF Scheme Results

The results in this section were generated from a numerical solution scheme which did not make use of the temporal limiting of Wuilbaut *et al.* [130]. The numerical results of this section

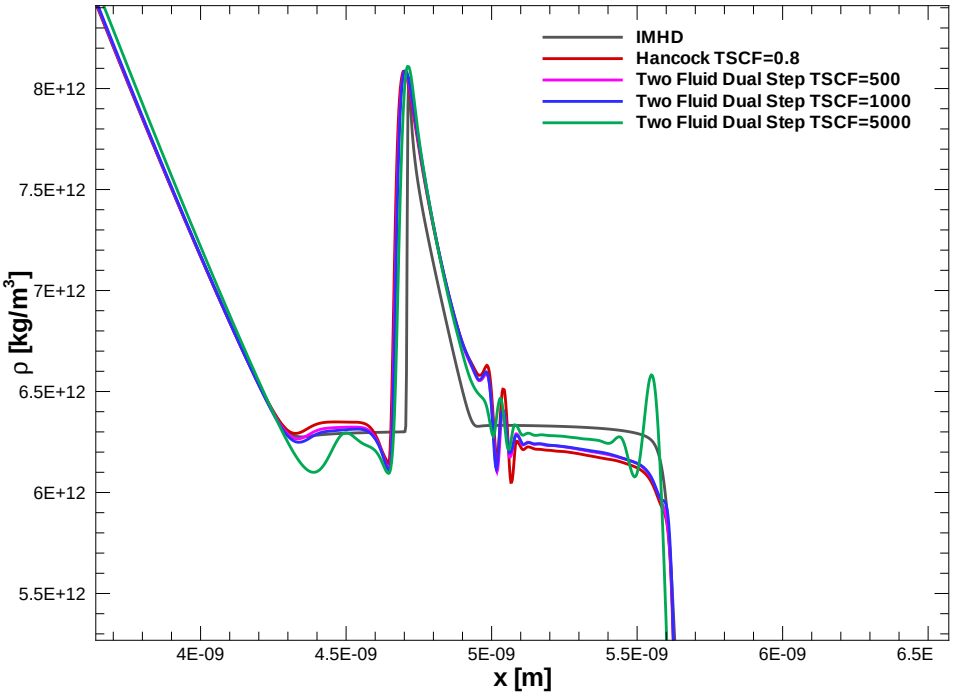

Figure 5.6: Close up of density, ρ, as a function of x for the compound shock in the MHD limit.

are important as they show the presence of numerical oscillations in the predicted solution, for which the temporal limiting was subsequently implemented in order to mitigate. The results from the non-temporal limited dual-time BDF scheme are compared with an explicit Hancock time marching scheme [146] for accuracy. The effect of TSCF and grid resolution on the predicted solutions are explored as well as the effect of collisions on the recovery of the equilibrium solution.

5.3.5 Ideal MHD Limit Results

Figure 5.5 shows the resulting density profile using an explicit Hancock scheme with a TSCF of 0.8 and 4000 cells along with profiles made with the implicit dual-time stepping scheme with a physical, outer, TSCF of 500, 1000 and 5000 with pseudo-time sub-iteration TSCFs of 50000, 100000 and 500000, respectively. Figure 5.6 provides a close up view of the compound shock in the ideal MHD limit. As can be seen in the two figures, the 10TFMHD model recovers the ideal MHD solution fairly well with only a few differences in terms of minor solution oscillations. Further, the explicit and implicit methods agree quite closely with each other for the physical TSCF of 500 and 1000 for the dual-time step method. However, when the TSCF is increased further, there is a clear degradation in accuracy and loss of solution monotonicity as Δt becomes

Table 5.1: Computational time for solving the Brio-Wu test case using the explicit Hancock scheme and an implicit dual-time stepping scheme

Scheme	Physical TSCF	Time (minutes)
Hancock	0.8	1093
Dual Step Implicit Euler	500	154
Dual Step Implicit Euler	1000	80
Dual Step Implicit Euler	5000	52

large. The loss of monotonicity here is due to the fact that monotonicity is not strictly enforced within the dual-time stepping scheme.

There is a significant computational advantage to using the implicit dual-time stepping method as illustrated in Table 5.1. As can be seen in the table, there is an order of magnitude increase in speed using the implicit dual-time stepping scheme. Referring back to Figures 5.5 and 5.6, it can be seen that a physical TSCF of about 1000 provides a satisfactory increase in speed without significantly degrading the quality of the predicted solution for this Brio-Wu case.

5.3.6 Comparison of Collisionless and Collisional Results

To investigate the effects of interspecies collisions, the IVP of Brio and Wu was computed with the 10TFMHD model and compared to the result with no interspecies collisions. Note that the two-fluid MHD 10-moment result with no interspecies collisions, but with self collisions, is virtually equivalent to a 5-moment isotropic result with no interspecies collisions when there is sufficient self collisions to maintain an isotropic pressure. The present interspecies collisionless results are expected to be similar to the previous results of Shumlak and Loverich [62].

In Figure 5.7, the resulting density profiles of the ideal MHD and collisionless 10TFMHD solutions are compared using 4000 cells, a physical TSCF of 1000 and with an electron/ion mass ratio of 0.01. In order to obtain a stable solution, the TSCF of the explicit Hancock method was set to 0.1. It can be seen that the fully collisional solution presented in the previous set of results is much closer to the ideal MHD result, eliminating, or minimizing many of the oscillations that are present in the interspecies collisionless solution. The reduction of many of the oscillations can be seen by looking more carefully at the slow compound wave as seen in Figure 5.8 compared to the density profiles of the collisional result in Figure 5.6. Further, the slow shock is resolved more accurately as compared to the ideal MHD result in the fully collisional solution as illustrated in Figure 5.9. Evidently, interparticle collisions are essential

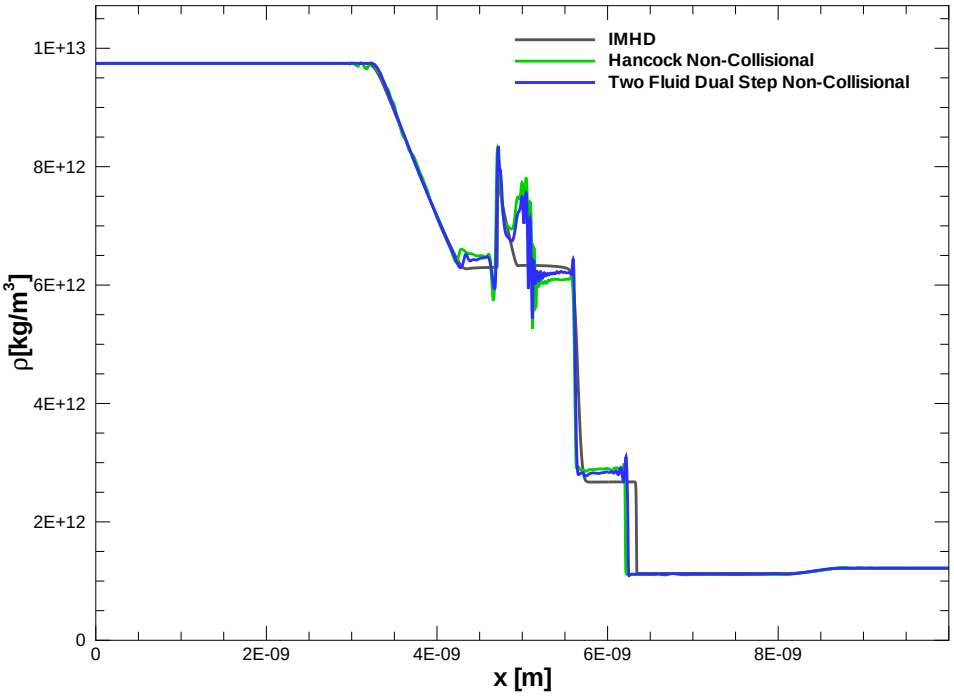

Figure 5.7: Density, ρ, as a function of x of the MHD limit of the two-fluid model comparing collisionless flows solved with the explicit Hancock and implicit dual-time stepping scheme.

Table 5.2: Computational time for solving the non-collisional Brio-Wu test case using the explicit Hancock scheme and an implicit dual-time stepping scheme

Scheme	Physical TSCF	Number of Cells	Time (minutes)
Hancock	0.1	4000	6229
Dual Step Implicit Euler	1000	4000	93

in order to properly recover the ideal MHD limit. The computational cost of generating the collisionless solutions using the explicit Hancock and the implicit dual-time stepping method for the 10TFMHD model were also measured and are included in Table 5.2. A nearly 70 fold decrease in computational cost is achieved by using the implicit dual-time step over the explicit Hancock method.

5.3.7 Grid Convergence Investigation Results

The effects of mesh resolution on the solution of the Brio-Wu test case using the two-fluid MHD model with the implicit dual-time stepping were studied. The Brio-Wu test case was solved using 4000, 6000, 8000, 10000 and 20000 cells using the implicit dual-time stepping scheme with

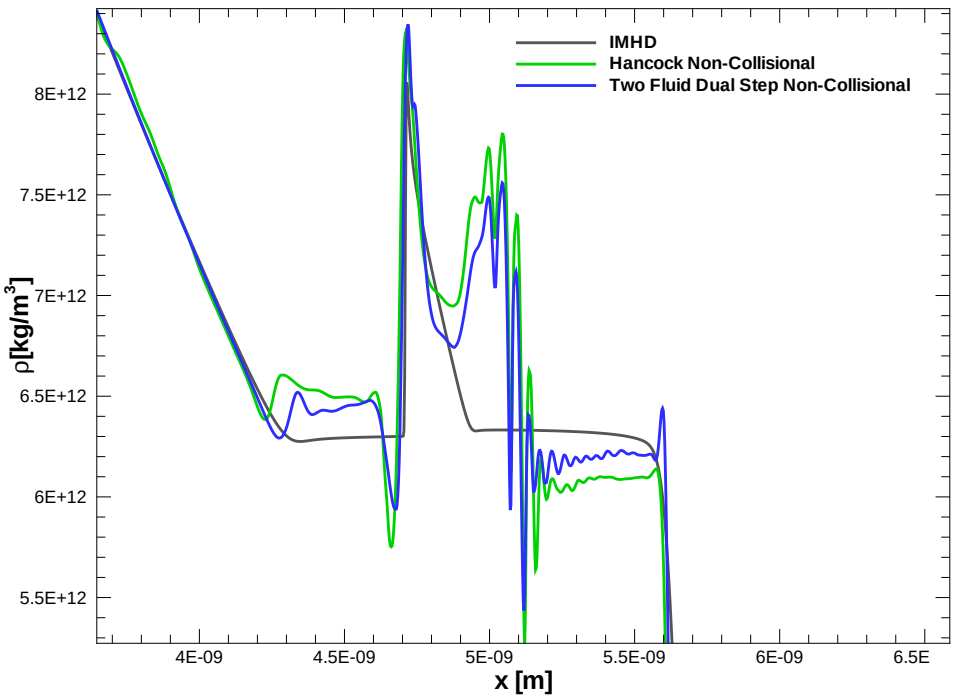

Figure 5.8: Close up density, ρ, as a function of x for the compound shock of the MHD limit comparing collisionless flows solved with the explicit Hancock and implicit dual-time stepping scheme.

a TSCF of 1000 and compared with the results of the Hancock explicit scheme for 4000 cells and a TSCF of 0.8, as well as the ideal MHD limit. The density profile results are presented in Figure 5.10 with a close up view of the slow compound wave given in Figure 5.11.

The oscillations that appear in the 4000 cell explicit method become smaller in amplitude when solved using the dissipative implicit dual-time step method, with several of the waves disappearing at high grid resolutions. The wavelength of the oscillations also decrease. The wavelength attenuation is most dramatic when going from 4000 to 6000 cells, with a smaller change going from 6000 to 8000 cells and when moving from 8000 to 10000 cells, the wavelength remains largely the same. Therefore, it is argued that the solution appears to converge for the most part at about 8000 cells. Unfortunately, an increase in grid resolution also causes new oscillations to appear and grow such as those in the contact discontinuity which can be seen on the right side of the slow compound wave in Figure 5.11. At 20000 cells there are now more oscillations. Once again, there is a loss of monotonicity brought about by the large time steps. Note, even though the time step taken by the implicit method defined by the TSCF remains the same, the time step is very large with respect to the cell size, as a characteristic wave can travel across many more cells in the same time step as Δx decreases. Table 5.3 lists

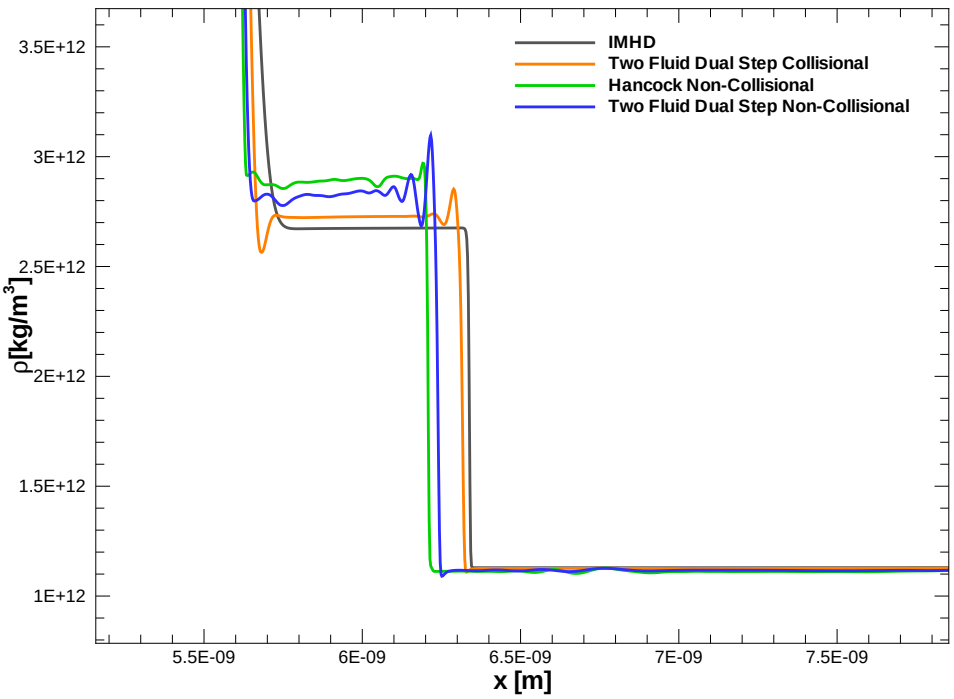

Figure 5.9: Close up density ρ as a function of x for the slow shock of the MHD limit comparing collisional and collisionless flows solved with the implicit dual-time stepping scheme.

the computational time for each solution. As can be seen, even with a grid resolution of 20000 cells, the computational cost is still significantly less than that of the explicit method with only 4000 cells.

5.3.8 Real Electron/Ion Mass Ratio Results

The artificial mass ratio, $m_e/m_{ion} = 0.01$, was then dropped and the physical ratio, $m_e/m_{ion} = 1836$, was adopted when considering solutions of the Brio-Wu IVP. Figure 5.12 compares the density profiles of the realistic Brio-Wu case using the explicit method with 4000 cells and a TSCF of 0.7 for stability, and several implicit dual-time step profiles with a TSCF of 1000 and cell resolutions of 4000, 6000, 8000 and 10000 to illustrate the spatial convergence with a close up of the slow compound shock presented in Figure 5.13. It is readily apparent from the predicted solutions that adopting a realistic electron/ion mass ratio introduces additional oscillatory behaviour in the predicted solutions since the system is now farther away from the equilibrium conditions required to produce a well defined Brio-Wu solution, due to the faster electrons. This behaviour is expected as similar oscillatory behaviour is observed in realistic mass ratio solutions by Liu *et al.* [73]. Further, the problem is now less stable, and as a

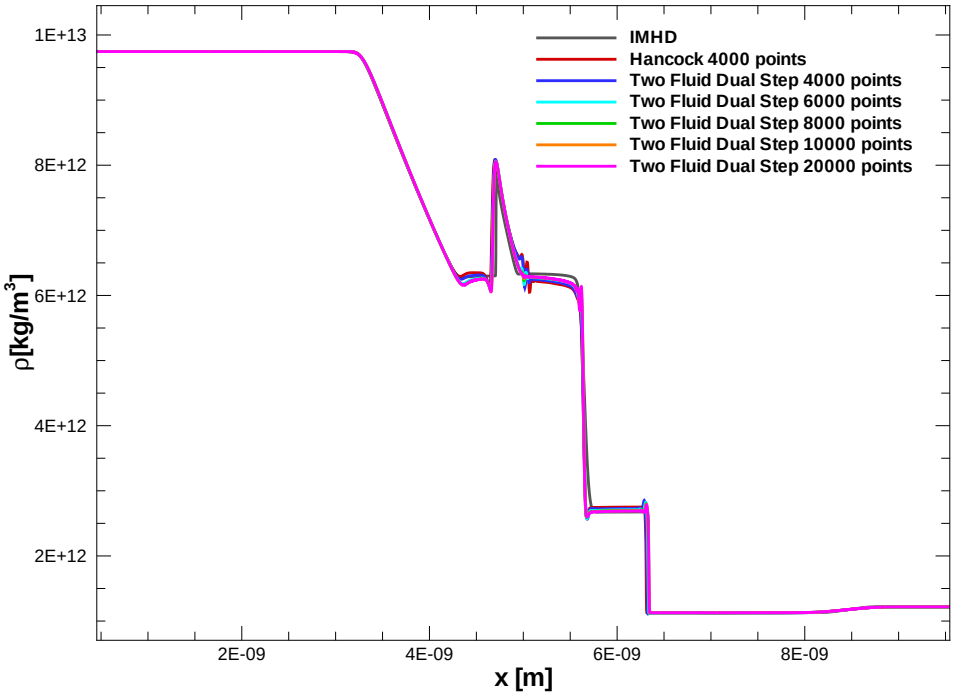

Figure 5.10: Density, ρ, as a function of x for the MHD limit of the two-fluid model for 4000, 6000, 8000, 10000, and 20000 cells solved with the implicit dual-time stepping scheme.

result, the explicit method must be run at a lower TSCF. The allowable time step is smaller as well due to an increase in the electron plasma frequency causing the computational cost to increase as illustrated in Table 5.4, which lists the computational times for the various solutions presented. Once again, the implicit dual-time step method yields an order of magnitude decrease in computational cost over the explicit Hancock method. At higher grid resolutions made possible by the implicit dual-time step method, a solution much closer in agreement to the ideal MHD case can be obtained.

5.3.9 Temporal Limited Results

The ideal MHD limit is considered using the temporal limited implicit dual-time BDF scheme described earlier in Section 5.2.4. The two blending coefficient were examined: the full theta condition as defined by Equation (5.18); and the relaxed square root theta condition as defined by Equation (5.17). The effect of temporal limiting was examined by comparing results to the previously obtained solutions with the non-temporal limited solution procedures of the 10TFMHD equations. The calculations were carried out on similar grid resolutions and TSCFs. Figure 5.14 shows the predicted density profiles of the Brio-Wu solution using the non-temporal

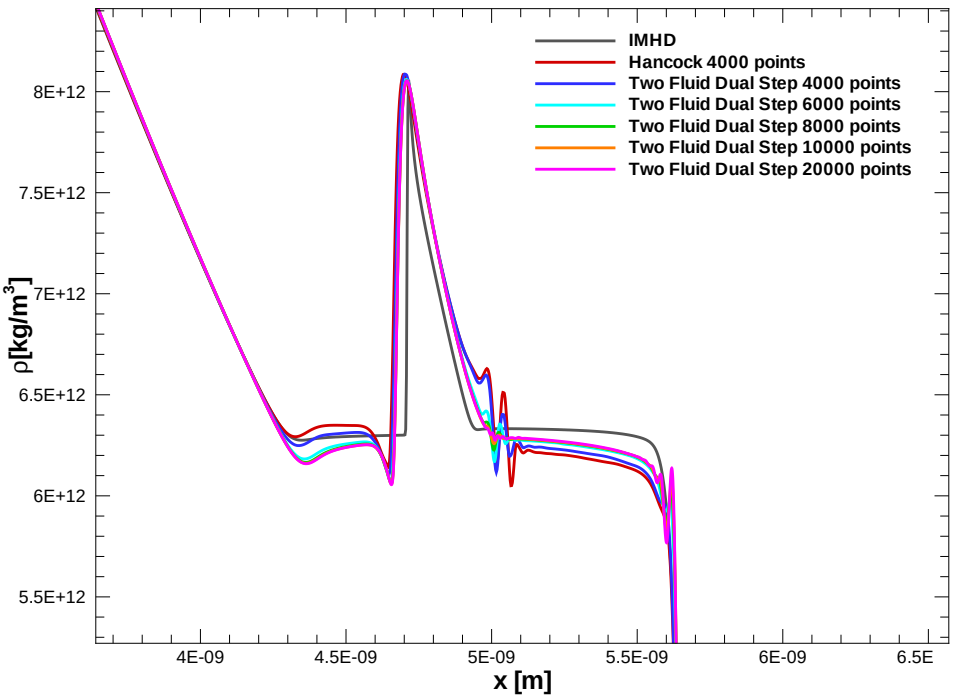

Figure 5.11: Close up density, ρ, as a function of x for the compound shock of the MHD limit 4000, 6000, 8000, 10000 and 20000 cells solved with the implicit dual-time stepping scheme.

limited BDF dual-time step scheme, and the explicit Hancock scheme, along with solutions from the temporal-limited schemes using the two blending coefficients. The grid resolution is 4000 cells and a TSCF of 1000 and 5000 is used. Some interesting observations to note from the figure are that the compound shock, a close-up view is provided in Figure 5.15, is well formed and some major oscillations that are present in the non-temporal limited case are now absent or severely reduced in the temporally limited results. The well formed compound shock is important, as this is a characteristic of a second-order solution. The first-order solution of the Brio-Wu test case results in a severely distorted compound shock as can be seen in Figure 5.14. Therefore, the temporal limiting does in fact generally preserve second-order accuracy for interesting structures such as the compound shock. However, at the same time, some oscillations, particularly the small bump at the front of the contact discontinuity, is reduced with the weaker blending coefficient, and completely absent with the full blending coefficient. Other oscillations are reduced as well, as can be seen in Figure 5.16 which shows that the oscillations on the forward shock are lessened, again, more with the full theta blending coefficient. Further, with a TSCF of 1000, there is a much better agreement with the ideal MHD limit compared to the explicit scheme, while at the same time reducing the oscillations that are present in the other numerical schemes. Figure 5.17 compares the explicit Hancock scheme to the time limited

Table 5.3: Computational time for solving the Brio-Wu test case using the explicit Hancock scheme and an implicit dual-time stepping scheme for various grid resolutions.

Scheme	Physical TSCF	Number of Cells	Time (minutes)
Hancock	0.8	4000	1093
Dual Step Implicit Euler	1000	4000	80
Dual Step Implicit Euler	1000	6000	152
Dual Step Implicit Euler	1000	8000	202
Dual Step Implicit Euler	1000	10000	267
Dual Step Implicit Euler	1000	20000	385

Table 5.4: Computational time for solving the Brio-Wu test case using the explicit Hancock scheme and an implicit dual-time stepping scheme for various grid resolutions and a physical electron/ion mass ratio.

Scheme	Physical TSCF	Number of Cells	Time (minutes)
Hancock	0.7	4000	4898
Dual Step Implicit Euler	1000	4000	323
Dual Step Implicit Euler	1000	6000	523
Dual Step Implicit Euler	1000	8000	660
Dual Step Implicit Euler	1000	10000	855

BDF schemes at the foot of the compound shock and once again, there is excellent agreement, especially with the full theta version, however, at the same time there is significant reductions in oscillations with the temporal limited schemes.

5.3.10 Effect of TSCF on the Temporal Limited Results

Next the role of the TSCF is examined. Taking a look at Figure 5.15, which depicts the density profiles of the Brio-Wu test case obtained using several TSCFs, it is evident that although the oscillations at the foot of the compound shock are lessened with increased TSCF, this is mainly due to the dissipative nature of a large time step. Nevertheless, the temporally limited result is a large improvement over the non-temporal limited scheme which has large oscillations at this TSCF (see Figures 5.5 and 5.6).

The TSCF was altered for other grid resolutions and it was found that at higher grid resolutions, a high TSCF resulted in unstable solutions. A TSCF of 5000 was not sustainable for higher grid

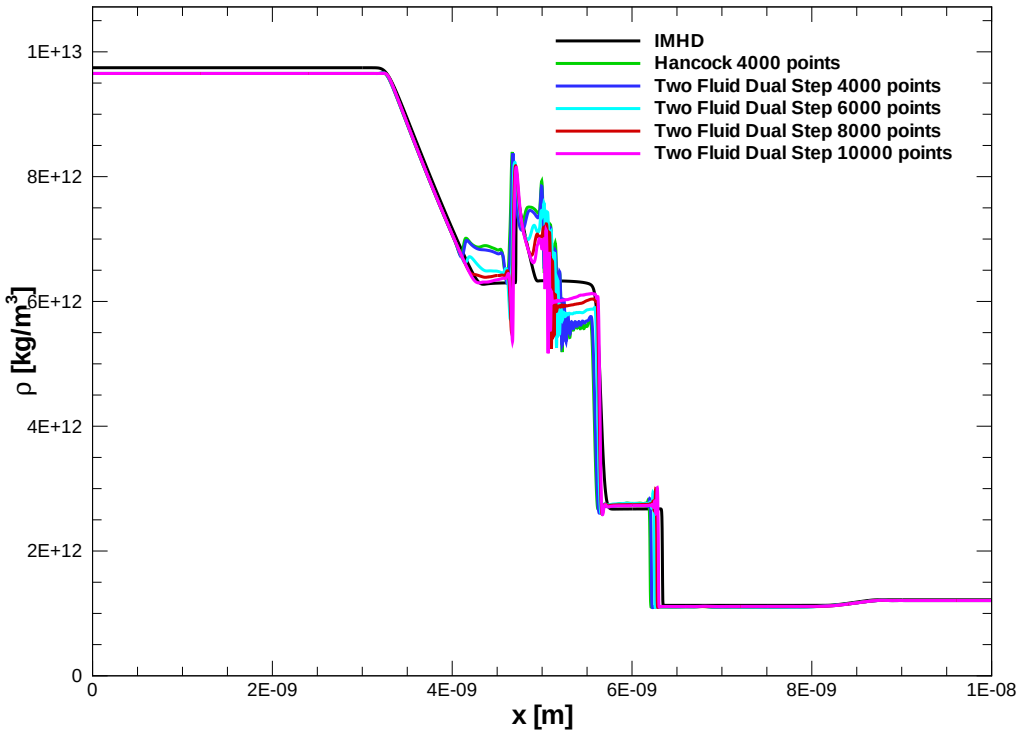

Figure 5.12: Density, ρ, as a function of x for the Brio-Wu test case with $m_e/m_{ion} = 1/1836$ of the two-fluid model for 4000, 6000, 8000, and 10000 cells solved with the implicit dual-time stepping scheme.

resolutions and TSCFs higher than 1000 were fairly washed out. As before, a TSCF of 1000 seems to be a good balance between solution accuracy and computational time. At this time, the temporal limiting makes the code about 120% slower than the scheme without temporal limiting. This results in a run time for the TSCF of 1000 and 4000 points to be approximately 180 minutes on an Intel Core2 E6750 2.66 GHz computer, which is still nearly an order of magnitude faster than the explicit Hancock scheme as seen in Table 5.3.

5.3.11 Effect of Grid Resolution on the Temporal Limited Results

The grid resolution was increased to observe its effects on the predicted temporally-limited solutions. Figure 5.18 shows the predicted solutions near the top of the contact discontinuity for the Brio-Wu test case obtained using 50,000 and 75,000 computational cells and a TSCF of 1000 for the two blending coefficients and also compares the results with the non-temporal limited and ideal MHD solutions. There is a dramatic difference between the limited and non-temporal limited solutions. The oscillations that plagued the non-limited scheme have vanished

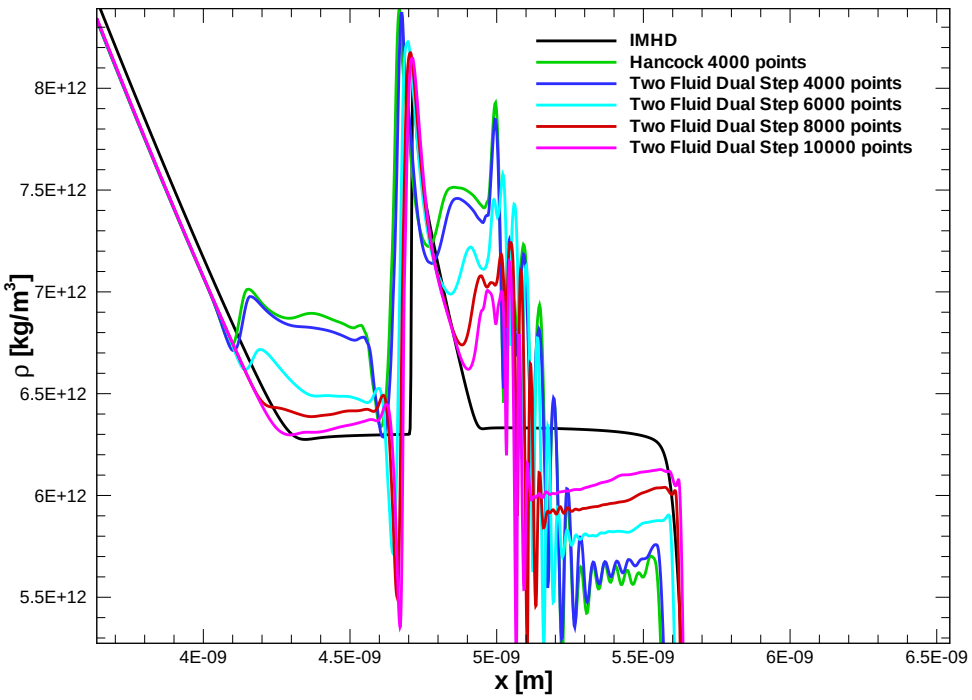

Figure 5.13: Close up density, ρ, as a function of x for the compound shock of the Brio-Wu test case with $m_e/m_{ion} = 1/1836$ of the two-fluid model for 4000, 6000, 8000, and 10000 cells solved with the implicit dual-time stepping scheme.

completely with the 50,000 point, full theta solution. Next the forward shock is examined in Figure 5.19. Once again, the oscillations present in the non-temporal limited scheme are reduced significantly.

5.3.12 Grid Independent Solution

An attempt to obtain a grid independent solution was made with the temporal limited numerical solution scheme. In Figure 5.21, which shows the predicted solution at the base of the compound shock, the oscillations are significantly reduced from the non-time limited case. Further, the phase of the oscillations are reversed from the non-time limited case. This suggests that the oscillations are numerical in nature. However, even at 75,000 points resolution, the oscillations are changing from the previous grid resolution of 50,000 points, although very slightly. It should be emphasized that these oscillations are small at these resolutions as seen in Figure 5.20, which shows the whole solution.

To verify the numerical origin of the oscillations seen in Figure 5.21, a comparison plot was made of the explicit Hancock solution at a TSCF of 0.7 and the temporal limited and non-

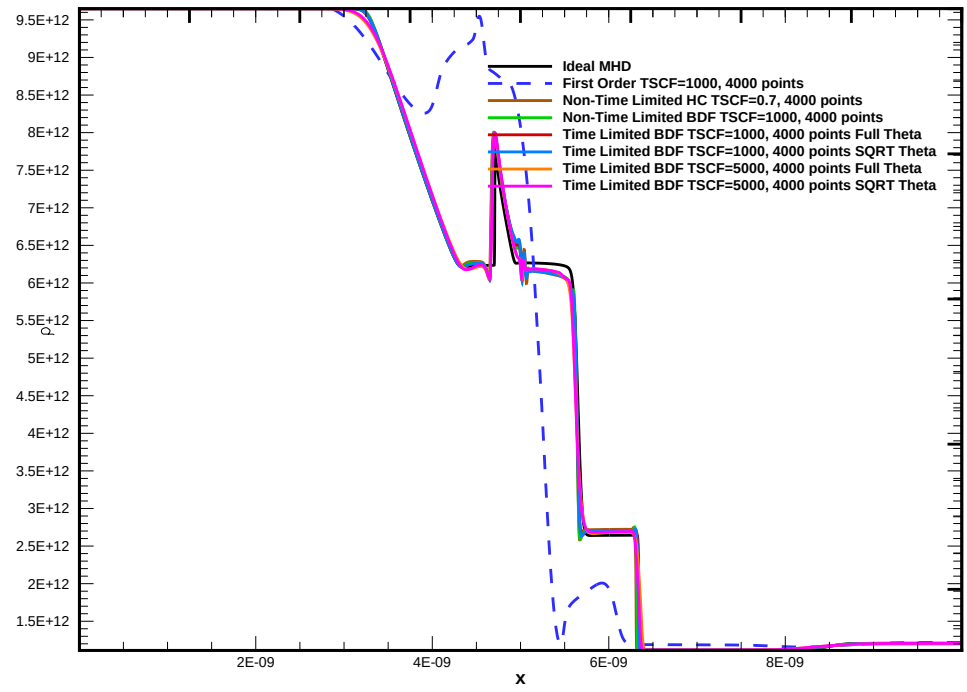

Figure 5.14: Density, ρ, for the Brio-Wu test case comparing temporal limited and non-limited schemes.

limited BDF scheme at a TSCF of 1000. The grid resolution examined was 30,000 points. As can be seen in Figure 5.22 the oscillations at this high resolution are completely eliminated by the temporal limiting. This suggests that the increased numerical frequency content of the solution generated by higher grid resolutions and large time steps can be effectively managed by temporal limiting.

At this time, computer memory requirements have prevented further investigation at higher grid resolutions. It should be stated that the need for extremely high grid resolutions when computing multi-fluid MHD solutions of this type has been encountered by other researchers. Hakim *et al.* [64, 65] observed similar findings when using a collisionless version of the 10TFMHD model and indicated that grid resolutions of at least 50,000 points were required to resolve the complex oscillations observed, especially at the base of the compound wave and also at the top of the forward shock. The solutions were also still changing at this resolution. Grid resolution issues have also been identified in other simpler MHD models [133, 134]. However, as was demonstrated here, some of these effects are numerical in origin and can be reduced by implementing temporal limiting to obtain reasonable solutions without increased grid resolutions.

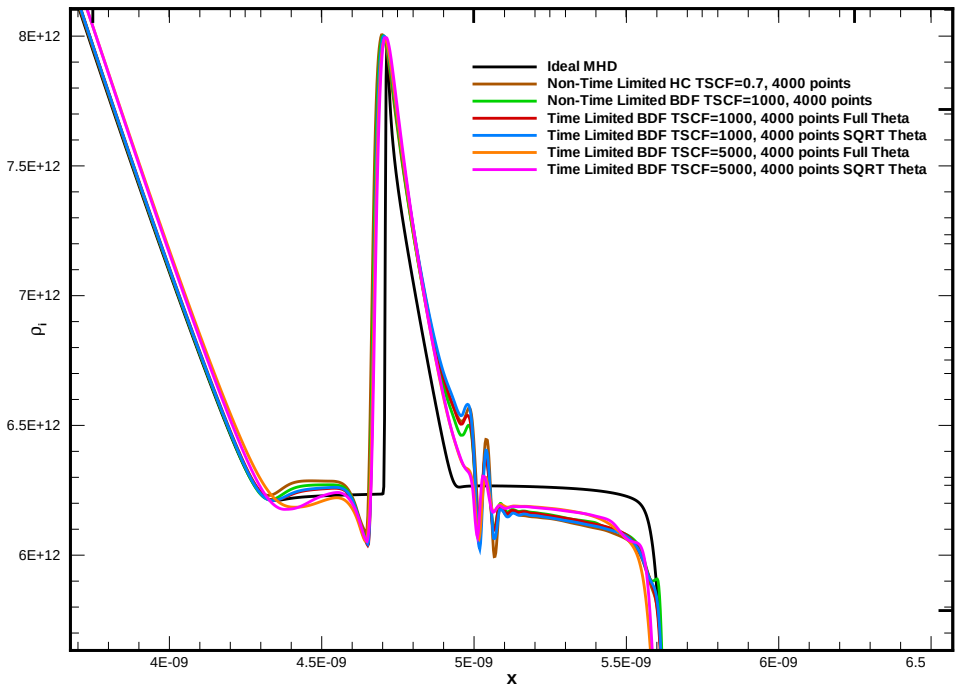

Figure 5.15: Density, ρ, for the Brio-Wu test case comparing temporal limited and non-limited schemes with a close up of compound shock.

5.3.13 Summary of 1D Plasma Flow Simulation Results

It has been shown in this section that the MMHD model for one-dimensional plasma flows can recover, reasonably well, the ideal MHD limit, however high grid resolutions are required and the presence of particle collisions are essential. It is clear that with the higher grid resolutions required to resolve small scale content and time scales such as the plasma frequency, numerical and physical oscillations start to become a problem, as will be seen when predicting GEM plasma flows in Chapter 8. It has been shown that implicit time-stepping reduces computational costs greatly. Further, it is clear that temporal limiting is beneficial to the solution of the implicit numerical procedure, resulting in a more stable and accurate solution. However, the particular blending coefficient used affects the accuracy and stability of the resulting solution. Comparing the two blending coefficients examined, it is concluded that the full theta blending coefficient given by Equation (5.18) would seem optimal. Although, more first-order and dissipative effects are introduced, the conservative nature of the limiting, which effectively eliminates some oscillations, outweighs these negative effects. It should also be noted that the 1D plasma flow solutions examined in this chapter are also used later in this thesis to verify the 2D MMHD model and numerical solution method described in the next chapter.

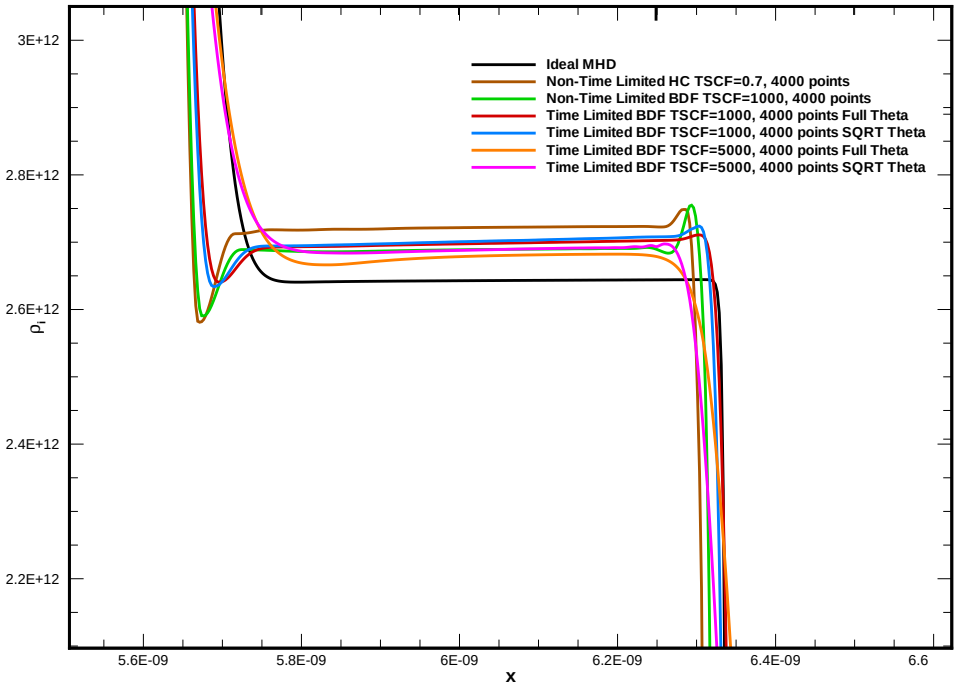

Figure 5.16: Density, ρ, for the Brio-Wu test case comparing temporal limited and non-limited schemes with a close up of shock.

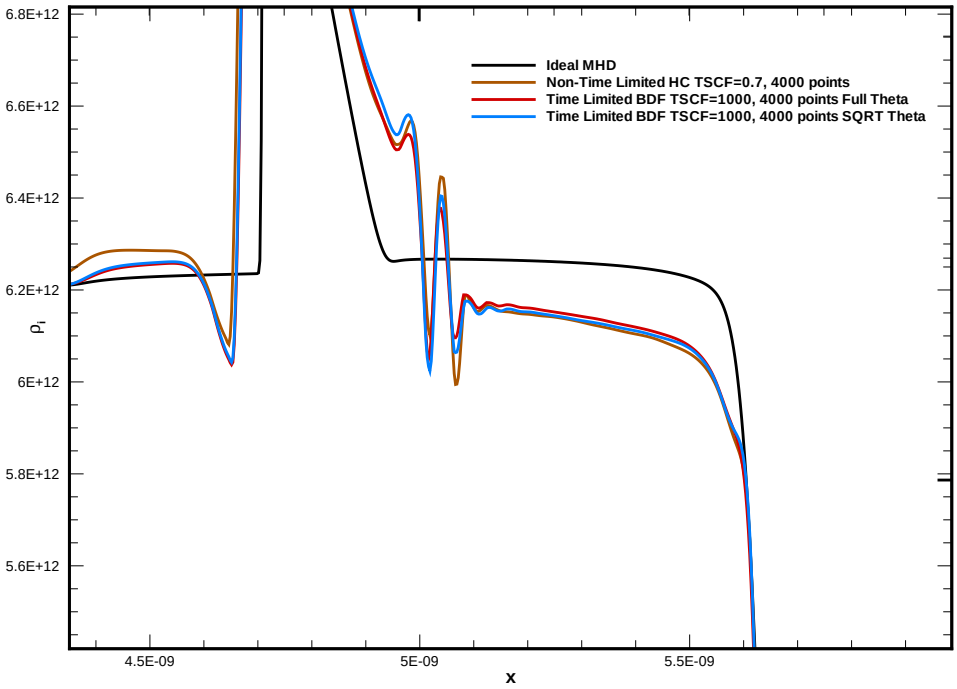

Figure 5.17: Density, ρ, for the Brio-Wu test case comparing temporal limited, and non-limited schemes showing a close up of the compound shock.

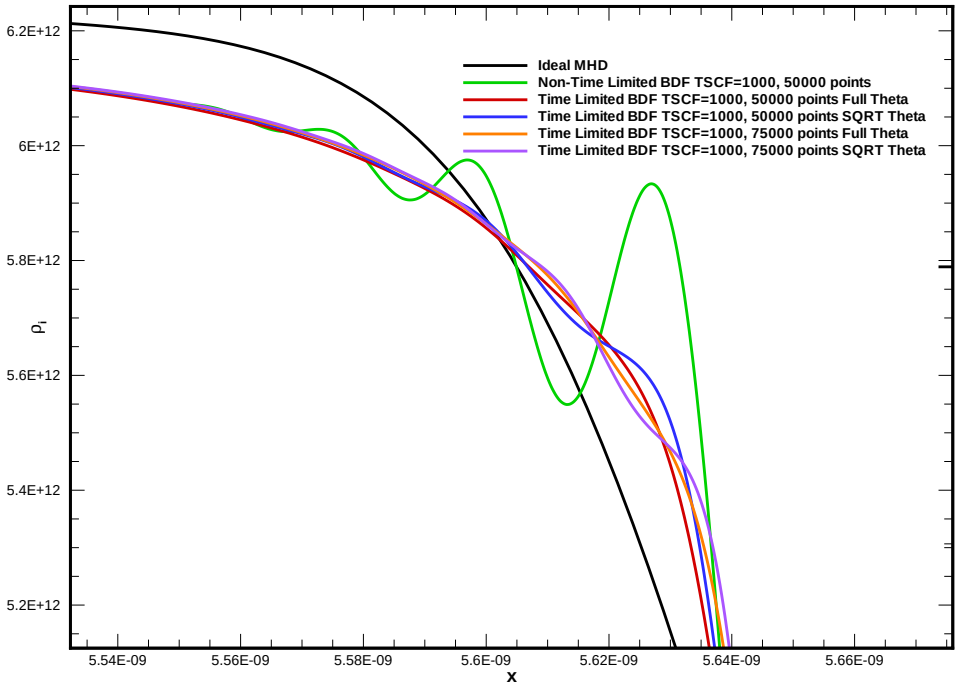

Figure 5.18: Density, ρ, for the high resolution Brio-Wu test case comparing 50000 and 75000 resolution solutions showing a close up of the top of contact discontinuity.

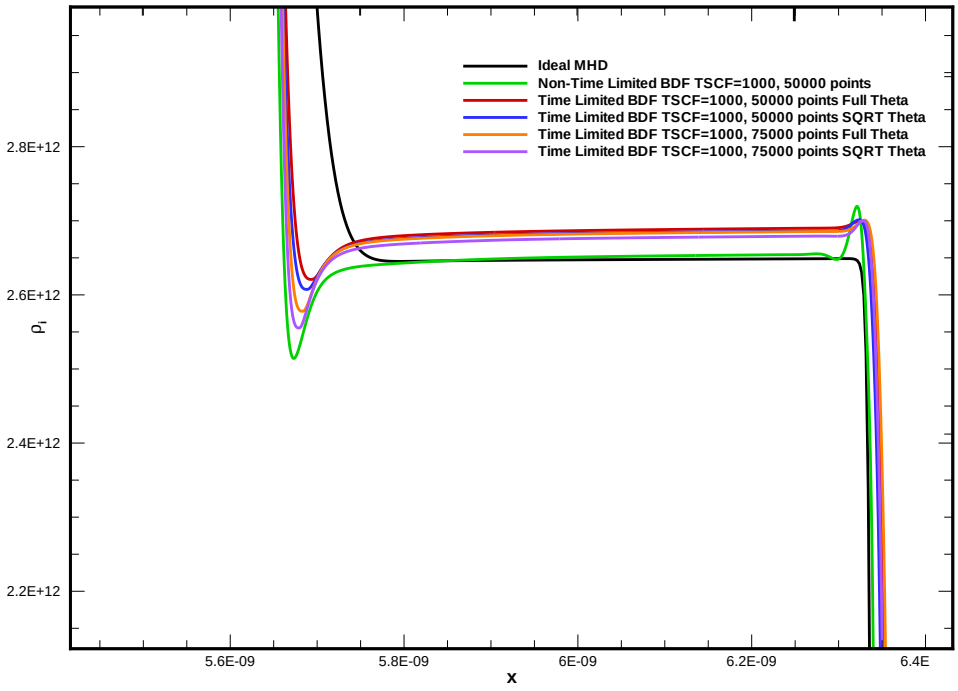

Figure 5.19: Density, ρ, for the high resolution Brio-Wu test case comparing temporal limited, and non-limited schemes showing the close up of the shock.

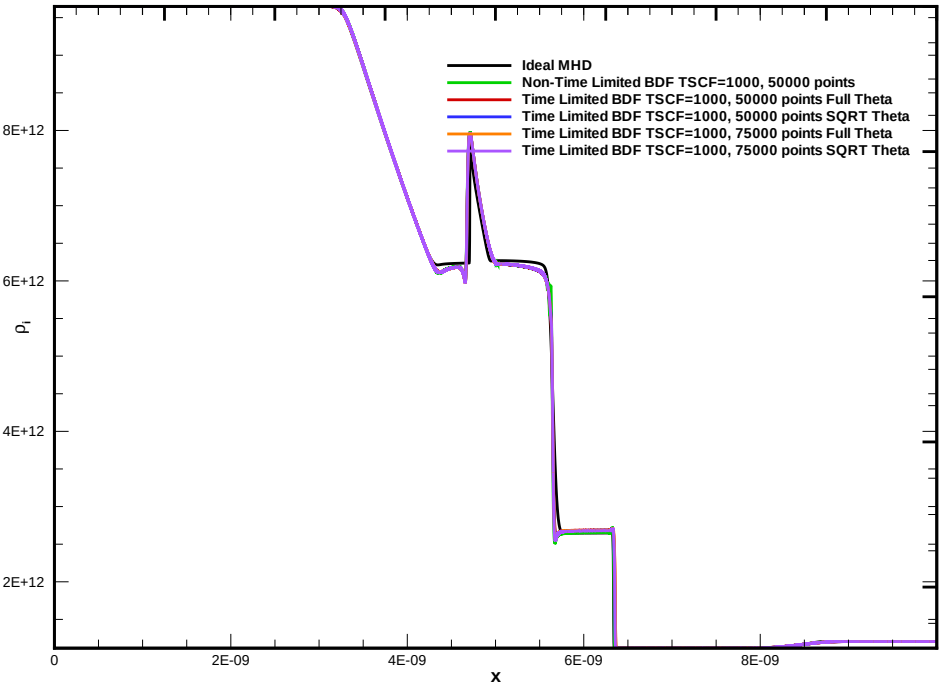

Figure 5.20: Density, ρ, for the high resolution Brio-Wu test case.

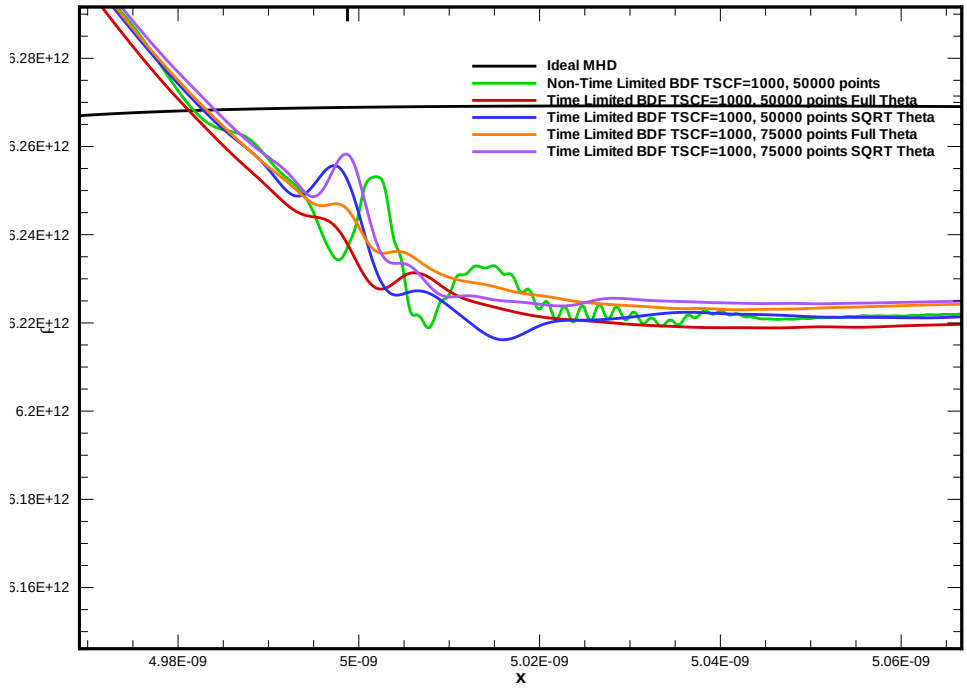

Figure 5.21: Density, ρ, for the high resolution Brio-Wu test case showing a close up of compound shock oscillations.

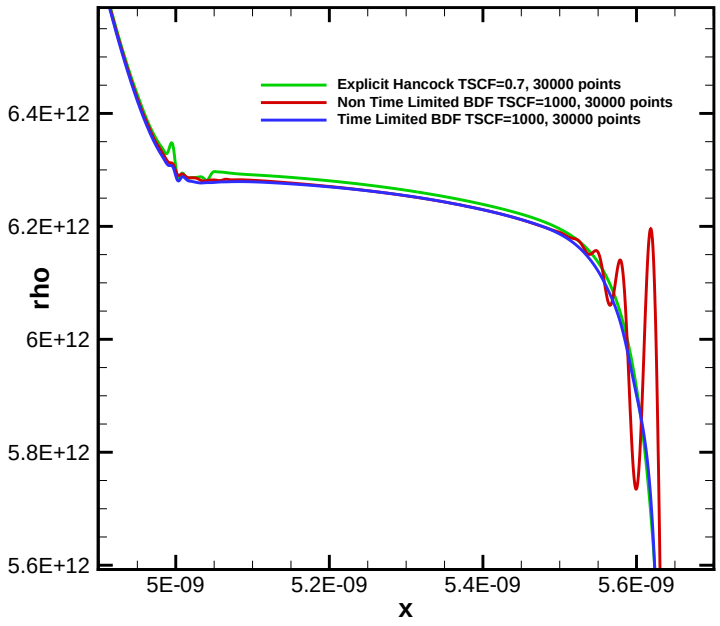

Figure 5.22: Density, ρ, for the high resolution Brio-Wu test case comparing explicit and implicit solutions showing a close up of compound shock oscillations.

Chapter 6

Two-Dimensional Numerical Solution Procedure

6.1 Overview of Parallel, Newton-Krylov-Schwarz Finite-Volume Scheme

The proposed two-dimensional numerical solution procedure that is used to solve the MMHD model with the FGLM and MGLM/MGLMED divergence cleaning procedures as presented in Chapter 3 is now described. The method has been constructed based on the findings of the previous one-dimensional studies and follows the one-dimensional scheme of Chapter 5 with the associated extensions to the two-dimensional case. The proposed scheme for two-dimensional plasma flow simulation makes use of a multi-block body-fitted quadrilateral mesh and a domain decomposition approach to parallel implementations as described by Groth *et al.* [36,37,91,147] and which has been applied to a wide range of applications including reacting [148–153], soot formation [154–157], multi-phase [158,159] and micron-scale [93,97] flows. The implicit temporal limited scheme used for the one-dimensional solution procedure is replaced with a Newton-Krylov-Schwarz (NKS) scheme [131,154,157] for solution of both steady and unsteady problems.

6.2 Godunov Finite-Volume Scheme

The Godunov finite-volume spatial discretization scheme of Section 5.2.1 is extended here to two-dimensional domains. In this case, Equation (3.8) becomes

$$\frac{\partial \mathbf{U}}{\partial t} + (\nabla \cdot \overrightarrow{\mathbf{F}}) = \frac{\partial \mathbf{U}}{\partial t} + \frac{\partial \mathbf{F}_x}{\partial x} + \frac{\partial \mathbf{F}_y}{\partial y} = \mathbf{S}, \tag{6.1}$$

where $\mathbf{U}$ is the conservative solution vector, $\overrightarrow{\mathbf{F}} = [\mathbf{F}_x, \mathbf{F}_y]$ is the conservative flux dyad, and $\mathbf{S}$ is the non-conservative source terms combining the collision and non-collision terms. Integrating the equation above over a control surface in 2D and using the divergence theorem [98, 129], it follows that

$$\iint_A \left(\frac{\partial \mathbf{U}}{\partial t} + \nabla \cdot \overrightarrow{\mathbf{F}} \right) dA = \frac{d}{dt} \iint_A \mathbf{U}\, dA + \oint_\Omega \overrightarrow{\mathbf{F}} \cdot \mathbf{n}\, d\Omega = \iint_A \mathbf{S}\, dA. \tag{6.2}$$

The semi-discrete form of the conservation equations can be obtained by considering Equation (6.2) applied to a 2D control area, A_{ij}, representing cell (i, j), and thereby obtaining coupled non-linear ODEs for the cell averaged values for $\mathbf{U}$. Performing the integration for polygonal cell (i, j), using mid-point rule quadrature, contained by a series of k straight line segments of length Δl_k and unit normals $\hat{\mathbf{n}}_k$, the resulting semi-discrete equations can be written as

$$\frac{d\mathbf{U}_{ij}}{dt} = -\frac{1}{A_{ij}} \sum_k \left(\overrightarrow{\mathbf{F}}_k \cdot \hat{\mathbf{n}}_k \Delta l_k \right)_{ij} + \mathbf{S}_{ij} \equiv -\mathbf{R}(\mathbf{U}_{ij}), \tag{6.3}$$

where $\mathbf{U}_{ij} = 1/A_{ij} \iint_{A_{ij}} \mathbf{U}\, dA$ and $\mathbf{S}_{ij} = 1/A_{ij} \iint_{A_{ij}} \mathbf{S}\, dA$ are the cell averaged values for the solution state and the source term vectors, respectively. We also take the flux dyad, $\overrightarrow{\mathbf{F}}_k$, to be evaluated at the mid-point of the kth face representing the cell boundary. The right hand side of Equation (6.3) is defined to be the residual. For the current work, a Cartesian mesh, with rectangular cells is assumed. This reduces the numerical fluxes to only those in the x- and y-directions, though the scheme can be extended to non-rectangular quadrilaterals, as shown in Section 7.4.

6.3 HLLE/Godunov Approximate Riemann Numerical Flux

The numerical fluxes, $\left(\overrightarrow{\mathbf{F}}_k \cdot \hat{\mathbf{n}}_k \Delta l_k \right)^n_{ijk}$, of Equations (6.19) and (6.3), through each cell face with unit normal $\hat{\mathbf{n}}_k$ and length of face Δl_k, are determined from the solution to an approximate Riemann problem. The Riemann problem can be viewed as a one-dimensional Riemann problem at the cell interface for each face, k, oriented in a direction normal to that face.

6.3.1 HLLE Numerical Flux for Fluid Equations

Due to the nature of being able to express the flux calculations across a boundary as a one-dimensional problem, the HLLE flux function from Section 5.2.3 can be used, as is, for the fluid

equations. The only modification in the previous procedure is in how the left and right solution values are determined, as will be outlined in Section 6.3.3.

6.3.2 Godunov Exact Flux Function for the Maxwell's Equations with GLM Divergence Cleaning

When the MMHD equations were extended to two-dimensions, it was found that there was a significant loss of accuracy due to round-off/cancellation errors in the HLLE numerical flux formulation for the Maxwell's and the GLM divergence cleaning equations. Due to the decoupled nature of Maxwell's equations, the flux calculations for the EM system could be separately calculated and an exact solver was developed for the system, replacing the HLLE numerical flux function described in Section 5.2.3 for the EM equations. The spatial reconstruction is performed in the same way as for the ion, electron and neutral fluid equations.

When the flux is linear, as in the case of Maxwell's equations, it is possible to evaluate the flux exactly. For detailed derivations of the solution procedure adopted here, please refer to the Appendix C. The Riemann problem at the cell interface corresponds to an IVP of the form

$$\frac{\partial \mathbf{U}}{\partial t} + \mathcal{C}\frac{\partial \mathbf{U}}{\partial x} = \mathbf{0}, \tag{6.4}$$

$$\mathbf{U}(x,0) = \begin{cases} \mathbf{U}_l & \text{for} \quad x < 0, \\ \mathbf{U}_r & \text{for} \quad x > 0, \end{cases} \tag{6.5}$$

for one space dimension. Here, $\mathcal{C}$ is equal to $\partial \mathrm{F}/\partial \mathrm{U}$. The method of characteristics is used to solve the IVP. For the non-GLM Maxwell's equations, there are three characteristics separating 4 solution states as shown in Figure 6.1. For the Maxwell's equations with GLM divergence cleaning, there are only two characteristic lines when $\chi = 1$ and $c_h = c$, separating 3 regions as depicted in Figure 6.2. The derivation for the case of the non-GLM equations can be found in Section C.4 of the Appendix, but here the flux function with GLM will be derived. In this case, there are three regions

$$\mathbf{U}_l, \mathbf{U}^*, \mathbf{U}_r. \tag{6.6}$$

where $\mathbf{U}_l$, $\mathbf{U}_r$, and $\mathbf{U}^*$ are the 'left', 'right' and intermediate conservative solution states obtained from the primitive solutions states $\mathbf{W}_i$, $\mathbf{W}_o$ and $\mathbf{W}$, respectively from Figure 6.2. The intermediate state, $\mathbf{U}^*$ can be found using

$$\mathbf{U}^* = \mathbf{U}_l + \Sigma_{i=1}^{3} \alpha_i \mathbf{r}_{GLM}^i = \mathbf{U}_r - \Sigma_{i=0}^{2} \alpha_{6-i} \mathbf{r}_{GLM}^{6-i} \tag{6.7}$$

where

$$\alpha_i = \mathbf{l}_{GLM}^i (\mathbf{U}_r - \mathbf{U}_l). \tag{6.8}$$

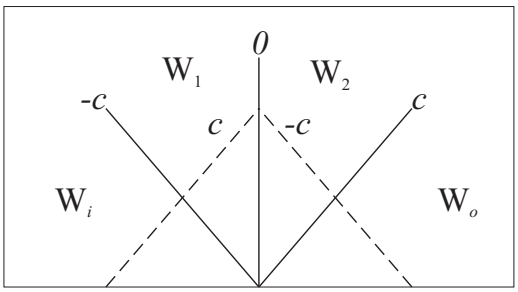

Figure 6.1: Riemann problem for Maxwell's equations with characteristic lines

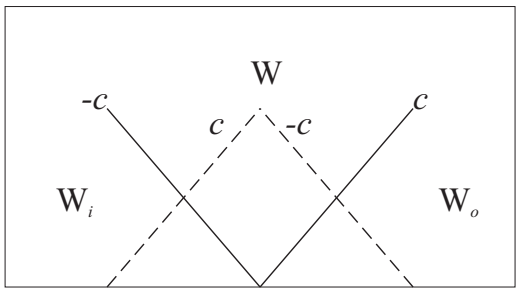

Figure 6.2: Riemann problem for Maxwell GLM equations with characteristic lines

The left and right conservative GLM eigenvectors $\mathbf{l}^i_{GLM}$ and $\mathbf{r}^i_{GLM}$, respectively, in matrix form are listed in Appendix C.3, as Equations (C.29) and (C.30). The intermediate flux is then

$$\mathbf{F}_x = \mathcal{C}\mathbf{U}_1 = \mathcal{C}\mathbf{U}_2. \tag{6.9}$$

Exact Maxwell GLM Flux Function

Because of the stationary wave pattern, the intermediate flux is always used. Therefore, the analytical solution for the exact Godunov flux for both the non-GLM and GLM version of Maxwell's equations are as follows:

$$\mathbf{F}_{x,MF} = \begin{bmatrix} 0 \\ \frac{1}{2}\left(c\left(B_{l,y} - B_{r,y}\right) - E_{l,z} - E_{r,z}\right) \\ \frac{1}{2}\left(c\left(B_{l,z} - B_{rz}\right) + E_{l,y} + E_{r,y}\right) \\ 0 \\ \frac{1}{2}\left(H_{l,z} + H_{r,z} + \sqrt{\frac{\varepsilon_0}{\mu_0}}\left(E_{l,y} - E_{r,y}\right)\right) \\ -\frac{1}{2}\left(H_{l,y} + H_{r,y} + \sqrt{\frac{\varepsilon_0}{\mu_0}}\left(E_{r,z} - E_{l,z}\right)\right) \end{bmatrix}, \tag{6.10}$$

$$\mathbf{F}_{x,GLM} = \begin{bmatrix} \frac{1}{2}\left(\psi_l + \psi_r - B_{r,x}\, c_h + B_{l,x}\, c_h\right) \\ \frac{1}{2}\left(c\left(B_{l,y} - B_{r,y}\right) - E_{l,z} - E_{r,z}\right) \\ \frac{1}{2}\left(c\left(B_{l,z} - B_{r,z}\right) + E_{l,y} + E_{r,y}\right) \\ \frac{1}{2}\left(\frac{1}{\mu_0}\left(\phi_l + \phi_r\right) + \sqrt{\frac{\varepsilon_0}{\mu_0}}\chi\left(E_{l,x} - E_{r,x}\right)\right) \\ \frac{1}{2}\left(H_{l,z} + H_{r,z} + \sqrt{\frac{\varepsilon_0}{\mu_0}}\left(E_{l,y} - E_{r,y}\right)\right) \\ -\frac{1}{2}\left(H_{l,y} + H_{r,y} + \sqrt{\frac{\varepsilon_0}{\mu_0}}\left(E_{r,z} - E_{l,z}\right)\right) \\ \frac{1}{2}c_h\left(c_h B_{l,x} + c_h B_{r,x} - \psi_r + \psi_l\right) \\ \frac{1}{2}\chi\left(\chi E_{l,x} + \chi E_{r,x} - c\,\phi_r + c\,\phi_l\right) \end{bmatrix}. \tag{6.11}$$

Neglecting the terms with particular GLM coefficients will result in the elimination of the associated divergence cleaning algorithm. Setting ψ, c_h, ϕ, and χ to 0 will reduce the GLM version of Maxwell's equations to the non-GLM Maxwell's equations. A common set of equations used in this work is the magnetic field divergence cleaning model with no electric field error cleaning (MGLM), which is achieved by setting $\psi = c_h = 0$. Use of the exact Godunov flux for Maxwell's equations was found to reduce both computational costs and round-off errors.

6.3.3 Least-Squares Piecewise Linear Limited Spatial Reconstruction

The left and right solution values appearing in Equation (5.12) are obtained by using a least-squares piecewise linear spatial reconstruction for higher-order spatial resolution very similar to that described in Section 5.2.2, but extended to two-dimensions. For the two-dimensional solution procedure, the primitive solution states are the basis for calculating the HLLE flux. The piecewise linear spatial reconstruction for the left and right primitive solution states are given by

$$\mathbf{W}^L_{i+\frac{1}{2},j} = \mathbf{W}_{i,j} + \phi_{i,j}\nabla\mathbf{W}_{i,j}\cdot\Delta\mathbf{x}_L, \tag{6.12}$$

$$\mathbf{W}^R_{i+\frac{1}{2},j} = \mathbf{W}_{i+1,j} + \phi_{i+1,j}\nabla\mathbf{W}_{i+1,j}\cdot\Delta\mathbf{x}_R, \tag{6.13}$$

for the interface between cells (i,j) and $(i+1,j)$, defined as $(i+\frac{1}{2},j)$, and where $\Delta\mathbf{x}_L$, $\Delta\mathbf{x}_R$ are the distance vectors defined from the centroid of the left and right cells to the interface in question, respectively. This procedure can be repeated for all interfaces by using the appropriate indices. Since the flux problem reduces to a one-dimensional Riemann problem, the same Barth-Jespersen, Equation (5.11), slope limiter can be used to calculate ϕ and limit the left and right reconstructed solution states using primitive solution state vectors.

The gradients in Equations (6.12) and (6.13) were evaluated using a least-squares method [136] which minimizes the least-squares error,

$$\sum_{k=1}^{k=N}\left((\mathbf{W}_{ij}-\mathbf{W}_k)-\nabla\mathbf{W}_{ij}\cdot(\mathbf{x}_{ij}-\mathbf{x}_k)\right)^2 \tag{6.14}$$

for each cell ij using information from the neighbouring cells k, which for the 2D case is 8 cells ($N=8$). The vector $\mathbf{x}$ is the location of the centroid of the cell. The problem is solved as a linear system of equations which can be written as

$$\begin{bmatrix} \overline{(\Delta x)^2} & \overline{\Delta x\Delta y} \\ \overline{\Delta x\Delta y} & \overline{(\Delta y)^2} \end{bmatrix}\begin{bmatrix} \frac{\partial\mathbf{W}}{\partial x} \\ \frac{\partial\mathbf{W}}{\partial y} \end{bmatrix} = \begin{bmatrix} \overline{\Delta\mathbf{W}\Delta x} \\ \overline{\Delta\mathbf{W}\Delta y} \end{bmatrix}, \tag{6.15}$$

with the averaged errors

$$\overline{(\Delta x)^2} = \frac{1}{N}\sum_{k=1}^{N}\Delta x_k^2, \tag{6.16}$$

$$\overline{\Delta x \Delta y} = \frac{1}{N}\sum_{k=1}^{N}\Delta x_k \Delta y_k, \tag{6.17}$$

$$\overline{\Delta \mathbf{W} \Delta y} = \frac{1}{N}\sum_{k=1}^{N}\Delta \mathbf{W}_k \Delta x_k, \tag{6.18}$$

where $\Delta x_k = x_{ij} - x_k$ and $\Delta \mathbf{W}_k = \mathbf{W}_{ij} - \mathbf{W}_k$.

6.4 Parallel Implementation

The 2D numerical scheme was parallelized using a block based domain decomposition algorithm [160] with Morton ordering [161] and follows the procedure outlined in [37, 162] for parallelization. The basics of this method is to break up the domain of the problem into smaller sub-domains, which is possible for the block based meshes used, and solve each sub-problem on a separate process for each physical time step. To maintain solution continuity, the sub-divided meshes communicate through boundary ghost cells for each mesh where the ghost cells for one interior domain were the interior cells of the neighbouring mesh that shares the domain interface. This solution information was communicated via the message passing interface (MPI) library [163].

6.5 Explicit Predictor-Corrector Time Stepping Scheme

The explicit time marching method employed here was an explicit predictor-corrector Runge-Kutta scheme with second-order time accuracy as proposed by MacCormack [129, 164]. This two-stage, second-order, explicit scheme applied to the semi-discrete form of the governing equations, Equation (6.3), can be written as

$$\tilde{\mathbf{U}}_{ij}^{n+1} = \mathbf{U}_{ij}^{n} - \frac{\Delta t}{A_{ij}}\left(\sum_k \left(\overrightarrow{\mathbf{F}}_k \cdot \hat{\mathbf{n}}_k \Delta l_k\right)_{ijk}^{n}\right) + \Delta t \mathbf{S}_{ij}^{n}, \tag{6.19}$$

$$\mathbf{U}_{ij}^{n+1} = \mathbf{U}_{ij}^{n} - \frac{\Delta t}{2A_{ij}}\left(\sum_k \left(\overrightarrow{\mathbf{F}}_k \cdot \hat{\mathbf{n}}_k \Delta l_k\right)_{ijk}^{n} + \sum_k \left(\tilde{\overrightarrow{\mathbf{F}}}_k \cdot \hat{\mathbf{n}}_k \Delta l_k\right)_{ijk}^{n+1}\right) + \frac{\Delta t}{2}\left(\mathbf{S}_{ij}^{n} + \tilde{\mathbf{S}}_{ij}^{n+1}\right), \tag{6.20}$$

which integrates the solution forward from time level n to $n+1$ with a time step of Δt for cell (i,j). Here, the cell averaged conservative solution state vector and source vector is $\mathbf{U}_{ij}^n$ and $\mathbf{S}_{ij}^n$, respectively and $\tilde{\mathbf{U}}_{ij}^{n+1}$ represents an intermediate solution state.

6.6 Implicit Newton-Krylov-Schwarz Algorithm

The implicit temporal scheme that was adopted for the 2D procedure is based on a NKS algorithm used in conjunction with a dual-time stepping scheme. For the most part, the procedure and algorithm of Northrup [131] and Charest *et al.* [154, 157] is adopted. Currently, the NKS solution method is formulated for the full GLM (FGLM) and non-GLM (NGLM) equations, but can be used with all other divergence error correction schemes.

6.6.1 Newton's Method

In the NKS method, Newton's method is used to solve simultaneously a coupled system of non-linear algebraic equations. The system of algebraic equations of interest arises from the semi-discrete form of the governing equations, Equation (6.3), following the spatial discretization procedure. Using the notation of the RHS being the residual $\mathbf{R}(\mathbf{U})$, results in

$$\frac{d\mathbf{U}}{dt} = -\mathbf{R}(\mathbf{U}) \tag{6.21}$$

where the cell indices ij have been dropped, with the understanding that the equation applies for all cells simultaneously. For steady state solutions, the residual is zero and solutions, $\mathbf{U}$, satisfying the non-linear algebraic equations

$$\mathbf{R}(\mathbf{U}) = \mathbf{0}, \tag{6.22}$$

are sought. Applying Newton's method to the solution of Equation (6.22) with Jacobian, $\mathbf{J} = \partial\mathbf{R}/\partial\mathbf{U}$, requires the solution of the linear system of equations

$$\mathbf{J}\Delta\mathbf{U}^k = -\mathbf{R}(\mathbf{U}^k) \qquad \longrightarrow \qquad \mathbf{A}\mathbf{x} = \mathbf{b} \tag{6.23}$$

with $\mathbf{A} = \mathbf{J}$, $\mathbf{x} = \Delta\mathbf{U}^k$ and $\mathbf{b} = -\mathbf{R}(\mathbf{U}^k)$ at each step of Newton's method, k. The solution is then updated at the next step using $\mathbf{x} = \Delta\mathbf{U}^k$ with $\mathbf{U}^{k+1} = \mathbf{U}^k + \Delta\mathbf{U}^k$.

6.6.2 GMRES Iterative Procedure

In the NKS scheme, it is not necessary to solve the system of linear equations defined by Equation (6.23) exactly at each step in order to converge the solution of the non-linear problem

defined by Equation (6.22). The linear problem in the NKS scheme of this thesis is solved using an iterative solution procedure known as the Generalized Minimal RESidual (GMRES) method [165, 166]. The GMRES method solves the linear problem of Equation (6.23) approximately, which can be very effective for the solution of large, sparse, non-symmetric linear equations. Please refer to Northup's thesis [131] for more details on the GMRES procedure applied here.

6.6.3 Normalization and Preconditioning

As was observed by Saad [167] and others such as Northrup [131], effective normalization and preconditioning is required for the GMRES iterative scheme to be efficient. A linear scaling is applied here using a diagonal matrix Γ so that a linearized system is formed and solved such that

$$\begin{aligned} \mathbf{J}\Delta\mathbf{U}^k &= -\mathbf{R}(\mathbf{U}^k) \\ \mathbf{\Gamma}_R\mathbf{J}\,(\mathbf{I})\,\Delta\mathbf{U}^k &= -\mathbf{\Gamma}_R\mathbf{R}(\mathbf{U}^k) \\ \left(\mathbf{\Gamma}_R\mathbf{J}\,\mathbf{\Gamma}_U^{-1}\right)\left(\mathbf{\Gamma}_U\Delta\mathbf{U}^k\right) &= -\mathbf{\Gamma}_R\mathbf{R}(\mathbf{U}^k) \\ \mathbf{J}'\Delta\mathbf{U}^{k\prime} &= -\mathbf{R}'(\mathbf{U}^k) \end{aligned} \tag{6.24}$$

The diagonal matrix is created by

$$\mathbf{\Gamma}_R = (\mathbf{I}\,\mathbf{R}_{norm})^{-1}, \qquad \mathbf{\Gamma}_U = (\mathbf{I}\,\mathbf{U}_{norm})^{-1}. \tag{6.25}$$

The scaling vectors, $\mathbf{R}_{norm}$ and $\mathbf{U}_{norm}$, were formed by scaling the system where each set of equations has a tailored scaling vector that attempts to make the order of magnitudes of the terms in each equation to be similar.

The row scaling that is used for the fluid equations is based on reference densities, $\rho_{0,s}$, and acoustic velocities, $a_{0,s}$, of the 10-moment system. For each species s, the scaling vectors are

$$\mathbf{U}_s = \begin{bmatrix} \rho_s \\ \rho_s u_{s,x} \\ \rho_s u_{s,y} \\ \rho_s u_{s,z} \\ \rho_s u_{s,x}^2 + P_{s,xx} \\ \rho_s u_{s,x} u_{s,y} + P_{s,xy} \\ \rho_s u_{s,x} u_{s,z} + P_{s,xz} \\ \rho_s u_{s,y}^2 + P_{s,yy} \\ \rho_s u_{s,y} u_{s,z} + P_{s,yz} \\ \rho_s u_{s,z}^2 + P_{s,zz} \end{bmatrix}, \qquad \mathbf{U}_{norm,s} = \begin{bmatrix} \rho_{0,s} \\ \rho_{0,s} a_{0,s} \\ \rho_{0,s} a_{0,s} \\ \rho_{0,s} a_{0,s} \\ \rho_{0,s} a_{0,s}^2 \\ \rho_{0,s} a_{0,s}^2 \\ \rho_{0,s} a_{0,s}^2 \\ \rho_{0,s} a_{0,s}^2 \\ \rho_{0,s} a_{0,s}^2 \\ \rho_{0,s} a_{0,s}^2 \end{bmatrix}, \qquad \mathbf{R}_{norm,s} = \begin{bmatrix} \rho_{0,s} a_{0,s} \\ \rho_{0,s} a_{0,s}^2 \\ \rho_{0,s} a_{0,s}^2 \\ \rho_{0,s} a_{0,s}^2 \\ \rho_{0,s} a_{0,s}^3 \\ \rho_{0,s} a_{0,s}^3 \\ \rho_{0,s} a_{0,s}^3 \\ \rho_{0,s} a_{0,s}^3 \\ \rho_{0,s} a_{0,s}^3 \\ \rho_{0,s} a_{0,s}^3 \end{bmatrix}, \tag{6.26}$$

where the solution state vector is provided for reference. The scaling for the electro-magnetic Maxwell GLM equations is based on reference magnetic and electric field values, $|B_0|$ and $|E_0|$, along with the associated magnetic field strength and electric displacement field, $|H_0|$ and $|D_0|$, respectively. The magnitude of the magnetic field due to the fluid pressure is also considered, given by

$$B_p = \sqrt{2p\mu}. \tag{6.27}$$

The largest values are chosen for the normalization such that

$$\begin{gathered} B_N = \max(|B_0|, B_p), \\ D_N = \max(|D_0|, \varepsilon c B_N), \quad E_N = \max(|E_0|, cB_N), \quad H_N = \max(|H_0|, \tfrac{B_N}{\mu}), \end{gathered} \tag{6.28}$$

where B_N is evaluated first. The row scaling vectors are then given by

$$\mathbf{U}_{GLM} = \begin{bmatrix} B_x \\ B_y \\ B_z \\ D_x \\ D_y \\ D_z \\ \psi \\ \phi \end{bmatrix}, \qquad \mathbf{U}_{norm,GLM} = \begin{bmatrix} B_N \\ B_N \\ B_N \\ D_N \\ D_N \\ D_N \\ E_N \\ \chi B_N \end{bmatrix}, \qquad \mathbf{R}_{norm,GLM} = \begin{bmatrix} E_N \\ E_N \\ E_N \\ H_N \\ H_N \\ H_N \\ c^2 B_N \\ \chi^2 E_N \end{bmatrix}, \tag{6.29}$$

with the conservative solution state vector provided for reference. The normalization vectors are then combined, for Equation (6.25), such that

$$\mathbf{R}_{norm} = \begin{bmatrix} \mathbf{R}_{norm,e} \\ \mathbf{R}_{norm,ion} \\ \mathbf{R}_{norm,n} \\ \mathbf{R}_{norm,GLM} \end{bmatrix}, \qquad \mathbf{U}_{norm} = \begin{bmatrix} \mathbf{U}_{norm,e} \\ \mathbf{U}_{norm,ion} \\ \mathbf{U}_{norm,n} \\ \mathbf{U}_{norm,GLM} \end{bmatrix}. \tag{6.30}$$

Further preconditioning is performed on the Jacobian of Equations (6.23) and (6.24) by employing right preconditioning which does not affect the right side residual [166, 167]. With preconditioning matrix $\mathbf{M}$, the preconditioning takes the form

$$\left(\mathbf{J}\,\mathbf{M}^{-1}\right)(\mathbf{M}\Delta\mathbf{U}) = -\mathbf{R}. \tag{6.31}$$

Though there are many different preconditioning options possible [168], the best preconditioner would be an easily invertible approximation to the Jacobian of the system. The preconditioners used here are the Schwarz global additive preconditioner [169] and a local Block Incomplete Lower-Upper (BILU) preconditioner.

The Schwarz preconditioner allows for easier computation of the implicit problem through domain decomposition and by solving the problem, using the Newton-Krylov scheme, on each subdomain separately. This decreases the memory and computational resources required significantly for large problems, despite an increase in the number of GMRES iterations needed for a converged solution. The inverted preconditioning matrix, $\mathbf{M}^{-1}$, for each sub-domain is determined through the local BILU factorization which makes use of the incomplete lower-upper (ILU) factorization [166] to approximate the approximate block Jacobian, which is discussed in the next section, such that

$$\mathbf{M} = \mathbf{L}(f)\mathbf{U}(f) \approx \tilde{\mathbf{J}} \tag{6.32}$$

where f is the level of fill for the ILU matricies. A level of fill of 2 is used for the results obtained in this thesis. Please refer to Northrup's work for more details on the preceding preconditioning strategies [131].

6.6.4 Approximate Jacobians of the MMHD GLM 2D Equations

As was mentioned in the previous section, the preconditioning matrix formed through BILU factorization is based on an approximation to the Jacobian of the system of Equations (6.23),

$$\tilde{\mathbf{J}} \approx \mathbf{J} = \frac{\partial \mathbf{R}}{\partial \mathbf{U}}. \tag{6.33}$$

The approximate Jacobians are based on the first-order terms of the discretization scheme employed to solve Equation (6.3).

For the fluxes in the Godunov-type finite-volume upwind scheme, the approximate flux solver of Section 6.3 is implemented by first rotating the solution state vectors, $\mathbf{W}^L, \mathbf{W}^R$, on either side of the interface into a common local frame (a positive x-direction). The 1D Riemann problem is then solved numerically using either the HLLE flux function for the fluid case, or the Godunov flux function, for the Maxwell-GLM case. The resulting conservative fluxes are then rotated back to the global frame. The resulting operation can be described as

$$\overrightarrow{\mathbf{F}}_k \cdot \hat{\mathbf{n}}_k = \mathbf{A}^{-1}\mathcal{F}\left(\mathbf{A}\mathbf{W}^L, \mathbf{A}\mathbf{W}^R\right) \tag{6.34}$$

where $\mathbf{A}$ is the rotation matrix and $\mathcal{F}$ is the numerical flux function. Keeping the left state as the cell in the center, (i, j),

$$\frac{\partial \mathbf{R}_{ij}}{\partial \mathbf{U}_{ij}} = -\frac{1}{A_{ij}} \sum_k \left(\mathbf{A}^{-1} \frac{\partial \mathcal{F}(\mathbf{A}\mathbf{W}^L, \mathbf{A}\mathbf{W}^R)}{\partial \mathbf{A}\mathbf{U}_L} \mathbf{A} \Delta l \right)_{ijk} + \frac{\partial \mathbf{S}_{ij}}{\partial \mathbf{U}_{ij}} \tag{6.35}$$

for every face k, where the chain rule was used noting $\partial\mathcal{F}/\partial\mathbf{U} = \partial\mathcal{F}/\partial(\mathbf{A}\mathbf{U})\,\mathbf{A}$. The scalar A_{ij} is the area of the cell. All of the flux Jacobian terms, $\partial\mathcal{F}(\mathbf{A}\mathbf{U}_L, \mathbf{A}\mathbf{U}_R)/\partial(\mathbf{A}\mathbf{U}_L)$ both for the fluid and Maxwell-GLM, can be calculated from analytic equations.

For the source terms, $\partial \mathbf{S}_{ij}/\partial \mathbf{U}_{ij}$, the calculation of the Jacobian is simpler as the source terms only required information from the local cell in question. Most of the Jacobian can be analytically determined. However, due to the complexity of the collision frequency models, the particle collision frequencies were assumed constant. Further, for the ionization-recombination and charge exchange terms, it was found that taking a first-order approximation, or dropping some small parameter terms, resulted in a severely reduced GMRES convergence. Therefore, the ionization-recombination and charge exchange Jacobian terms were determined using a finite difference approximation, which is quite costly, but resulted overall in a faster convergence and computational time within the NKS scheme.

6.6.5 Jacobian-Free GMRES Procedure

As detailed in the work by Northrup [131], the GMRES procedure requires a Krylov space orthogonalization which requires the evaluation of the matrix-vector product, $\mathbf{Av}$, where $\mathbf{A}$ is defined in Equation (6.23) and $\mathbf{v}$ is an arbitrary solution change vector. In the Jacobian-free GMRES procedure used by Northrup [131], this product is evaluated numerically by using Fréchet derivatives [170,171], which is simply derived from an approximation for the first-order derivative and can be written as

$$\mathbf{Av} \approx \frac{\mathbf{R}(\mathbf{U} + \varepsilon \mathbf{v}) - \mathbf{R}(\mathbf{U})}{\varepsilon}, \tag{6.36}$$

where the perturbation parameter is given by $\varepsilon = \varepsilon_0 / \|\mathbf{v}\|_2^{1/2}$ as suggested by Nielsen *et al.* [170]. For the simulations given in this thesis, $\varepsilon_0 = 10^{-6}$. However, with the numerical stiffness issues of the MMHD GLM 2D equations, the perturbation of the solution state vector resulted in acute round off/cancellation errors. To mitigate this issue, a hybrid procedure is proposed. The cancellation errors were found to mostly occur in the source terms involving the electromagnetic forces. Because it occurred in the source terms, it is possible to evaluate $\mathbf{Av}$ using the analytic source term Jacobian for the EM terms only. Therefore the modified matrix-vector product of Equation (6.36) is given by

$$\mathbf{Av} \approx \frac{\mathbf{Q}(\mathbf{U} + \varepsilon \mathbf{v}) - \mathbf{Q}(\mathbf{U})}{\varepsilon} + \frac{\partial \mathbf{S}_{EM}}{\partial \mathbf{U}} \mathbf{v}, \tag{6.37}$$

where $\mathbf{Q}(\mathbf{U})$ is the modified residual, which is calculated in the same way as $\mathbf{R}(\mathbf{U})$, but with all source terms associated with the electromagnetic equations excluded. Likewise, $\partial \mathbf{S}_{EM}/\partial \mathbf{U}$ is the analytic Jacobian of all the source terms excluded from $\mathbf{Q}(\mathbf{U})$. When the above modification is applied, the convergence rates of the GMRES method are significantly improved to the point where convergence could be achieved for previously non-converging problems.

6.7 Dual-Time Stepping-Like NKS

In addition to the steady state implicit solver outlined in the previous section, a dual-time formulation was also implemented, which can provide time accurate solutions to the MMHD GLM model [172,173]. This was easily accomplished by adding a pseudo-time term to Equation (6.21) such that

$$\frac{d\mathbf{U}}{d\tau} + \frac{d\mathbf{U}}{dt} = -\mathbf{R}(\mathbf{U}). \tag{6.38}$$

This can be arranged so that the pseudo-time replaces the physical time in all the calculations in the steady NKS scheme in Section 6.6 making each physical time step a steady problem in the pseudo-time τ so that

$$\frac{d\mathbf{U}}{d\tau} = -\frac{d\mathbf{U}}{dt} - \mathbf{R}(\mathbf{U}) = -\mathbf{R}^*(\mathbf{U}) = \mathbf{0}. \tag{6.39}$$

Equation (6.39) is the equivalent of Equation (6.22) in this regard. The physical time derivative of Equation (6.39) is discretized using the second-order BDF scheme given by

$$\mathbf{R}^*\left(\mathbf{U}^{n+1}\right) = \frac{\frac{3}{2}\mathbf{U}^{n+1} - 2\mathbf{U}^n + \mathbf{U}^{n-1}}{\Delta t} + \mathbf{R}\left(\mathbf{U}^{n+1}\right) \tag{6.40}$$

where the index n now represents the physical time level. Therefore, the approximate residual Jacobian of Equation (6.33) can be extended to include the dual-time formulation to give

$$\tilde{\mathbf{J}} \to \tilde{\mathbf{J}}^* \approx \mathbf{J}^* = \left(\frac{3}{2\Delta t}\right)\mathbf{I} + \frac{\partial \mathbf{R}}{\partial \mathbf{U}}, \tag{6.41}$$

to solve the pseudo-time steady system of non-linear equations given by Equation (6.39). This then requires the solution of a corresponding linear system of equations at each Newton step of the form

$$\left[\left(\frac{3}{2\Delta t}\right)\mathbf{I} + \frac{\partial \mathbf{R}}{\partial \mathbf{U}}\right]\Delta\mathbf{U}_k^{n+1} = \mathbf{J}^*\Delta\mathbf{U}_k^{n+1} = -\mathbf{R}^*\left(\mathbf{U}_k^{n+1}\right), \tag{6.42}$$

for each Newton iteration k in pseudo-time τ. Each Newton iteration updates the pseudo-time steady problem solution in k (with physical step $n+1$ being solved for) with

$$\mathbf{U}_{k+1}^{n+1} = \mathbf{U}_k^{n+1} + \Delta\mathbf{U}_k^{n+1} \tag{6.43}$$

where a natural choice for $k = 0$ is the previous physical time solution such that

$$\mathbf{U}_0^{n+1} = \mathbf{U}^n. \tag{6.44}$$

The GMRES procedure also needs to incorporate the dual-time element. The Fréchet derivative expression of Equation (6.37) is also modified to incorporate the dual-time BDF2 scheme by adding a physical time term resulting in

$$\mathbf{A}\mathbf{v} \approx \frac{\mathbf{Q}(\mathbf{U} + \varepsilon\mathbf{v}) - \mathbf{Q}(\mathbf{U})}{\varepsilon} + \left[\frac{\partial \mathbf{S}_{EM}}{\partial \mathbf{U}} + \frac{3}{2\Delta t}\right]\mathbf{v}. \tag{6.45}$$

6.7.1 Switched Evolution and Relaxation Procedure

For both the steady state and dual-time NKS schemes, a Switched Evolution/Relaxation (SER) [174] procedure is employed to discretize the dual-time or steady-state Jacobian (Equations (6.41) and (6.33)) and steady-state Newton problem (Equation (6.39)) in Section 6.7. The pseudo-time derivative of Equation (6.39) is discretized using an implicit Euler formulation, ultimately resulting in the SER version of the dual-time Equation (6.42) which is

$$\left[\left[\frac{1}{\Delta\tau}+\left(\frac{3}{2\Delta t}\right)\right]\mathbf{I}+\frac{\partial\mathbf{R}}{\partial\mathbf{U}}\right]\Delta\mathbf{U}_k^{n+1}=\mathbf{J}^*\Delta\mathbf{U}_k^{n+1}=-\mathbf{R}^*\left(\mathbf{U}_k^{n+1}\right), \tag{6.46}$$

noting that the index k is associated with the pseudo time τ. This allows for a slow ramp up towards full Newton for stability purposes by increasing the $\Delta\tau$. This is particularly useful when the initial guess is far off from the solution. When $\Delta\tau\to\infty$, the full Newton method is recovered. Further, the steady state NKS solution is achieved with an arbitrarily large time step and seeking a zero residual so that $\partial\mathbf{U}/\partial t=0\approx\Delta\mathbf{U}_k^{n+1}/\Delta t$. This is achieved when the residual norm becomes sufficiently small.

As suggested by Mulder *et al.* [174] and modified slightly herein, the method of determining the ramp up for the pseudo-time step is defined by the time step multiplication factor

$$\nu^n=\nu^{min}\max\left(1,\frac{1}{\|\mathbf{R}\|_2}\right), \tag{6.47}$$

which multiplies the pseudo-time TSCF. This increases as the residual decreases.

This procedure has been used for both steady and time dependent calculations. In the time dependent calculations it was used for each sub-problem in the pseudo-time Newton steps when convergence stability was an issue. Constant pseudo-time TSCFs can be utilized as well when stability is an issue.

6.7.2 Problems with the Maxwell-GLM Preconditioning Approximate Jacobians

It should be noted here that the residual Jacobian, and therefore the right block preconditioning matrix, for the Maxwell-GLM subsystem is ill conditioned, and in fact singular for a Godunov upwind scheme. While numerical inversion was possible, using the preconditioning matrix for most of the problems presented in this thesis resulted in significantly poorer convergence rates. Some variations on the preconditioning matrix were examined, including other flux function approximations, and regularization techniques. One that seemed to work particularly well with respect to convergence was arbitrarily making the diagonal of the preconditioning

matrix dominant by multiplying the off diagonal terms of the preconditioning matrix by a small constant. However, it was found that while this significantly accelerated convergence (on the order of 10 to 100 times), it introduced some strange numerical oscillation modes in solutions, particularly for DTS NKS solutions such as the plane wave sinusoidal case of Section 7.2.8. Unless otherwise stated, the approximation to the Jacobian, $\partial\mathbf{R}/\partial\mathbf{U}$, in Equation (6.33) and in the dual-time formulation, Equation (6.41), for the Maxwell-GLM equations only, is set to $\mathbf{0}$. Since the SER procedure of Section 6.7.1 is used this results in a diagonal right preconditioning matrix for the NKS scheme, but a Fréchet derivative for the actual residual Jacobian.

The Jacobian for the fluid equations were still computed as described in Section 6.6.4. This generally provided a superior convergence to the block preconditioning procedure outlined in Section 6.6.4 for when applied to the Maxwell-GLM subsystem, though there were exceptions such as for the LEO GEM case in Section 8.7. Strategies for improved preconditioning of the Maxwell subsystem should certainly be the subject of future follow-on studies.

6.8 Implementation of Electric Diffusion

The inclusion of the electric error diffusion terms described in Section 3.8.5 requires the computation of a second order diffusion term as seen in Equation (3.80). This was accomplished by first calculating the divergence of the electric field in Equation (3.80) using the diamond path stencil, and assuming a linear variation in the solution at the four points of the diamond. Gauss's law is used to approximate the solution gradient at the middle of the diamond to calculate the divergence components [175, 176].

The electric diffusion coefficient λ_E is chosen to be

$$\lambda_E = c\Delta x, \tag{6.48}$$

where Δx is the average, or the smallest grid spacing of the mesh. The von Neumann stability requirements for a 2D diffusion scheme, requires that the limiting time scale associated with the diffusion coefficient is 1/4 that of an explicit inviscid time scale. Therefore, the limiting time scale for the electric error diffusion equations is $1/4\,c$.

6.9 Time Step Control Factor (TSCF)

The time step, Δt, is determined as before through the non-dimensional TSCF relation to control the size of the time step. A greater number of time step restrictions are checked for the 2D MMHDGLM model than in the 1D MMHD model. To facilitate the ability to simulate non magnetized flows the 10-moment fluid dynamics acoustic time scales given by

$$\tau_{10m} = \min\left(\frac{\Delta d_k}{\sqrt{3}a_{s,k} + |v_{s,k}|}\right), \tag{6.49}$$

which results from the eigenvalues of the 10-moment system, are checked. In the equation, s is for the ion, electron and neutral species, and k is the direction normal to the interface examined. The acoustic and bulk velocity in the k direction is $a_{s,k}$ and $v_{s,k}$, respectively. The quantity d_k is an approximate distance to the face. The approximation used results in the exact distance for a Cartesian grid. Next, all EM time scales are examined and given by

$$\tau_{EM} = \min\left(\frac{d_k}{\max(c, \chi c, c_h)}, \frac{1}{\omega_{UH}}\right), \tag{6.50}$$

where c, χc, c_h are the speed of light and the electric and magnetic GLM wavespeeds, respectively. The electron plasma, cyclotron and upper hybrid frequencies are defined as follows, respectively:

$$\omega_{pe} = \sqrt{\frac{n_e e^2}{m_e \varepsilon_0}}, \qquad \omega_{ce} = \frac{|e\mathbf{B}|}{m_e}, \qquad \omega_{UH} = \sqrt{\omega_{pe}^2 + \omega_{ce}^2}. \tag{6.51}$$

In general, the ion hybrid, cyclotron or plasma frequencies are not checked as the ion mass makes these time scales orders of magnitude larger.

As discussed in Section 6.8, when the electric diffusion equations are enabled, Equation (6.50) must be replaced with

$$\tau_{EMEdiff} = \min\left(\frac{d_k}{\max(4c, c_h)}, \frac{1}{\omega_{UH}}\right). \tag{6.52}$$

The definition of the TSCF is therefore

$$\text{TSCF} = \frac{\Delta t}{\min\left(\tau_{10m}, \tau_{EM}\right)}, \tag{6.53}$$

for a time step Δt. The stability condition used here is

$$\Delta t \leq \min\left(\tau_{10m}, \tau_{EM}\right), \tag{6.54}$$

where a TSCF of unity represents the boundary between unstable (TSCF > 1.0) and stable (TSCF ≤ 1.0) explicit schemes.

6.10 Boundary Conditions for the GLM Version of Maxwell's Equations

The boundary relations for the GLM version of Maxwell's equations are presented here. For a more complete derivation of the characteristics, please refer to Appendix C. The boundary conditions were calculated by using the method of characteristics to solve for the intermediate solution state, Equation (6.7), using the influence of the solution states on either side of the boundary. It can be shown that the following relations hold at the the boundary:

$$\begin{aligned}
B_x^* &= \tfrac{1}{2}\left((B_{i,x}+B_{o,x})+\tfrac{1}{c_h}(\psi_i-\psi_o)\right),\\
B_y^* &= \tfrac{1}{2}\left((B_{i,y}+B_{o,y})+\tfrac{1}{c}(E_{o,z}-E_{i,z})\right),\\
B_z^* &= \tfrac{1}{2}\left((B_{i,z}+B_{o,z})+\tfrac{1}{c}(E_{i,y}-E_{o,y})\right),\\
E_x^* &= \tfrac{1}{2}\left((E_{i,x}+E_{o,x})+\tfrac{c}{\chi}(\phi_i-\phi_o)\right),\\
E_y^* &= \tfrac{1}{2}\left(c(B_{i,z}-B_{o,z})+(E_{i,y}+E_{o,y})\right),\\
E_z^* &= \tfrac{1}{2}\left(c(B_{o,y}-B_{i,y})+(E_{o,z}+E_{i,z})\right),\\
\psi^* &= \tfrac{1}{2}\left(c_h(B_{i,x}-B_{o,x})+(\psi_i+\psi_o)\right),\\
\phi^* &= \tfrac{1}{2}\left(\tfrac{\chi}{c}(E_{i,x}-E_{o,x})+(\phi_o+\phi_i)\right),
\end{aligned} \tag{6.55}$$

where $()^*$ is the intermediate boundary state, $()_i$ is the internal domain state, and $()_o$ is the outside of the domain state. Because of the linear nature of the equations, an exact Riemann solution for the hyperbolic part of the equations for the intermediate state can be obtained. Also, because the characteristics are constant, if one of the variables in the characteristic is fixed, the other must be allowed to float to prevent the Riemann problem from becoming ill posed. For the x-direction and GLM variables, either the GLM variable, or the x-direction component of $\mathbf{E}$ or $\mathbf{B}$ may be held constant. For the remainder of the variables, only the magnetic or the electric field component can be held constant. For example, if the magnetic field is held constant on a boundary, ψ and $\mathbf{E}$ must float. However, ϕ should be held constant and set to zero so that the electric field error on the boundary is enforced to be zero.

Chapter 7

Evaluation and Verification of the Two-Dimensional MMHD GLM Model

7.1 Overview

Prior to considering the two-dimensional plasma flows associated with the GEM magnetic reconnection challenge, which are of primary interest here, verification of the proposed numerical solution procedure and GLM divergence cleaning algorithm was sought. This chapter summarizes efforts carried out as part of this thesis to verify the accuracy of the proposed finite-volume scheme as well as assess the performance of the various divergence cleaning algorithms. The predictions of the 2D solution procedure are also compared to those of the previously described 1D solution method (See Chapter 5). Finally, the predictions of the 2D MMHD solution procedure are compared to results obtained by a previously developed solution scheme for the single-fluid Gaussian moment equations describing non-conducting gaseous flows. In particular, supersonic flow past a circular cylinder is considered for various flow regimes.

7.2 Assessment of Spatial and Temporal Accuracy

The spatial and temporal accuracy of the MMHD numerical solution procedure was first verified by examining several simple test cases for which the predicted solutions could be compared directly to known analytical solutions. Each system of equations were considered separately. For

the 10-moment fluid model, a sinusoidal periodic test case was considered with grid refinement. For the magnetic field, a magnetostatic test case was assessed, and a static line charge problem was assessed for electrostatics. Planar electro-magnetic wave propagation was also considered for the full Maxwell's equations.

7.2.1 Non-Dimensional Parameters and Reference State

For all the test cases considered, reference states were calculated as suggested by Ohsawa [48] using the non-dimensional parameters

$$\hat{r}_{\mathrm{c,i}} = \frac{r_{\mathrm{c,i}}}{L} = \frac{v_{\mathrm{th,i}}}{L\,\omega_{\mathrm{c,i}}} = \frac{\sqrt{2kT_0/m_{\mathrm{i}}}}{eB_0L/m_{\mathrm{i}}} = \frac{\sqrt{2m_{\mathrm{i}}kT_0}}{eB_0L}, \tag{7.1}$$

$$\hat{\lambda}_{\mathrm{D}} = \frac{\lambda_{\mathrm{D}}}{r_{\mathrm{c,i}}} = \frac{1}{L\,\hat{r}_{\mathrm{c,i}}}\left(\frac{2\varepsilon_0 kT_0}{e^2 n_0}\right)^{\frac{1}{2}}, \tag{7.2}$$

$$\hat{c} = \frac{c}{v_{\mathrm{th,i}}} = \frac{c}{\sqrt{2kT_0/m_{\mathrm{i}}}}, \tag{7.3}$$

which define the non-dimensional ion cyclotron (Larmour) radius, Debye length, and speed of light, respectively. Also, $r_{\mathrm{c,i}}$ is the dimensional Larmour radius, L is the characteristic length, $v_{\mathrm{th,i}}$ is the thermal ion velocity, $\omega_{\mathrm{c,i}}$ is the ion cyclotron frequency, λ_{D} is the dimensional Debye length. Solving for the reference number density, n_0, temperature, T_0, and magnetic field, B_0, from above results in

$$n_0 = \frac{2\varepsilon_0 kT_0}{e^2}\cdot\frac{1}{L^2}\cdot\frac{1}{\hat{r}_{\mathrm{c,i}}^2\hat{\lambda}_{\mathrm{D}}^2}, \tag{7.4}$$

$$T_0 = \frac{m_{\mathrm{i}}c^2}{2k}\cdot\frac{1}{\hat{c}^2}, \tag{7.5}$$

$$P_0 = n_0 kT_0, \tag{7.6}$$

$$B_0 = \frac{\sqrt{2m_{\mathrm{i}}kT_0}}{e}\cdot\frac{1}{L}\cdot\frac{1}{\hat{r}_{\mathrm{c,i}}}. \tag{7.7}$$

In general, the following values for the preceding non-dimensional parameters were employed, which correspond to a two-fluid, nearly fully ionized limit:

$$L = 1.0\times 10^2, \qquad \hat{r}_{\mathrm{c,i}} = 1.0, \qquad \hat{\lambda_{\mathrm{D}}} = 0.01, \qquad \hat{c} = 100.0. \tag{7.8}$$

For divergence cleaning, the following values for the GLM parameters were adopted:

$$c_h = c \quad (c_{h,\mathrm{ratio}} = 1.0), \qquad \chi = 1.0, \qquad c_r = 0.18, \tag{7.9}$$

which correspond to all GLM divergence cleaning waves propagating at the speed of light. The value of c_r above is what is recommended by Dedner [118]. Unless otherwise indicated, the physical electron-ion mass ratio is used. The second-order, unlimited, explicit predictor corrector and implicit NKS schemes were both assessed.

7.2.2 Periodic Sinusoidal Fluid Wave Propagation

The first computational test performed was to assess the accuracy of the implementation of the fluid equations of the MMHD solution procedure. For this test, the electromagnetic equations were decoupled from the equation set and not solved. Further, the three sets of fluid equations (representing ions, electrons and neutrals) were uncoupled and solved separately. The simulation was carried out for variations in both the x- and y-directions where the number of cells in the direction of wave propagation were varied from 10 or 25 cells (10 cells proved too coarse for the electrons) and up to 200 cells while the number of cells perpendicular to the direction of propagation was 10. The domain used was a rectangular box where $-50 \leq d \leq 50$ for the direction of propagation and $-5 \leq p \leq 5$, for the perpendicular direction.

The reference state from Section 7.2.1 was used, but in the interest of speeding up computation and stability, the electron-ion mass ratio was artificially set to 0.01. The various fluid solution values were initialized according to

$$\mathbf{W_s} = [m_s n_0, v_0, 0, 0, P_0, 0, 0, P_0, 0, P_0]\,, \qquad \mathbf{W_m} = [0, 0, 0, 0, 0, 0]\,, \tag{7.10}$$

where $s \in \{\text{electron, ions, neutrals}\}$ and the direction of propagation is in the x-direction. These vectors represent the uniform state populating the domain. A sinusoidal variation is then applied to the density field according to

$$\rho_s = \rho_{\text{ref,s}} \cdot \left(2 + \sin\left(2 \cdot \left(\frac{x}{L} + \frac{1}{2}\right) \cdot \pi\right)\right) \tag{7.11}$$

where x is the direction of propagation and the reference density is simply $\rho_{\text{ref,s}} = m_s n_0$ from above. An additional propagation velocity for the density variation was also imposed given by

$$v_0 = 1.0 \times 10^6 \,\frac{\text{m}}{\text{s}}. \tag{7.12}$$

This means for the domain used, a time of $t = 1.0 \times 10^4\,\text{s}$ corresponds to the propagation of the density wave by one period.

In Figure 7.1, the initial condition for the sinusoidal test case in density is plotted alongside the solution after one period. The result corresponds to the particular case of the the x-direction variation with 20 points in the direction of propagation. The grid convergence plot is shown in Figure 7.2 which provides the L1- and L2-norms of the errors for both the electron and ion densities in both the x- and y-directions versus number of points in the direction of propagation on a logarithmic scale. The right angle triangle in the plots shows a second-order slope. It can be seen that both the L1- and L2-norms of the errors converge with second-order accuracy.

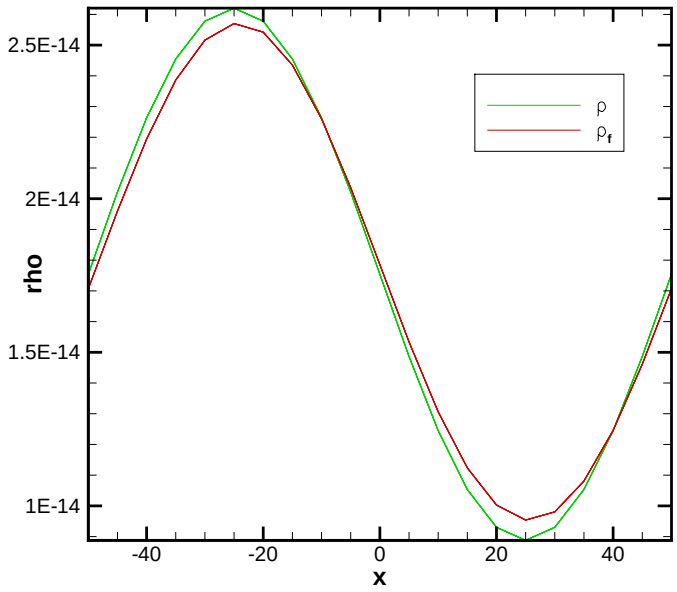

Figure 7.1: Sinusoidal fluid wave propagation test case initial (ρ) and after one period (ρ_f) for the x-direction with 20 cells.

7.2.3 Sinusoidal Fluid Wave Propagation with Dual-Time Stepping NKS

Next, the periodic sinusoidal test case was examined using the dual-time NKS solution procedure of Section 6.7. The sinusoidal base function considered was

$$\rho_s = \rho_{\text{ref,s}} \cdot \left(200 + \sin\left(2 \cdot \left(\frac{x}{L} + \frac{1}{2}\right) \cdot \pi\right)\right). \tag{7.13}$$

For a comparison between explicit and implicit time steps, the 100×10 cell case was considered using both the explicit predictor-corrector and the dual-time NKS schemes. The explicit TSCF was set at 0.5 while the dual-time physical TSCF was set to 10. Figure 7.3 compares the sinusoidal wave after one period using the explicit predictor corrector and the dual-time NKS scheme using second-order BDF for the physical time step. As can be seen, the two solutions are very similar, however the dual-time solution has a slight temporal lag, along with a slight loss of amplitude. This is expected for the dissipative implicit time accurate solution. However, at these resolutions, the variations are very slight. A higher TSCF, for such a coarse mesh was not possible as the number of time steps were too low to produce a stable solution. For the above case, only 37 physical time steps were performed with a TSCF of 10. A higher mesh resolution 500×10 case was also examined which allowed a larger physical time step due to the stiffer problem. For the 500×10 mesh periodic sinusoidal case, a physical TSCF of 100 was

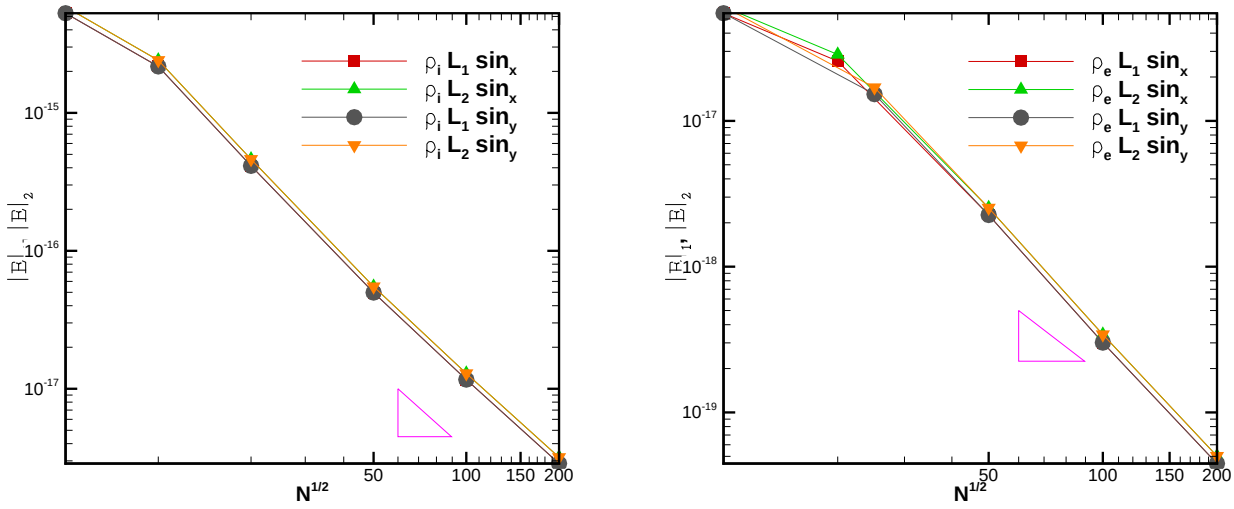

Figure 7.2: Grid convergence error plots for the sinusoidal fluid wave propagation test case with electron and ion density for the x- and y-directions showing L1 and L2 error norms versus number of points. Triangle represents a second-order slope.

able to be used. The results of accuracy and computational costs of the dual-time NKS scheme compared with the explicit predictor corrector scheme are included in Table 7.1. The dual-time NKS scheme clearly has a computational advantage at the cost of some accuracy. The dual-time NKS scheme has a higher advantage for stiff problems in the purely fluid dynamic cases. In contrast, for the 100×10 case, which was less stiff and had a lower TSCF, the computational cost was approximately the same. Additional computational tests using the fluid dynamics portion of the MMHD model with the dual-time NKS scheme are explored in Section 7.4.

7.2.4 Priest Magnetostatic Test Case

To assess the accuracy of the magnetic error correction scheme, the irrotational magnetic field ($\nabla \cdot \mathbf{B} = \mathbf{0}$) 2D test case proposed by Priest [177] is examined. The domain for this problem was a 1.0 m by 1.0 m box with exact fluxes for the boundaries. The fluid equations are not

Table 7.1: Periodic sinusoidal wave propagation accuracy comparison

Scheme	Resolution	CFL(TSCF)	CPU Time	L1 Norm	L2 Norm
Explicit	500 × 10	0.5	21.46	4.7596×10^{-21}	5.2866×10^{-21}
NKS	500 × 10	100	8.2	7.6117×10^{-18}	8.4595×10^{-18}

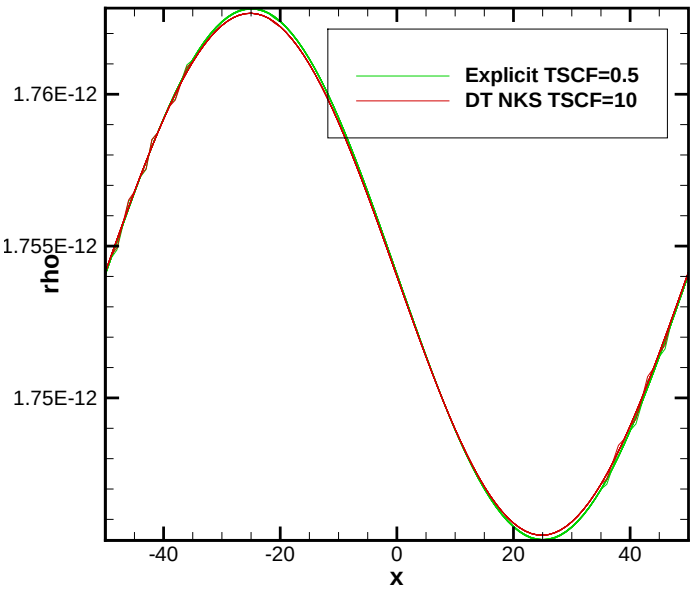

Figure 7.3: Sinusoidal fluid wave propagation test case explicit and dual-time NKS comparison after one period for the x-direction with 100 cells.

simulated.

The reference solution values were set as in Section 7.2.1 where the B_0 reference value is used to scale the 2-D magnetostatic test case whose dimensional equations are given by

$$\mathbf{W_i} = \begin{bmatrix} m_i n_0 \\ 0 \\ 0 \\ 0 \\ P_0\left(19.84 + \frac{e^{\left(-2\pi\frac{y}{L}+\frac{1}{2}\right)}}{2}\right) \\ 0 \\ 0 \\ P_0\left(19.84 + \frac{e^{\left(-2\pi\frac{y}{L}+\frac{1}{2}\right)}}{2}\right) \\ 0 \\ P_0\left(19.84 + \frac{e^{\left(-2\pi\frac{y}{L}+\frac{1}{2}\right)}}{2}\right) \end{bmatrix}, \qquad \mathbf{W_m} = \begin{bmatrix} B_0\left(-\cos\left(\pi\frac{x}{L}+\frac{1}{2}\right)e^{\left(-\pi\frac{y}{L}+\frac{1}{2}\right)}\right) \\ B_0\left(\sin\left(\pi\frac{x}{L}+\frac{1}{2}\right)e^{\left(-\pi\frac{y}{L}+\frac{1}{2}\right)}\right) \\ 0 \\ 0 \\ 0 \\ 0 \end{bmatrix}. \quad (7.14)$$

The domain is $-0.5\,\mathrm{m} \leq x \leq 0.5\,\mathrm{m}$ and $0.5\,\mathrm{m} \leq y \leq 0.5\,\mathrm{m}$ and exact flux (Dirichlet) boundary conditions were imposed at the domain boundaries based on the exact solution. This eliminated errors associated with the imposition of boundary data.

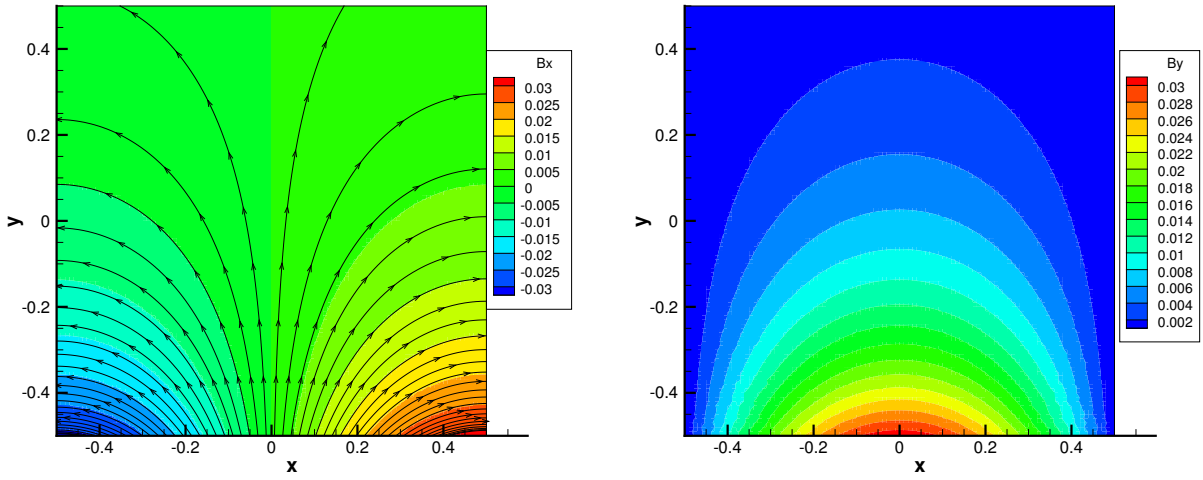

Figure 7.4: Initial conditions (Exact) for the 2-D magnetostatic test case of Priest showing B_x and B_y with streamlines showing 2-D magnetic field lines for a 100×100 mesh.

The contour plots of the initial conditions for the components of the magnetic fields given in Figure 7.4, correspond to the solution on a 100×100 cell mesh where the exact solution is assigned to B_x and B_y. In Figure 7.5, the L1 and L2 error norms in both B_x and B_y are plotted versus the number of total cells on a logarithmic scale. The total number of cells was varied from 100 to 10,000 (100, 625, 2500, 10000 for this case). The triangle on the plot represents a second-order slope. Once again second-order accuracy is demonstrated for the proposed scheme. It should be noted that a small amount of E_z error results from the small $\nabla \cdot \mathbf{B}$ errors due to the transverse components associated with the E_z conservation equations. The errors result in a cumulative E_z field which reaches a steady state as the $\nabla \cdot \mathbf{B}$ error approaches machine zero. The plot of the E_z component for the 50×50 (2500 cells) case is shown in Figure 7.6. Note that in this regime the electric flux density is scaled equivalent to the speed of light over the magnetic flux density, which makes the relative values negligible.

7.2.5 Priest Magnetostatic Test Case Results with NKS

The Priest magnetostatic case was also examined using the steady state NKS scheme. It was found that in order to arrive at a converged solution as fast as possible, the block diagonal preconditioner of Section 6.6.4 had to be neglected for the Maxwell's equations subsystem as discussed in Section 7.2.12. The order for grid convergence is second-order as can be seen in Figure 7.7 where the L1 and L2 error norms for B_x is plotted versus the square root of the total

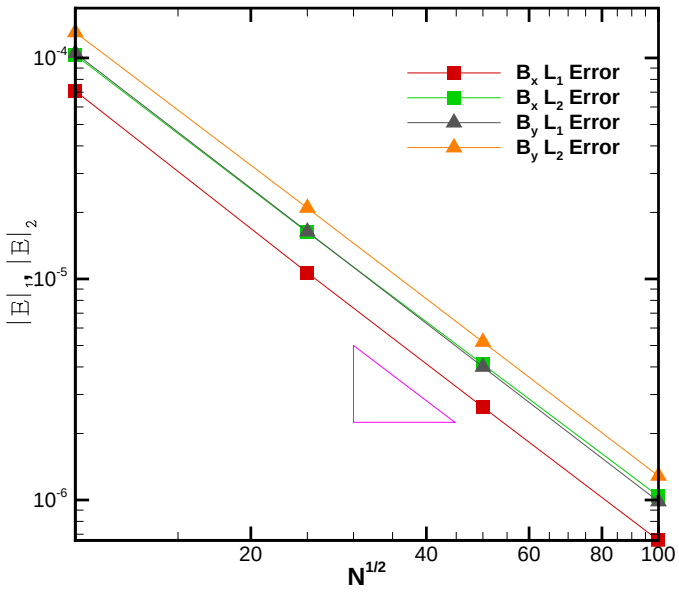

Figure 7.5: Grid convergence error plots for B_x, B_y magnetic field showing L1 and L2 error norms versus number of cells. Triangle represents a second-order slope.

Table 7.2: Magnetostatic test case accuracy comparison

Scheme	Resolution	CFL(TSCF)	CPU Time	L1 Norm	L2 Norm
Explicit	100×100	0.7	833	6.5679×10^{-7}	1.0410×10^{-6}
NKS	100×100	1.0×10^5	40.6	9.8428×10^{-7}	1.2849×10^{-6}

number of cells on a logarithmic scale. The number of cells considered were 625, 2500, 10,000, 40,000 (mesh varied from 25×25 to 200×200). The TSCF was limited to 1.0×10^5 for stability and the residual was driven down more than 10 orders of magnitude.

The computational advantage of using the NKS steady state scheme is again quite evident for this problem when solving only the Maxwell's equations with GLM based divergence cleaning. In Table 7.2, the various parameters, accuracy, and computational costs are compared between the NKS and explicit solutions. It can be seen that at the cost of a very small increase in error, a CPU time speed up of around 20 times is achieved. The explicit scheme required around 140,000 time steps while the NKS scheme required around 195 newton steps with a total of 5840 GMRES iterations.

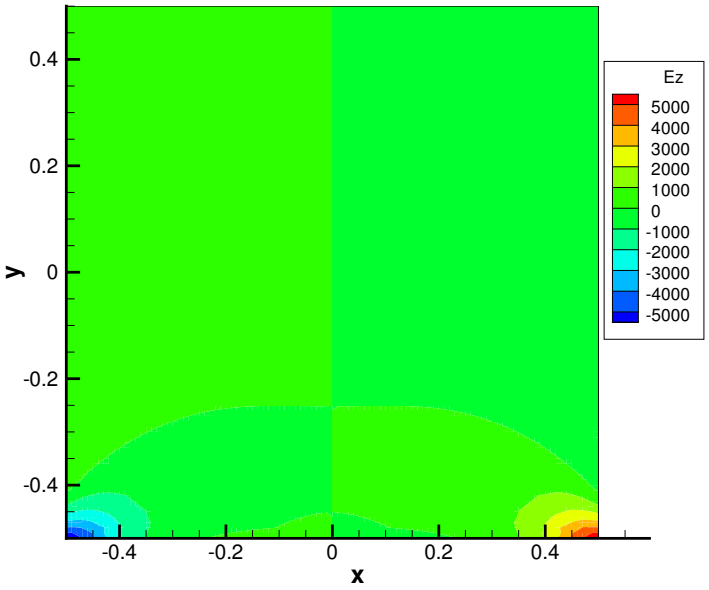

Figure 7.6: Plot of E_z component for 50×50 mesh for the magnetostatic test case.

7.2.6 Modified Priest Test Case to Explore Divergence Cleaning

The mechanism by which divergence errors are cleaned from the solution of Maxwell's equations with GLM divergence cleaning is briefly examined here by introducing a defect in the magnetic field of the Priest test case. The effect of the divergence cleaning was observed by how the defect error was advected away and removed from the computational domain. The Priest test case outlined in Section 7.2.4 was modified with a point defect in the magnetic field near the center of the domain. The defect takes the form of a 50% increase in the x-direction magnetic field intensity and a reduction of the y-direction magnetic field by 50% at the exact center of the computational domain. Using this as the initial data, the test case was then run on a 200×200 grid of length and width 1 m and fixed Dirichlet boundary conditions for the magnetic field. The GLM variable, ψ, was allowed to flow out of the domain. Time-accurate simulations were then carried out for time up to 1.0×10^{-8} and 1.0×10^{-6} seconds, respectively, and the errors were compared to the simulation of the non-GLM equations for the same time periods. Figures 7.8 and 7.9 compare the $\nabla \cdot \mathbf{B}$ error between the non-error corrected and GLM error corrected simulations of the modified Priest test case for the time scale 1.0×10^{-9} and 1.0×10^{-6} seconds, respectively. As can be seen, the $\nabla \cdot \mathbf{B}$ error slowly numerically dissipates in the non-GLM simulation along the Cartesian axis, but propagates outward as a wave in the GLM simulation.

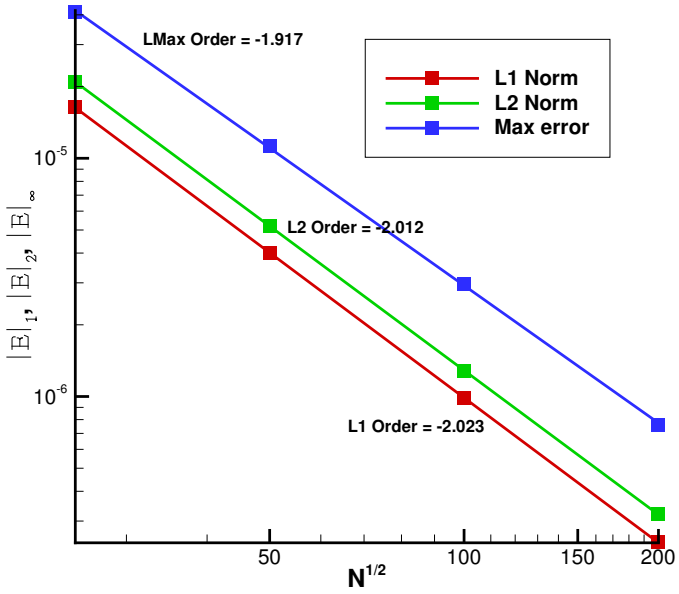

Figure 7.7: Grid convergence error plots for the Priest magnetostatic test case with B_x magnetic field showing L1 and L2 error norms versus number of cells using the NKS scheme.

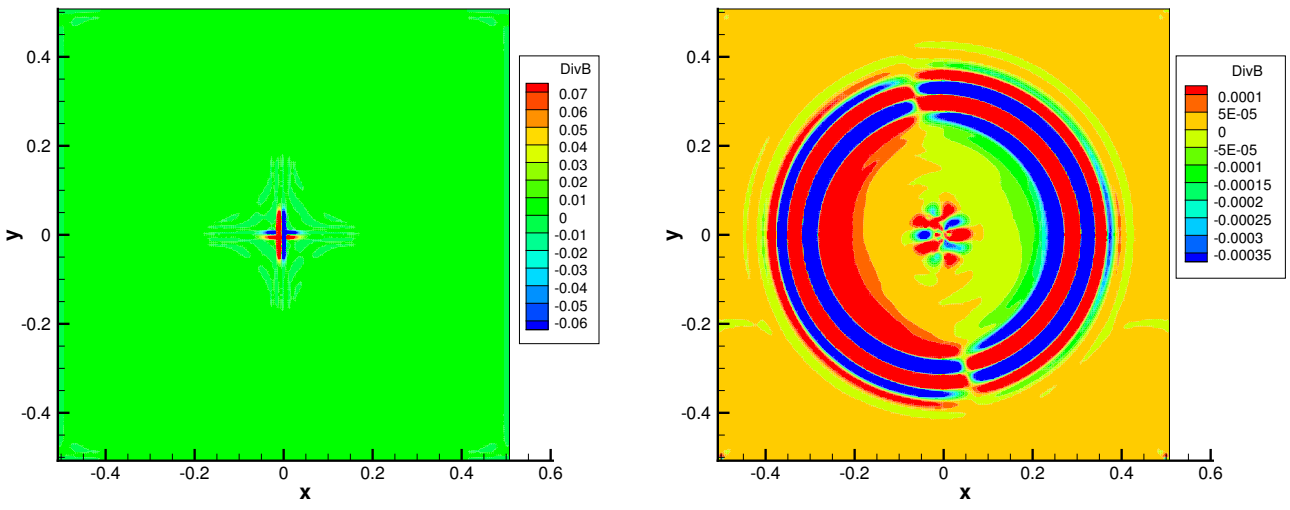

Figure 7.8: Modified Priest test case comparing $\nabla \cdot \mathbf{B}$ for the non-GLM (left) and GLM (right) equations at t=1.0×10^{-9}s.

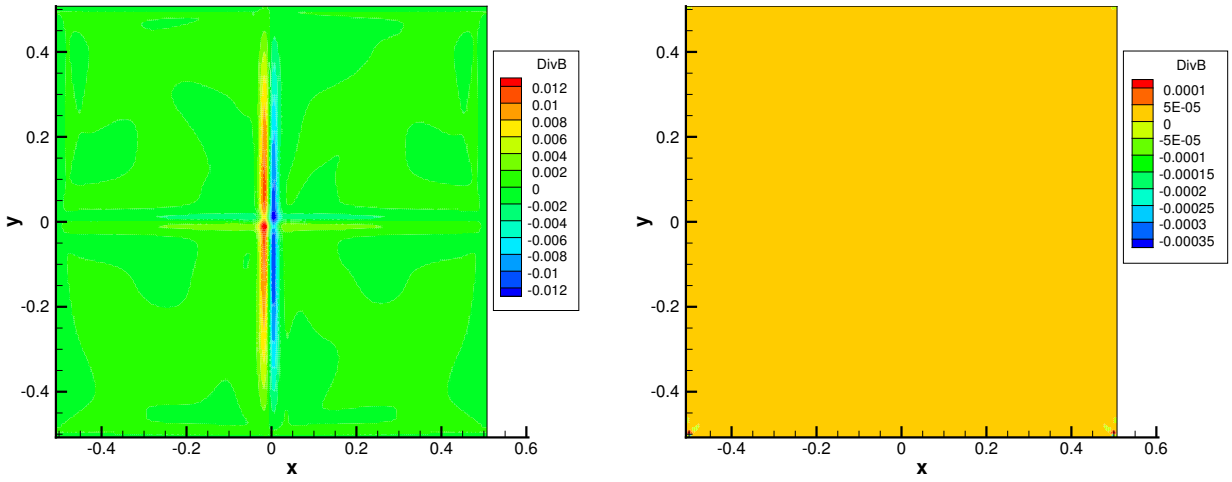

Figure 7.9: Modified Priest test case comparing $\nabla \cdot \mathbf{B}$ for the non-GLM (left) and GLM (right) equations at t=1.0×10^{-6}s.

7.2.7 Electrostatic Line Charge Test Case

To assess the accuracy of the electric field equations, a simple infinite line charge which results in a radial electric field was examined. Specifically, a box of width 1.5 m by 1.0 m whose centroid is located 0.7 m below the point at which the infinite line charge intersects the 2D computational plane was considered. The charge is set to equal 5% of the background electrons per meter. The resulting electric field exact solution is given by

$$\mathbf{E} = \frac{q}{2\pi\varepsilon}\frac{x}{r^2}\mathbf{i} + \frac{q}{2\pi\varepsilon}\frac{y}{r^2}\mathbf{j} \tag{7.15}$$

where q is the charge per unit length of the line charge, and x and y is the x and y distance from the line charge with $r^2 = x^2 + y^2$. Once again, only the Maxwell's equations with GLM divergence cleaning were simulated. The boundaries of the test case are the exact fluxes (while constant extrapolation is used for the GLM variable) for the problem and the exact solution is used as the initial conditions. The reference state is as described in Section 7.2.1.

Figure 7.10 shows the exact initial solution showing E_x and E_y with streamlines depicting the electric field lines. The mesh for this result is 70 cells wide and 50 cells high. For the grid convergence test considered here, numerical results ovtained using 14×10, 21×15, 35×25, and 70×50 grids were compared. In Figure 7.11, the L1 and L2 grid convergence error norms for E_x and E_y are plotted versus number of cells on a logarithmic scale. A second-order convergence rate is achieved as can be seen by comparing the slopes to the triangle which represents a second-order slope.

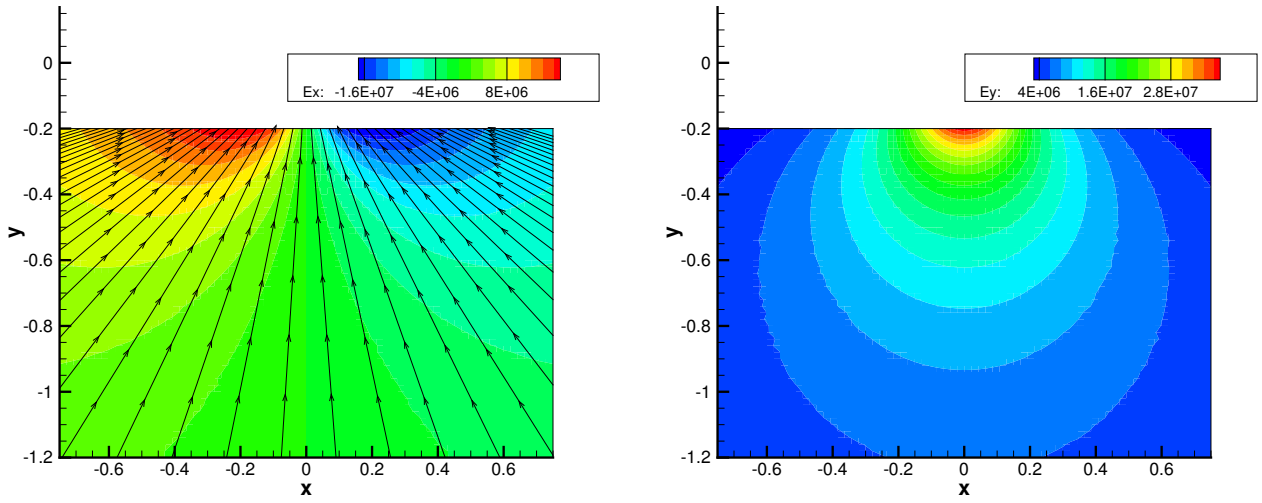

Figure 7.10: Initial conditions (Exact) for the 2-D electrostatic line charge test case showing E_x and E_y with streamlines showing 2-D electric field lines for 70×50 cells.

As a counterpart to the magnetostatic case, there is a small level of B_z error that results from $\nabla \cdot \mathbf{E}$ errors due to the transverse components associated with the B_z conservation equations. These approach steady-state as the residual converges to machine zero. The plot of the B_z component for the 70×50 cells case is shown in Figure 7.12. It is similarly negligible.

7.2.8 Sinusoidal Electromagnetic Plane Wave Case Examining Magnetic Field with Explicit Time Stepping

The last set of accuracy assessment test cases considered for the proposed solution scheme for Maxwell's equations involved electromagnetic plane wave propagation. The problems examined consisted of a sinusoidal wave that exists in both the electric and magnetic field equations which can be represented by the following equations:

$$\mathbf{B} = \begin{bmatrix} \frac{E_0}{c}\cos(\theta)\cos(2\pi k\mathbf{r} - \omega t)\sin(\phi) \\ -\frac{E_0}{c}\cos(\theta)\cos(2\pi k\mathbf{r} - \omega t)\cos(\phi) \\ \frac{E_0}{c}\sin(\theta)\cos(2\pi k\mathbf{r} - \omega t + \alpha_y) \end{bmatrix}, \qquad \mathbf{E} = \begin{bmatrix} -E_0\sin(\theta)\cos(2\pi k\mathbf{r} - \omega t + \alpha_y)\sin(\phi) \\ E_0\sin(\theta)\cos(2\pi k\mathbf{r} - \omega t + \alpha_y)\cos(\phi) \\ E_0\cos(\theta)\cos(2\pi k\mathbf{r} - \omega t) \end{bmatrix}, \tag{7.16}$$

with the initial conditions corresponding to $t = 0$. The initial data results in a wave propagating at the speed of light, alternating between the electric and magnetic fields in the perpendicular directions [178]. The above expressions have been formulated such that the plane wave can be rotated to exercise the numerical scheme in various directions, and also to specifically exercise

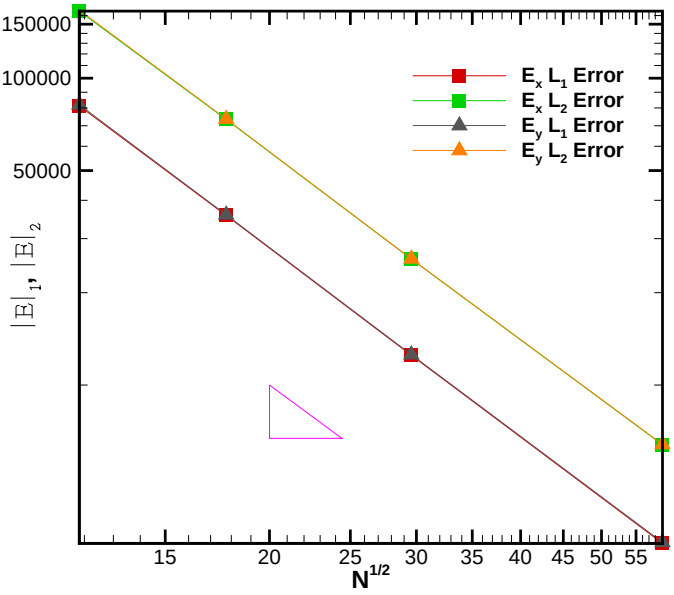

Figure 7.11: Grid convergence error plots for E_x, E_y electric flux density for the electrostatic line charge test case showing L1 and L2 error norms versus number of cells. Triangle represents a second-order slope.

and assess the magnetic or electric error cleaning algorithms. The parameter θ controls the projection of the sinusoidal function into the magnetic or electric field plane while ϕ represents a rotation in the x-y plane which allows us to assess accuracy in various directions. In Equation (7.16), the parameter E_0, is the amplitude, k is the wavenumber, ω is the wave frequency, t is time and α_y is the phase shift. Also

$$\mathbf{r} = x\cos(\phi) + y\sin(\phi) \tag{7.17}$$

to be consistent with the rotation.

The sinusoidal electromagnetic plane wave case was first examined by selecting the following solution parameters:

$$E_0 = 1.0 \times 10^7, \qquad \theta = 0^\circ, \qquad k = 1.0, \qquad \omega = 2\pi c, \qquad \alpha_y = 0, \qquad t_f = \frac{k}{c}, \tag{7.18}$$

with $\phi = 0^\circ$ for the x-direction case and $\phi = 90^\circ$ for the y-direction case on a domain of $-0.5\,\mathrm{m} \leq d \leq 0.5\,\mathrm{m}$ on the axis of the direction of propagation and $-0.05\,\mathrm{m} \leq p \leq 0.05\,\mathrm{m}$ in the perpendicular direction. To exercise the magnetic error cleaning algorithm, θ was set to 0°, which projects the sinusoidal function in the magnetic x-y plane, and places the electric

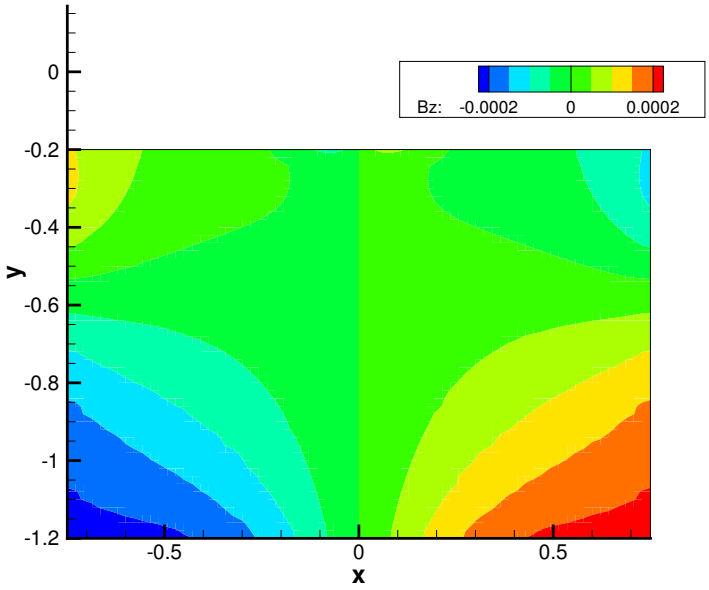

Figure 7.12: Plot of B_z component for a 70×50 mesh for the electrostatic line charge test case.

field in the z-direction. The final time, t_f, was chosen so that the wave propagated one full cycle. Periodic boundary conditions were used throughout, and the resolutions considered in the direction of propagation, were 100, 250, 500, and 750 cells, while 20 cells were used in the perpendicular direction for the x- and y-direction cases.

The errors in B_y and B_x, for the x and y cases, respectively, versus the propagation direction grid resolution on a logarithmic scale are plotted in Figure 7.13. There is no error in the other magnetic field directions. As can be seen, the x- and y-direction cases have identical errors, as expected, and have second-order convergence in the L1 error norm.

With the 1D case verified in the x- and y-directions, the above case was then modified so the plane wave propagated at a 45° angle. This exercises the full 2D error cleaning for the magnetic field. The parameters of Equation (7.18) were used again, but with

$$k = \sqrt{2}, \qquad \phi = 45^\circ, \tag{7.19}$$

and an associated change in t_f as in Equation (7.18). Periodic boundary conditions were used throughout and the domain was square, using grid resolutions of 100×100, 250×250, 400×400, and 500×500 cells. The resulting convergence plot is included in Figure 7.14 which plots the errors in B_x and B_y versus the square root of the resolution on a logarithmic scale. Both B_x and B_y are plotted together since there is solution content, and thus error, in both these

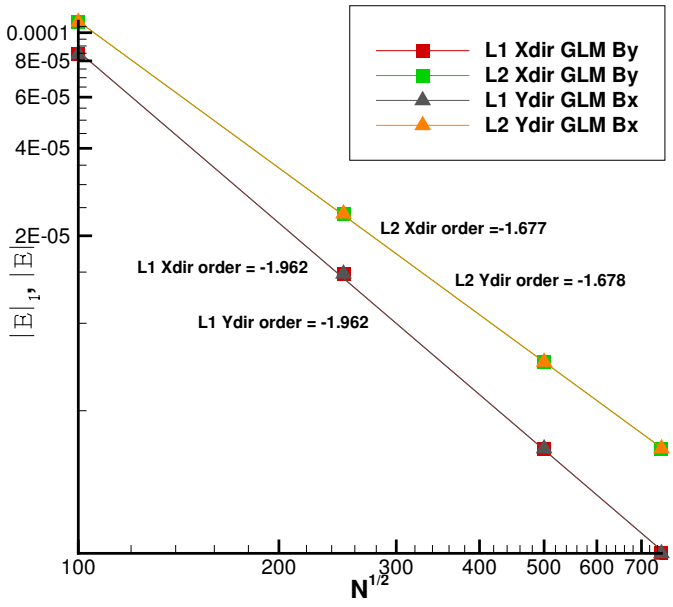

Figure 7.13: Error in B_y and B_x versus 1D grid resolution for the sinusoidal EM plane wave case for the x- and y-direction, respectively using the MGLM error correction scheme.

variables. As expected, the errors are identical in the x- and y-direction due to the symmetry of the problem, and is second-order in the L1 error norm.

Note that only the convergence for the magnetic error cleaning, MGLM, equations are presented here, but all the variations of the error correction schemes for the MMHD equations (FGLM, MGLM, MGLMED) were examined. There were no differences in the error in **B** as was expected since there is no solution content in the x-y plane for the electric field.

7.2.9 Sinusoidal Electromagnetic Plane Wave Case Examining Electric Field with Explicit Time Stepping

The electromagnetic sinusoidal plane wave case of Equation (7.16) was considered for the electric field errors. The parameters are mostly the same as for Section 7.2.8, Equation (7.18), along with the angles, domain and times, however, in order to project the plane wave into the x-y plane of the electric field, θ was set to 90°.

The grid convergence study errors in E_y and E_x, for the x and y cases respectively, versus 1D resolution on a logarithmic scale are plotted together in Figures 7.15 and 7.16, which are for the two divergence cleaning algorithms: the full GLM and the electric error diffusion (FGLM and

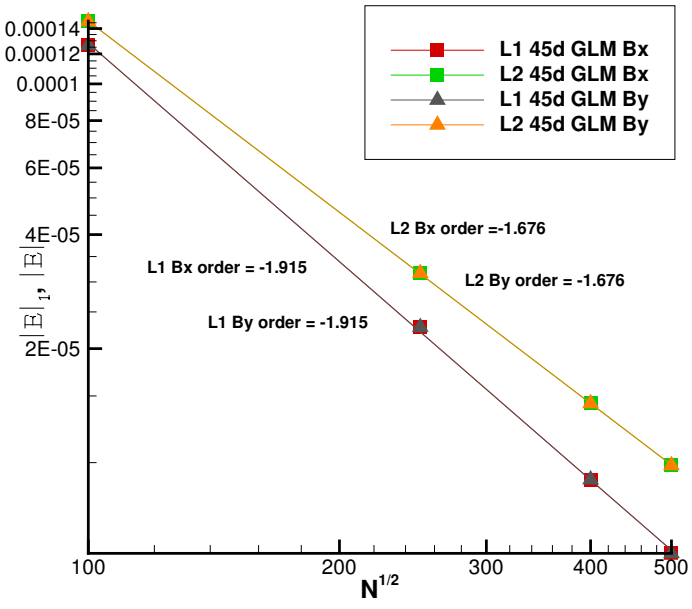

Figure 7.14: Error in B_x and B_y versus square root of resolution for the sinusoidal EM plane wave case for the 45° direction using the MGLM error correction scheme.

MGLMED), respectively. There are no errors in the other electric field directions for each case in the 1D case. The x- and y-direction errors agree well and the L1 error norms are second-order for both schemes. The absolute errors for both the schemes are also quite similar.

To exercise the full 2D divergence cleaning equations, the 45° case was simulated for the electric field similar to the magnetic field using

$$k = \sqrt{2}, \qquad \phi = 45°, \qquad \theta = 90°. \tag{7.20}$$

The errors in E_x and E_y versus the square root of the 1D resolution on a logarithmic scale for the FGLM scheme is plotted in Figure 7.17. The error plot provides a nice second-order convergence for the L1 error, with both the E_x and E_y errors matching.

7.2.10 Sinusoidal Electromagnetic Plane Wave Case Examining Magnetic Field with Dual-Time Stepping NKS

The electromagnetic sinusoidal plane wave test case examining error cleaning for the magnetic field was also considered using the DTS NKS scheme from Section 6.7. The parameters used were identical to the explicit scheme test cases of Section 7.2.8. For accuracy assessment

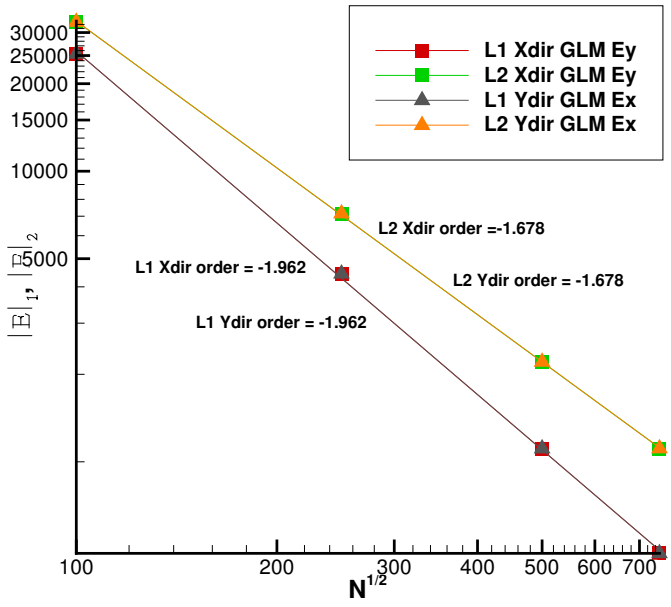

Figure 7.15: Error in E_y and E_x versus 1D resolution for the sinusoidal plane wave case for the x- and y-direction respectively using the FGLM error correction scheme.

purposes, the physical time step chosen was set to 10 and GMRES iterations driven down at least two orders of magnitude. NKS did not result in a computationally advantageous simulation for this case. As shown in Section 7.2.3, for sufficiently stiff problems, usually arising from an increase in resolution compared to the explicit case, a computational advantage does often evolve when making use of the NKS scheme. However, because the time accurate solutions here were designed to be solved in a reasonable amount of time with an explicit scheme, the resolutions examined did not result in a computationally advantageous simulation.

The results for the convergence of the x and y cases are presented in Figure 7.18. In the coarser mesh regime, where the DTS scheme does not converge per iteration as well, the errors are larger and do not converge to second-order. However, as the grid refines, the errors approach second-order and also agree nicely when comparing with the results in the x- and y-directions.

7.2.11 Sinusoidal Electromagnetic Plane Wave Case Examining Electric Field with Dual-Time Stepping NKS

The sinusoidal electric field case of Section 7.2.9 was simulated using the DTS NKS scheme with a TSCF of 10 with all other parameters the same as in Section 7.2.10. Figure 7.19 shows the

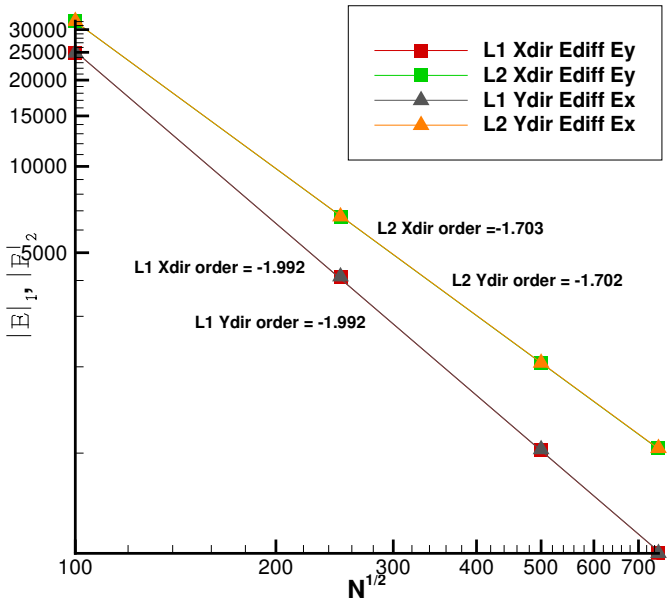

Figure 7.16: Error in E_y and E_x versus 1D resolution for the sinusoidal plane wave case for the x- and y-direction respectively using the MGLMED error correction scheme.

E_y and E_x error against the square root of the 1D mesh resolution on a logarithmic scale. As in the magnetic field case, the coarse mesh solutions did not result in a good error convergence. However, as the resolution increased, the errors converged to second-order for both the L1 and L2 error norms in both the x- and y-direction cases.

7.2.12 NKS Accuracy Assessment Conclusions

Preliminary results are very encouraging for the steady and dual-time NKS schemes. Note that, as mentioned in Section 6.7.2, due to the poor performance of the approximate Jacobian for the Maxwell GLM equations based on the exact Godunov flux function, the residual Jacobian was neglected in all cases in this chapter. While cases could be identified for which the approximate Jacobian would provide superior performance when included, these cases were quite specific and tended to be extremely stiff. As shown in Section 7.2.3, the steady-state and dual-time NKS algorithms can perform significantly faster than the explicit scheme while still providing comparable solution accuracy.

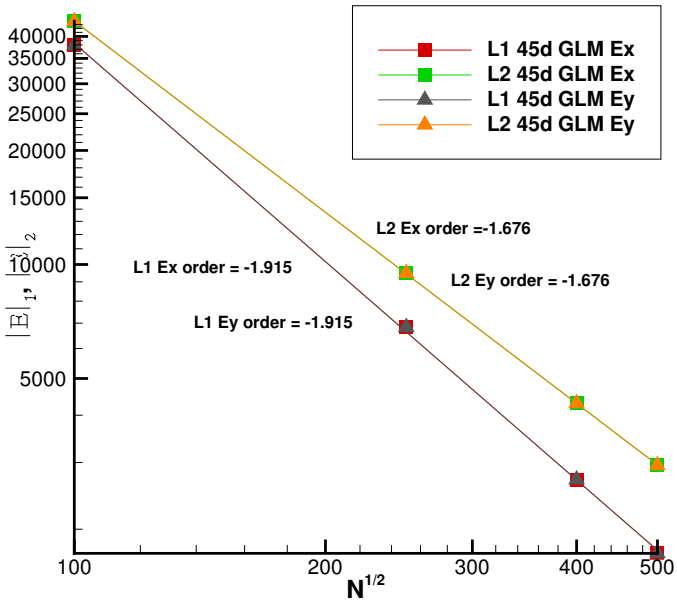

Figure 7.17: Error in E_x and E_y versus square root of 1D resolution for the sinusoidal EM plane wave case for the 45° case using the FGLM error correction scheme.

7.3 Comparison to One-Dimensional MMHD Results

Validation of the two-dimensional numerical solution procedure was also considered by comparing predicted solutions to those of the one-dimensional scheme previously described in Chapter 5. This was accomplished by solving a shock-tube type problem using both the 1D and 2D versions of the multi-fluid MHD models and comparing the solutions obtained using various solving methods in the x- and y-directions for the 2D procedure.

7.3.1 Two-Fluid Limit One-Dimensional Test Case

The two-fluid limit test case was a test case originally proposed by Ohsawa [48] and was used to compare 1D solutions between the two-fluid and three-fluid MHD models as the conditions produced a nearly fully ionized plasma. The two-fluid limit test case is used to compare the 1D and 2D schemes using the multi-fluid MHD model. This IVP results in some complex interactions between the two plasma species and the Maxwell's equations. It is loosely based on the classic Brio-Wu test case outlined in Section 5.3.2 of Chapter 5. The conditions of the

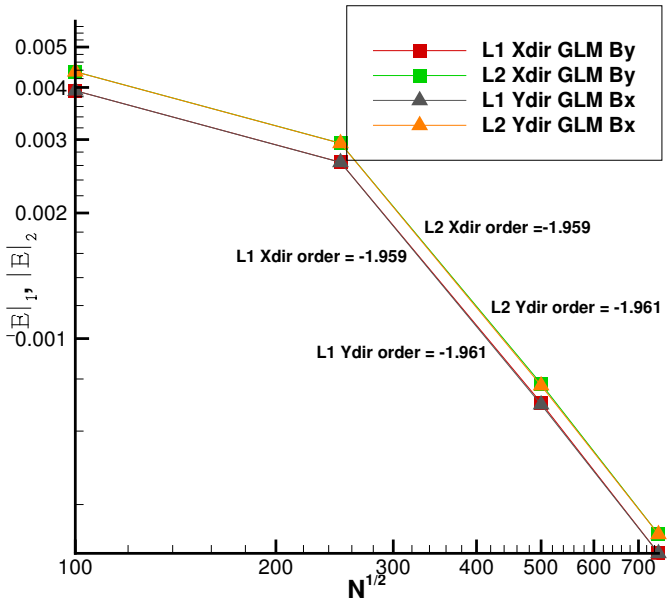

Figure 7.18: Error in B_y and B_x versus 1D resolution for the sinusoidal EM plane wave case for the x- and y-direction respectively using the DTS NKS MGLM solution procedure.

Brio-Wu test case of Section 5.3.2 were modified by using the following parameters:

$$L = 1.0, \qquad \hat{r}_{\mathrm{c,i}} = 1.0, \qquad \hat{\lambda_{\mathrm{D}}} = 0.01, \qquad \hat{c} = 100.0, \tag{7.21}$$

with GLM parameters

$$c_h = c \quad (c_{h,\mathrm{ratio}} = 1.0), \qquad \chi = 1.0, \qquad c_r = 0.18. \tag{7.22}$$

The above set of parameters dimensionalize the Brio-Wu problem as described in Section 7.2.1 and is referred to as the two-fluid limit. The IVP was then set using the following conditions:

$$\mathbf{W} = \begin{cases} \mathbf{W}^{\mathrm{L}} & \text{for} \quad 0 \leq d < L/2, \\ \mathbf{W}^{\mathrm{R}} & \text{for} \quad L/2 < d \leq L, \end{cases} \tag{7.23}$$

for $\{d \,|\, d \in [0, L]\}$, and d is the axis of the 1D problem, with

$$\mathbf{W}^{\mathrm{L}} = \begin{pmatrix} \mathbf{W}_e^{\mathrm{L}} \\ \mathbf{W}_{ion}^{\mathrm{L}} \\ \mathbf{W}_n^{\mathrm{L}} \\ \mathbf{W}_M^{\mathrm{L}} \end{pmatrix}, \qquad \mathbf{W}^{\mathrm{R}} = \begin{pmatrix} \mathbf{W}_e^{\mathrm{R}} \\ \mathbf{W}_{ion}^{\mathrm{R}} \\ \mathbf{W}_n^{\mathrm{R}} \\ \mathbf{W}_M^{\mathrm{R}} \end{pmatrix}, \tag{7.24}$$

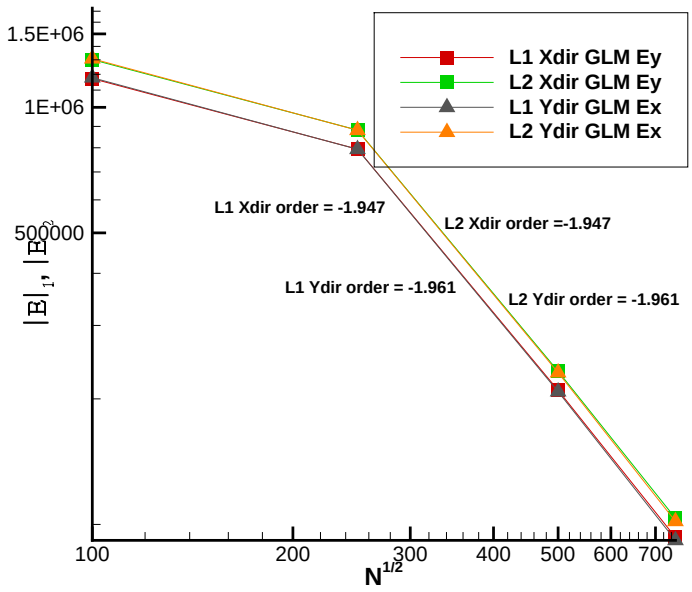

Figure 7.19: Error in E_y and E_x versus 1D resolution for the sinusoidal EM plane wave case for the x- and y-directions respectively using the DTS NKS FGLM error correction scheme.

with

$$\mathbf{W}_e^{\mathrm{L}} = \begin{pmatrix} m_e n_0 \\ \mathbf{0} \\ \frac{p_0}{2}\delta_{jk} \end{pmatrix}, \quad \mathbf{W}_{ion}^{\mathrm{L}} = \begin{pmatrix} m_{ion} n_0 \\ \mathbf{0} \\ p_0 \delta_{jk} \end{pmatrix}, \quad \mathbf{W}_n^{\mathrm{L}} = \begin{pmatrix} m_n n_{n,0} \\ \mathbf{0} \\ p_{n,0}\delta_{jk} \end{pmatrix}, \quad \mathbf{W}_M^{\mathrm{L}} = \begin{pmatrix} \frac{3}{4}B_0 \\ B_0 \\ 0 \\ 0 \\ 0 \\ 0 \end{pmatrix}, \tag{7.25}$$

and

$$\mathbf{W}_e^{\mathrm{R}} = \begin{pmatrix} \frac{m_e n_0}{8} \\ \mathbf{0} \\ \frac{p_0}{10}\delta_{jk} \end{pmatrix}, \quad \mathbf{W}_{ion}^{\mathrm{R}} = \begin{pmatrix} \frac{m_{ion} n_0}{8} \\ \mathbf{0} \\ \frac{p_0}{10}\delta_{jk} \end{pmatrix}, \quad \mathbf{W}_n^{\mathrm{R}} = \begin{pmatrix} \frac{m_n n_{n,R}}{8} \\ \mathbf{0} \\ p_{n,R}\delta_{jk} \end{pmatrix}, \quad \mathbf{W}_M^{\mathrm{R}} = \begin{pmatrix} \frac{3}{4}B_0 \\ -B_0 \\ 0 \\ 0 \\ 0 \\ 0 \end{pmatrix}. \tag{7.26}$$

The Maxwell's equations primitive solution vector is ordered with the magnetic flux density, then electric field density. The reference values were calculated according to Equations (7.4) to

(7.7) using hydrogen gas, except for the neutral species, which was evaluated according to

$$n_{n,0} = \frac{n_0^2}{\kappa(T_{e,0})}, \qquad p_{n,0} = n_{n,0} k T_{i,0}, \tag{7.27}$$

noting $T_{e,0} = T_{i,0} = T_0$ for the left side and

$$n_{n,R} = \frac{n_{e,R}^2}{\kappa T_{e,R}}, \qquad p_{n,R} = n_{n,R} k T_{n,R}, \tag{7.28}$$

for the right. The right side values for the electron equations above are simply

$$n_{e,R} = \frac{n_0}{8}, \qquad p_{e,R} = \frac{p_0}{10}, \qquad T_{e,R} = \frac{p_{e,R}}{n_{e,R} k}, \tag{7.29}$$

with the Saha's equilibrium relation κ as defined in Eq. (3.37) in order to preserve the ionization-recombination equilibrium state.

The preceding one-dimensional problem was used to validate the two-dimensional solution procedure by simulating the IVP in both the x- and y-directions and comparing the resulting solutions to those obtained by the 1D three-fluid MHD model. For the 2D simulations, 500 cells were used for the direction of propagation, and 10 cells were used for the perpendicular direction with constant extrapolation boundary conditions all around. For the 1D simulations, 500 nodes were used. The simulations were performed for a simulated time up to $t = 3.33564 \times 10^{-8}$ s in a domain of 1.0 m in the direction of propagation (0.1 m in the perpendicular direction for the two-dimensional cases).

7.3.2 Comparisons of Explicit Time Stepping Two-Fluid Limit Results

The first results that were examined were obtained using the explicit schemes. The 1D model used a Hancock scheme while the 2D model used an explicit predictor corrector with no divergence cleaning (NGLM). The TSCF for both methods was 0.7. Neither solution method (1D or 2D) made use of divergence cleaning. The comparisons of the 1D and 2D predicted results can be seen in Figure 7.20 which depicts the total density ρ, showing the predicted profiles of the x- and y-directions of the 2D simulated solutions compared to the 1D solution. The solutions agree quite well with a small deviation at around $x = -0.225$. This can be explained by the slightly different 2-stage explicit schemes as well as the fact that a different numerical flux was used for the Maxwell's equations. The HLLE numerical flux function was used for the 1D method and the exact numerical flux function was used for the 2D results. The 2D solution procedure was found to be sensitive to cancellation errors and using the HLLE numerical flux function for the Maxwell's equation in 2D resulted in large deviations from the 1D results. Use of the exact flux function greatly reduced these errors.

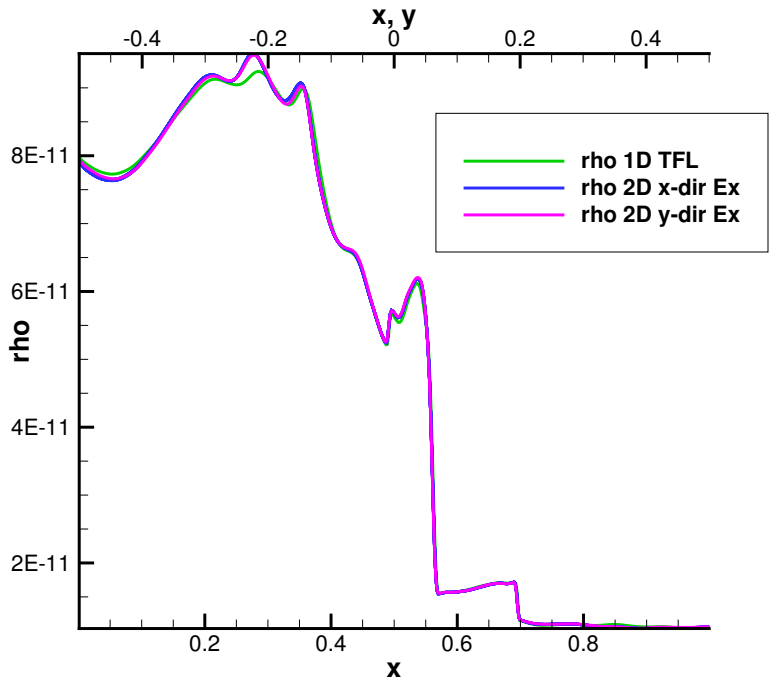

Figure 7.20: Comparison of 1D explicit three fluid model versus 2D x- and y-direction multifluid MHD model solutions to the two fluid limit Brio-Wu IVP showing predicted density distribution obtained using 500 points/cells in the 1D direction.

7.3.3 Comparisons of NKS Two-Fluid Limit Results

Next the NKS solutions to the two-fluid limit problem were examined. The dual-time NKS implicit time marching scheme of Section 6.6 was used. The two-fluid limit problem was simulated using a physical TSCF of 5 and 10 and compared to the explicit result which can be seen in Figure 7.21. The explicit result used a TSCF of 0.7 and an explicit predictor corrector scheme. All of the three simulations had a spatial resolution of 500×10 cells with 500 cells in the x-direction. The 1D three-fluid model solution is also included for comparison and has a 500 cell resolution.

The four sets of predicted results all agree very well despite a physical TSCF speed up of over 10 times. It should be noted that while the NKS dual-time solutions ended up taking about the same or longer than using the explicit predictor corrector scheme, they are presented here for validation of the numerical results. Additionally, it was found that the NKS solutions were unstable past a TSCF of 10.

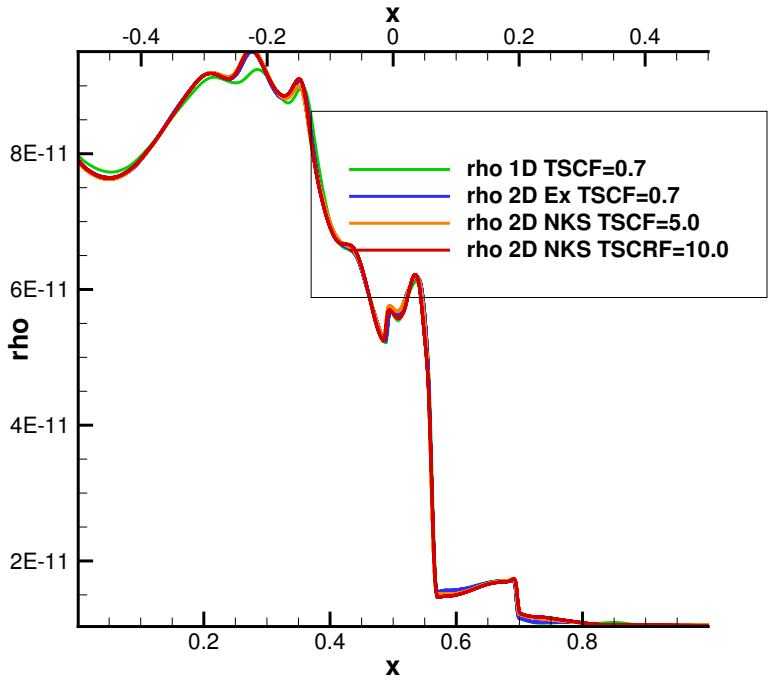

Figure 7.21: Comparison of 2D explicit multifluid MHD versus 2D NKS multifluid MHD solutions to the two-fluid limit Brio-Wu IVP showing predicted density profiles obtained using 500 points/cells with various TSCF.

7.4 Application to Non-Conducting Gases in Two Dimensions

As a last set of assessments, the non-equilibrium fluid portion of the MMHD numerical method and steady-state NKS scheme have been validated in this thesis by comparing predicted steady-state solutions of the fluid equation to those obtained using a two-dimensional NKS solution method developed separately for the solution of the 10-moment Gaussian closure for non-conducting gases by Mcdonald *et al.* [93, 96] and Tensuda *et al.* [179–181]. A simple blunt body problem was examined using various collision regimes and the convergence of the NKS implicit time marching scheme was compared.

7.4.1 Gaussian Based Fluid Dynamics Model

In order to validate the fluid portion of the MMHD solver, solutions were generated and compared with predicted numerical solutions of the Gaussian model developed by McDonald *et al.* [93, 96] and extended with the NKS method by Tensuda *et al.* [179–181].

Table 7.3: Flow regimes

Continuum	Transition	Free-Molecular
$\mathrm{Kn} < 0.01$	$0.01 \leq \mathrm{Kn} < 10$	$10 \leq \mathrm{Kn}$

For the case considered, all reactions were neglected and the intra-species collisions were held constant to a common time scale or frequency. Only one species was examined in the MMHDGLM solver and the NKS preconditioner, for the fluid case, was based on the first-order approximation for the numerical flux function.

7.4.2 Knudsen Number and Flow Regimes

Specifying intra-species collision frequencies allowed for the examination of various flow regimes as defined by the Knudsen number,

$$\mathrm{Kn} = \frac{\lambda}{L}, \tag{7.30}$$

where λ is the mean free path between collisions and L is the characteristic length scale of the problem being examined. This ratio between the mean free path and problem scale describes how dominant the molecular phenomenon is versus the macroscopic flow effects. For larger Knudsen numbers, the free-molecular effects dominate and like-wise macroscopic fluid effects dominate for smaller Knudsen numbers. Generally, there are three regimes defined by the Knudsen number. They are listed in Table 7.3.

7.4.3 Supersonic Flow Past a Blunt Body Cylinder Test Case

The test case examined was a blunt body where the computational domain consisted of a curved quadrant in front of a circular cylinder with a radius of 1.0 m. This case is similar to the one examined by Groth *et al.* [147], but with a free stream Mach number of 3.0 and a different working fluid. The mesh shown in Figure 7.22 defines the geometry where the boundary on the lower right is the cylinder front. The boundary on the axis at the bottom used reflection conditions, while the left curved boundary used constant free stream conditions, and constant extrapolation was used for the straight boundary on the right. A free stream uniform flow with a working gas of argon was imposed having the following conditions

$$\rho_{Ar} = 1.225\,\mathrm{kg/m^3}, \qquad p_{Ar} = 101325\,\mathrm{Pa}, \qquad \mathrm{M}_x = 3.0, \tag{7.31}$$

where the number M_x defines the velocity in the positive x-direction impacting the face of the cylinder. All sheer pressures and non x-direction velocities were taken to be zero. For

Table 7.4: Examined flow regimes for the supersonic flow past a blunt body test case

Case	ν	Kn
Collisionless	0	∞
Transitional	5.0×10^3	~ 0.03
Continuum	5.0×10^{12}	~ 0

the case examined here, for which the main interest is the solution agreement between the two implementations of the Gaussian closure, a somewhat coarse computational mesh of 16×16 cells was considered. For the two models, the mean free path used to calculate the Knudsen number is

$$\lambda = \frac{v_{th}}{\nu} \tag{7.32}$$

where v_{th} is the thermal velocity and ν is the fixed collision frequency. The length scale L is equal to the diameter of the cylinder.

7.4.4 Results of the Supersonic Flow Past a Blunt Body Test Case Using Steady-State NKS

The blunt body problem described in the last section was simulated using various collision frequencies associated with the free-molecular, transitional, and continuum regimes. The three cases considered are presented in Table 7.4. For the transitional, and continuum cases, a second-order spatial reconstruction was used with Barth-Jespersen slope limiting [136]. For the collisionless case, only first-order spatial reconstruction could be used due to the instabilities of running a supersonic flow collisionlessly.

The steady state solutions for the three cases are presented in Figures 7.23, 7.24 and 7.25. The figures matched exactly those obtained from the previous solution method developed for the Gaussian closure by Tensuda *et al.* [179–181]. This was verified by examining the predicted solution profiles throughout the domain. A sample comparison of the predicted profiles is included in Figure 7.26. The NKS convergence plots for the three cases for both the MMHD and Gaussian models are included in Figures 7.27 to 7.32. The convergence histories match very well, though it should be noted that the TSCF is calculated differently for both methods so an exact match was not possible. Further, it should be noted that when simulating only the gasdynamic portion of the MMHDGLM solution procedure, the NKS performance is excellent.

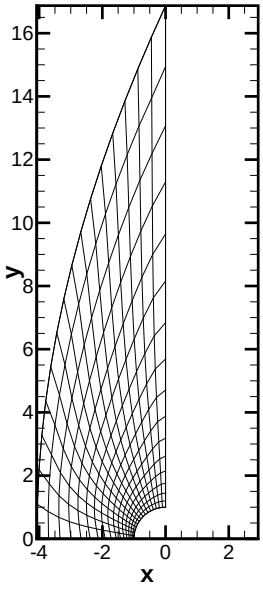

Figure 7.22: Mesh defining the blunt body cylinder using 16×16 computational cells.

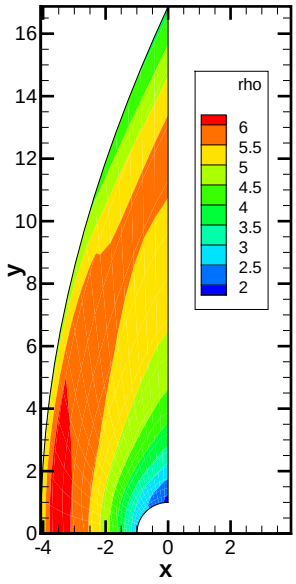

Figure 7.23: Supersonic blunt body test case, collisionless, using NKS and 1st order reconstruction on a 16×16 mesh.

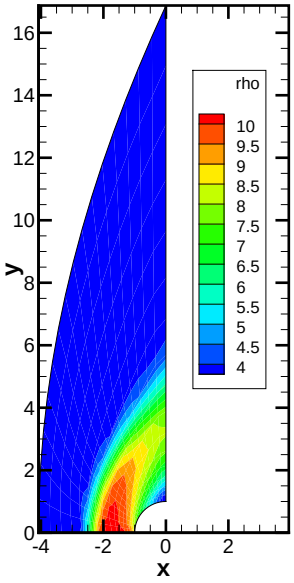

Figure 7.24: Supersonic blunt body test case, transitional constant collision frequency 5.0×10^3, using NKS and 2nd order reconstruction on a 16×16 mesh.

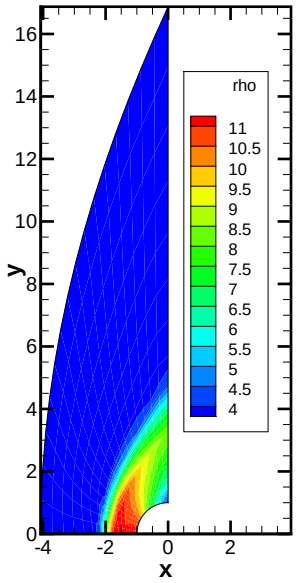

Figure 7.25: Supersonic blunt body test case, continuum constant collision frequency 5.0×10^{12}, using NKS and 2nd order reconstruction on a 16×16 mesh.

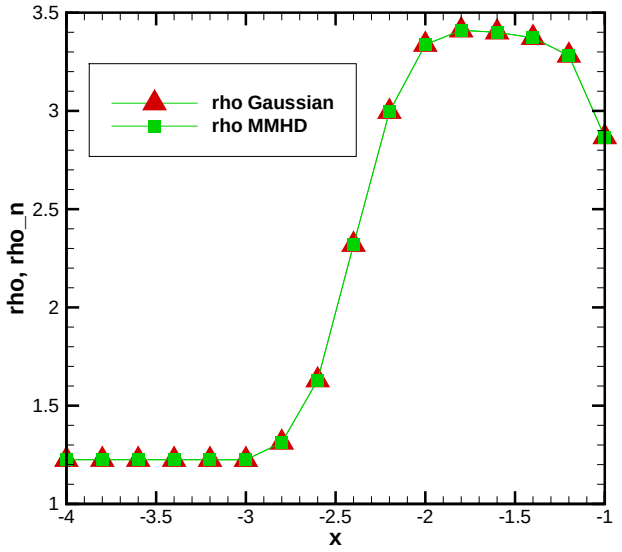

Figure 7.26: Comparison of predicted density profiles, ρ, along the axial direction for the supersonic blunt body test case obtained using the two implementations of the NKS solution method for the Gaussian closure: the non-conducting gas and MMHD models.

7.5 Summary

In this chapter, it was verified that the numerical solution procedure is in fact second-order accurate in both time and space in agreement with theoretical expectations and that the proposed solution method for two-dimensional plasma flows can recover the 1D results of the previously described 1D solution method. Additionally, the GLM divergence cleaning algorithm was found to work well alleviating divergence errors associated with the magnetic field and charge separation. Also, it was shown that the MMHD model can recover the predicted solutions of the 2D Gaussian non-conducting fluid equations, providing further confidence in the implementation of the proposed finite-volume solution method.

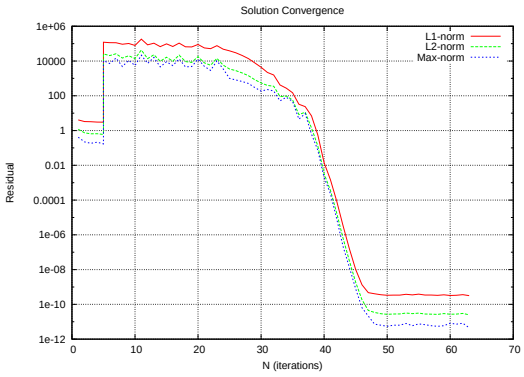

Figure 7.27: NKS convergence plot for the MMHD model, collisionless test case.

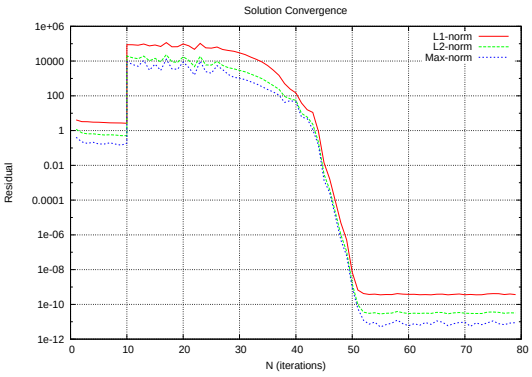

Figure 7.28: NKS convergence plot for the Gaussian model, collisionless test case.

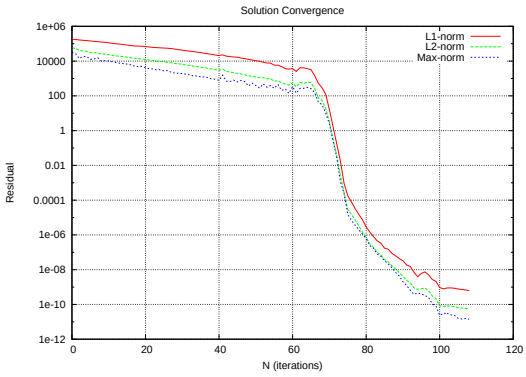

Figure 7.29: NKS convergence plot for the MMHD model, transitional test case.

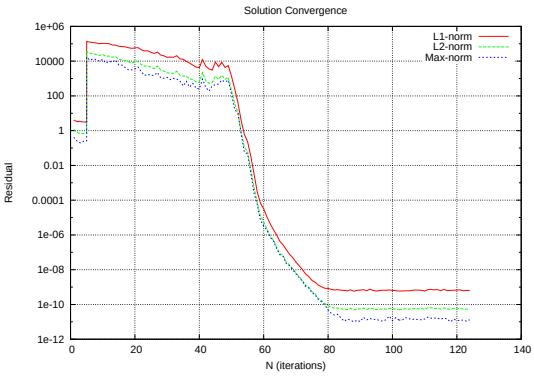

Figure 7.30: NKS convergence plot for the Gaussian model, transitional test case.

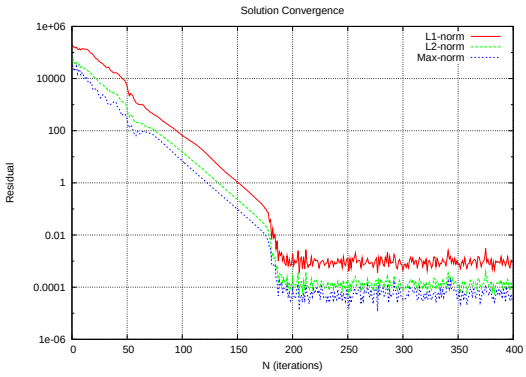

Figure 7.31: NKS convergence plot for the MMHD model, continuum test case.

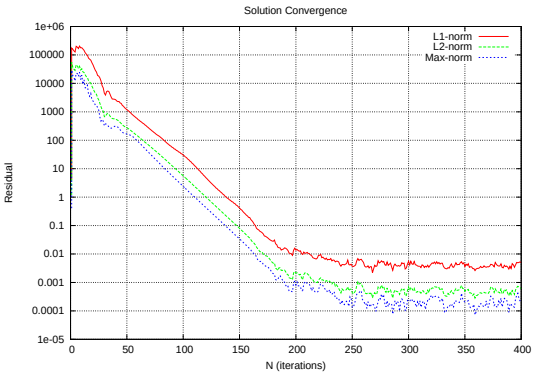

Figure 7.32: NKS convergence plot for the Gaussian model, continuum test case.

Chapter 8

Numerical Results for Two-Dimensional Plasma Flows

8.1 Overview

This chapter will describe the application of the proposed two-dimensional multifluid MHD GLM plasma model and finite-volume solution procedure to a representative and relevant plasma flow problem of interest within the space physics community: the GEM magnetic reconnection challenge. In this chapter, the original GEM problem definition is first stated in non-dimensional form. A dimensional equivalent of the problem is then presented, and a grid convergence study is subsequently undertaken to establish some estimates of the resolution requirements for the problem. The resulting numerical solutions for the GEM case are then compared to similar numerical results obtained for modified versions of the problem in different collision regimes and with the application of the different divergence cleaning techniques considered herein. Numerical results associated with the exploration of the effectiveness of the NKS implicit time marching scheme for the GEM case are also discussed. The present multifluid MHD solutions are also compared to other published results from the literature. Finally, two more realistic sets of conditions for the GEM reconnection problem, corresponding more closely to the actual conditions occurring in the Earth's magnetosphere, are proposed and the numerical solutions for these additional cases are also described and discussed.

8.2 Geospace Environmental Modeling Magnetic Reconnection Challenge

The GEM challenge [2–4, 27, 38, 54, 70–72] has become a standard space plasma problem for numerical validation studies and involves the interaction of magnetic fields and plasmas, approximating their behaviour in the magnetosphere. Please refer to Section 1.3 of Chapter 1 for more background and history of the GEM challenge.

8.2.1 Definition of GEM Problem

As originally posed, the GEM problem is defined as a collisionless problem for a fully ionized plasma comprised of a Harris current sheet with an imposed magnetic perturbation. The Harris current sheet equilibrium solution is a widely known one-dimensional equilibrium solution to the Maxwell-Vlasov equation [182] and is defined by the magnetic field and plasma number density which are taken to have the form

$$\mathbf{B}_H = B_0 \tanh\left(\frac{y}{\lambda}\right)\hat{\mathbf{e}}_x, \qquad n = n_0\left(0.2 + \operatorname{sech}^2\left(\frac{y}{\lambda}\right)\right), \tag{8.1}$$

where λ here is a scaling length. The Harris current sheet equilibrium solution is subsequently perturbed so that

$$\mathbf{B} = \mathbf{B}_H + \mathbf{B}_P, \tag{8.2}$$

where

$$\mathbf{B}_P = \nabla\psi \times \hat{\mathbf{e}}_z, \tag{8.3}$$

and where ψ is given by

$$\psi = \psi_0 \cos\left(\frac{2\pi x}{L_x}\right)\cos\left(\frac{\pi y}{L_y}\right). \tag{8.4}$$

The two-dimensional, rectangular, computational domain is taken to be defined by $-L_x/2 \leq x \leq L_x/2$ and $-L_y/2 \leq y \leq L_y/2$. The standard parameters defining the GEM problem are as follows:

$$\begin{gathered} L_x = 8\pi\delta_{ion}, \qquad L_y = 4\pi\delta_{ion}, \qquad \lambda = 0.5\delta_{ion}, \qquad \tfrac{T_{ion}}{T_e} = 5, \qquad \tfrac{m_{ion}}{m_e} = 25, \\ \psi_0 = \tfrac{1}{10}B_0\delta_{ion}, \qquad \tfrac{c}{v_A} = 20, \end{gathered} \tag{8.5}$$

where δ_{ion} is the ion inertial length and v_A is the Alfvèn velocity.

Two reference values for the magnetic field and number density can be selected, which for this study are taken to be

$$B_{ref} = B_0 = 0.972173605\,\mathrm{T}, \qquad n_{ref} = n_0 = 2.0 \times 10^{18}\,\mathrm{m}^{-3}. \tag{8.6}$$

Using the reference values and assuming a fully ionized, two-fluid plasma with inter-species reactions neglected, the GEM problem parameters are calculated using the following values for the quantities:

$$\delta_{ion} = \frac{v_A}{\omega_{ion}}\,\mathrm{m}, \qquad \Omega_{ion} = \frac{eB_0}{m_{ion}}\,\mathrm{s}^{-1}, \qquad v_A = \frac{B_0}{\sqrt{\mu n_o m_{ion}}}\,\frac{\mathrm{m}}{\mathrm{s}}, \tag{8.7}$$

where Ω_{ion} is the ion gyrofrequency and ω_{ion} is the ion plasma frequency. The above reference values were selected so that a realistic value for the speed of light can be used in defining the last parameter of Equation (8.5) and results in

$$\delta_{ion} = 0.161\,\mathrm{m}, \qquad \text{and} \qquad v_A = 1.5 \times 10^7\,\frac{\mathrm{m}}{\mathrm{s}}. \tag{8.8}$$

In order to compare the dimensional solutions of the GEM case with the non-dimensional solutions, it is useful to note that one unit of non-dimensional time is equivalent to

$$t = \frac{1}{\Omega_{ion}} = 1.0745 \times 10^{-8}\,\mathrm{s} \tag{8.9}$$

in physical time and one unit of non-dimensional magnetic flux is

$$B \cdot l = B_{ref}\delta_{ion} = 0.156\,\mathrm{T} \cdot \mathrm{m}, \tag{8.10}$$

in physical units. The latter is used in normalizing the computed values for the magnetic reconnection fluxes. The revised definition of the Harris current sheet and perturbation is then

$$\mathbf{B}_H(y) = B_0 \tanh\left(\frac{y}{\lambda}\right)\hat{\mathbf{e}}_x, \qquad n_{ion}(y) = n_e(y) = n(y) = n_0\left(0.2 + \mathrm{sech}^2\left(\frac{y}{\lambda}\right)\right), \tag{8.11}$$

$$\mathbf{B}_P = \begin{bmatrix} \psi_0(-\frac{\pi}{L_y}\cos\left(2\pi\frac{x}{L_x}\right)\sin\left(\pi\frac{y}{L_y}\right) \\ \psi_0(\frac{2\pi}{L_x}\sin\left(2\pi\frac{x}{L_x}\right)\cos\left(\pi\frac{y}{L_y}\right) \\ 0 \end{bmatrix}. \tag{8.12}$$

In addition, the other initial conditions that are implied can be determined using definitions for magnetic pressure, total temperature, and solving Maxwell's equation for initial current. They are given by

$$p(y) = \frac{B_0^2}{2\mu}\frac{n(y)}{n_0}, \qquad p_{ion}(y) = \frac{T_{ion}}{T_{ion}+T_e}p(y), \qquad p_e(y) = \frac{T_e}{T_{ion}+T_e}p(y), \tag{8.13}$$

$$\mathbf{J} = \begin{bmatrix} 0 \\ 0 \\ -\frac{B_0}{\lambda\mu}\mathrm{sech}^2\left(\frac{y}{\lambda}\right) \end{bmatrix}, \qquad \mathbf{J}_e(y) = -\frac{m}{e\,m_e n(y)}\mathbf{J}, \qquad \mathbf{J}_{ion}(y) = \frac{m}{e\,m_{ion}n(y)}\mathbf{J}, \tag{8.14}$$

where

$$m = \frac{m_e m_{ion}}{m_e + m_{ion}}. \tag{8.15}$$

The above initial total current is the same as that suggested by Hakim [65], but while Hakim let the electrons carry the entire current, the current work splits the current between the ions and electrons using a momentum balance as suggested by Johnson [6]. Further, the initial electric field, which is zero for the original GEM problem due to the formulation within the context of ideal MHD, is evaluated according to the solution of Ohm's law derived from the momentum equations and the definition of current. When the momentum equation defined in Section 3.9 is multiplied by q_s/m_s, the current equation for each species is given by

$$\frac{\partial \mathbf{J}_s}{\partial t} + \nabla \cdot \left(\mathbf{J}_s \mathbf{u}_s + \frac{q_s}{m_s} \mathbf{P}_s \right) = \frac{q_s^2}{m_s} \left(\mathbf{E} + \mathbf{u}_s \times \mathbf{B} \right) + \mathbf{S}_s^{cols}. \tag{8.16}$$

Assuming a fully ionized plasma in a two-fluid, quasi-neutral formulation, noting that the collision terms vanish when summed over the two species and solving for the electric field while focusing on the pressure balance as suggested by Johnson [6], the initial electric field can be approximated as

$$\mathbf{E}_{initial} \approx \frac{m}{e\, n} \nabla \cdot \left(\frac{\mathbf{P}_{ion}}{m_{ion}} - \frac{\mathbf{P}_e}{m_e} \right), \tag{8.17}$$

which results in the following expression for the y-component of the electric field:

$$E_y(y) = \frac{m_{ion} - 5m_e}{6e\, n(y) \left(m_{ion} + m_e \right)} \frac{B_0^2}{\mu\, \lambda} \mathrm{sech}^2 \left(\frac{y}{\lambda} \right) \tanh \left(\frac{y}{\lambda} \right) \tag{8.18}$$

with the other two components of the electric field assumed to be initially zero.

8.2.2 Reconnected Magnetic Flux

There are various ways to calculate the total reconnected flux. By definition, the reconnected flux is the amount of y-component magnetic flux that crosses the x-axis center line of the GEM problem. The y-component of the magnetic flux density along the $y = 0$ line can be integrated to arrive at the reconnected magnetic flux and is traditionally divided by two.

Another way to evaluate the reconnected magnetic flux, as described by Johnson *et al.* [7], is to consider Ohm's law at the origin of the domain for the problem. The electric field at the origin represents the reconnection rate for the magnetic flux. Thus integrating this value over time would give the total reconnected flux. However, the most common way to determine the reconnected flux is to take the negative of the change of the x-component of the magnetic flux across the center line y-axis between the top two quadrants. The magnetic flux is calculated by integrating the x-component of the magnetic flux density along the $x = 0$ line which leads to the definition for the total reconnected flux to be

$$\Phi_{\mathrm{REC}} = \Phi_{\mathrm{initial}} - \int_{y=0}^{y=L_y/2} B_x \, dy \Bigg|_{x=0}. \tag{8.19}$$

This is how the reconnected flux is calculated in the present study unless otherwise indicated. In order to compare the predicted reconnected flux to the non-dimensional results in the literature, Φ_{REC}, which has the units of T · m, must be non-dimensionalized using the magnetic flux normalization factor of

$$B \cdot l = B_{ref}\delta_{ion}. \tag{8.20}$$

8.2.3 Boundary Conditions of Problem

The boundary conditions for the rectangular computational domain of the original GEM problem and other modified variants considered in this thesis consist of a periodic boundary on the east (right) and west (left) boundaries, and conducting boundaries for the north (top) and south (bottom) boundaries, respectively. At the conducting boundary, the fluid properties of the ions and electrons are reflected, while the electric field is made perpendicular, and the magnetic field is enforced to be parallel at the boundary. For the reflected fluid properties, the following boundary conditions are imposed:

$$\begin{array}{llll} & \dfrac{\partial u_{s,x}}{\partial y} = 0, & \dfrac{\partial P_{s,xx}}{\partial y} = 0, & P_{s,xy} = 0, \\ \dfrac{\partial \rho_s}{\partial y} = 0, & u_{s,y} = 0, & \dfrac{\partial P_{s,yy}}{\partial y} = 0, & \dfrac{\partial P_{s,xz}}{\partial y} = 0, \\ & \dfrac{\partial u_{s,z}}{\partial y} = 0, & \dfrac{\partial P_{s,zz}}{\partial y} = 0, & P_{s,yz} = 0. \end{array} \tag{8.21}$$

For the electro-magnetic fields, the boundary data

$$\begin{array}{lll} \frac{\partial B_x}{\partial y} = 0, & B_y = 0, & \frac{\partial B_z}{\partial y} = 0, \\ E_x = 0, & \frac{\partial E_y}{\partial y} = 0, & E_z = 0, \end{array} \tag{8.22}$$

is used and the GLM parameters, ψ and ϕ if used, are extrapolated to the boundary with constant extrapolation.

8.3 Modified GEM Cases

Due to the capabilities of the multifluid GLM MHD model, and the fact that the original GEM case has been redefined in dimensional form, two modified and more realistic GEM cases were also examined here to explore more fully the predictive capabilities of the proposed MMHDGLM2D solution procedure. To be realistic, the artificial values defining the electron-ion mass ratio and the speed of light were replaced with the true values for the mass ratio and speed of light. Additionally, more realistic values for the magnetosphere plasma parameters were used

to dimensionalize the GEM problem. Further, real intra- and inter-species collisions and the option for real charge-exchange and ionization-recombination reactions were also explored.

In order to approximate the original GEM conditions, the following inequality must be satisfied:

$$\lambda_{\mathrm{D}} \ll \delta_{ion} \ll \lambda = \frac{\sqrt{3a}}{\nu_{0,max}} \tag{8.23}$$

or in other words, the Debye length should be much smaller than the ion inertial length, which should be much smaller than the smallest mean free path of the initial conditions. The cases described in the following subsections conform to this condition.

8.3.1 LEO Version of GEM Problem

As a first modified case, a set of established Low Earth Orbit (LEO) plasma and magnetic field conditions were examined. The LEO conditions were initially chosen as the presence of collisions at this density and energy should provide a more stable solution. Most authors infer a totally collisionless plasma at the magnetopause, while many of the models and results in the literature reviewed have included collisions or an isotropic pressure to stabilize the results. Some characteristic plasma conditions were determined for this case using information from Kelley [183] for the 1000 km altitude for plasma density and energy as well as the average magnetic intensity of the earth's ionosphere. The conditions are tabulated in Table 8.1, which lists the conditions used for both the LEO and magnetopause plasmas.

Using the constants suggested in Table 8.1, the dimensional parameters defining the LEO version of the GEM problem are

$$\delta_{ion} = 2.28 \times 10^3\,\mathrm{m}, \qquad v_A = 3.49 \times 10^6\,\frac{\mathrm{m}}{\mathrm{s}}, \qquad \text{and} \qquad t = \frac{1}{\Omega_{ion}} = 6.529 \times 10^{-4}\,\mathrm{s}. \tag{8.24}$$

The magnetic flux normalization constant for the LEO case is

$$B \cdot l = B_{ref}\delta_{ion} = 0.0364\,\mathrm{T} \cdot \mathrm{m}. \tag{8.25}$$

Table 8.1: Plasma properties for LEO and Magnetopause [183, 184]

Region	$n_H^+\,(\mathrm{m}^{-3})$	$B_0\,(\mathrm{T})$	T_{ion}(simulation)(J)	T_{ion}(J)
LEO	1.0×10^{10}	1.6×10^{-5}	8.49×10^{-5}	-
Magnetopause	1.0×10^{7}	1.5×10^{-8}	7.4×10^{-11}	8.0×10^{-17}

8.3.2 Magnetopause Version of GEM Problem

The magnetopause is typically located at a radial distance that is approximately ten times the radius of the earth. It is not well understood or easily measured as observations via ground based or space based instruments are exceedingly difficult to perform [185]. However, data analysed from Cluster and the recently launched MMS have advanced the understanding of the magnetopause considerably [68, 69]. Taking typical values found at the magnetotail and magnetopause from readings of the Cluster mission [184,186,187], a set of conditions is obtained for the reference values as presented in Table 8.1. It should be noted that the conditions reported by Cluster state a lower energy than that which results from the modified dimensionalized GEM case. However, for this study, and for some consistency, the values specified by the GEM case with the magnetopause reference values and a true electron mass and true speed of light were used. The dimensionalizing parameters for the so-called magnetopause GEM case considered herein are

$$\delta_{ion} = 7.20 \times 10^4 \,\mathrm{m}, \qquad \text{and} \qquad v_A = 1.03 \times 10^5 \,\frac{\mathrm{m}}{\mathrm{s}}, \qquad t = \frac{1}{\Omega_{ion}} = 6.964 \times 10^{-1} \,\mathrm{s}, \quad (8.26)$$

and the magnetic flux normalization constant is given by

$$B \cdot l = B_{ref} \delta_{ion} = 1.08 \times 10^{-3} \,\mathrm{T} \cdot \mathrm{m}. \quad (8.27)$$

8.4 Numerical Results for the Original GEM Case

In this section, the numerical results for the standard GEM case are presented. A grid convergence study was first undertaken to determine the mesh requirements for a converged solution of the GEM case. Several baseline grids were then selected for further consideration. Predicted results obtained using the multifluid MHD model on these grids are then compared to other known results from the literature. The effects of collisions on the GEM problem are examined as well as the effects of various error cleaning algorithms for the Maxwell's equations. Finally, the performance of the proposed implicit time marching method is examined and discussed.

8.4.1 Computational Domain and Initial Conditions

The grids considered were all uniform Cartesian meshes with square cells. The horizontal cell resolution is twice the vertical cell resolution. A typical mesh is shown in Figure 8.1 which corresponds to a very coarse 100×50 grid. The sequence of meshes considered here is summarized in Table 8.2.

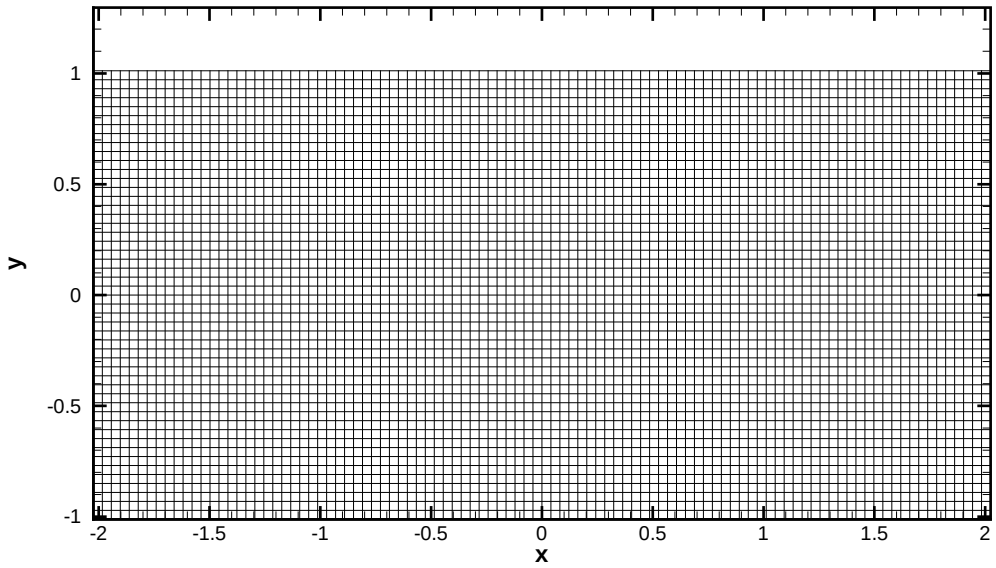

Figure 8.1: GEM test case example mesh (100×50).

Table 8.2: Meshes considered for GEM problem.

Dimensions	Number of Cells
400×200	80,000
512×256	131,072
800×400	320,000
1600×800	1,280,000
3200×1600	5,120,000

Contour plots of the initial conditions for the original GEM case plotted on a 1600×800 uniform grid are presented in Figures 8.2 and 8.3, showing the initial distribution of the magnitude of the y-component of the magnetic field, $|B_y|$, along with the magnetic field lines and the corresponding electron pressure in the x-direction, respectively. The initial normalized magnetic reconnected flux is 0.2 in this case.

8.4.2 Grid Convergence Study with Magnetic GLM Error Cleaning

A grid convergence study was undertaken for the original GEM case as outlined above by considering the sequence of meshes with increasing resolution defined in Table 8.2. For the study, a constant collision frequency was assumed as suggested by Johnson [6]. The elastic collision

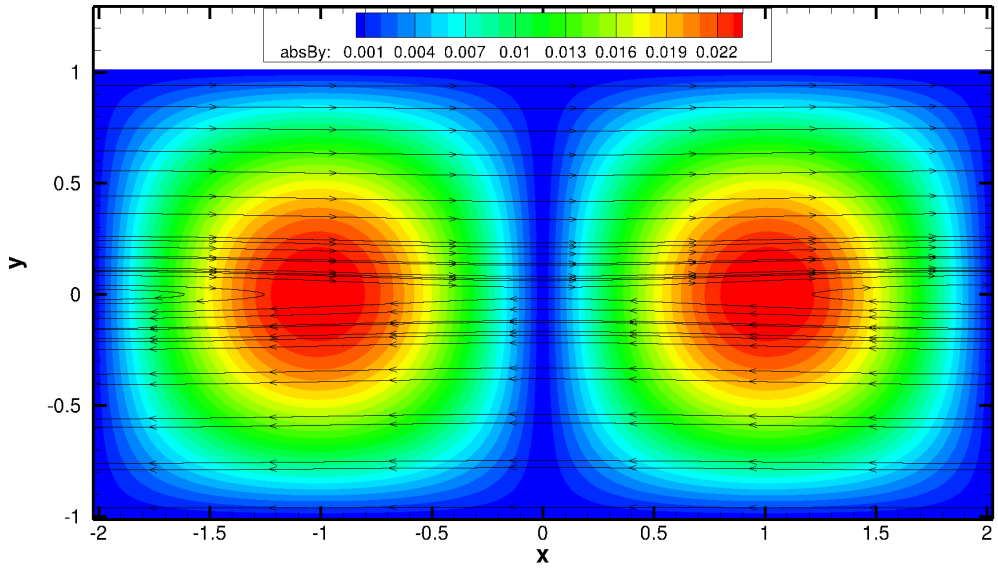

Figure 8.2: GEM test case solution showing $|B_y|$ and magnetic field lines at $t = 0\,\Omega_{ion}^{-1}$ and mesh resolution 1600×800. Normalized magnetic reconnected flux is 0.2.

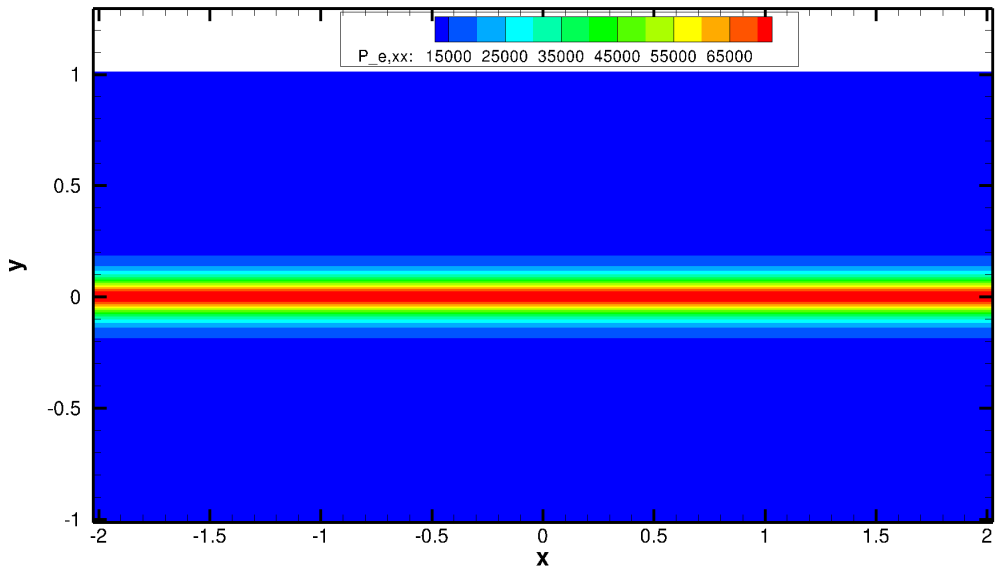

Figure 8.3: GEM test case solution showing $P_{e,xx}$ at $t = 0\,\Omega_{ion}^{-1}$ and mesh resolution 1600×800. Normalized magnetic reconnected flux is 0.2.

terms outlined in Section 3.5 were modified and the collision frequencies defined in Equation (3.17) were held constant. The inter-species collisions were neglected and the intra-species (self) collision terms were modified by assigning a fixed value to the self collision frequency, ν_s, such that

$$\tilde{\nu}_{st} = 0, \qquad \text{and} \qquad \nu_s = 10^7 \, \mathrm{s}^{-1}. \tag{8.28}$$

This value for ν_s was found to produce solutions similar to the results obtained by Johnson [6].

Figures 8.4 to 8.11 show the predicted distributions of the magnitude of the y-component of the magnetic field, $|B_y|$, along with the magnetic field lines and the corresponding electron pressure in the x-direction, for the GEM case obtained for a succession of uniform Cartesian meshes wih increasing resolution as summarized in Table 8.2. The predicted, instantaneous, normalized magnetic reconnected flux is included in the caption for each figure. The time index for the plots is at $t = 18\,\Omega_{ion}^{-1}$, which corresponds approximately to an instance for which one unit of magnetic flux (see Equation (8.10)) has reconnected in many of the previous results found in the literature not based on PIC simulations. PIC simulations predicted an earlier time for one unit of magnetic flux to reconnect, which was generally found to be around $t = 15\,\Omega_{ion}^{-1}$.

As can be seen in Figures 8.4 to 8.11, the reconnected magnetic flux increases with increasing mesh resolution. At mesh resolutions higher than 800×400, a magnetic island appears in the vicinity of the origin. The formation of a magnetic island was found previously by other authors and is quite common place in many simulations [3,28,54,63,66,70,71,188]. The magnetic island is composed of opposite direction magnetic field lines so that the integration of the y-direction magnetic field does not accurately reflect the total reconnected magnetic flux, hence the absolute value of the B_y component is used in the integration. The reconnected flux converges to a value of approximately 1.93 at high mesh resolutions as shown in Figure 8.12, which shows the normalized magnetic reconnection versus the x-direction grid resolution. As was mentioned, though the time index $t = 18\,\Omega_{ion}^{-1}$ was chosen based on when most fluid based results had a normalized magnetic reconnected flux of unity, it was later found that there was an error in the flux reported by Johnson *et al.* [6,7] and the test case used for the various two-fluid solvers of Hakim *et al.* [64,65], and Loverich *et al.* [66], were not exactly the original GEM problem, while most Hall MHD results had to be tuned to obtain the reconnection results desired. However, reconnection information for this time index is still readily available for other simulations and several are included in Figure 8.12. A special test case with a grid resolution of 512×256 and no collisions is examined later in this chapter and is also included in the convergence plot as a separate data point and results in the desired reconnection value of approximately one normalized unit of magnetic flux; however, it was quite unstable and these results are discussed in Section 8.4.3. At high mesh resolutions, the reconnected magnetic flux is approximately

double the value found by other researchers using fluid based models. Nevertheless, this high value for the reconnected magnetic flux was found to be closer in line with the values obtained using either the PIC or hybrid PIC simulations, such as those reported by Pritchett [3], Shay *et al.* [2], and Kuznetsova *et al.* [54]. It should be also noted that a similar doubling of reconnection was encountered by Johnson [6] while investigating the so called 'pair plasma' case.

Referring again to Figure 8.12, at grid resolutions close to those used by many researchers [2,4,5] using PIC (512×256) and Vlasov equation (512×256) modelling approaches, approximately one unit of normalize reconnected flux is obtained by the MMHDGLM2D model. As can be seen, the Darwin-Vlasov simulations are closest to the MMHDGLM2D results for similar mesh resolutions, while the pure PIC simulations and the hybrid simulations result in non-dimensional values for the reconnected flux closest to the converged MMHDGLM2D results found here, albeit at lower mesh resolutions (but also at much higher computational cost). The higher reconnection values reported in some PIC simulations [3, 54, 70] are often attributed to the formation of magnetic islands, such as those found at higher mesh resolutions in the current study. This can explain the better agreement of the reconnected flux with the PIC simulations at higher mesh resolutions, while at the same time agreeing with the Darwin-Vlasov simulations [4, 5] at lower mesh resolutions, when there are no magnetic islands, as the Darwin-Vlasov simulations also do not exhibit the magnetic islands at mesh resolutions similar to those used in this study.

The effect of the magnetic island on reconnection rate is also illustrated by Hesse *et al.* [70]. Their results show a dramatic drop in reconnection rate when going from the PIC simulations to the Hall MHD simulations which lack a magnetic island. A more recent result from Rieke *et al.* [5] shows that using Hakim *et al.*'s two-fluid 5-moment scheme for the original GEM problem and not the modified version from [64, 65] agrees with a lower reconnection value as would be predicted when going to a fully collisional plasma as will be examined in Section 8.4.6. It can be seen that most results are reasonably close to the results of the current study for similar resolutions. However, the predicted rate is also very sensitive to the numerical scheme employed [2–6, 54, 70]. Therefore, based on the current mesh refinement study, The current results shown here and those of other researchers are thought not to be fully converged for the lower mesh resolutions considered.

8.4.3 Baseline Solutions on Nominal Grids

Due to the observed sensitivity of the reconnection value to mesh resolution, several base cases were chosen as standard results to compare with other results in the literature. Examining

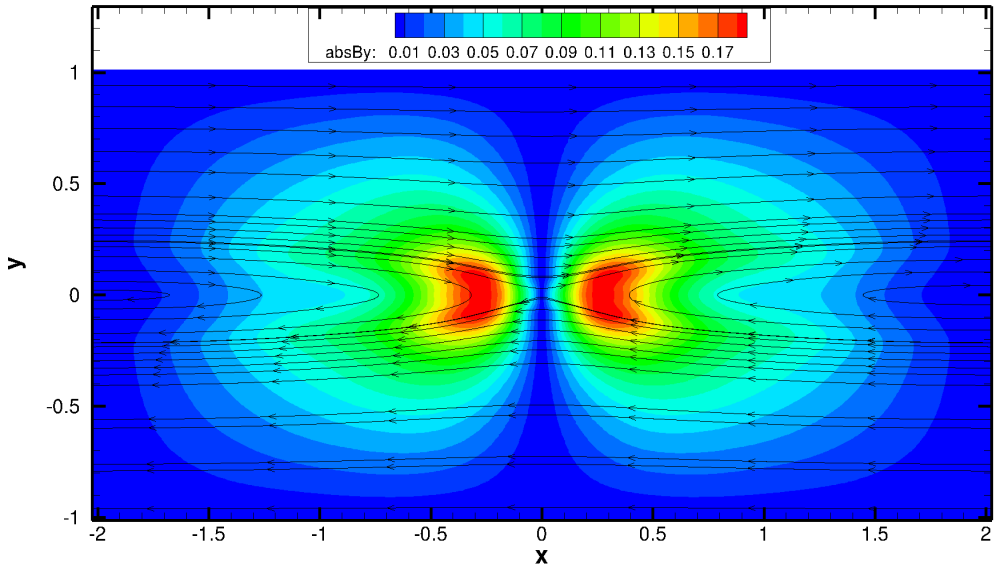

Figure 8.4: GEM test case solution with MGLM error cleaning showing $|B_y|$ and magnetic field lines at $t = 18\,\Omega_{ion}^{-1}$ and mesh resolution 400×200 with collision frequency $10^7\,\mathrm{s}^{-1}$. Normalized magnetic reconnected flux is 0.82.

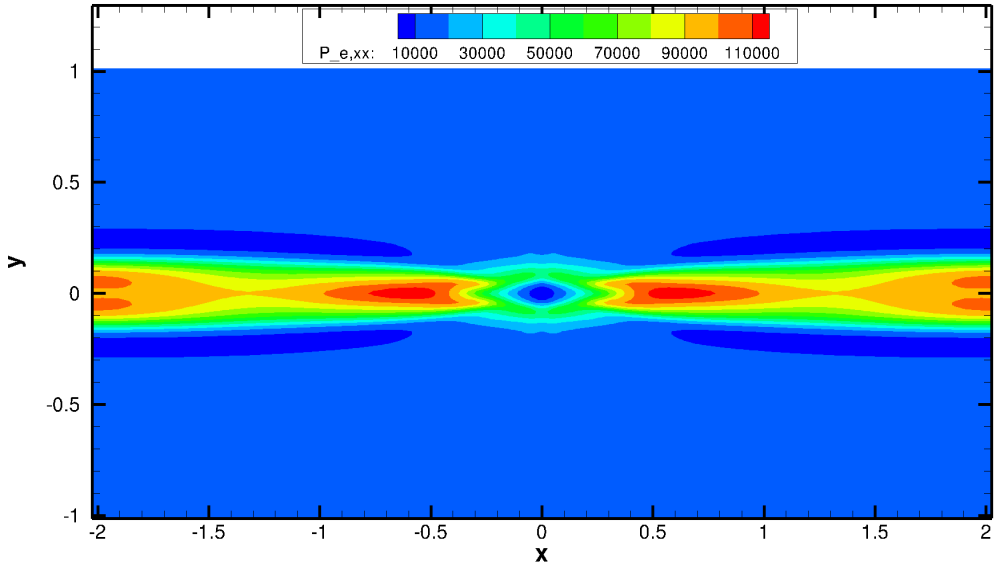

Figure 8.5: GEM test case solution with MGLM error cleaning showing $P_{e,xx}$ at $t = 18\,\Omega_{ion}^{-1}$ and mesh resolution 400×200 with collision frequency $10^7\,\mathrm{s}^{-1}$. Normalized magnetic reconnected flux is 0.82.

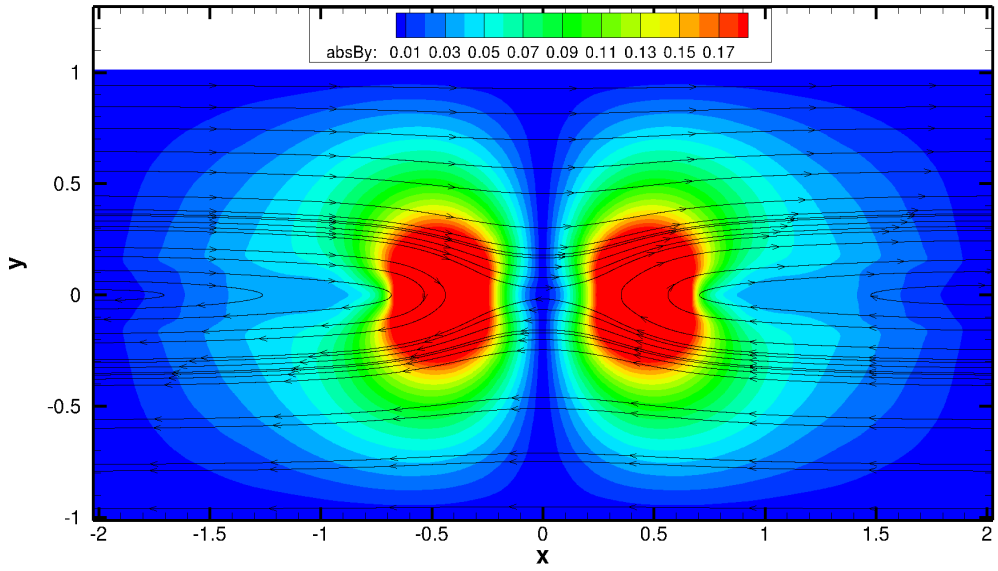

Figure 8.6: GEM test case solution with MGLM error cleaning showing $|B_y|$ and magnetic field lines at $t = 18\,\Omega_{ion}^{-1}$ and mesh resolution 800×400 with collision frequency $10^7\,\mathrm{s}^{-1}$. Normalized magnetic reconnected flux is 1.32.

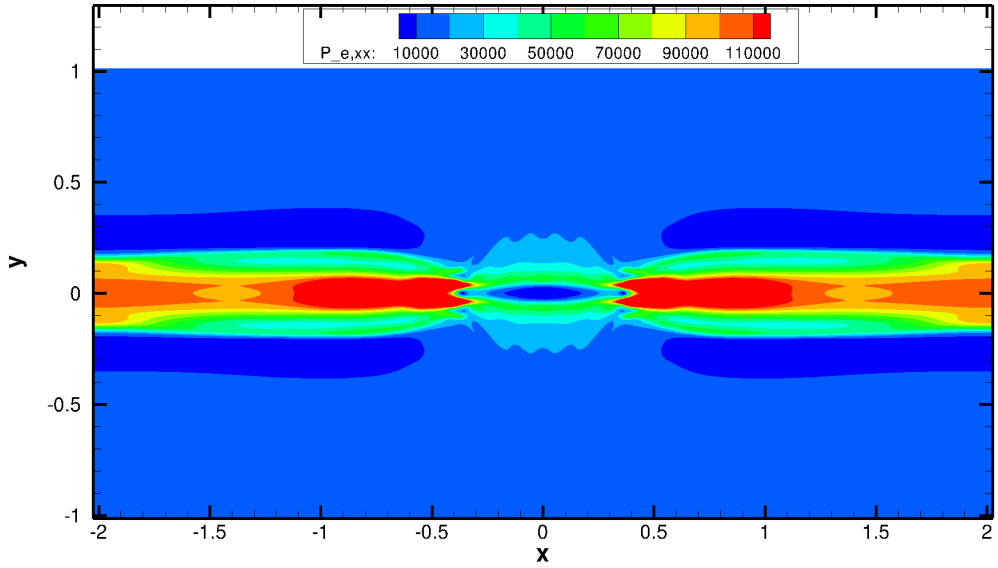

Figure 8.7: GEM test case solution with MGLM error cleaning showing $P_{e,xx}$ at $t = 18\,\Omega_{ion}^{-1}$ and mesh resolution 800×400 with collision frequency $10^7\,\mathrm{s}^{-1}$. Normalized magnetic reconnected flux is 1.32.

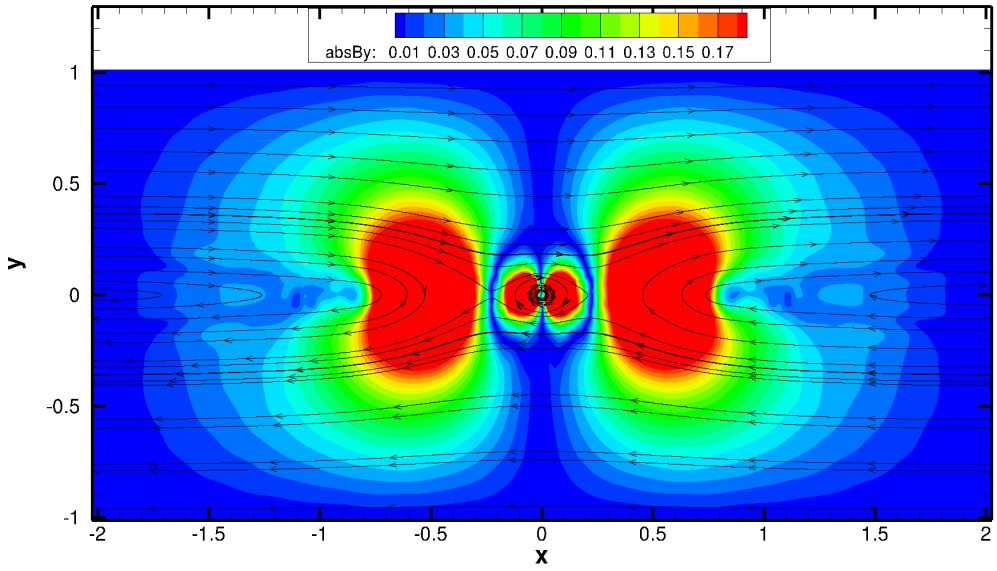

Figure 8.8: GEM test case solution with MGLM error cleaning showing $|B_y|$ and magnetic field lines at $t = 18\,\Omega_{ion}^{-1}$ and mesh resolution 1600×800 with collision frequency $10^7\,\mathrm{s}^{-1}$. Normalized magnetic reconnected flux is 1.77.

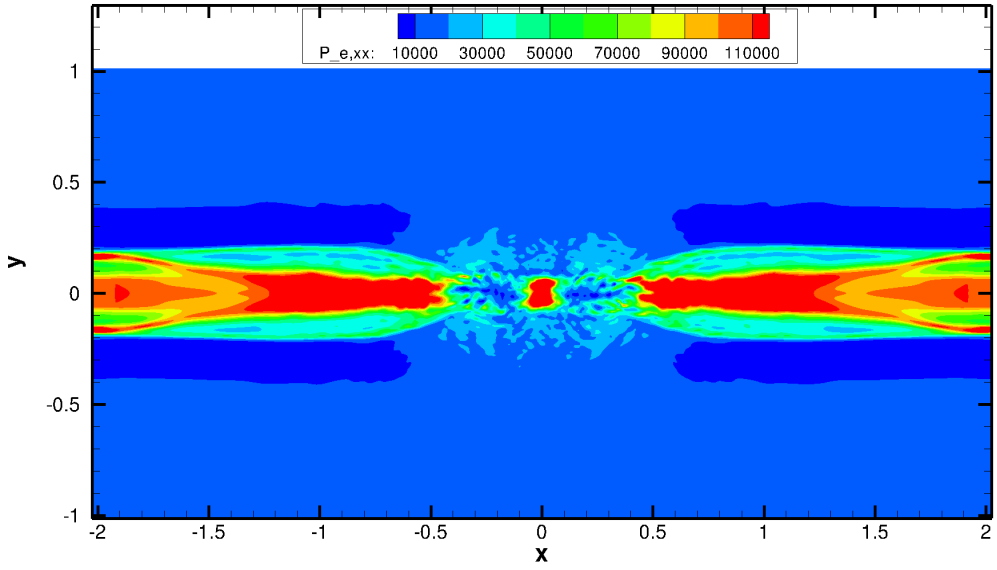

Figure 8.9: GEM test case solution with MGLM error cleaning showing $P_{e,xx}$ at $t = 18\,\Omega_{ion}^{-1}$ and mesh resolution 1600×800 with collision frequency $10^7\,\mathrm{s}^{-1}$. Normalized magnetic reconnected flux is 1.77.

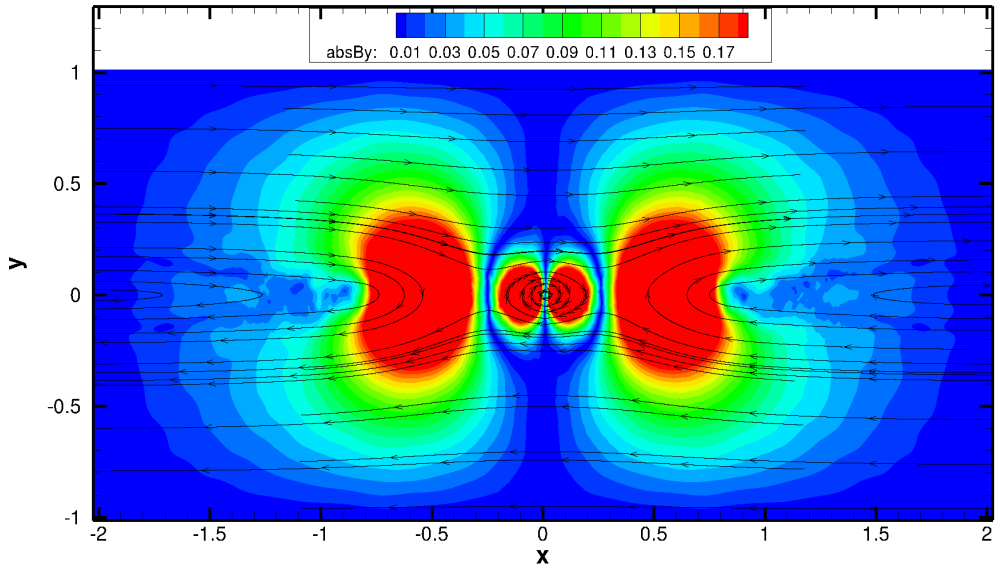

Figure 8.10: GEM test case solution with MGLM error cleaning showing $|B_y|$ and magnetic field lines at $t = 18\,\Omega_{ion}^{-1}$ and mesh resolution 3200×1600 with collision frequency $10^7\,\mathrm{s}^{-1}$. Normalized magnetic reconnected flux is 1.93.

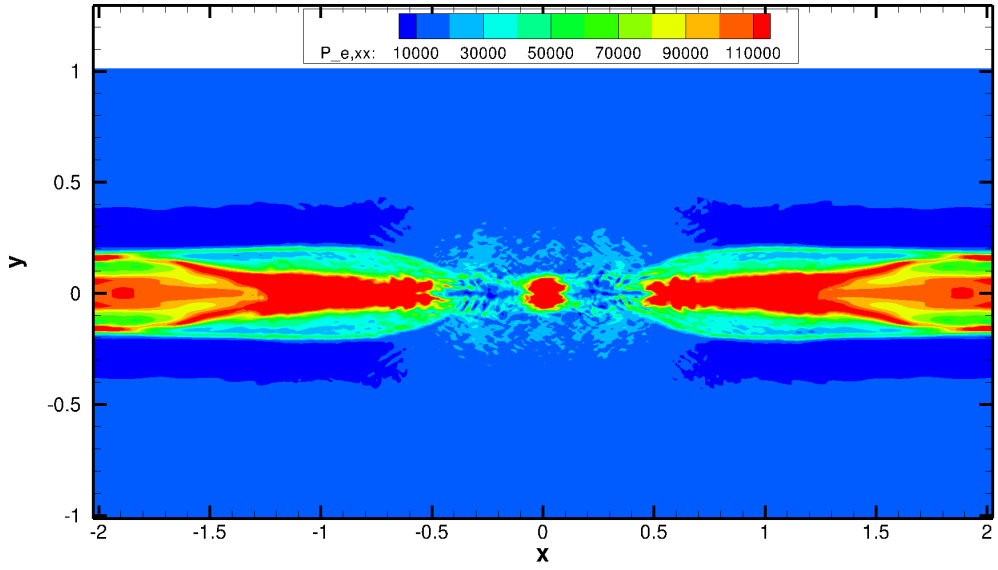

Figure 8.11: GEM test case solution with MGLM error cleaning showing $P_{e,xx}$ at $t = 18\,\Omega_{ion}^{-1}$ and mesh resolution 3200×1600 with collision frequency $10^7\,\mathrm{s}^{-1}$. Normalized magnetic reconnected flux is 1.93.

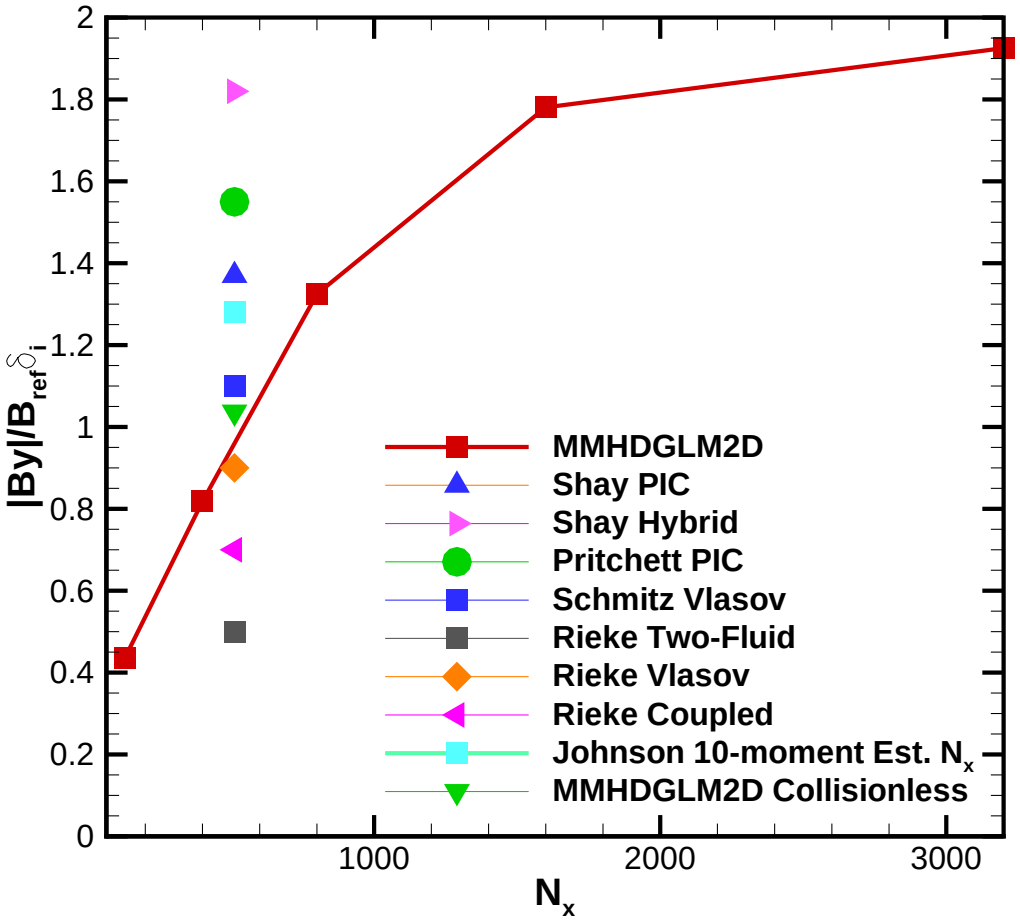

Figure 8.12: Convergence plot of normalized magnetic reconnected flux versus x-direction resolution for GEM test case at $t = 18\,\Omega_{ion}^{-1}$ for the MGLM error correction scheme. Results from Shay *et al.* [2], Pritchett *et al.* [3], Schmitz *et al.* [4], Rieke *et al.* [5], and Johnson [6] are also included.

Figure 8.12, a reasonably converged solution for the original GEM case, balancing computational considerations, was identified to be the results obtained using a uniform Cartesian mesh containing 1600×800 cells. This is the grid used for most of the comparisons herein and exploration of the effect of various parameters and properties. A lower resolution grid of 400×200 cells was also used for a few of the comparisons and is stated clearly when used.

One additional grid resolution was examined in order to see how the MMHDGLM2D solution result compared specifically to the Darwin-Vlasov results examined in Section 8.4.5. In order to compare to the Darwin-Vlasov simulations, completely collisionless MGLM simulations were carried out. As was expected, with collisionless fluid equations, the results were less stable than the base case solutions. Figures 8.13 and 8.14 shows the predicted y-direction magnetic field magnitude with magnetic field lines and the electron pressure in the x-direction, respectively, for the collisionless case at the standard time, $t = 18\,\Omega_{ion}^{-1}$ obtained using a 512×256 grid. The normalized magnetic reconnection was 1.04 at this time for this case as is predicted by Schmitz *et al.* [4, 75] and Johnson [6] for the original GEM case. This simulation proved to be fairly unstable, and was very unstable past the standard $18\,\Omega_{ion}^{-1}$ time. The final result that was used to study the temporal evolution of the magnetic reconnected flux of Figure 8.17 for this case is at $t = 48\,\Omega_{ion}^{-1}$ and is included in Figures 8.15 and 8.16. As can be seen at longer time, there is considerable instability and asymmetry in the predicted solutions for this collisionless case. The instability of the results is to be expected as will be shown later in Section 8.4.6 of this chapter. Note that there was no instance of magnetic island formation, at least for the lower mesh resolution considered here.

8.4.4 Time Evolution of Normalized Magnetic Reconnected Flux

The time evolution of the magnetic reconnected flux is examined here. The normalized magnetic reconnected flux versus time for the base case is plotted in Figure 8.17 along with the results of Pritchett *et al.* [3] and a collisionless GEM case at a mesh resolution of 512×256 that is examined in Sections 8.4.3 and 8.4.5. As can be seen, the predicted reconnected flux initially starts off at a low value and quickly ramps up and then continues to increase, levelling off at a value of around 3.85. It should be noted that at times after $18\,\Omega_{ion}^{-1}$, the magnetic island seen in Figure 8.8 moves to the left and eventually merges, which reduces the rate of reconnection as the opposing magnetic field lines eliminate each other. Due to the asymmetric movement of the magnetic island, the reconnected flux value was determined by the integration of $|B_y|$ across the entire domain divided by 2 to be consistent with the definition of magnetic reconnected flux in the literature.

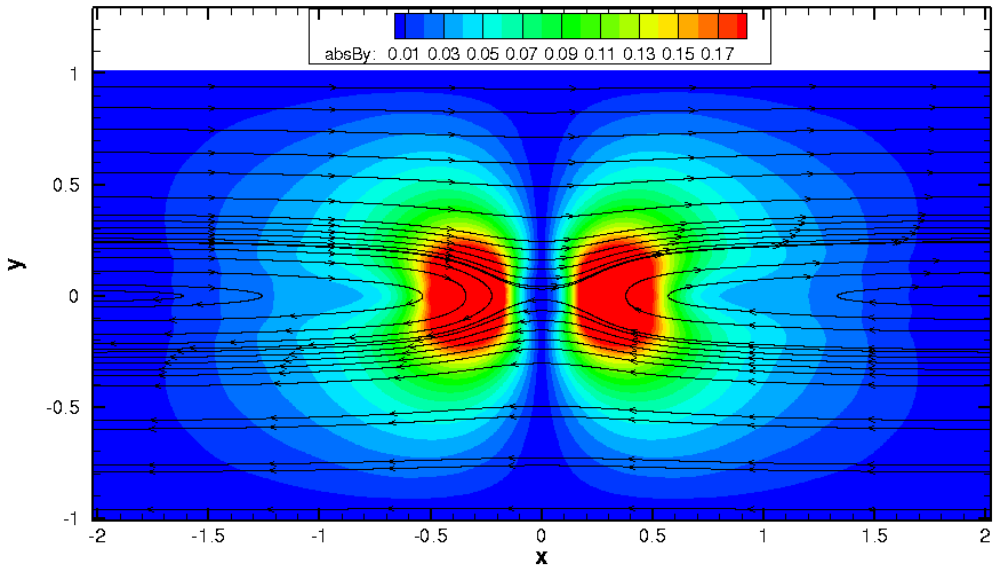

Figure 8.13: GEM test case solution with MGLM error cleaning showing $|B_y|$ and magnetic field lines at $t = 18\,\Omega_{ion}^{-1}$ and mesh resolution 512×256 with no collisions. Normalized magnetic reconnected flux is 1.04.

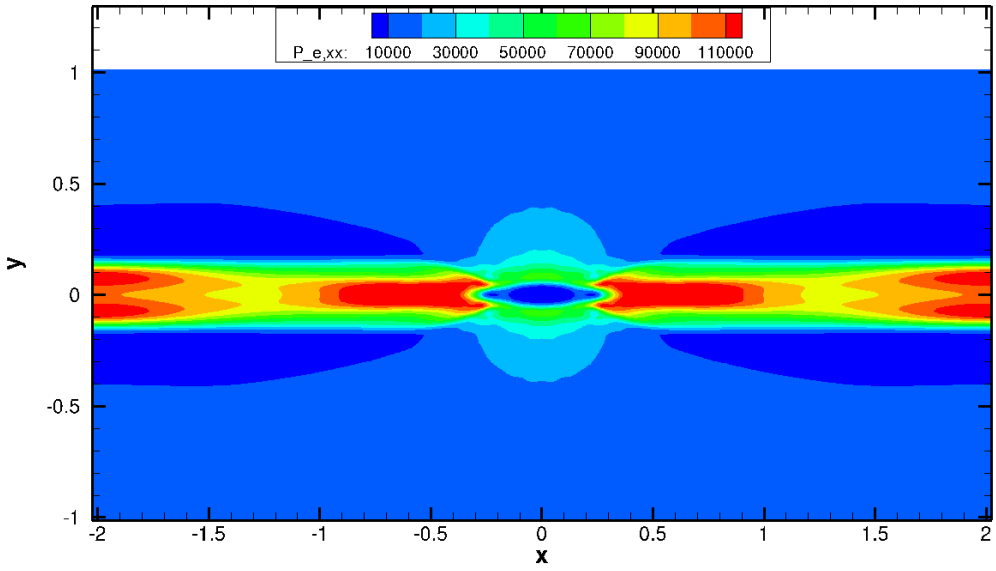

Figure 8.14: GEM test case solution with MGLM error cleaning showing $P_{e,xx}$ at $t = 18\,\Omega_{ion}^{-1}$ and mesh resolution 512×256 with no collisions. Normalized magnetic reconnected flux is 1.04.

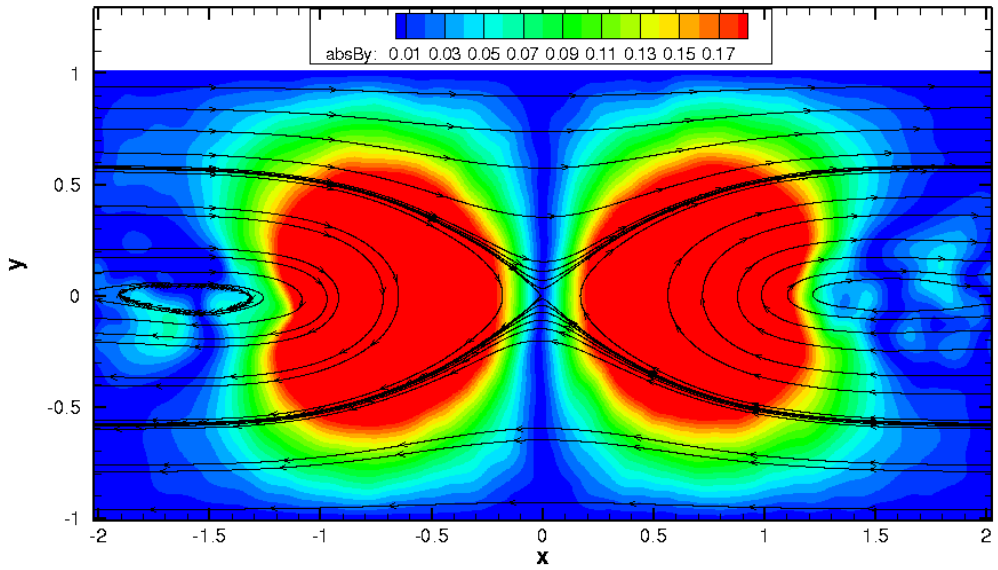

Figure 8.15: GEM test case solution with MGLM error cleaning showing $|B_y|$ and magnetic field lines at $t = 48\,\Omega_{ion}^{-1}$ and mesh resolution 512×256 with no collisions. Normalized magnetic reconnected flux is 3.14.

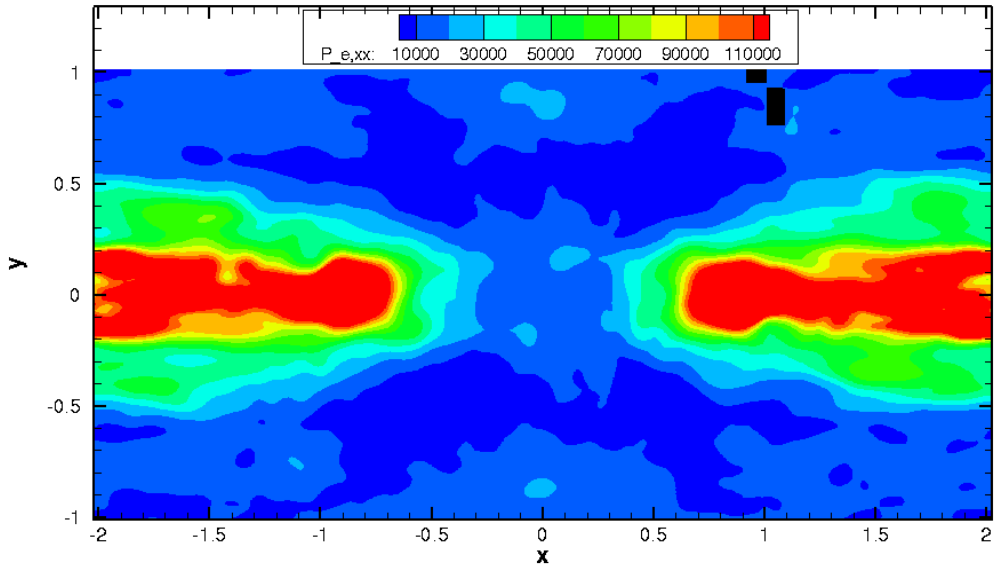

Figure 8.16: GEM test case solution with MGLM error cleaning showing $P_{e,xx}$ at $t = 48\,\Omega_{ion}^{-1}$ and mesh resolution 512×256 with no collisions. Normalized magnetic reconnected flux is 3.14.

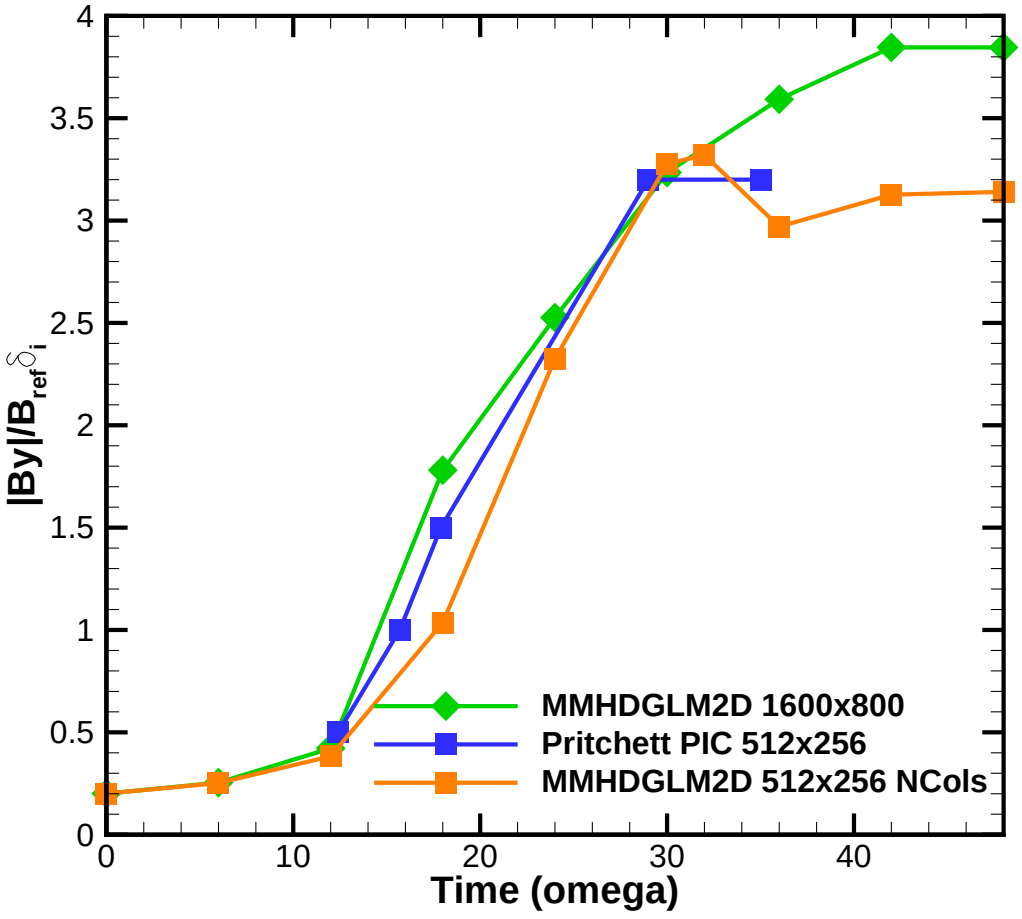

Figure 8.17: Normalized magnetic reconnected flux versus time for GEM test case at a mesh resolution of 1600×800 and a collisionless GEM test case at a mesh resolution of 512×256 for the MGLM error correction scheme. Also includes data from PIC simulations of Pritchett *et al.* [3].

The movement of the magnetic island can be seen in Figures 8.18 and 8.19, which show plots of $|B_y|$ with the magnetic field lines and the electron pressure, $P_{e,xx}$, respectively, for time $24\,\Omega_{ion}^{-1}$ obtained using the base grid resolution of 1600×800. The movement and eventual merger has also been observed in the literature [28, 63, 66, 70, 71], though the direction the island moves is not consistent and differs with the scheme used. However, the leftward direction is often documented [28, 71]. Taking a look at the slope of the time evolution plot, the maximum normalized magnetic reconnection rate is approximately 0.2 which is also in good agreement with values reported in the literature [2, 3, 6, 27, 71, 189]. The agreement of the time evolution of the predicted reconnected flux with the PIC simulations of Pritchett *et al.* [3] is in fact quite good and this behaviour is typical of most PIC and hybrid simulations. Though the resolution of the base case is much higher than the PIC grid resolution of 512×256, the computational resources required are much less. It should also be noted that the reconnected flux generally converges to around 3.3 in the literature, but the increased value observed here can be attributed to the higher resolution employed, which is evidenced by the lower final reconnected flux of the lower (collisionless) mesh resolution case of 512×256 cells. The collisionless 512×256 case has a slightly different profile, agreeing well to around $t = 12\,\Omega_{ion}^{-1}$ for all solutions compared, but then the reconnected value goes lower until the peak near $30\,\Omega_{ion}^{-1}$ where it once again agrees with the other simulations. However, the reconnected flux then suddenly drops down and then recovers to a value of approximately 3.27 as is expected for this lower mesh resolution case. The drop in reconnected flux before reaching a final value has also been observed by other researchers [2, 4, 5, 27, 66, 189, 190].

8.4.5 Comparison of Predicted Solutions to Other Results

Examining further the results for the base grid of 1600×800 computational cells, the predicted distributions of the out of plane magnetic field are presented in Figure 8.20, and Figures 8.26 and 8.27 show the diagonal and off diagonal components of the electron pressure tensor, respectively. The plots of the out of plane variables, namely $B_z, P_{e,xz}, P_{e,yz}$, are shown using the negative of the values obtained as done by Johnson [6]. This is to be consistent with the original GEM results which were defined to be in the x-z plane. This made the out of plane results positive into the plane, while the results obtained with the x-y plane definition of the GEM problem has the out of plane axis positive out of the plane.

Significant instabilities can be seen in the pressure tensors of Figures 8.26 and 8.27. However, the quadrupole structure of of the out of plane magnetic field in Figure 8.20 shows very good agreement with the literature [2–4, 6–8, 54]. For comparison, the out of plane magnetic

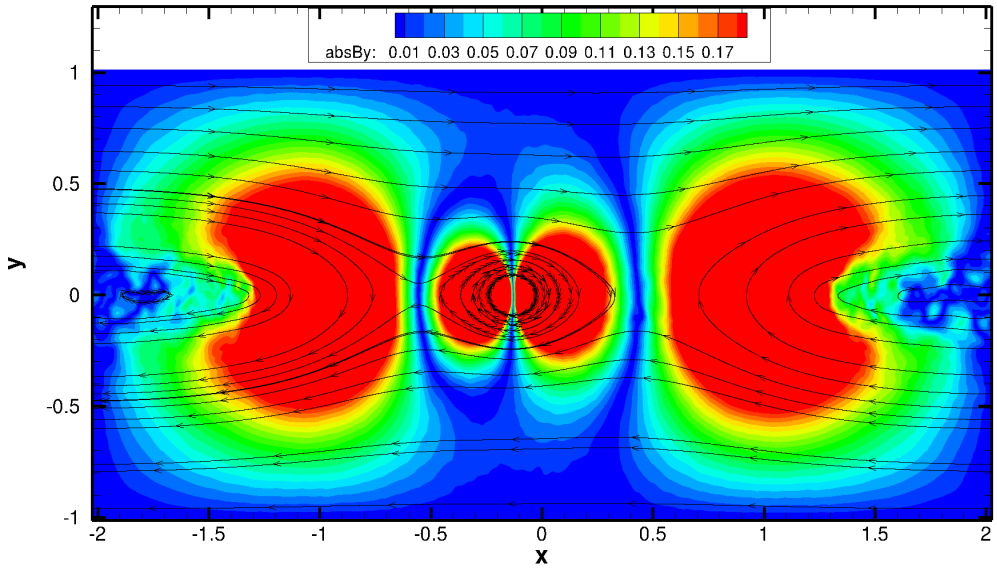

Figure 8.18: GEM test case solution with MGLM error cleaning showing $|B_y|$ and magnetic field lines at $t = 24\,\Omega_{ion}^{-1}$ and mesh resolution 1600×800 with collision frequency $10^7\,\mathrm{s}^{-1}$. Normalized magnetic reconnected flux is 2.53.

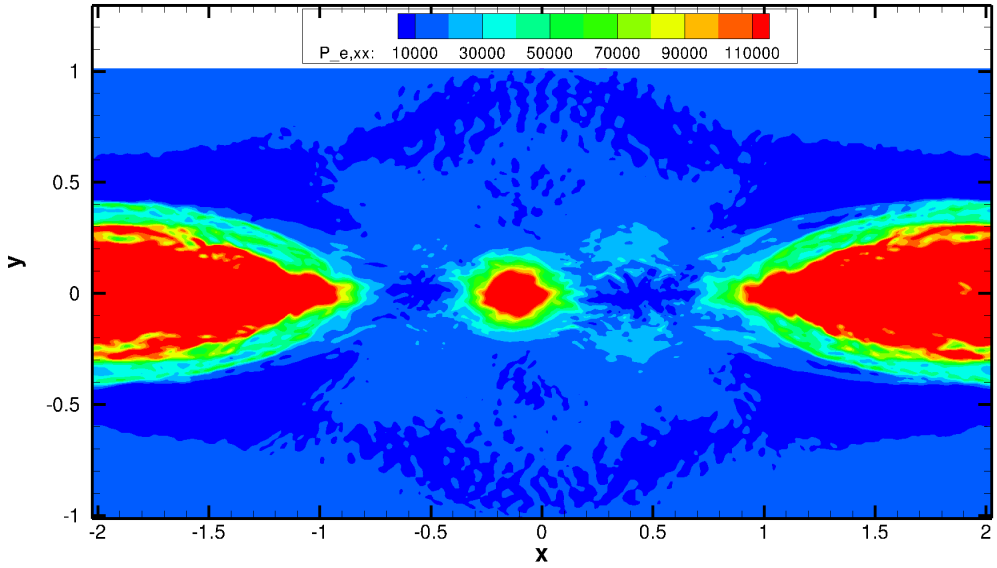

Figure 8.19: GEM test case solution with MGLM error cleaning showing $P_{e,xx}$ at $t = 24\,\Omega_{ion}^{-1}$ and mesh resolution 1600×800 with collision frequency $10^7\,\mathrm{s}^{-1}$. Normalized magnetic reconnected flux is 2.53.

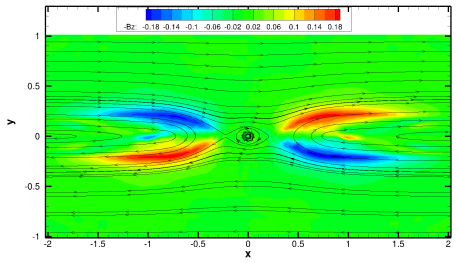

Figure 8.20: GEM test case solution with MGLM error cleaning showing negative out of plane magnetic field $-B_z$ and magnetic field lines at $t = 18\,\Omega_{ion}^{-1}$ and mesh resolution 1600×800 with collision frequency $10^7\,\mathrm{s}^{-1}$. Normalized magnetic reconnected flux is 1.77.

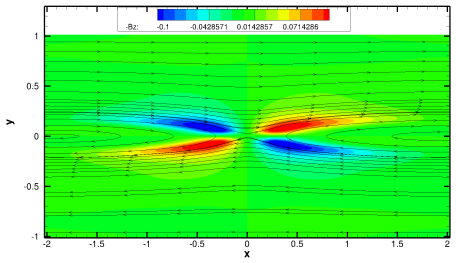

Figure 8.21: GEM test case solution with MGLM error cleaning showing negative out of plane magnetic field $-B_z$ and magnetic field lines at $t = 18\,\Omega_{ion}^{-1}$ and mesh resolution 400×200 with collision frequency $10^7\,\mathrm{s}^{-1}$. Normalized magnetic reconnected flux is 0.82.

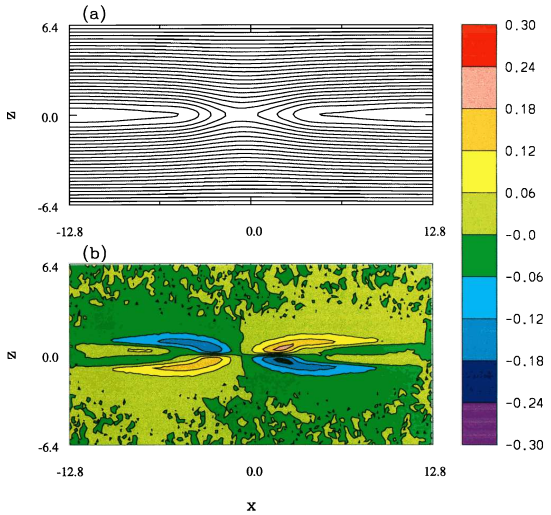

Figure 8.22: Results from PIC simulations by Pritchett *et al.* [3] showing magnetic field lines (a) and out of plane magnetic field (b) at a grid resolution of 512×256 at $t = 15.7\,\Omega_{ion}^{-1}$. Normalized magnetic reconnected flux is 1.0.

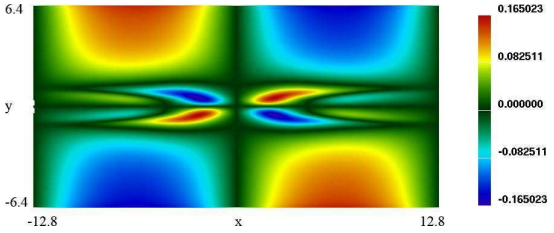

Figure 8.23: Results from Darwin-Vlasov simulations by Schmitz *et al.* [4] showing out of plane magnetic field at a total grid resolution of 512×256 at $t = 17.7\,\Omega_{ion}^{-1}$. Normalized magnetic reconnected flux is 1.0.

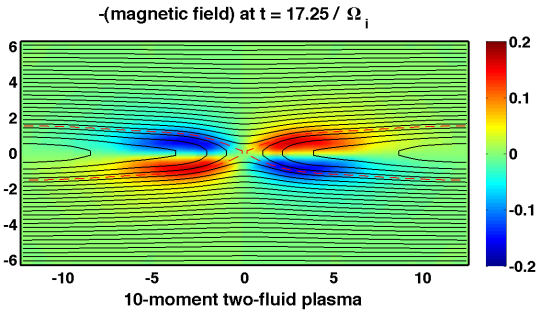

Figure 8.24: Results from 10-moment two-fluid simulations by Johnson *et al.* [7] showing out of plane magnetic field at $t = 17.25\,\Omega_{ion}^{-1}$. Normalized magnetic reconnected flux is 1.2.

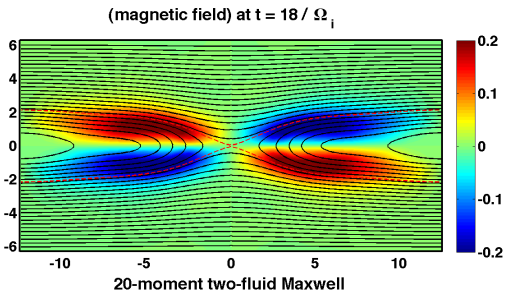

Figure 8.25: Results from 20-moment two-fluid simulations by Johnson *et al.* [8] showing out of plane magnetic field at $t = 18\,\Omega_{ion}^{-1}$.

quadrupole results of Pritchett *et al.* [3], Schmitz *et al.* [4], and Johnson *et al.* [7,8] are included in Figures 8.22, 8.23 and 8.24-8.25, respectively. This illustrates the somewhat decoupled nature of the fluid dynamic behaviour of the electrons and ions with the behaviour of the magnetic field. As can be seen by comparing the results, the fine detail found in the PIC and Vlasov solutions between the quadrupoles close to the x-axis is recreated with the current high resolution base grid solution using the MMHDGLM2D model. The predicted solution is more stable than the PIC code and the agreement is better than that obtained by Johnson's 10- and 20-moment two-fluid results. Note that the scales are approximately correct as the magnitude of the dimensionalization constant for the magnetic field is approximately one.

The predicted distribution of the pressure tensor of Figures 8.26 and 8.27 exhibit the major elements which agree with the results in the literature; however, with a concentration of electron pressure at the center coinciding with the existence of a magnetic island. For comparison, the electron pressure tensor results from the Darwin-Vlasov simulation of Schmitz *et al.* [4] is included in Figure 8.28 and the 10- and 20-moment two-fluid results of Johnson *et al.* [7] are included in Figures 8.29 and 8.30. The results presented in Figures 8.26 and 8.27 have better agreement than the two-fluid formulation of Johnson *et al.* [7] when compared to the Darwin-Vlasov solutions, with the main difference being the effect of the magnetic island on the pressure profile at the center of the domain.

It should be stated that the results for the base case are at a higher grid resolution than those of Johnson *et al.* [6–8], so a lower mesh resolution of 400×200 is also examined, which is more

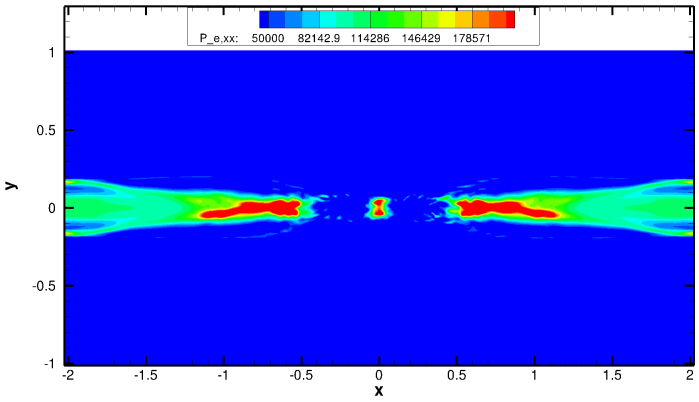

(a) Electron pressure $P_{e,xx}$.

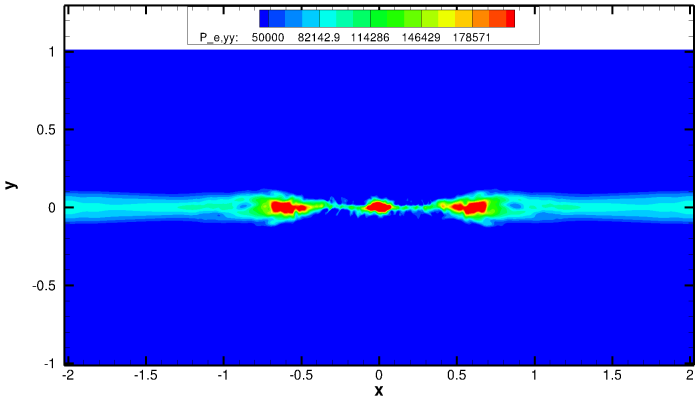

(b) Electron pressure $P_{e,yy}$.

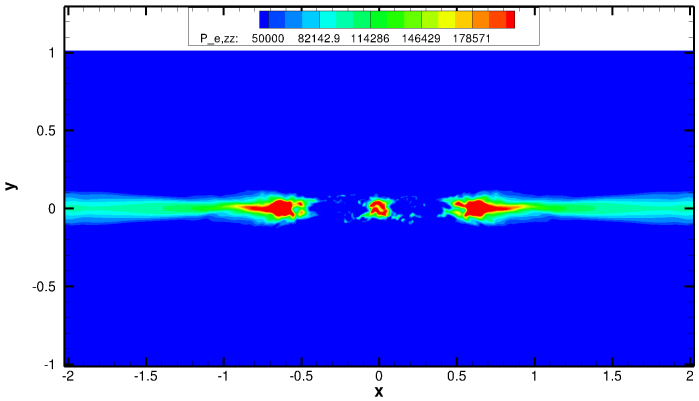

(c) Electron pressure $P_{e,zz}$.

Figure 8.26: GEM test case solution with MGLM error cleaning showing diagonals of the electron pressure tensor at $t = 18\,\Omega_{ion}^{-1}$ and mesh resolution 1600×800 with collision frequency $10^7\,\mathrm{s}^{-1}$. Normalized magnetic reconnected flux is 1.77.

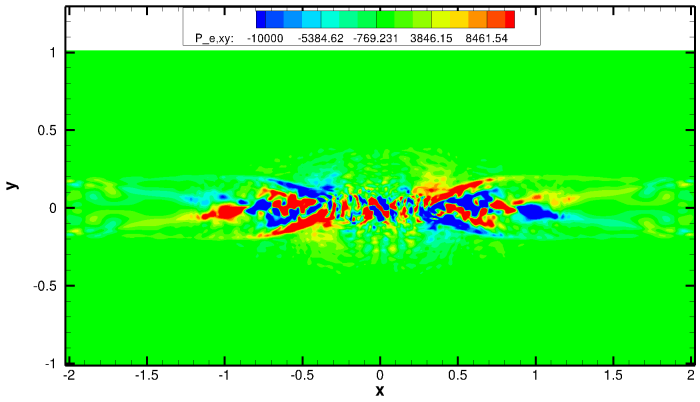

(a) Electron pressure $P_{e,xy}$.

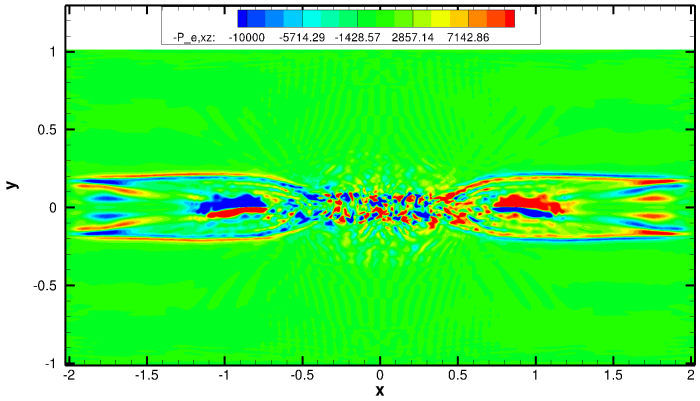

(b) Negative electron pressure $-P_{e,xz}$.

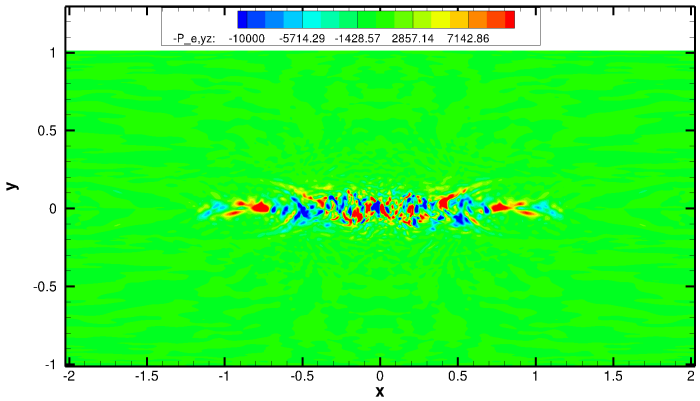

(c) Negative electron pressure $-P_{e,yz}$.

Figure 8.27: GEM test case solution with MGLM error cleaning showing off-diagonals of the electron pressure tensor at $t = 18\,\Omega_{ion}^{-1}$ and mesh resolution 1600×800 with collision frequency $10^7\,\mathrm{s}^{-1}$. Normalized magnetic reconnected flux is 1.77.

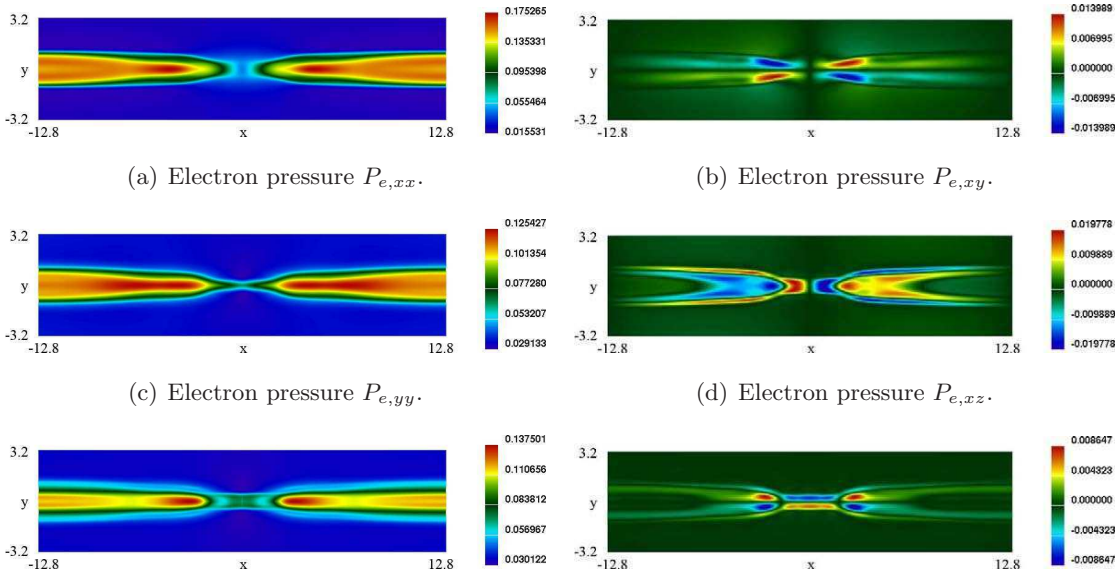

(a) Electron pressure $P_{e,xx}$.

(b) Electron pressure $P_{e,xy}$.

(c) Electron pressure $P_{e,yy}$.

(d) Electron pressure $P_{e,xz}$.

(e) Electron pressure $P_{e,zz}$.

(f) Electron pressure $P_{e,yz}$.

Figure 8.28: Results from Darwin-Vlasov simulations by Schmitz *et al.* [4] showing electron pressure tensor at $t = 17.7\,\Omega_{ion}^{-1}$ and total grid resolution 512×256. Normalized magnetic reconnected flux is 1.0.

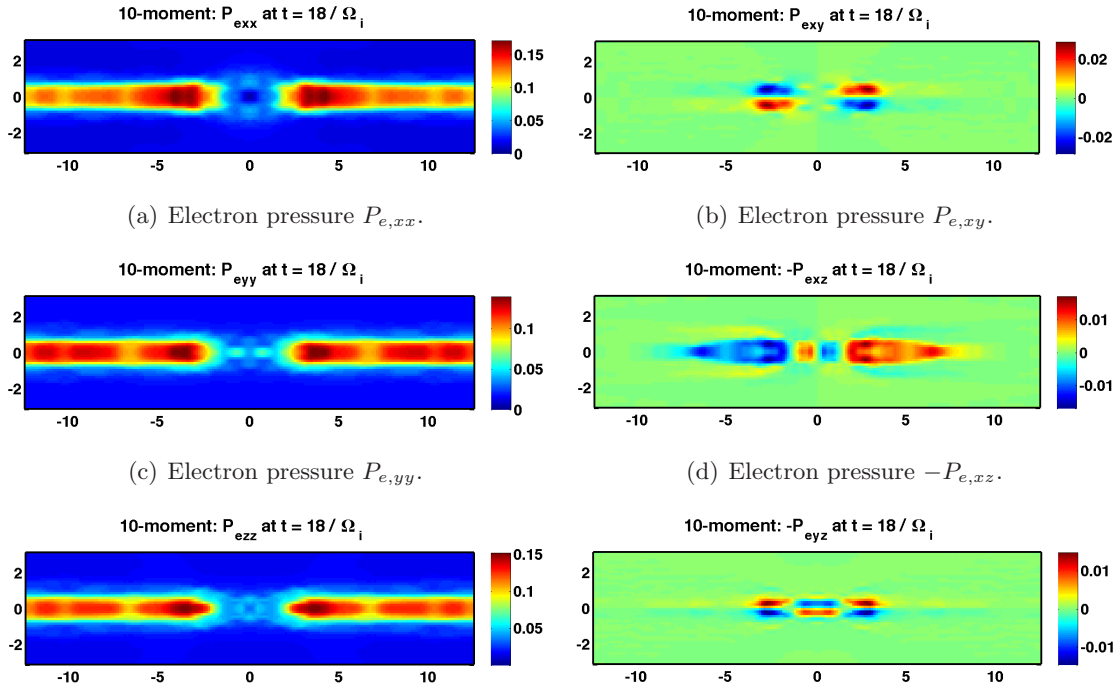

(a) Electron pressure $P_{e,xx}$.

(b) Electron pressure $P_{e,xy}$.

(c) Electron pressure $P_{e,yy}$.

(d) Electron pressure $-P_{e,xz}$.

(e) Electron pressure $P_{e,zz}$.

(f) Electron pressure $-P_{e,yz}$.

Figure 8.29: Results from 10-moment two-fluid simulations by Johnson *et al.* [7] showing electron pressure tensor at $t = 18\,\Omega_{ion}^{-1}$. Normalized magnetic reconnected flux is 1.28.

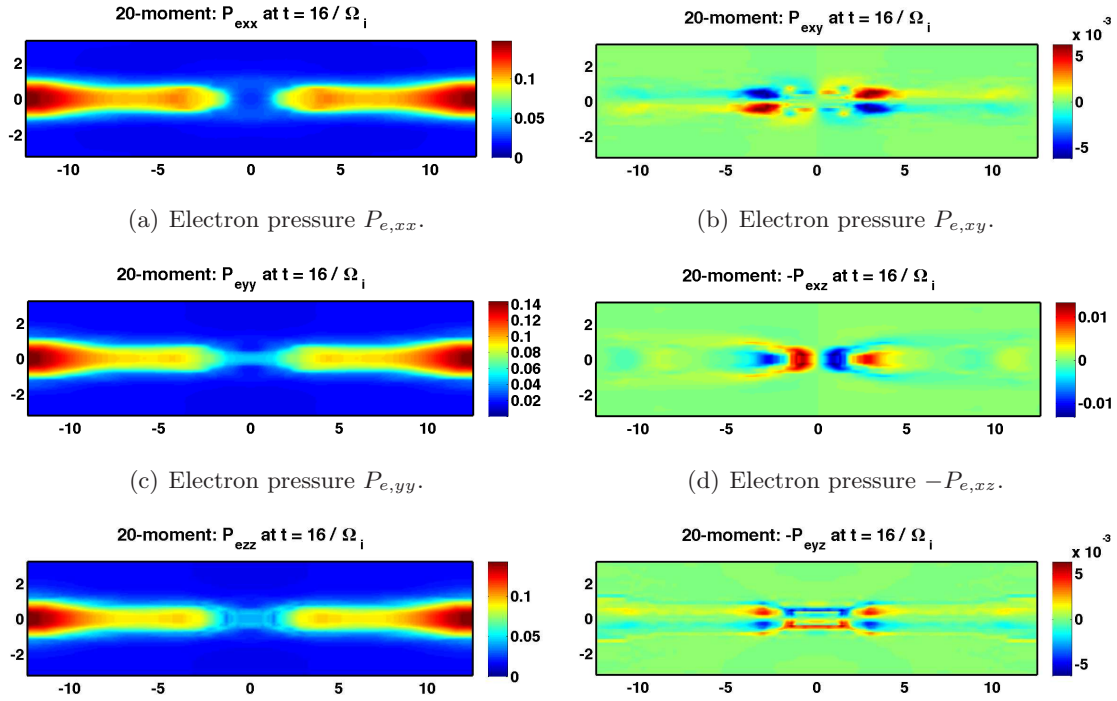

(a) Electron pressure $P_{e,xx}$.

(b) Electron pressure $P_{e,xy}$.

(c) Electron pressure $P_{e,yy}$.

(d) Electron pressure $-P_{e,xz}$.

(e) Electron pressure $P_{e,zz}$.

(f) Electron pressure $-P_{e,yz}$.

Figure 8.30: Results from 20-moment two-fluid simulations by Johnson *et al.* showing electron pressure tensor at $t = 16\,\Omega_{ion}^{-1}$.

stable than the high mesh resolution case for the predicted fluid results. Returning to the results previously shown in Figure 8.21, it is evident that the predicted distribution of the out of plane magnetic field now resembles very closely the 10- and 20-moment out of plane magnetic quadrupole results of Johnson *et al.*, which are shown in Figures 8.24 and 8.25. The predicted electron pressure tensor for the 400×200 coarse mesh was also examined, and the predicted distribution of these quantities are presented in Figures 8.31 and 8.32 for the diagonal and off diagonal terms, respectively. The pressure plots at the coarser mesh also agree very well with the Vlasov simulations of Schmitz *et al.* [4], particularly the off-diagonal terms which play a large role in the evolution of the magnetic field through the Ohm's law as noted by Schmitz *et al.* The present results also agree fairly well with Johnson's 10-moment results, but captures the results of the Vlasov simulation more closely, though it should be mentioned at the resolutions being used, the results are not converged and may simply agree better because the resolutions of the results are similar. Johnson *et al.*'s 20-moment results for the off-diagonal pressures now agrees very well with the results of the current study. The only major difference between the results presented here and those of Schmitz *et al.* and Johnson *et al.*'s results is the y-direction electron pressure. A rectangular region of high anisotropic pressure exists in the center here which makes sense since the electrons would want to spiral along the field lines.

Next, three sets of results were examined to compare the reconnected flux values and the out of plane currents to the coupled Vlasov solutions of Rieke *et al.* [5]. The three cases were a collisionless 512×256 mesh resolution case, and a case with mesh resolution of 400×200 with both physical collisions and no collisions. All cases made use of the proposed MGLM error cleaning algorithm. The results at a time of $t = 32\,\Omega_{ion}^{-1}$ showing the negative out of plane current, $-J_z$, for the three cases considered are presented in Figures 8.33(b), 8.33(d) and 8.33(c) for the collisionless 512×256 mesh, the physical 400×200 mesh and the collisionless 400×200 mesh cases, respectively. The 400×200 grid solutions at a time of $t = 32\,\Omega_{ion}^{-1}$ resulted in a normalized reconnected flux of 3.34 and 3.37 for the physical collisions and completely collisionless solutions respectively, while the 512×256 grid collisionless case resulted in a normalized magnetic reconnected flux of 3.32.

All three of the numerical solutions summarized in Figure 8.33 are very similar, with the collisionless and higher grid resolution solutions exhibiting more oscillations in the plasma. The reconnected flux value agrees with the majority of the literature for long time runs past $t = 30\,\Omega_{ion}^{-1}$ using a variety of solution procedures [2, 4, 54, 65, 66, 70, 71]. When compared with the coupled Darwin-Vlasov two-fluid results obtained by Rieke *et al.* [5], which is included in Figure 8.33(a), it can be seen that the results agree extremely well, both for the normalized magnetic reconnected flux value and also for the predicted form of the out of plane current.

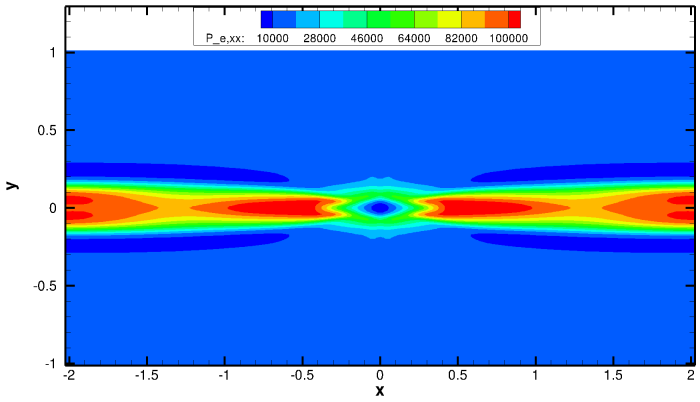

(a) Electron pressure $P_{e,xx}$.

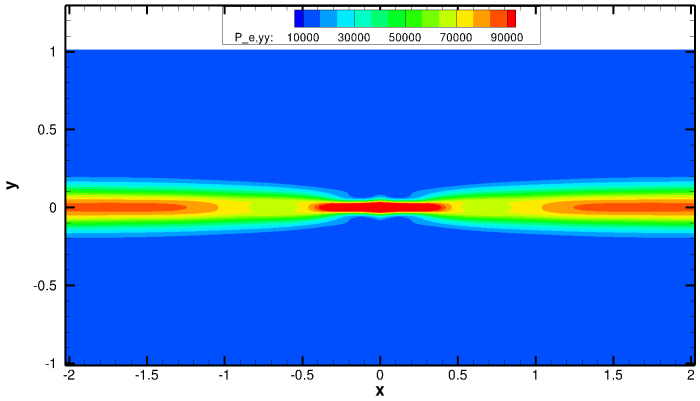

(b) Electron pressure $P_{e,yy}$.

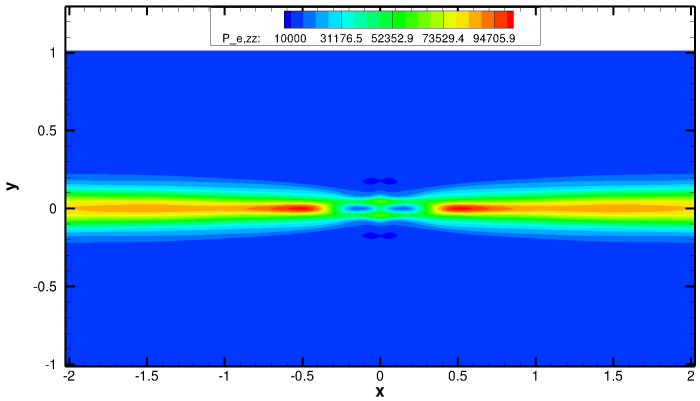

(c) Electron pressure $P_{e,zz}$.

Figure 8.31: GEM test case solution with MGLM error cleaning showing diagonals of the electron pressure tensor at $t = 18\,\Omega_{ion}^{-1}$ and mesh resolution 400×200 with collision frequency $10^7\,\mathrm{s}^{-1}$. Normalized magnetic reconnected flux is 0.82.

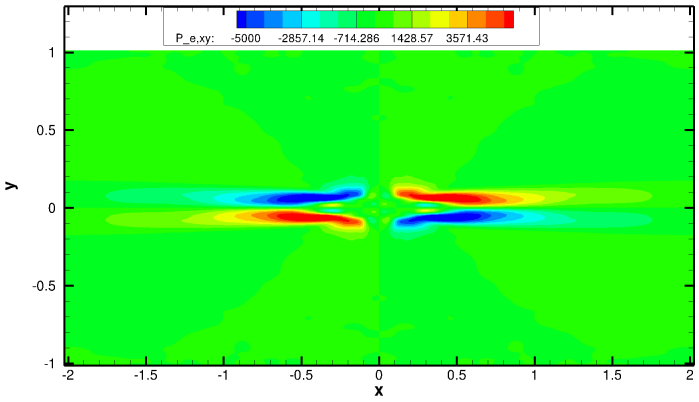

(a) Electron pressure $P_{e,xy}$.

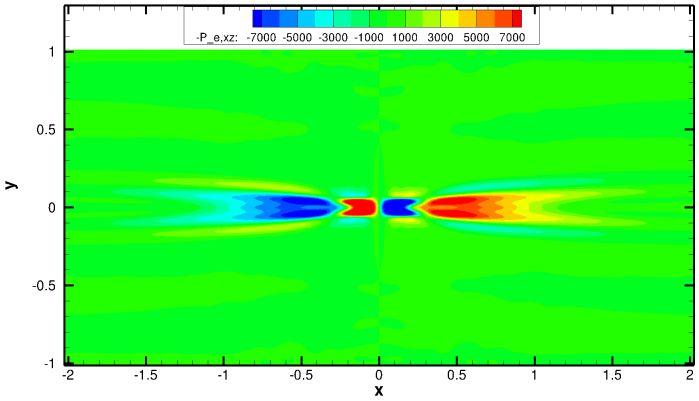

(b) Negative electron pressure $-P_{e,xz}$.

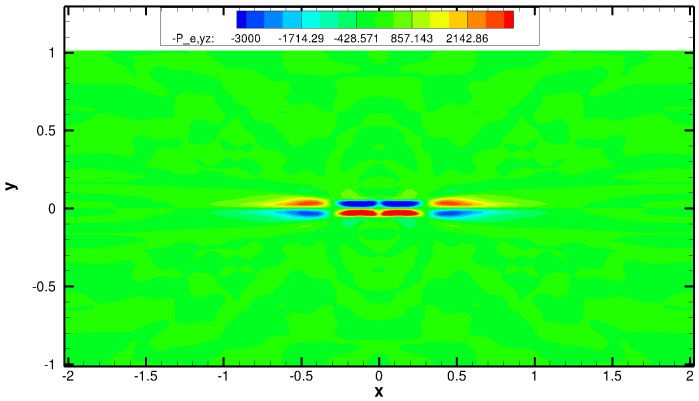

(c) Negative electron pressure $-P_{e,yz}$.

Figure 8.32: GEM test case solution with MGLM error cleaning showing off-diagonals of the electron pressure tensor at $t = 18\,\Omega_{ion}^{-1}$ and mesh resolution 400×200 with collision frequency $10^7\,\mathrm{s}^{-1}$. Normalized magnetic reconnected flux is 0.82.

The peaks and outline of the current regions occur in the same place and the values also agree (note that the results must be non-dimensionalized by $e\,n_{ref}\,v_A$).

8.4.6 Collisional Effects on Reconnection

The collision frequency for the base, 1600×800, grid with MGLM error correction was altered to explore the effects of collisions on the solution and values of the reconnected magnetic flux. Three different collision regimes were examined: the collisionless ($\nu_s = 0\,\mathrm{s}^{-1}$), transitional ($\nu_s = 10^7\,\mathrm{s}^{-1}$), and fully collisional ($\nu_s = 10^{12}\,\mathrm{s}^{-1}$) regimes. Figures 8.34 and 8.35 provide comparisons showing $|B_y|$ with magnetic field lines and $P_{e,xx}$ for $t = 18\,\Omega_{ion}^{-1}$ for the cases examined. In general, with less collisions, the solution becomes less stable, with the rate of reconnection increasing when going from collisional to collisionless. As mentioned before, this trend has also been found in the literature [71]; however, the actual predicted differences in the reconnected flux between the transitional and collisionless regimes are not large here. Also, as can be seen in Figures 8.34(a) and 8.35(a), which shows the base case with magnetic divergence cleaning at $t = 18\,\Omega_{ion}^{-1}$, with no collisions, the solution is asymmetric with the magnetic island having moved already towards the left along with other asymmetries that can be seen in the solution. However, when the regime moves towards an isotropic 5-moment fluid description, with fully collisional inter- and intra-species collision terms, results such as those plotted in Figures 8.34(c) and 8.35(c) are obtained. The magnetic island has been eliminated and the region where the magnetic field lines have reconnected is much larger; however, the total magnetic reconnected flux is lower due to the absence of the magnetic island. This finding is to be expected as shown in Figure 8.12, which depicts the 5-moment result of Rieke *et al.* [5] as being much lower in reconnected flux than the anisotropic models.

Results for Modified Johnson's Case

In a 2013 presentation for the SIAM Conference on Computational Science and Engineering [8], Johnson and Rossmanith revealed the collision relationship used to obtain Johnson's thesis results. These ultimately were slightly different than the constant collision frequencies used for the results presented in this chapter. To compare how the results differed for the modified collisional rates, the collision frequencies of Johnson and Rossmanith were reproduced and the base case was examined with these new collision frequencies. The collision frequencies were separate for the electron and ion species and determined to be approximately $2.0 \times 10^5\,\mathrm{s}^{-1}$ and $2.0 \times 10^6\,\mathrm{s}^{-1}$ for the ions and electrons, respectively. Figures 8.36(b) and 8.37(b) present predicted values of $|B_y|$ along with magnetic field lines and $P_{e,xx}$, respectively at $t = 18\,\Omega_{ion}^{-1}$ for

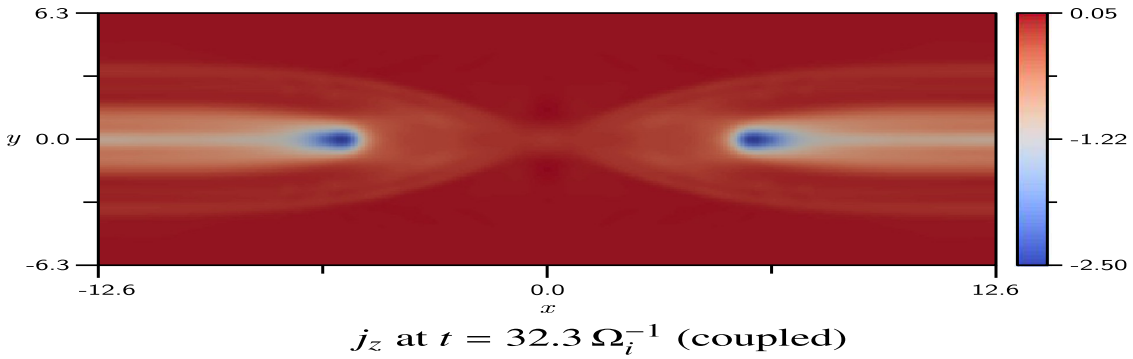

(a) Coupled Darwin-Vlasov two-fluid results, Rieke *et al.* [5]. Normalized magnetic reconnected flux is 3.2.

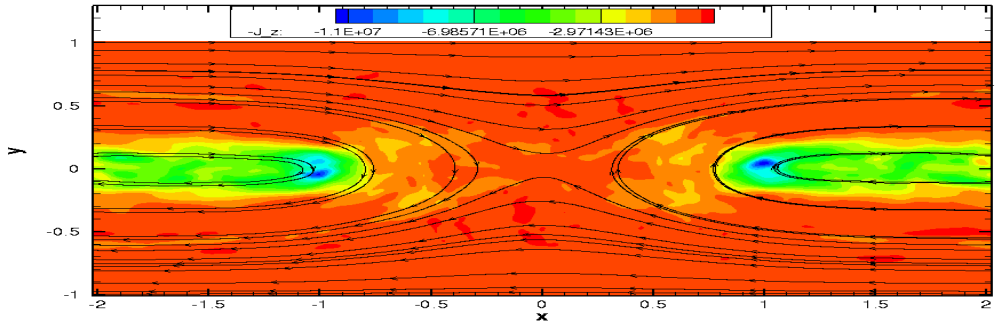

(b) Collisionless MGLM results with a 512×256 mesh. Normalized magnetic reconnected flux is 3.32.

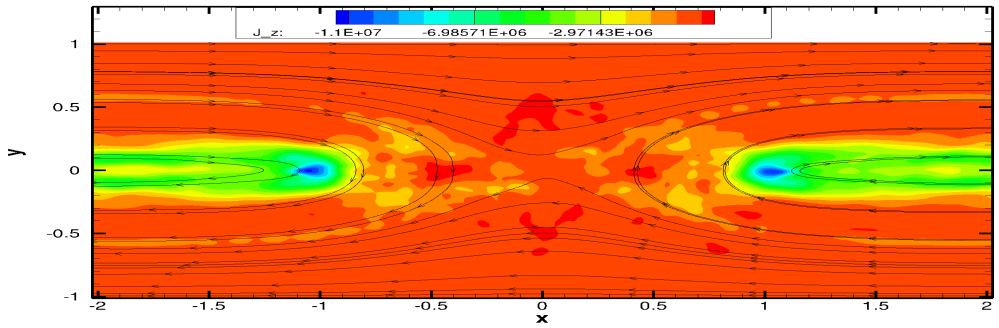

(c) Collisionless MGLM results with a 400×200 mesh. Normalized magnetic reconnected flux is 3.37.

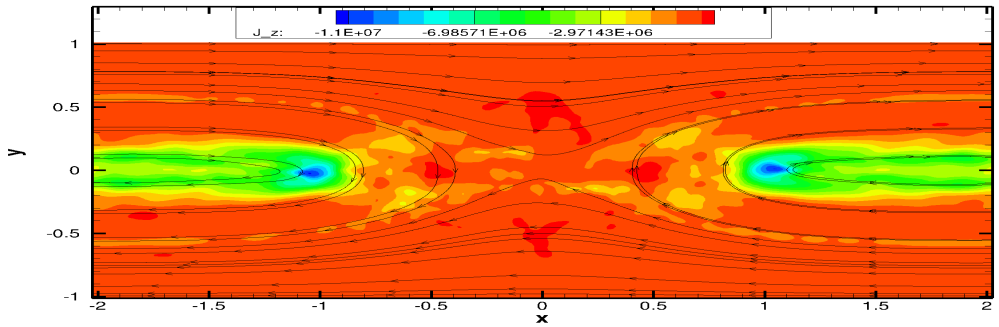

(d) Physical collisions MGLM results with a 400×200 mesh. Normalized magnetic reconnected flux is 3.34

Figure 8.33: Out of plane current results comparison for the GEM problem at $t = 32\,\Omega_{ion}^{-1}$.

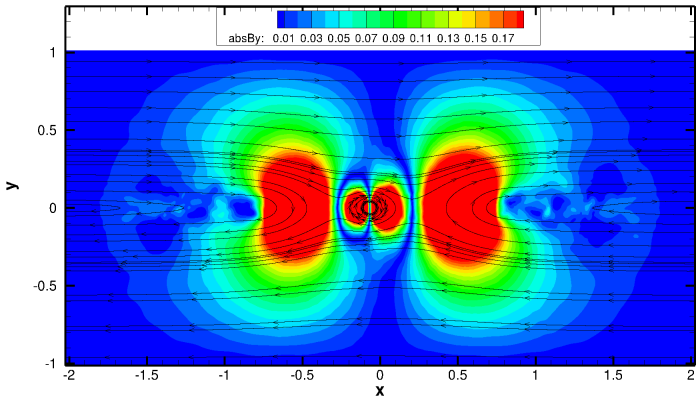

(a) Collisionless. Normalized magnetic reconnected flux is 1.822.

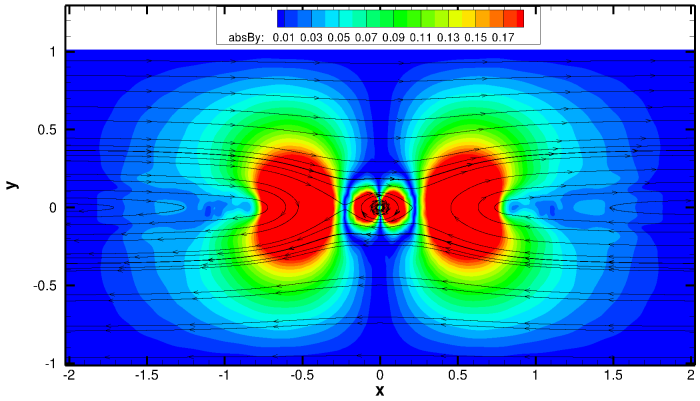

(b) Collision frequency $10^7\,\mathrm{s}^{-1}$. Normalized magnetic reconnected flux is 1.77.

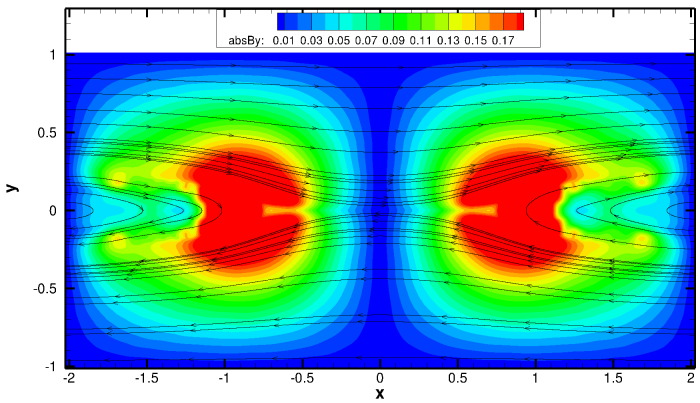

(c) Collision frequency $10^{12}\,\mathrm{s}^{-1}$. Normalized magnetic reconnected flux is 1.433.

Figure 8.34: GEM test case solution comparison with MGLM error cleaning showing $|B_y|$ and magnetic field lines at $t = 18\,\Omega_{ion}^{-1}$ and a mesh resolution of 1600×800 for various collision frequencies.

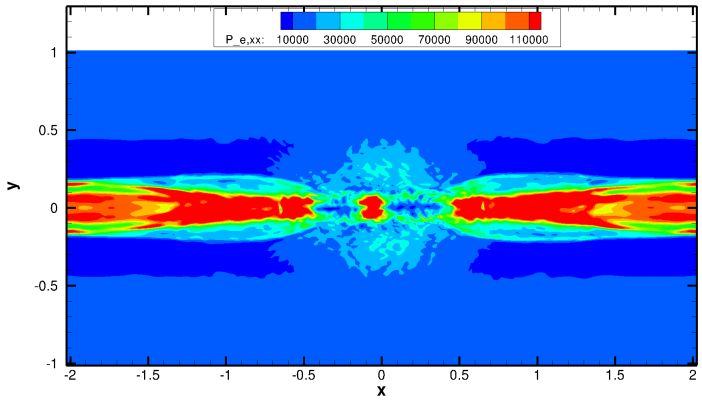

(a) Collisionless. Normalized magnetic reconnected flux is 1.822.

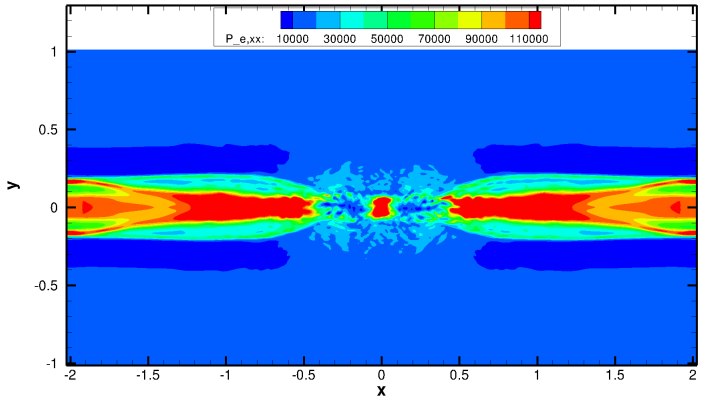

(b) Collision frequency $10^7\,\mathrm{s}^{-1}$. Normalized magnetic reconnected flux is 1.77.

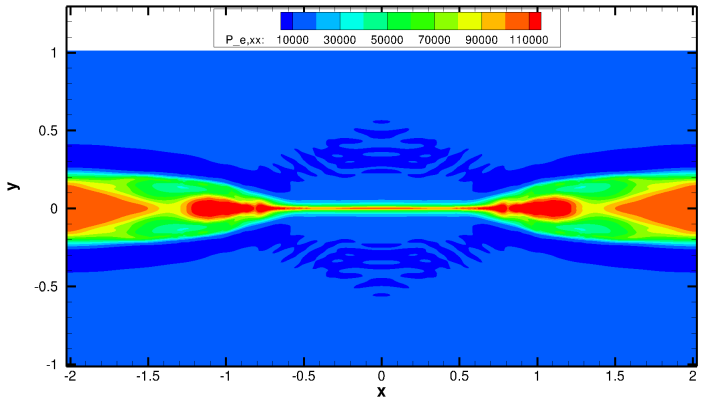

(c) Collision frequency $10^{12}\,\mathrm{s}^{-1}$. Normalized magnetic reconnected flux is 1.433.

Figure 8.35: GEM test case solution comparison with MGLM error cleaning showing $P_{e,xx}$ at $t = 18\,\Omega_{ion}^{-1}$ and a mesh resolution of 1600×800 for various collision frequencies.

the base mesh resolution of 1600×800 using the modified, Johnson and Rossmanith, collision frequencies. Predictably, the results are slightly less stable, but do not differ greatly from the results in the rest of this section both qualitatively and also for total magnetic reconnected flux.

A set of alternate initial conditions were also examined, as outlined by Johnson [6], which included second-order effects for initial current, usually left to evolve on their own. Equation (8.14) is modified with an addition so that

$$\mathbf{J} = \begin{bmatrix} 0 \\ 0 \\ -\frac{B_0}{\lambda\mu}\mathrm{sech}^2\left(\frac{y}{\lambda}\right) + \frac{\pi^2\psi_0}{\mu}\left(\frac{4}{L_x^2} + \frac{1}{L_z^2}\right)\cos(2\pi\frac{x}{L_x})\cos(\pi\frac{y}{L_z}) \end{bmatrix}, \tag{8.29}$$

which resulted in Figures 8.36(c) and 8.37(c). This was coupled with the separate collision frequencies of Johnson and Rossmanith [8]. There is not much difference in the final solution as compared with Figures 8.36(b) and 8.37(b), except that there is slightly less reconnection and there is a curious move to the right for the magnetic island. Ultimately the magnetic island merges with the right lobe in this case.

8.4.7 Comparison of the Effect of Mass Ratio on the Electron Diffusion Thickness

The effect of the electron-ion mass ratio was briefly examined, by considering the low mesh resolution 400×200 base case with a physical electron-ion mass ratio. It was found that using a physical mass ratio resulted in a much stiffer and more unstable solution, requiring a smaller time step as was expected and found by other researchers [189].

In order to compare the results obtained with the physical mass ratio, the out of plane electron currents were plotted at $t = 18\,\Omega_{ion}^{-1}$ for both $m_{ion}/m_e = 25$ and for the physical mass ratio, $m_{ion}/m_e = 1836$, in Figures 8.38(a) and 8.38(b), respectively. The change in the mass ratio causes an equivalent change in the electron diffusion region as found in the literature where the diffusion region decreases with increasing ion-electron mass ratio [2, 70, 189]. Approximately measuring the peak to peak distance of the diffusion region normalized by the respective ion inertial length, δ_{ion}, results in

$$\frac{d_{xe}^{(25)}}{d_{xe}^{(Real)}} = 2.76. \tag{8.30}$$

The theoretical value for this ratio as found by Ricci *et al.* [189] is 2.92, however, measured values in simulations are often lower. The value obtained is close to the value obtained by Ricci *et al.*, which was 2.8.

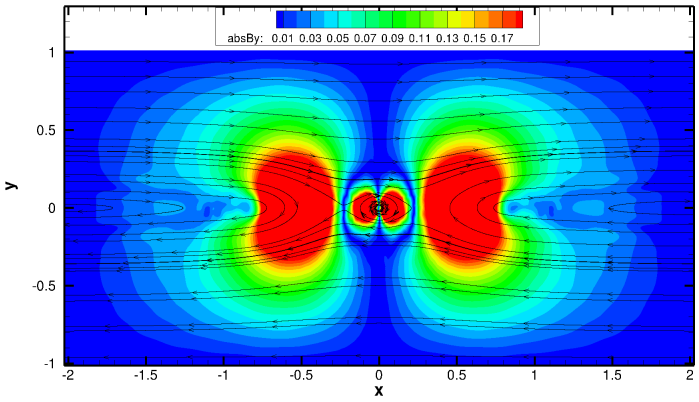

(a) Collision frequency $10^7\,\mathrm{s}^{-1}$. Normalized magnetic reconnected flux is 1.77.

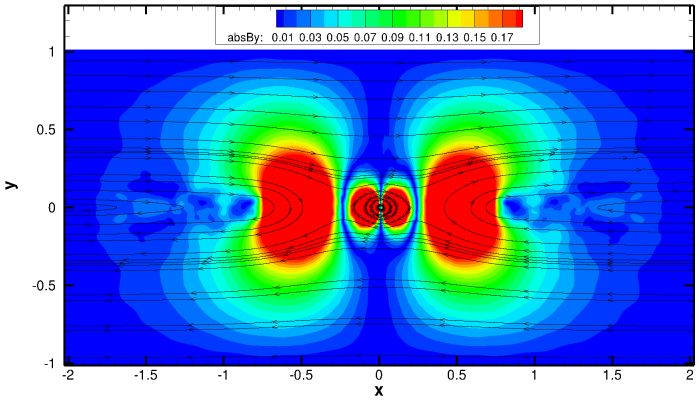

(b) Johnson collision frequency. Normalized magnetic reconnected flux is 1.865.

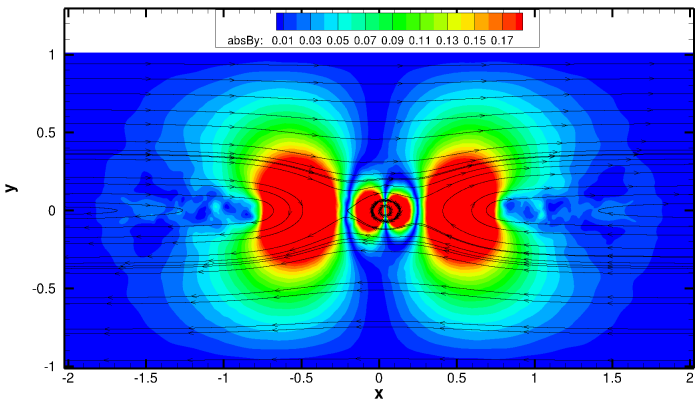

(c) Johnson conditions. Normalized magnetic reconnected flux is 1.839.

Figure 8.36: GEM test case solution comparison with MGLM error cleaning showing $|B_y|$ and magnetic field lines at $t = 18\,\Omega_{ion}^{-1}$ and mesh resolution 1600×800 with changes in collision frequency and initial conditions.

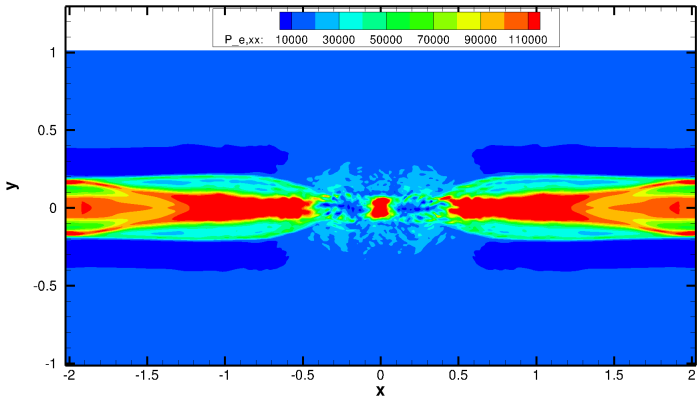

(a) Collision frequency $10^7\,\mathrm{s}^{-1}$. Normalized magnetic reconnected flux is 1.77.

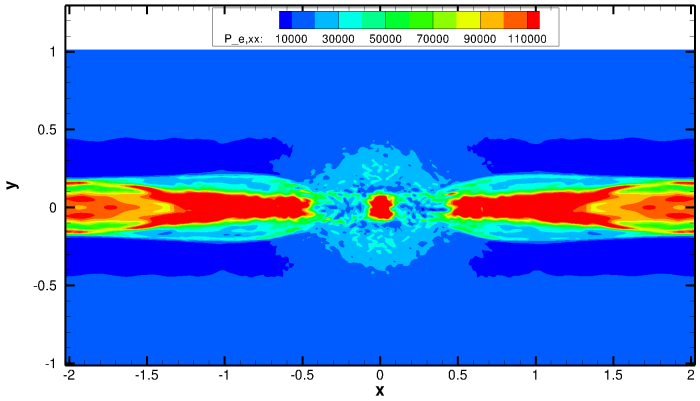

(b) Johnson collision frequency. Normalized magnetic reconnected flux is 1.865.

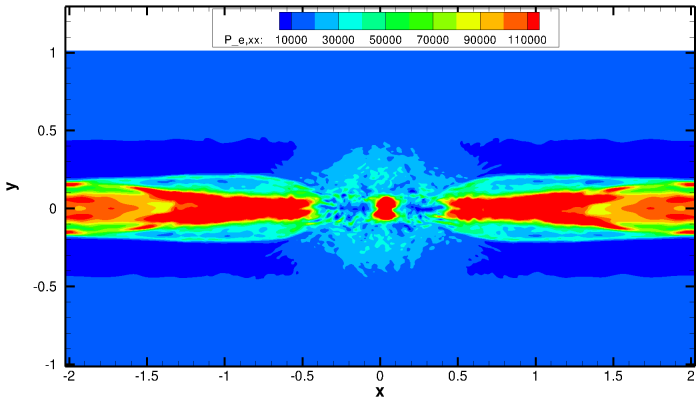

(c) Johnson conditions. Normalized magnetic reconnected flux is 1.839.

Figure 8.37: GEM test case solution comparison with MGLM error cleaning showing $P_{e,xx}$ at $t = 18\,\Omega_{ion}^{-1}$ and a mesh resolution of 1600×800 with changes in collision frequency and initial conditions.

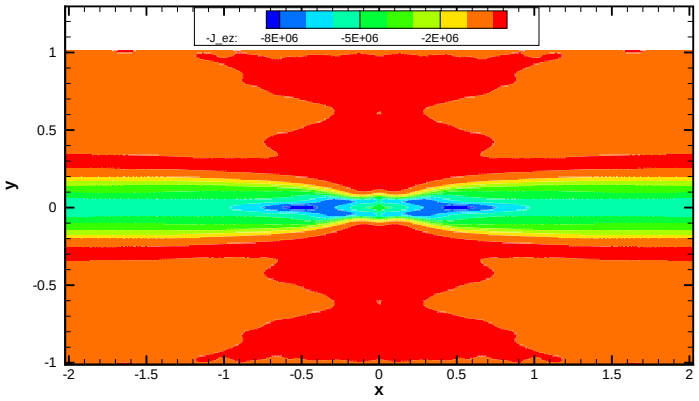

(a) GEM mass ratio $m_{ion}/m_e = 25$. Normalized magnetic reconnected flux is 0.82. Normalized peak to peak diffusion region distance $d_{xe}^{(25)} = 1.37$.

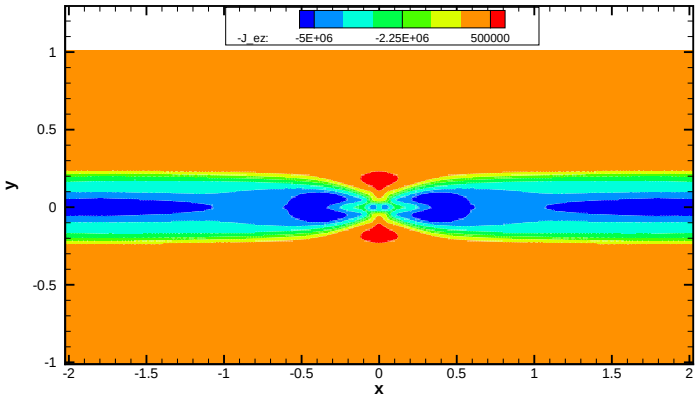

(b) Physical mass ratio $m_{ion}/m_e = 1836$. Normalized magnetic reconnected flux is 1.05. Normalized peak to peak diffusion region distance $d_{xe}^{(Real)} = 0.497$.

Figure 8.38: Comparison of GEM test case solutions with MGLM error cleaning showing $-J_{e,z}$ at $t = 18\,\Omega_{ion}^{-1}$ and a mesh resolution of 400×200.

8.4.8 Effects of Divergence Cleaning Strategies on Numerical Solutions

To assess the quality of the solution obtained, predicted solutions for various combinations of error correction schemes were examined and compared. The error correction combinations examined were FGLM (refer to Section 3.8.4), MGLMED (refer to Section 3.8.5), and no error correction (NGLM). The MGLM scheme (refer to Section 3.8.4) is the error correction used for the base case and was examined in the previous section. Each error correction scheme was examined using the GEM case for a mesh resolution of 1600×800 to a time of $18\,\Omega_{ion}^{-1}$ for the three different constant collision regimes of collisionless ($\nu_s = 0\,\mathrm{s}^{-1}$), transitional ($\nu_s = 10^7\,\mathrm{s}^{-1}$), and fully collisional ($\nu_s = 10^{12}\,\mathrm{s}^{-1}$). Note that solution results could not be obtained in all cases due to instabilities. All obtained results in this section are placed into figures showing either $|B_y|$ with magnetic field lines (Figures 8.39, 8.40 and 8.42) or the electron x-direction pressure (Figures 8.41 and 8.43) and are discussed in the following sections.

FGLM Error Correction Results

As was found by other researchers [7, 65, 66, 73], utilizing a full GLM error correction on the electric and magnetic fields resulted in very unstable results. The results for the collisionless and transitional regimes could not be obtained due to negative energies or densities, however the fully collisional regime could be obtained, but as can be seen from the results of Figure 8.39, the numerical simulation appears to be unstable with a large number of oscillations in the predicted solutions.

MGLMED Error Correction Results

A less strict method of electric field divergence cleaning is achieved using the electric diffusion method, MGLMED, as discussed in Section 3.8.5. Results obtained with this scheme were far more stable than with the FGLM method. Despite this, solutions obtained using MGLMED were less stable than with the MGLM scheme and only the transitional and fully collisional simulations could be completed successfully.

The predicted transitional solutions, Figures 8.40(b) and 8.41(b), are very similar to the MGLM counterparts (Figures 8.40(a) and 8.41(a)), which shows that the effect of charge separation errors on the GEM problem are minimal. These findings agree with what other researchers have found when examining alternate charge separation error cleaning methods related to the Langdon-Marder corrections [7, 66, 70]. This was verified by examining the charge separation

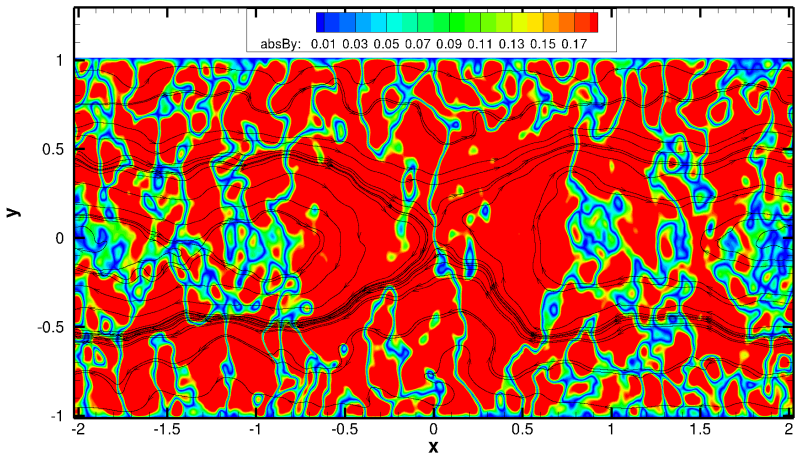

Figure 8.39: GEM test case solution with Full GLM cleaning showing $|B_y|$ and magnetic field lines at $t = 18\,\Omega_{ion}^{-1}$ and a mesh resolution of 1600×800 with collision frequency $10^{12}\,\mathrm{s}^{-1}$.

errors for the MGLM and MGLMED solutions, where in the MGLM solution the errors are high, but concentrated, while in the MGLMED solutions, the errors are negligible. The variance in the magnetic reconnected flux is around 4% between the two solutions. This is expected as altering the error cleaning of the Maxwell's equations may produce differences in the final magnetic fields. Even so, the differences are fairly minor.

Figure 8.44 depicts the predicted magnetic reconnected flux versus x-direction grid resolution for the MGLMED scheme based on the base case collision frequency of $\nu_s = 10^7\,\mathrm{s}^{-1}$. The magnetic reconnected flux approaches a value of 2, like the MGLM case; however, at extremely high resolutions, the MGLMED scheme becomes increasingly unstable and the results became unreliable and is reflected in the final data point of the plot.

The fully collisional cases depicted in Figures 8.42(b) and 8.43(b) are nearly identical to the MGLM versions. The magnetic reconnection value is also very close to the MGLM result and reflects the disappearance of the magnetic island in the drastic reduction in reconnection as compared with the NGLM results. The added stability of the fully collisional scheme contributes to the convergence of both the MGLM and MGLMED solutions.

No Error Correction Results

As with the MGLMED solutions, when there is no error correction, the solution for the collisionless regime could not be obtained due to the instabilities which caused non physical solutions.

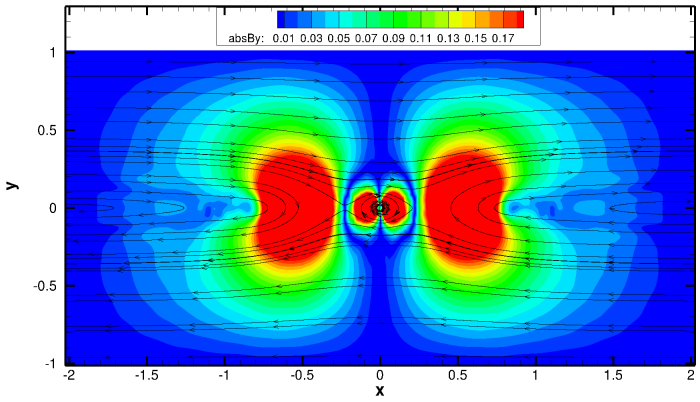

(a) MGLM error correction. Normalized magnetic reconnected flux is 1.77.

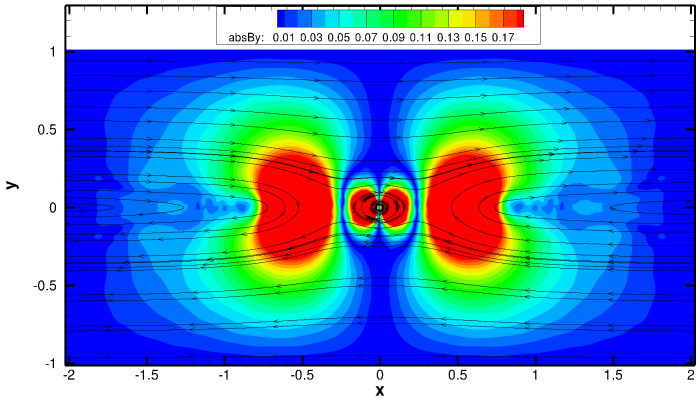

(b) MGLMED error cleaning. Normalized magnetic reconnected flux is 1.84.

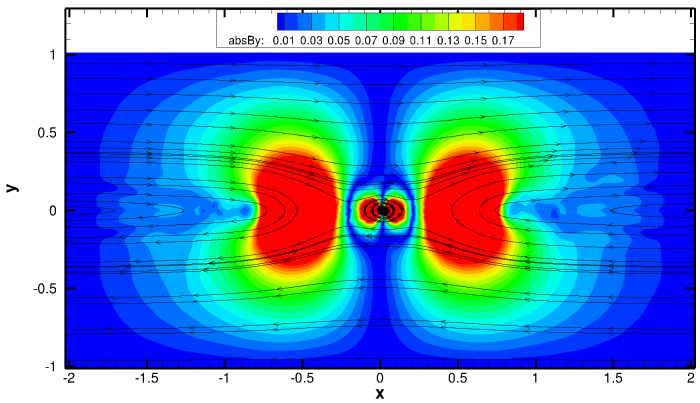

(c) No error cleaning. Normalized magnetic reconnected flux is 1.722.

Figure 8.40: GEM test case solution with MGLM, MGLMED and NGLM error cleaning showing $|B_y|$ and magnetic field lines at $t = 18\,\Omega_{ion}^{-1}$ and a mesh resolution of 1600×800 with collision frequency $10^7\,\mathrm{s}^{-1}$.

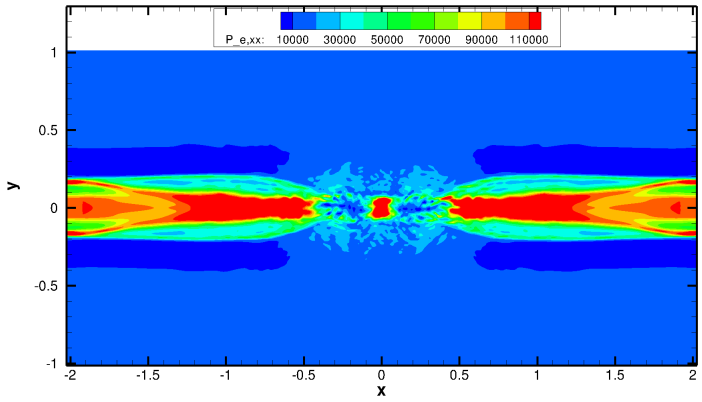

(a) MGLM error correction. Normalized magnetic reconnected flux is 1.77.

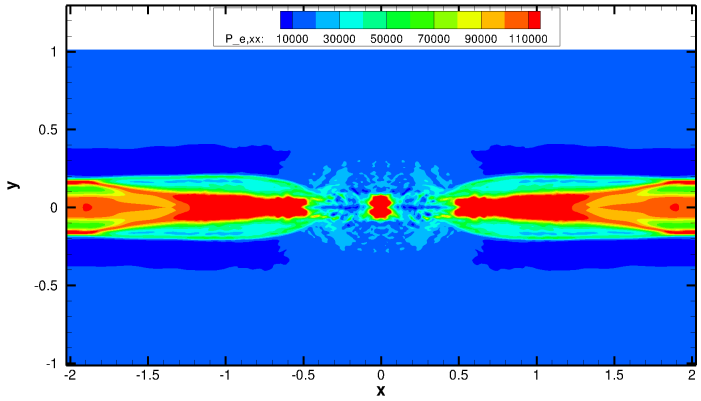

(b) MGLMED error cleaning. Normalized magnetic reconnected flux is 1.84.

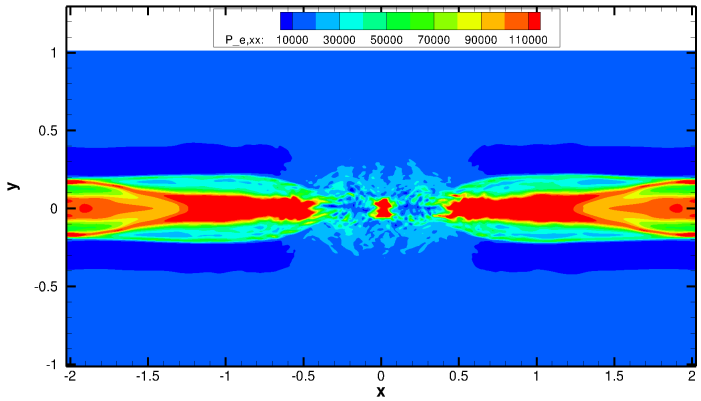

(c) No error cleaning. Normalized magnetic reconnected flux is 1.722.

Figure 8.41: GEM test case solution with MGLM, MGLMED and NGLM error cleaning showing $P_{e,xx}$ at $t = 18\,\Omega_{ion}^{-1}$ and a mesh resolution of 1600×800 with collision frequency $10^7\,\mathrm{s}^{-1}$.

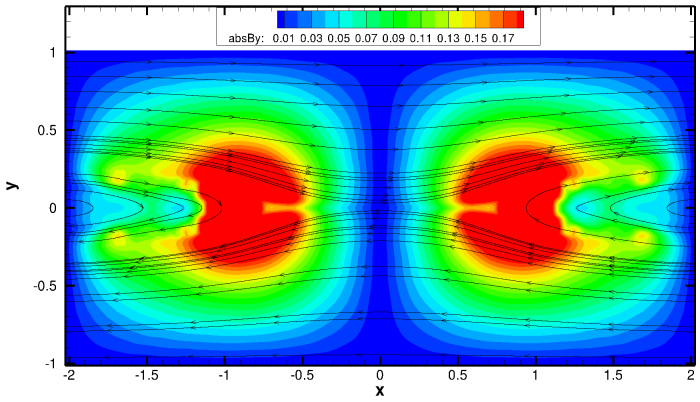

(a) MGLM error correction. Normalized magnetic reconnected flux is 1.433.

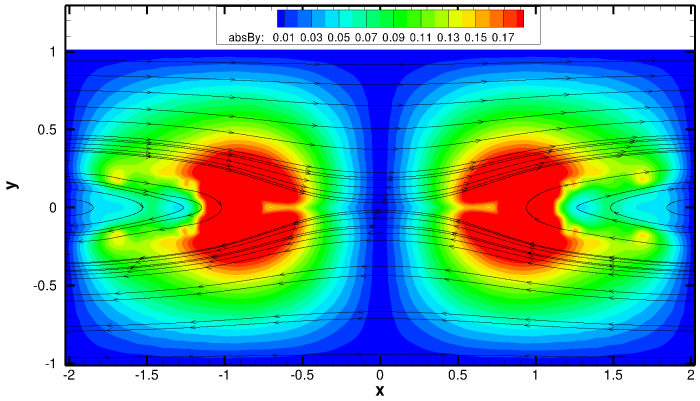

(b) MGLMED error cleaning (MGLMED). Normalized magnetic reconnected flux is 1.436.

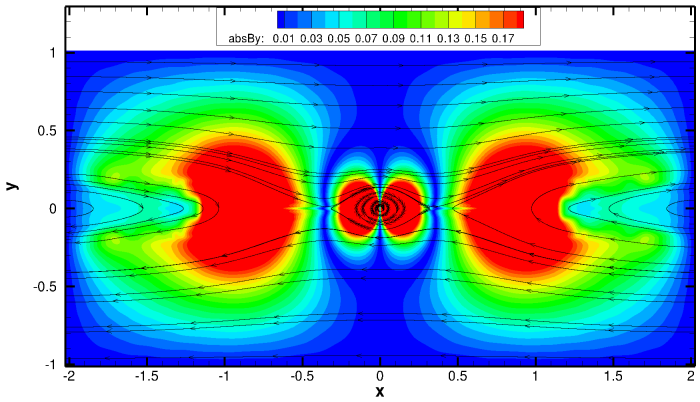

(c) No error cleaning. Normalized magnetic reconnected flux is 2.341.

Figure 8.42: GEM test case solution with MGLM, MGLMED and NGLM error cleaning showing $|B_y|$ and magnetic field lines at $t = 18\,\Omega_{ion}^{-1}$ and a mesh resolution of 1600×800 with a constant collision frequency of $10^{12}\,\mathrm{s}^{-1}$.

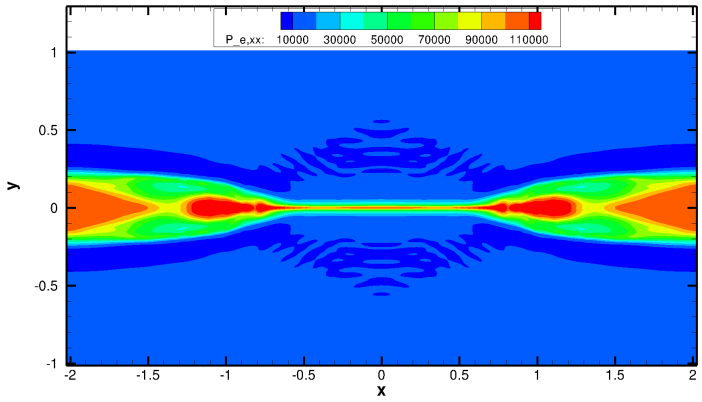

(a) MGLM error correction. Normalized magnetic reconnected flux is 1.433.

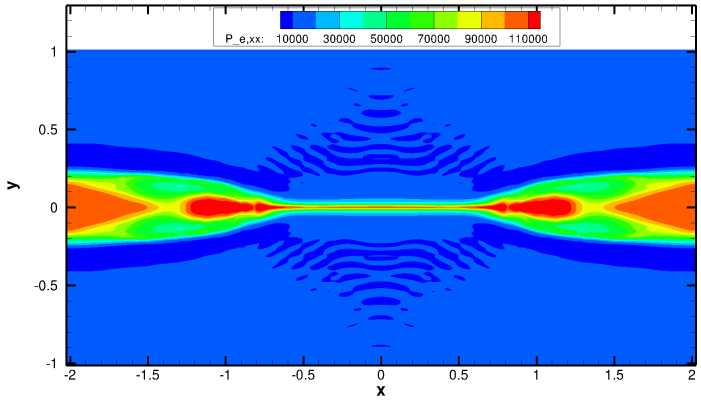

(b) MGLMED error cleaning. Normalized magnetic reconnected flux is 1.436.

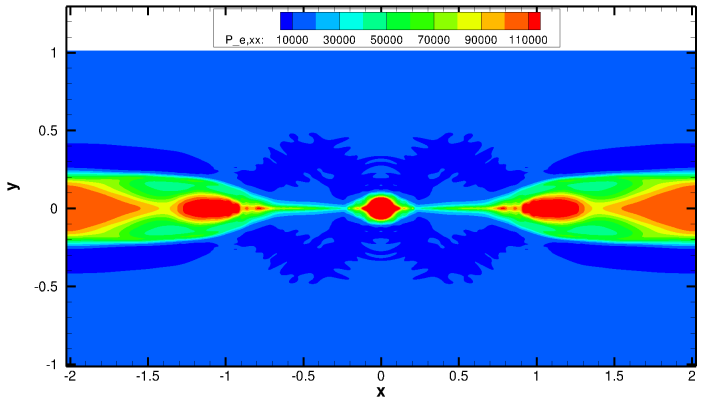

(c) No error cleaning. Normalized magnetic reconnected flux is 2.341.

Figure 8.43: GEM test case solution with MGLM, MGLMED and NGLM error cleaning showing $P_{e,xx}$ at $t = 18\,\Omega_{ion}^{-1}$ and a mesh resolution of 1600×800 with a constant collision frequency of $10^{12}\,\mathrm{s}^{-1}$.

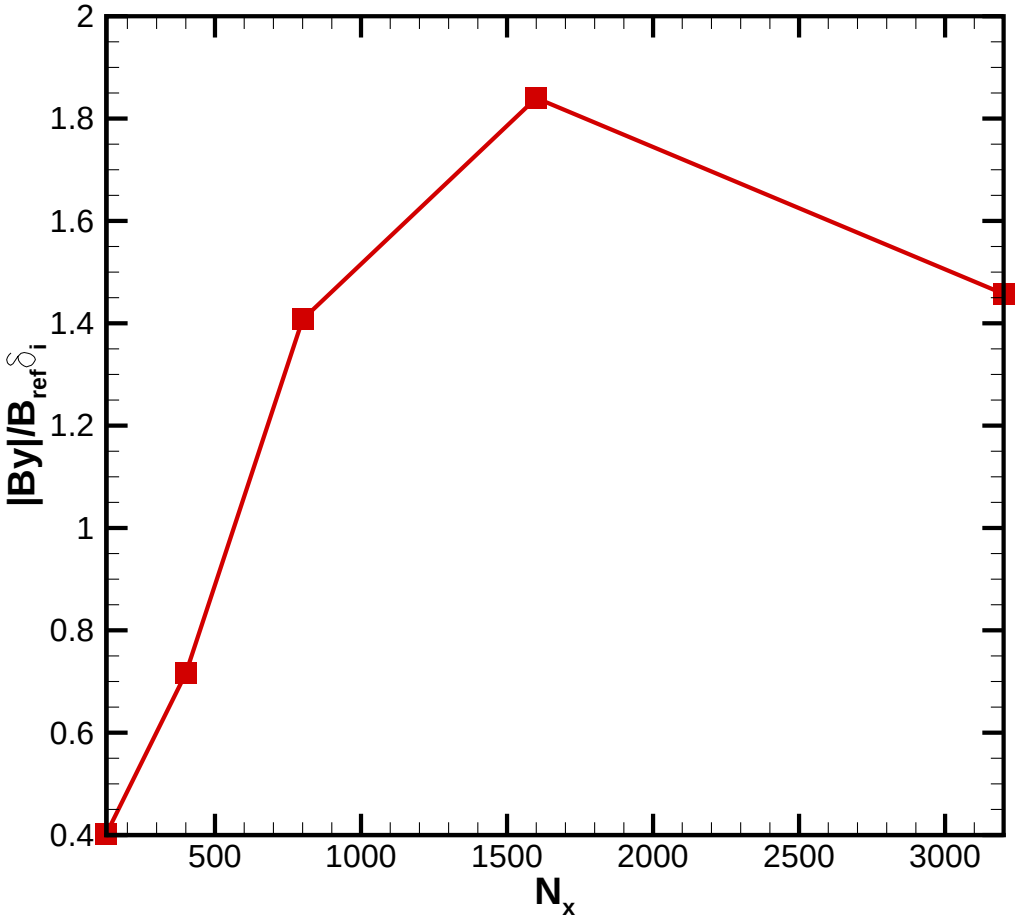

Figure 8.44: Convergence plot of normalized magnetic reconnected flux versus x-direction resolution for GEM test case at $t = 18\,\Omega_{ion}^{-1}$ for the MGLMED error correction.

Solutions were obtained for the transitional and fully collisional regimes. Once again, the predicted transitional regime solutions for NGLM differs very little compared to the MGLMED and MGLM counterparts as can be seen in Figures 8.40(c) and 8.41(c). The predicted magnetic reconnected flux is similar to that of the MGLM scheme, but is consistently lower, as can be seen by the magnetic reconnected flux versus x-direction grid resolution convergence plot, Figure 8.45, which approaches 1.7 instead of 2 as in the MGLM case. There is also additional instability at higher mesh resolutions when there is no error cleaning.

A surprising development occurs when the fully collisional regime with no error correction is examined. As can be seen in Figures 8.42(c) and 8.43(c), the magnetic island remains at the center, instead of disappearing as in the other schemes. Despite the existence of the magnetic island, other elements of the fully collisional case from the other schemes remain such as the very large magnetic reconnection region. This, combined with the magnetic island results in a very large value for the reconnection flux of 2.341. This finding indicates a few things. First, the larger reconnection region and characteristic pressure profile (except at the magnetic island) is largely driven by fluid mechanical factors instead of the form of Maxwell's equations. Further, the magnetic island tends to appear when the simulation is less stable. Exploring the origins of the magnetic island would be of some interest and is discussed further in the future work section of the next chapter.

8.4.9 Summary of Findings

The major conclusions arising from this section of the thesis dealing with the GEM case results are summarized here. As was previously found by all researchers that have commented on the matter, the magnetic reconnection does not seem to be affected greatly by the underlying fluid dynamics. Varying fluid parameters, such as mass, isotropization and collisions, do not contribute greatly to changes in the reconnected fluxes when the solution procedures are the same [2, 3, 54, 65, 71, 189]. As was also found by most other researchers [7, 66], enforcing the solenoidal condition through divergence cleaning of the magnetic field errors results in the most stable solutions, while aggressive charge separation error cleaning results in generally unstable solutions. Using a Langdon-Marder diffusive error cleaning scheme (MGLMED) [7,66,70] results in a stable solution to the GEM case, but does not result in a significantly different solution over the MGLM scheme and results in an overall less stable solution.

Collisions, though not strictly physical for the GEM conditions, results in solutions for the GEM case which are more stable. Simulations with transitional collision frequencies results in predictions that resemble closely those of the collisionless results, but exhibit greater stability.

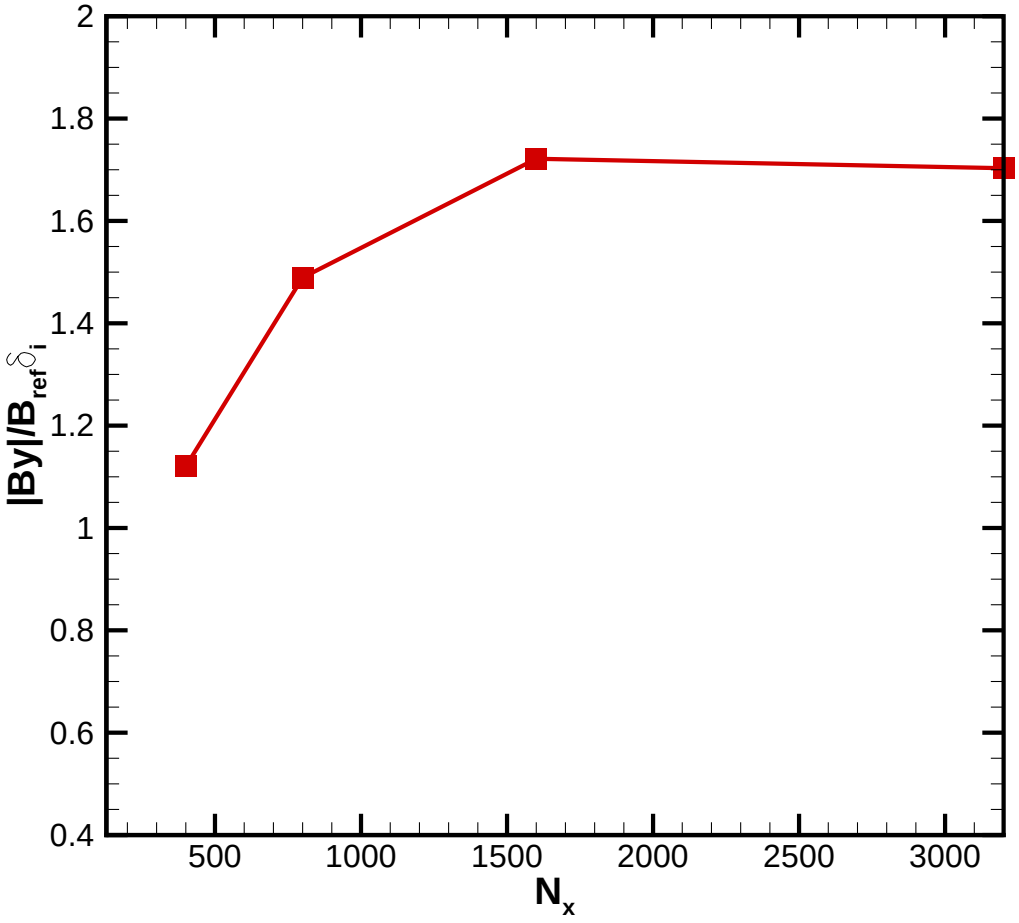

Figure 8.45: Convergence plot of normalized magnetic reconnected flux versus x-direction resolution for GEM test case at $t = 18\,\Omega_{ion}^{-1}$ for no error correction.

It was found that the grid resolution has the greatest effect on the predicted values of the magnetic reconnected flux. The influence of mesh resolution was observed to be greater than other parameters and even divergence error correction schemes used. However, the reconnected flux appears to show convergence at very high mesh resolutions. The results of the mesh resolution study presented here also suggests that most solutions in the literature may not be fully converged solutions. The requirements for high resolution meshes when simulating plasmas in general has been noted by other researchers [3, 47, 65, 134].

Qualitatively, the solutions presented in this chapter agree well with the majority of the solutions in the literature, and also reproduce the reconnected fluxes of PIC simulations [2, 54, 189] for lower computational cost, but at higher mesh resolutions. A comparison of the temporal evolution of the predicted magnetic reconnection between the MMHDGLM2D model and the full PIC simulations [3] agree well for a low and high resolution mesh. The final reconnected flux value is affected by mesh resolutions. The results from Darwin-Vlasov simulations [4, 5] also agree well with the solutions obtained with the MMHDGLM2D numerical procedure for similar resolutions and the out of plane currents match very well, while computationally the MMHDGLM2D model is significantly cheaper. The relatively small computational effort of the MMHDGLM2D model has allowed the generation of very high mesh resolution solutions of the GEM test case. The differences that are seen in the reconnected fluxes and plasma solutions could be a result of the set of equations used, as well as the numerical approached employed, as many have commented that significant changes can and do result from these differences [2, 4, 5, 38, 71].

It is up to debate whether the magnetic island observed in some results is a physical structure or a result of mathematical or computational artefacts. Magnetic islands appear in solutions with very little collisions, higher mesh resolutions, or from a lack of error cleaning, which all characteristically results in less stable solutions. On the other hand, the MGLM scheme, which seems to produce the most stable results, reduces the occurrence of the magnetic island. Note that the divergence error cleaning has a dissipative effect on the overall scheme which contributes to a reduction in the unstable oscillatory behaviour. Increasing the collision frequency also generally reduces oscillatory behaviour and results in a reduction of the occurrence of the magnetic island except when there is no error cleaning. The relationship between properties that affect the stability of the simulations and the occurrence of the magnetic island has been observed in other studies [28, 54, 63, 66, 188]. Further, Kuznetsova *et al.* [54] attributed the magnetic island to PIC instabilities and observed they reduce with an increase in isotropic effects. Others have studied the role of turbulence in the formation of magnetic islands [191]. A higher-order time and space algorithm also eliminated a low mesh resolution magnetic island as

found by Loverich *et al.* [63] which also illustrates the possible numerical origin of the magnetic island. The seemingly random, asymmetric motion observed in this study and also by other researchers above seems to indicate that many factors can cause the formation and evolutions of the magnetic island.

8.5 Numerical Results for LEO GEM Case

An initial high resolution solution for the LEO GEM case of Section 8.3.1 was obtained at 1600×800 cells using realistic self collisions, but without reactions or inter-particle collisions. The MGLM error correction scheme was used. The results of this simulation can be seen in Figures 8.46 and 8.47, which shows $|B_y|$ with magnetic field lines and the x-direction electron pressure, respectively. This case was slightly unstable with some wave-like numerical instabilities manifesting in the magnetic field. This case was also stiffer, resulting in a 2400% increase in computational time over the base GEM case. The limiting time scale for this problem, and also for the magnetopause GEM case, changed from the error advection (which is set to be 5% faster than the set speed of light in the GEM case), to the upper hybrid frequency due to the now significantly smaller electron mass. This is consistent with PIC simulations where plasma frequencies are often the limiting time scales [140]. This case has very similar characteristics to the base GEM case along with the formation of a magnetic island that is moving towards the right lobe. The normalized magnetic reconnected flux, which is once again the integration of the $|B_y|$ magnetic field along the x-axis across the entire domain divided by 2, is close to that expected at 1.238. Because of the instability, despite running at a TSCF of only 0.1, a lower resolution case was examined for further investigations.

A second case was considered at a mesh resolution of 400×200 which was far more stable. The results of this simulation are presented in Figures 8.48 and 8.49. Once again similar structures are observed with a very small magnetic island forming. The reconnected flux is quite low at 0.331, and a lower reconnection rate is expected as in the original GEM case. In order to investigate the effect of interparticle collisions and reactions, this case was again examined at the 400×200 grid resolution and MGLM correction, but with both inter- and intra-particle collisions enabled as well as charge exchange and ionization-recombination reactions. The results can be seen in Figures 8.50 and 8.51 which shows $|B_y|$ with magnetic field lines and the x-direction electron pressure, respectively. As was expected at these conditions, the effects of the reactions and interparticle collisions were very small. The time scales for the reactions are at least ten million times that of the limiting time scale due to the rarefied nature of the plasma. Although the distribution of the magnetic field was slightly different, it was not

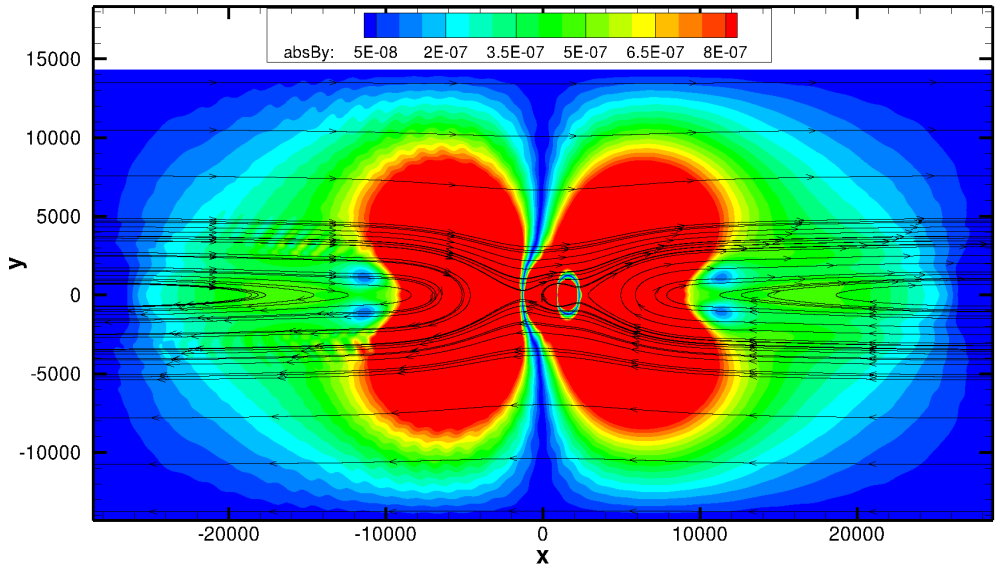

Figure 8.46: LEO GEM test case solution with MGLM error cleaning showing $|B_y|$ and magnetic field lines at $t = 18\,\Omega_{ion}^{-1}$ and a mesh resolution of 1600×800. Normalized magnetic reconnected flux is 1.238.

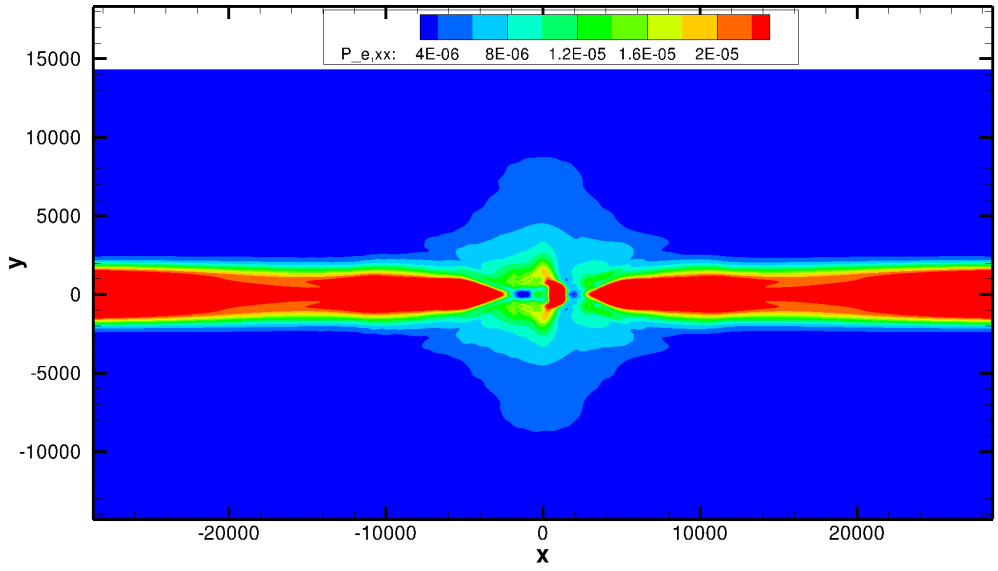

Figure 8.47: LEO GEM test case solution with MGLM error cleaning showing $P_{e,xx}$ at $t = 18\,\Omega_{ion}^{-1}$ and a mesh resolution of 1600×800. Normalized magnetic reconnected flux is 1.238.

enough to change the reconnected flux significantly, which is indicated slightly lower at 0.330. The reduction in normalized magnetic reconnected flux, in general, is expected as was found by others when moving towards the real electron mass [2, 70, 189]. Clearly, the conditions are essentially collisionless in reaction and interparticle collisions as is expected [74]. The stiffness of the problem was also expected as moving to the physical electron/ion mass ratio increases the stiffness of the problem by an exponential factor [189].

8.6 Numerical Results for Magnetopause GEM Case

The magnetopause GEM case of Section 8.3.2 was found to be extremely stiff, resulting in more than a three order magnitude increase in computational effort to perform the simulation compared to the original and LEO GEM case. Once again, the TSCF had to be reduced to 0.1. The reduction in TSCF was due to increased instability from the more fully collisionless and rarefied case. This resulted in not being able to obtain a high resolution solution due to the added computational cost and instability. A test case with a resolution of 384×192 was obtained, and the results for this case at the standard time of $t = 18\,\Omega_{ion}^{-1}$ are shown in Figures 8.52 and 8.53 for $|B_y|$ with magnetic fieldlines and the electron pressure in the x-direction, respectively. Once again, the solution has many of the features of the GEM and LEO GEM case though with a smaller normalized magnetic reconnected flux value. The even smaller reconnected flux value over the LEO GEM case can be attributed to the fact that the speed of light is not constant to the reference values. The domain for this problem is significantly larger and so could change the expected behaviour of electromagnetic waves as travel times change across the domain.

An even lower resolution case was examined to verify the unconverged nature of the solution. A mesh resolution of 192×96 was examined for the magnetopause GEM case. The results are presented in Figure 8.54 and 8.55 for $|B_y|$ with magnetic fieldlines and the electron pressure in the x-direction, respectively. The normalized magnetic reconnected flux is significantly lower and it is clear that the results are not converged at this resolution.

8.7 LEO GEM Case Results with NKS Implicit Time Marching Scheme

The LEO GEM case of Section 8.3.1 presented a problem that was significantly stiffer than the original GEM case making it an ideal candidate for the NKS dual-time scheme. A small

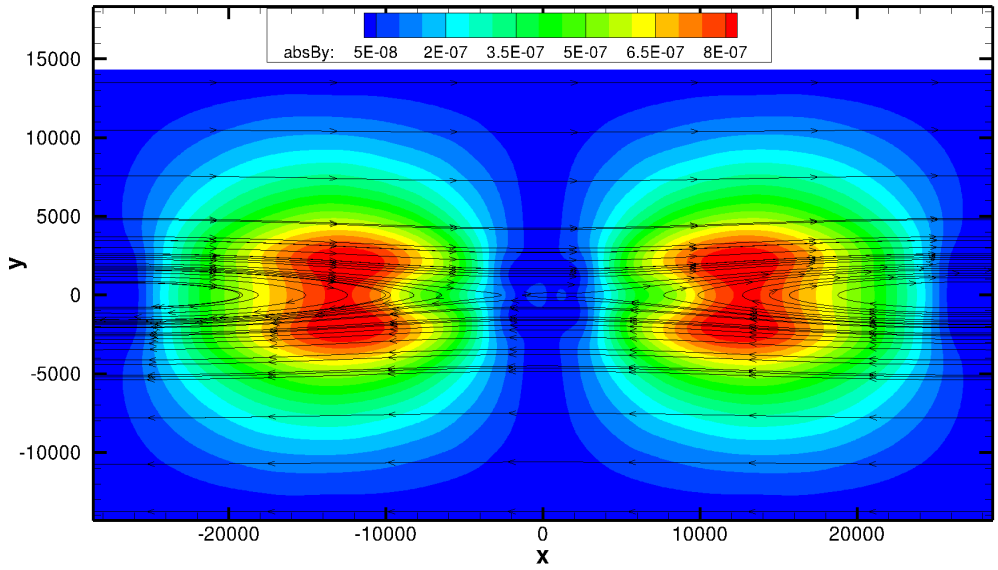

Figure 8.48: LEO GEM test case solution with MGLM error cleaning showing $|B_y|$ and magnetic field lines at $t = 18\,\Omega_{ion}^{-1}$ and a mesh resolution of 400×200. Normalized magnetic reconnected flux is 0.331.

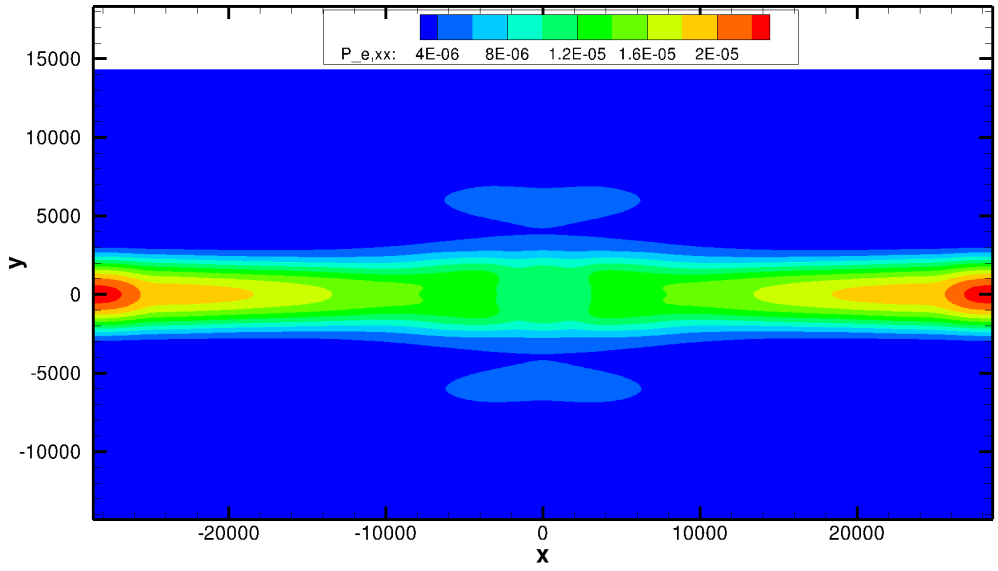

Figure 8.49: LEO GEM test case solution with MGLM error cleaning showing $P_{e,xx}$ at $t = 18\,\Omega_{ion}^{-1}$ and a mesh resolution of 400×200. Normalized magnetic reconnected flux is 0.331.

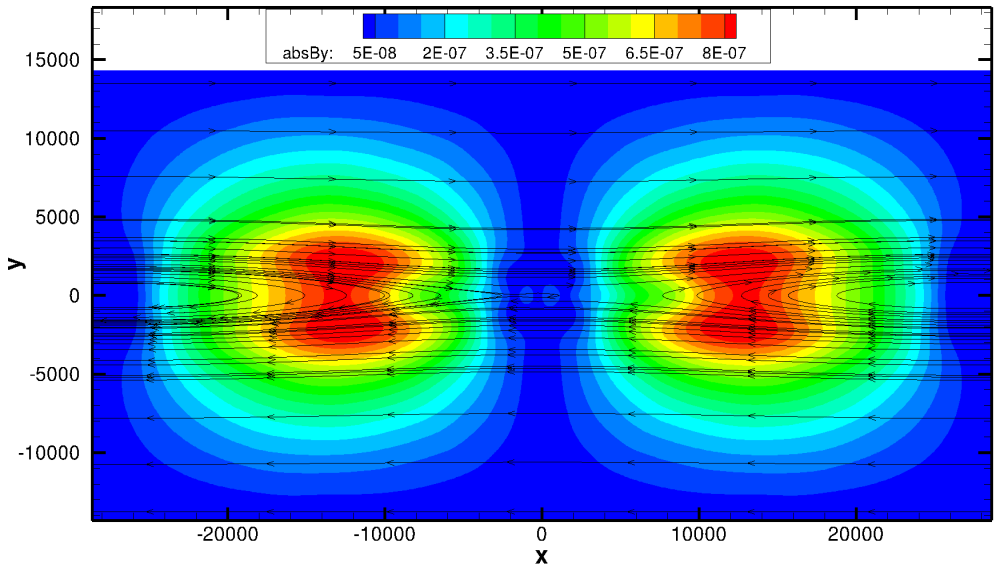

Figure 8.50: LEO GEM test case solution with MGLM error cleaning showing $|B_y|$ and magnetic field lines at $t = 18\,\Omega_{ion}^{-1}$ and a mesh resolution of 400×200 including reactions and interparticle collisions. Normalized magnetic reconnected flux is 0.330.

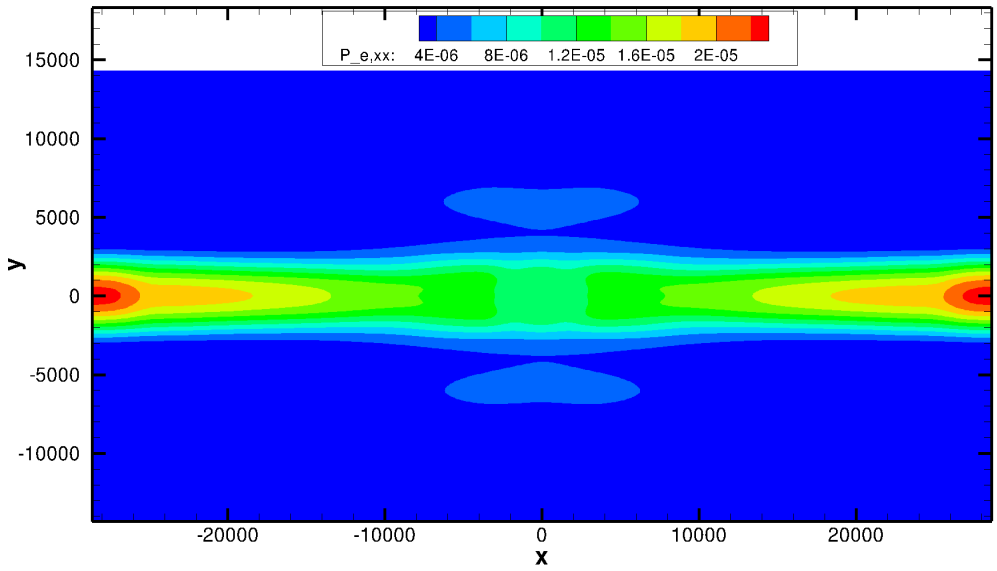

Figure 8.51: LEO GEM test case solution with MGLM error cleaning showing $P_{e,xx}$ at $t = 18\,\Omega_{ion}^{-1}$ and a mesh resolution of 400×200 including reactions and interparticle collisions. Normalized magnetic reconnected flux is 0.330.

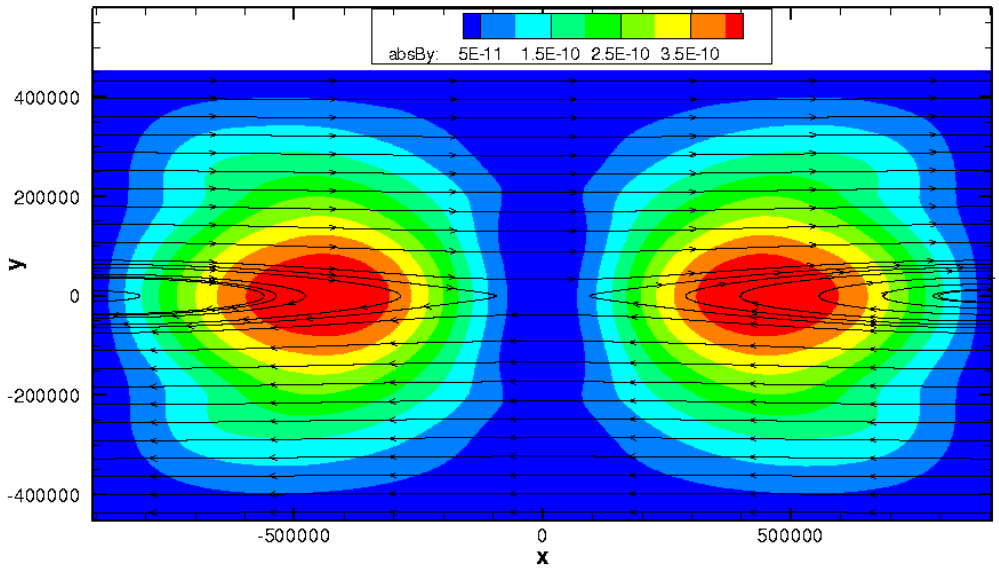

Figure 8.52: Magnetopause GEM test case solution with MGLM error cleaning showing $|B_y|$ and magnetic field lines at $t = 18\,\Omega_{ion}^{-1}$ and a mesh resolution of 384×192. Normalized magnetic reconnected flux is 0.232.

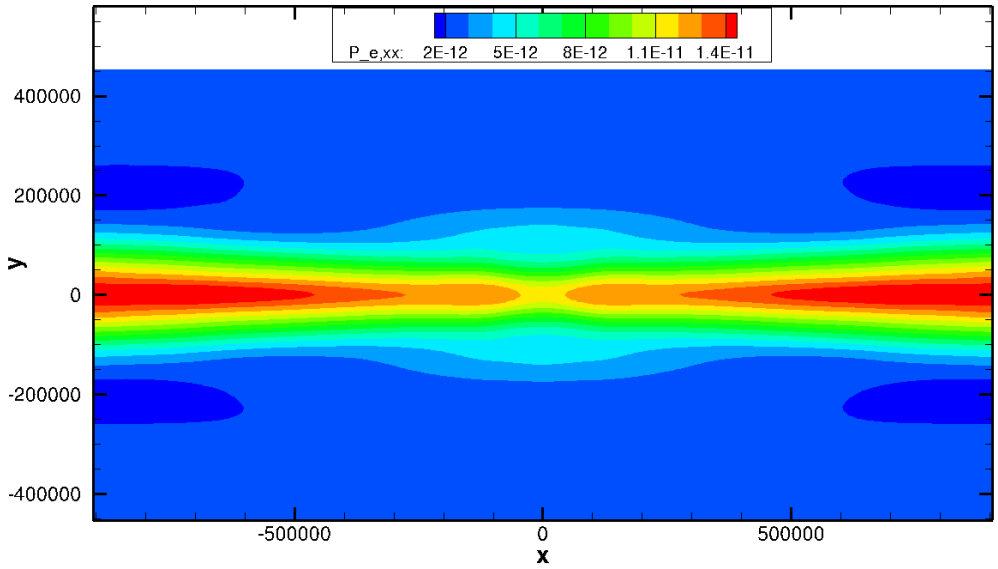

Figure 8.53: Magnetopause GEM test case solution with MGLM error cleaning showing $P_{e,xx}$ at $t = 18\,\Omega_{ion}^{-1}$ and a mesh resolution of 384×192. Normalized magnetic reconnected flux is 0.232.

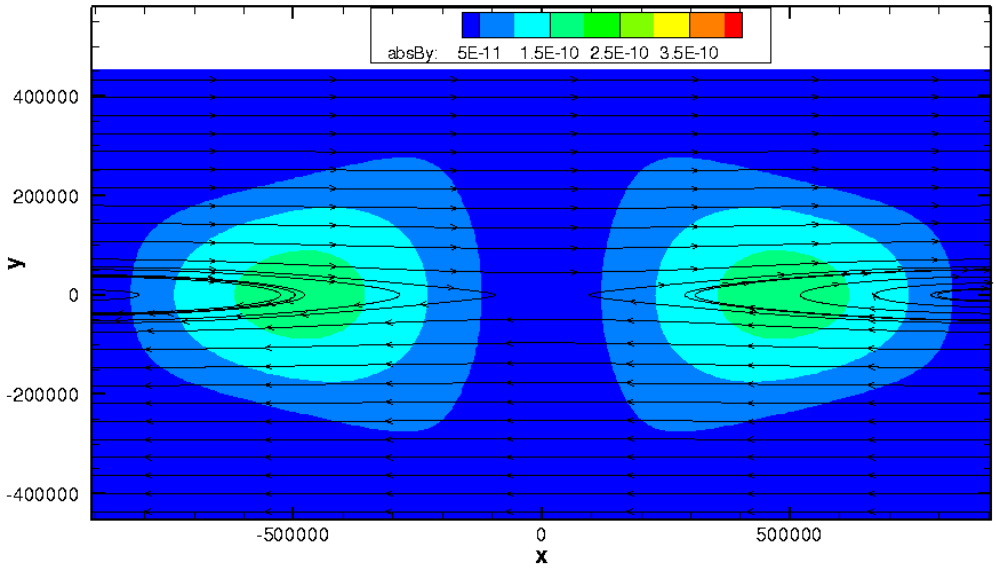

Figure 8.54: Magnetopause GEM test case solution with MGLM error cleaning showing $|B_y|$ and magnetic field lines at $t = 18\,\Omega_{ion}^{-1}$ and a mesh resolution of 192×96. Normalized magnetic reconnected flux is 0.087.

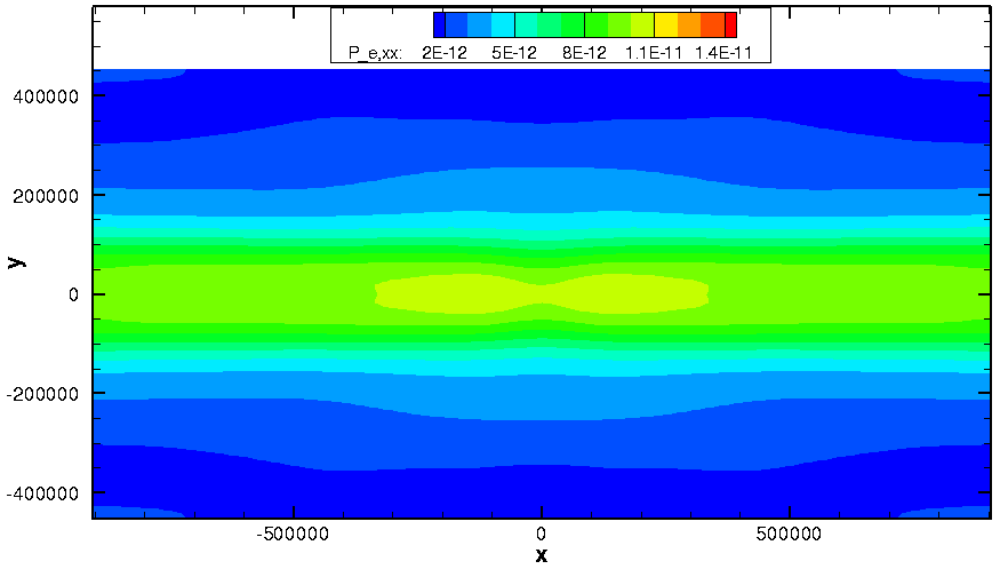

Figure 8.55: Magnetopause GEM test case solution with MGLM error cleaning showing $P_{e,xx}$ at $t = 18\,\Omega_{ion}^{-1}$ and a mesh resolution of 192×96. Normalized magnetic reconnected flux is 0.087.

Table 8.3: Comparison of MGLM Realistic LEO GEM case at 128×64 resolution

Scheme	TSCF	CPU Time	$\lvert B_{\text{rec}} \rvert$ (T · m)
Explicit	0.3	2732	1.264×10^{-2}
NKS Godunov	25	1125	1.264×10^{-2}
NKS Godunov	50	921.2	1.263×10^{-2}
NKS Neglected	25	5319	1.264×10^{-2}
NKS Neglected	50	-	-

sample problem of 128×64 cells was used in order to eliminate Schwarz preconditioning issues, which was found to be a significant obstacle in simulating the GEM problem using the NKS scheme. The Schwarz preconditioning issue is discussed further in the future work Section 9.2 of the last chapter of the thesis. Using MGLM error correction and particle collisions, the computational times for the various simulations are included in Table 8.3. The system with no residual Jacobian (neglected) on the block right preconditioner of the NKS Maxwell's equations as discussed in Section 6.7.2 did not converge at a TSCF of 50. As can be seen, the NKS dual-time scheme with the Godunov approximate Jacobian for the Maxwell's equations has a significant advantage over both the non-preconditioned and explicit method with no degradation in reconnected flux results. The NKS scheme did not perform as well with the original GEM case. It is theorized that the stiffer LEO case gave an advantage to the preconditioned system, since with the smaller time step needed for the LEO case, the LHS preconditioning matrix becomes diagonally dominant and compensates for the singular nature of the preconditioning matrix as mentioned in Section 6.7.2. NKS seems to excel at stiff systems when not heavily Schwarz preconditioned as seen in Chapter 7. It was found that the optimal ratio of diagonal dominance was approximately constant for the highest TSCF for a converging preconditioned system regardless of the preconditioning type.

8.8 Discussion of Results for the Realistic GEM Cases

The findings from the two realistic GEM cases were somewhat to be expected with the increased computational difficulty and lower reconnected flux when going to the real electron-ion mass ratio and speed of light as was found in the literature [2, 70, 189]. These factors, and the more collisionless regime using physical gas properties, resulted in significantly less stable solutions. The computational difficulty and reduced stability made obtaining high mesh resolution solutions difficult, and beyond the scope of this thesis. The realistic GEM cases examined here are

deemed to be not fully grid converged. Obtaining a stable high mesh resolution solution would be desirable in future studies, but a more effective implementation of the NKS scheme would be essential. Adaptive mesh refinement may also be a way to obtain a converged high mesh resolution solution and is recommended for future follow-on studies.

Chapter 9

Conclusions and Future Work

9.1 Concluding Remarks

In this thesis, a new model for predicting the flow and behaviour of multispecies, anisotropic, non-equilibrium, multi-temperature, partially ionized, plasmas was proposed and developed using extended fluid dynamics. Additionally, a finite-volume numerical solution procedure was developed for the multifluid non-equilibrium plasma model. The combined approach was shown to offer significant computational advantages over direct particle simulation techniques, while recovering known solutions to the particle simulations and other published results.

The multifluid MHD model consisted of three plasma species (ion, electron, neutral) that takes into consideration pressure and temperature anisotropies by making use of a 10-moment, Gaussian moment closure. The non-equilibrium collisional processes are modelled using a BGK collision approximation. A full set of Maxwell's equations is included with GLM and Langdon-Marder divergence error cleaning schemes for treating the electro-magnetic field errors and are coupled to the plasma species equations through the source terms. Chemical kinetic mechanisms are used to model the plasma reactions, including charge exchange and ionization-recombination. The separation of the plasma species equations and the Maxwell's equations with coupling through the source terms allows for flexibility in the problems that can be considered with the MMHD model and can include large temperature anisotropies and differences in plasma species flows as well as being able to simulate very high to low density plasma species and strong to weakly magnetized plasmas.

The numerical solution procedure made use of a Godunov-type upwind finite-volume discretization scheme. The Godunov-type scheme used here is second-order in time and space and makes

use of an HLLE and Godunov numerical flux function to solve the Riemann based fluxes for the fluid and Maxwell's equations, respectively. A block-based domain decomposition scheme is used to partition the problem for large-scale parallel computation. Two time marching schemes are considered: A standard explicit method and an implicit scheme. The explicit numerical solution procedure is a second-order predictor-corrector scheme. The implicit scheme made use of a NKS algorithm with GMRES to solve the system of equations for each Newton step. The implicit numerical solution procedure is used for steady problems, or unsteady problems with a second-order backwards difference time integration in a dual-time formulation making use of the NKS algorithm to solve each physical time step sub-problem.

The mathematical properties of the multifluid MHD model were examined through a dispersion analysis. The system of equations were shown to be hyperbolic, and the semi-discrete form of the equations were found to be suitable for solution by Godunov-type finite volume schemes. The numerical solution procedure for the multifluid MHD model was evaluated through various accuracy assessment test cases for both steady and unsteady problems using both the explicit and implicit solution procedures. The error correction schemes for the Maxwell's equations was found to effectively clean errors arising from the divergence of the electric and magnetic fields. Further comparisons were made with 1D solutions from a 1D multifluid MHD model and 2D non-magnetized flows. The scheme produced second-order solutions in time and space, recovered known 1D multifluid MHD and 2D non-magnetized results, and the implicit scheme provided significant computational performance improvements over the explicit scheme for the cases considered during evaluation and validation.

To explore the computational capabilities of the proposed multifluid MHD model, the GEM problem was examined along with various modified versions including the LEO and magnetopause versions. It was shown that the multifluid MHD scheme is able to recover results from the literature generated by PIC schemes and Darwin-Vlasov simulations with significantly less computational cost. Simulated results were found to be close to other multi-fluid models. Due to the relative low computational cost of the scheme, high mesh resolution results were able to be obtained. A grid convergence study was also performed showing convergence of the magnetic reconnected flux at high mesh resolutions. It was found that at unconverged mesh resolutions, the greatest factor that affected the magnetic reconnection was the grid resolution, and not other factors such as the collisions or electron-ion mass ratios. The GEM case was examined using the implicit dual-time NKS scheme which shows promise, however the computational advantages of the scheme were not consistent in all the GEM cases examined.

The original contributions of the thesis include:

- A multifluid MHD model based on the 10-moment Gaussian closure capable of simulating anisotropic temperatures and pressures, with a full modelling of Maxwell's equations with divergence error cleaning, along with collisional and reaction processes was developed.
- A computationally tractable, second-order, numerical solution procedure was developed for one- and two-dimensions using a Godunov-type upwind finite-volume scheme with HLLE and Godunov numerical flux functions.
- Dispersion analysis of the two-fluid plasma subset of the MMHD model.
- Application of implicit temporal limiting in mitigating numerical oscillations in the 1D MMHD model.
- Development of an early two-dimensional implicit NKS scheme for the MMHD model and application to sample test problems and the GEM challenge.
- The developed MMHD model and numerical solution procedure was applied to the GEM challenge, with a grid convergence study and the effect of various error correction schemes and collisional regimes was explored.
- Application of the MMHD model and numerical solution procedure to physical electron/ion masses and LEO and magnetopause plasma conditions.

9.2 Future work

9.2.1 Adaptive Mesh Refinement

One avenue of research that should be considered is adaptive mesh refinement or AMR [192]. AMR is a procedure by which a mesh can be refined in areas that require higher mesh resolutions to resolve features of the simulation, while keeping the rest of the computational domain in a coarser, lower computational load, mesh resolution. As was mentioned in various parts of this work and by other researchers [3, 39, 43, 47, 63, 65, 65, 66, 134], high resolutions are required to resolve many plasma flows. AMR can help alleviate the computational difficulties that come with the need for high resolutions as well as reducing the number of total computational domains to support the high resolutions. A good candidate for future research, is the block-based AMR that uses physics-based refinement criteria similar to the schemes developed by Groth *et al.* [147], Northrup *et al.* [131, 193, 194], Charest *et al.* [157, 195, 196] and Gao *et al.* [153]. This type of AMR would be a good fit for the parallel block based implementation of the MMHD numerical solution procedure. Further, an anisotropic AMR scheme has also been

developed [197–199] which could prove useful particularly with magnetized, anisotropic flows. There are also avenues for choosing physics-based refinement criteria for plasmas, such as those proposed by Powell [200]. Additionally, more recent output- or error-based AMR methods such as the methods developed by Narechania *et al.* [201] and Ngigi *et al.* [202] would also be worth considering.

9.2.2 Physical Partially Ionized Transitional Test Cases

Though various parts of the multifluid MHD model were exercised in the current work, a test case that challenges all aspects of the model, including reactions, and large species anisotropies at once should be part of the future work going forward. Further, modelling shocks with magnetized flows has been difficult and is a known issue, particularly when keeping errors in the electric and magnetic fields low [66]. Solving test cases with the characteristics above would be a notable challenge to tackle. Also, as noted in Section 8.3.2, the parameters used to generate the magnetopause GEM case did not result in the correct energies. Formulating a GEM case that would result in the correct conditions found at the magnetopause would be a problem of interest.

A possible test case is a blunt body re-entry problem with a magnetic shield that holds the potential to increase the plasma shock stand-off distance from the blunt body. This has generated interest due to possible applications in practical high speed transportation and spacecraft. There have been experiments based around the Ziemer experiment [203–205] on the subject as well as numerous numerical simulations attempting to recover the experimental results and to prove the practicality of the various shielding [205,206], flow control [207], power [208] and drag enhancement [209] techniques proposed. The models used to simulate the experiment assumed strong magnetic fields, isotropic energies, or generalized Ohm's laws. A simulation with the multifluid MHD model would have none of these deficiencies. However, the existence of the shock presents numerical difficulties that are beyond the scope of this thesis. Future work in examining ways to treat shocks in the multifluid MHD scheme would be important in creating a general magnetized flow solver.

9.2.3 Exploration of the Magnetic Island

As was reported in Chapter 8, the cause, formation, and evolution of the magnetic island should be considered for extra study as it is not immediately clear whether it is a result of a physical effect or a numerical artefact. There is inconsistency in the direction of the movement of the

island, sometimes changing with the numerical scheme, and the magnetic island tends to occur at higher, noisier, mesh resolutions, or when there are less stabilizing collisions, or when there is less dissipative error cleaning. Higher-order schemes also seem to eliminate the magnetic island for low mesh resolution solutions for 5-moment two-fluid models [63]. While the relationship between the stability of a scheme and the formation of the magnetic island have been observed [28, 54, 63, 66, 188] and studies of turbulence models on the formation of the magnetic island have been performed [191], it would be an interesting avenue of research to determine the origin of the magnetic island's formation. The effect of temporal limiting would be a good start for this study.

9.2.4 Further Study of Implicit Time Marching Scheme

While there is significant computational advantage to the MMHD model and numerical solution procedure, problems with more fluid species, complex reactions and shocks will present significant challenges in terms of stiffness and computational resources. An obvious avenue of future work is through an implicit computational scheme. Preliminary investigation of the implicit NKS scheme considered in this work shows potential in reducing computational costs as in the evaluation and verification chapter, Chapter 7, where a speed up of several orders of magnitude could be obtained over an explicit scheme. In Section 7.4 the NKS MMHD scheme is used to predict non-magnetized flows and in this situation, the NKS scheme performs excellently. However, when applied to the GEM challenge, the results were inconsistent and dependent on the problem and grid resolution being examined. Further study is required to produce a consistent, robust, general implicit solution procedure.

In this work, two main problems were identified with the NKS MMHD scheme. One was the degradation in computational performance due to the Schwarz preconditioning. As an example, the base case GEM problem of Chapter 8, required the domain to be decomposed into 512 blocks in order to fit in the node memory, while splitting the GEM problem into just 8 domains was found to cause a significant increase in computational time making it more expensive than an explicit scheme. This issue is well known and a balance between the computational advantage of solving smaller problems versus the increase in computational iterations due to reduced global accuracy is an important consideration [131]. The observed rapid degradation in iterative convergence and need for future improvements was also mentioned in Northrup's thesis [131]. The NKS MMHD scheme is particularly sensitive to the memory requirement, not just because of the large number of governing equations, but due to the second issue encountered which was the singular nature of the block right preconditioning matrix for the

Maxwell's equations as discussed in Section 6.7.2. The Maxwell's equations are a degenerate system, and if it were not for the temporal entries in the diagonal of the Maxwell's equations preconditioning matrix, a matrix inversion would be impossible. As discussed in Sections 8.7 and 7.2.12, the ill-posed nature of the Maxwell's equations is such that for larger time steps, the diagonal dominance of the preconditioning matrix is reduced and the singular nature of the matrix takes over and increasingly poses a challenge to GMRES convergence. In general, NKS MMHD GMRES iterations are at least an order of magnitude greater than the number of iterations expected for a similar non-magnetized flow. The larger the GMRES iterations, the higher the memory requirements, which aggravate the Schwarz preconditioning issue. Solving the Maxwell's equations preconditioning matrix issue would go a long way towards producing an effective implicit algorithm for the MMHD model.

As mentioned, effective preconditioning is essential to an effective NKS GMRES scheme. As was seen in Chapters 7 and 8, for certain problems, neglecting the approximate residual Jacobian for the Maxwell's equations can produce faster results than fully preconditioned simulations, which indicate that an effective preconditioner has the potential to greatly accelerate solution convergence. One area of study would be to identify what factors or entries in the preconditioning matrix most affects the convergence of the GMRES procedure. In Section 8.7 some studies were undertaken to determine the diagonal dominance of the preconditioning matrix used and it was found that the ratio between the absolute sum of the diagonal entries versus the absolute sum of the off-diagonal entries of the preconditioning matrix was approximately the same for the limit of converging solutions for the LEO GEM problem. This indicates a threshold for numerical inversion of the preconditioning matrix.

There are other promising avenues of research that is suggested by the results of Chapter 5, where a temporal limiting implicit method was studied for the 1D version of the MMHD model. The high resolutions needed for plasma simulations often result in numerical noise and oscillations. As with the 1D case, temporal limiting has the potential to significantly reduce these numerical oscillations. Temporal limiting should be applicable to the NKS scheme with not too much difficulty and is one of the first things that should be considered for improving the 2D numerical solution procedure.

Appendix A

Dispersion Analysis of the 5-Moment Two Fluid Model

A.1 Overview

To gain a better understanding of the Two-Fluid Model proposed by Shumlak and Loverich [62] a dispersion analysis on the 16 equations is performed. The basic equations are slightly modified from the form presented in Loverich's paper. The equations are non-dimensionalized and linearized about an equilibrium state, then the complex eigen equations are solved and suitable parameters are chosen to create locus plots.

A.2 The Shumlak and Loverich Two-Fluid Model

The two-fluid model equations proposed by Shumlak and Loverich are based on a system of collisionless 5-moment Eulerian transport equations; one set of equations for the ions and electrons and also a set of equations to model the electromagnetic forces. The equations are listed below.

Ion and Electron Conservative Continuity

$$\begin{aligned} \frac{\partial n_{ion}}{\partial t} + \nabla \cdot n_{ion}\mathbf{u}_{ion} = 0, \\ \frac{\partial n_e}{\partial t} + \nabla \cdot n_e\mathbf{u}_e = 0, \end{aligned} \tag{A.1}$$

Ion and Electron Conservative Momentum

$$\begin{aligned}\frac{\partial n_{ion} m_{ion} \mathbf{u}_{ion}}{\partial t} + \nabla \cdot \left(n_{ion} m_{ion} \mathbf{u}_{ion} \mathbf{u}_{ion} + p_{ion} \mathbf{I}\right) &= n_{ion} e \left(\mathbf{E} + \mathbf{u}_{ion} \times \mathbf{B}\right), \\ \frac{\partial n_e m_e \mathbf{u}_e}{\partial t} + \nabla \cdot \left(n_e m_e \mathbf{u}_e \mathbf{u}_e + p_e \mathbf{I}\right) &= -n_e e \left(\mathbf{E} + \mathbf{u}_e \times \mathbf{B}\right),\end{aligned} \tag{A.2}$$

Ion and Electron Conservative Energy

$$\begin{aligned}\frac{\partial \varepsilon_{ion}}{\partial t} + \nabla \cdot \left[\left(\varepsilon_{ion} + p_{ion}\right) \mathbf{u_{ion}}\right] &= e n_{ion} \mathbf{u}_{ion} \cdot \mathbf{E}, \\ \frac{\partial \varepsilon_e}{\partial t} + \nabla \cdot \left[\left(\varepsilon_e + p_e\right) \mathbf{u_e}\right] &= -e n_e \mathbf{u}_e \cdot \mathbf{E},\end{aligned} \tag{A.3}$$

where

$$\begin{aligned}\varepsilon_{ion} &= \frac{1}{\gamma - 1} p_{ion} + \frac{1}{2} n_{ion} m_{ion} \mathbf{u}_{ion}^2, \\ \varepsilon_e &= \frac{1}{\gamma - 1} p_e + \frac{1}{2} n_e m_e \mathbf{u}_e^2,\end{aligned} \tag{A.4}$$

Faraday's Law

$$\frac{\partial \mathbf{B}}{\partial t} = -\nabla \times \mathbf{E}, \tag{A.5}$$

Ampère's Law

$$\frac{\partial \mathbf{E}}{\partial t} = c^2 \nabla \times \mathbf{B} - \frac{1}{\epsilon_0} e n_{ion} \mathbf{u}_{ion} + \frac{1}{\epsilon_0} e n_e \mathbf{u}_e. \tag{A.6}$$

A.3 Non-Dimensional Two-Fluid Model Equations

The following basic quantities are used to non-dimensionalize the above equations:

$$\nu, \quad n_{ref}, \quad p_{ref}, \quad m_{ref}, \quad \mu_0, \quad \gamma. \tag{A.7}$$

All variables are non-dimensionalized as follows:

$$\begin{gathered}t = \bar{t} \frac{1}{\nu}, \quad x = \bar{x} \sqrt{\gamma \frac{p_{ref}}{n_{ref} m_{ref}}} \frac{1}{\nu}, \quad m_{ion} = \bar{m}_{ion} m_{ref}, \quad m_e = \bar{m}_e m_{ref}, \\ n_{ion} = \bar{n}_{ion} n_{ref}, \quad n_e = \bar{n}_e n_{ref}, \quad \mathbf{u}_{ion} = \bar{\mathbf{u}}_{ion} \sqrt{\gamma \frac{p_{ref}}{n_{ref} m_{ref}}}, \quad \mathbf{u}_e = \bar{\mathbf{u}}_e \sqrt{\gamma \frac{p_{ref}}{n_{ref} m_{ref}}}, \\ p_{ion} = \bar{p}_{ion} \gamma p_{ref}, \quad p_e = \bar{p}_e \gamma p_{ref}, \quad \mathbf{E} = \bar{\mathbf{E}} \gamma p_{ref} \sqrt{\frac{\mu_0}{n_{ref} m_{ref}}}, \quad \mathbf{B} = \bar{\mathbf{B}} \sqrt{\mu_0 \gamma p_{ref}}.\end{gathered} \tag{A.8}$$

The following non-dimensionalized transport equation are obtained:

Non-Dimensional Ion and Electron Conservative Continuity

$$\begin{aligned}\frac{\partial \bar{n}_{ion}}{\partial \bar{t}} + \bar{\nabla} \cdot \bar{n}_{ion} \bar{\mathbf{u}}_{ion} &= 0, \\ \frac{\partial \bar{n}_e}{\partial \bar{t}} + \bar{\nabla} \cdot \bar{n}_e \bar{\mathbf{u}}_e &= 0,\end{aligned} \tag{A.9}$$

Non-Dimensional Ion and Electron Conservative Momentum

$$\begin{aligned}\frac{\partial \bar{n}_{ion}\bar{m}_{ion}\bar{\mathbf{u}}_{ion}}{\partial \bar{t}} + \bar{\nabla}\cdot\left(\bar{n}_{ion}\bar{m}_{ion}\bar{\mathbf{u}}_{ion}\bar{\mathbf{u}}_{ion} + \bar{p}_{ion}\mathbf{I}\right) &= \mathrm{Ke}\,\bar{n}_{ion}\left(\bar{\mathbf{E}} + \bar{\mathbf{u}}_{ion}\times\bar{\mathbf{B}}\right),\\ \frac{\partial \bar{n}_{e}\bar{m}_{e}\bar{\mathbf{u}}_{e}}{\partial \bar{t}} + \bar{\nabla}\cdot\left(\bar{n}_{e}\bar{m}_{e}\bar{\mathbf{u}}_{e}\bar{\mathbf{u}}_{e} + \bar{p}_{e}\mathbf{I}\right) &= -\mathrm{Ke}\,\bar{n}_{e}\left(\bar{\mathbf{E}} + \bar{\mathbf{u}}_{e}\times\bar{\mathbf{B}}\right),\end{aligned} \tag{A.10}$$

where

$$\mathrm{Ke} = \frac{e}{\nu m_{ref}}\sqrt{\gamma\mu_0 p_{ref}}, \tag{A.11}$$

Non-Dimensional Ion and Electron Conservative Energy

$$\begin{aligned}\frac{\partial \bar{\varepsilon}_{ion}}{\partial \bar{t}} + \bar{\nabla}\cdot\left[\left(\bar{\varepsilon}_{ion} + \bar{p}_{ion}\right)\bar{\mathbf{u}}_{ion}\right] &= \mathrm{Ke}\,\bar{n}_{ion}\bar{\mathbf{u}}_{ion}\cdot\bar{\mathbf{E}},\\ \frac{\partial \bar{\varepsilon}_{e}}{\partial \bar{t}} + \bar{\nabla}\cdot\left[\left(\bar{\varepsilon}_{e} + \bar{p}_{e}\right)\bar{\mathbf{u}}_{e}\right] &= -\mathrm{Ke}\,\bar{n}_{e}\bar{\mathbf{u}}_{e}\cdot\bar{\mathbf{E}},\end{aligned} \tag{A.12}$$

where

$$\begin{aligned}\bar{\varepsilon}_{ion} &= \frac{1}{\gamma-1}\bar{p}_{ion} + \frac{1}{2}\bar{n}_{ion}\bar{m}_{ion}\bar{\mathbf{u}}_{ion}^2,\\ \bar{\varepsilon}_{e} &= \frac{1}{\gamma-1}\bar{p}_{e} + \frac{1}{2}\bar{n}_{e}\bar{m}_{e}\bar{\mathbf{u}}_{e}^2,\end{aligned} \tag{A.13}$$

Non-Dimensional Ion and Electron Non-Conservative Pressure

$$\begin{aligned}\frac{\partial \bar{p}_{ion}}{\partial \bar{t}} + \bar{\mathbf{u}}_{ion}\cdot\bar{\nabla}\bar{p}_{ion} + \frac{5}{3}\bar{p}_{ion}\bar{\nabla}\cdot\bar{\mathbf{u}}_{ion} &= 0,\\ \frac{\partial \bar{p}_{e}}{\partial \bar{t}} + \bar{\mathbf{u}}_{e}\cdot\bar{\nabla}\bar{p}_{e} + \frac{5}{3}\bar{p}_{e}\bar{\nabla}\cdot\bar{\mathbf{u}}_{e} &= 0,\end{aligned} \tag{A.14}$$

Non-Dimensional Faraday's Law

$$\frac{\partial \bar{\mathbf{B}}}{\partial \bar{t}} = -\bar{\nabla}\times\bar{\mathbf{E}}, \tag{A.15}$$

Non-Dimensional Ampère's Law

$$\frac{\partial \bar{\mathbf{E}}}{\partial \bar{t}} = \frac{c^2}{a_{ref}^2}\bar{\nabla}\times\bar{\mathbf{B}} - \frac{c^2}{a_{ref}^2}\mathrm{Ke}\,\bar{n}_{ion}\bar{\mathbf{u}}_{ion} + \frac{c^2}{a_{ref}^2}\mathrm{Ke}\,\bar{n}_{e}\bar{\mathbf{u}}_{e}, \tag{A.16}$$

where $a_{ref}^2 = \gamma p_{ref}/n_{ref}m_{ref}$, the reference speed of sound.

For the rest of this document we will drop the bar indicating non-dimensional terms.

A.4 Linearized Equations About the Equilibrium State

The system of equations is linearized by expanding around a constant equilibrium state with small perturbations so that second-order terms in the perturbed solution are neglected. The

primitive perturbative solution vector is

$$\mathbf{W}^* = \left[\tilde{n}_{ion}, \tilde{n}_e, \tilde{u}_{ion,x}, \tilde{u}_{ion,y}, \tilde{u}_{ion,z}, \tilde{u}_{e,x}, \tilde{u}_{e,y}, \tilde{u}_{e,z}, \tilde{p}_{ion}, \tilde{p}_e, \tilde{E}_x, \tilde{E}_y, \tilde{E}_z, \tilde{B}_x, \tilde{B}_y, \tilde{B}_z\right]^T \tag{A.17}$$

and the equilibrium state is defined to be

$$\mathbf{W_0} = [n_{0,ion}, n_{0,e}, 0, 0, 0, 0, 0, 0, p_{0,ion}, p_{0,e}, 0, 0, 0, B_{0,x}, B_{0,y}, B_{0,z}]^T \tag{A.18}$$

where the background electric field and bulk equilibrium velocities are set to zero.

Taking the non-dimensional two-fluid equations and substituting in for

$$\mathbf{W} = \mathbf{W_0} + \mathbf{W}^*, \tag{A.19}$$

and neglecting all higher order terms, the following linearized equations are obtained:

Linearized Ion and Electron Continuity

$$\frac{\partial \tilde{n}_{ion}}{\partial t} + n_{0,ion}\left(\nabla \cdot \tilde{\mathbf{u}}_{ion}\right) = 0, \tag{A.20}$$

$$\frac{\partial \tilde{n}_e}{\partial t} + n_{0,e}\left(\nabla \cdot \tilde{\mathbf{u}}_e\right) = 0, \tag{A.21}$$

Linearized Ion and Electron Momentum

$$\begin{aligned}\frac{\partial \tilde{\mathbf{u}}_{ion}}{\partial t} + \frac{1}{n_{0,ion} m_{ion}} \nabla \tilde{p}_{ion} = \frac{\mathrm{Ke}}{m_{ion}} \Big(\tilde{\mathbf{E}} + \left(B_{0,z}\tilde{u}_{ion,y} - B_{0,y}\tilde{u}_{ion,z}\right)_x \\ - \left(B_{0,z}\tilde{u}_{ion,x} - B_{0,x}\tilde{u}_{ion,z}\right)_y + \left(B_{0,y}\tilde{u}_{ion,x} - B_{0,x}\tilde{u}_{ion,y}\right)_z\Big),\end{aligned} \tag{A.22}$$

$$\begin{aligned}\frac{\partial \tilde{\mathbf{u}}_e}{\partial t} + \frac{1}{n_{0,e} m_e} \nabla \tilde{p}_e = -\frac{\mathrm{Ke}}{m_e} \Big(\tilde{\mathbf{E}} + \left(B_{0,z}\tilde{u}_{e,y} - B_{0,y}\tilde{u}_{e,z}\right)_x \\ - \left(B_{0,z}\tilde{u}_{e,x} - B_{0,x}\tilde{u}_{e,z}\right)_y + \left(B_{0,y}\tilde{u}_{e,x} - B_{0,x}\tilde{u}_{e,y}\right)_z\Big),\end{aligned}$$

(a power expansion is used to simplify the coefficient in front of the pressure term)

Linearized Ion and Electron Energy

$$\begin{aligned}\frac{\partial \tilde{p}_{ion}}{\partial t} + \frac{5}{3} p_{ion} \nabla \cdot \tilde{\mathbf{u}}_{ion} = 0, \\ \frac{\partial \tilde{p}_e}{\partial t} + \frac{5}{3} p_e \nabla \cdot \tilde{\mathbf{u}}_e = 0,\end{aligned} \tag{A.23}$$

Ampère's Law

$$\begin{aligned}\frac{\partial \tilde{\mathbf{E}}}{\partial t} - \frac{c^2}{a_{ref}^2}\left(\left(\frac{\partial \tilde{B}_z}{\partial y} - \frac{\partial \tilde{B}_y}{\partial z}\right)_x - \left(\frac{\partial \tilde{B}_z}{\partial x} - \frac{\partial \tilde{B}_x}{\partial z}\right)_y + \left(\frac{\partial \tilde{B}_y}{\partial x} - \frac{\partial \tilde{B}_x}{\partial y}\right)_z\right) \\ = -\frac{c^2}{a_{ref}^2}\mathrm{Ke}\, n_{ion}\tilde{\mathbf{u}}_{ion} + \frac{c^2}{a_{ref}^2}\mathrm{Ke}\, n_e \tilde{\mathbf{u}}_e,\end{aligned} \tag{A.24}$$

Faraday's Law

$$\frac{\partial \tilde{\mathbf{B}}}{\partial t} + \left(\frac{\partial \tilde{E}_z}{\partial y} - \frac{\partial \tilde{E}_y}{\partial z} \right)_x - \left(\frac{\partial \tilde{E}_z}{\partial x} - \frac{\partial \tilde{E}_x}{\partial z} \right)_y + \left(\frac{\partial \tilde{E}_y}{\partial x} - \frac{\partial \tilde{E}_x}{\partial y} \right)_z = 0. \tag{A.25}$$

A.4.1 The Coefficient Matricies

The above equations can be put into coefficient matrices in the following form:

$$\frac{\partial \mathbf{W}^*}{\partial t^*} + \mathcal{A}^* \frac{\partial \mathbf{W}^*}{\partial x^*} + \mathcal{B}^* \frac{\partial \mathbf{W}^*}{\partial y^*} + \mathcal{C}^* \frac{\partial \mathbf{W}^*}{\partial z^*} = \mathcal{S}^* \mathbf{W}^* \tag{A.26}$$

where as an example

$$\mathcal{A}^* = \begin{bmatrix}
0 & 0 & n_{0,ion} & 0 & 0 & 0 & 0 & 0 & 0 & 0 & 0 & 0 & 0 & 0 & 0 & 0 \\
0 & 0 & 0 & 0 & 0 & n_{0,e} & 0 & 0 & 0 & 0 & 0 & 0 & 0 & 0 & 0 & 0 \\
0 & 0 & 0 & 0 & 0 & 0 & 0 & 0 & \frac{1}{n_{0,ion} m_{ion}} & 0 & 0 & 0 & 0 & 0 & 0 & 0 \\
0 & 0 & 0 & 0 & 0 & 0 & 0 & 0 & 0 & 0 & 0 & 0 & 0 & 0 & 0 & 0 \\
0 & 0 & 0 & 0 & 0 & 0 & 0 & 0 & 0 & 0 & 0 & 0 & 0 & 0 & 0 & 0 \\
0 & 0 & 0 & 0 & 0 & 0 & 0 & 0 & 0 & \frac{1}{n_{0,e} m_e} & 0 & 0 & 0 & 0 & 0 & 0 \\
0 & 0 & 0 & 0 & 0 & 0 & 0 & 0 & 0 & 0 & 0 & 0 & 0 & 0 & 0 & 0 \\
0 & 0 & 0 & 0 & 0 & 0 & 0 & 0 & 0 & 0 & 0 & 0 & 0 & 0 & 0 & 0 \\
0 & 0 & \frac{5}{3} p_{0,ion} & 0 & 0 & 0 & 0 & 0 & 0 & 0 & 0 & 0 & 0 & 0 & 0 & 0 \\
0 & 0 & 0 & 0 & 0 & \frac{5}{3} p_{0,e} & 0 & 0 & 0 & 0 & 0 & 0 & 0 & 0 & 0 & 0 \\
0 & 0 & 0 & 0 & 0 & 0 & 0 & 0 & 0 & 0 & 0 & 0 & 0 & 0 & 0 & 0 \\
0 & 0 & 0 & 0 & 0 & 0 & 0 & 0 & 0 & 0 & 0 & 0 & 0 & 0 & 0 & \frac{c^2}{a_{ref}^2} \\
0 & 0 & 0 & 0 & 0 & 0 & 0 & 0 & 0 & 0 & 0 & 0 & 0 & 0 & -\frac{c^2}{a_{ref}^2} & 0 \\
0 & 0 & 0 & 0 & 0 & 0 & 0 & 0 & 0 & 0 & 0 & 0 & 0 & 0 & 0 & 0 \\
0 & 0 & 0 & 0 & 0 & 0 & 0 & 0 & 0 & 0 & 0 & 0 & -1 & 0 & 0 & 0 \\
0 & 0 & 0 & 0 & 0 & 0 & 0 & 0 & 0 & 0 & 0 & 1 & 0 & 0 & 0 & 0
\end{bmatrix}. \tag{A.27}$$

The source term matrix is

$$\mathcal{S}^{*(1-8)} = \begin{bmatrix} 0 & 0 & 0 & 0 & 0 & 0 & 0 & 0 \\ 0 & 0 & 0 & 0 & 0 & 0 & 0 & 0 \\ 0 & 0 & 0 & \frac{\mathrm{Ke}}{m_{ion}}B_{0,z} & -\frac{\mathrm{Ke}}{m_{ion}}B_{0,y} & 0 & 0 & 0 \\ 0 & 0 & -\frac{\mathrm{Ke}}{m_{ion}}B_{0,z} & 0 & \frac{\mathrm{Ke}}{m_{ion}}B_{0,x} & 0 & 0 & 0 \\ 0 & 0 & \frac{\mathrm{Ke}}{m_{ion}}B_{0,y} & -\frac{\mathrm{Ke}}{m_{ion}}B_{0,x} & 0 & 0 & 0 & 0 \\ 0 & 0 & 0 & 0 & 0 & 0 & \frac{\mathrm{Ke}}{m_e}B_{0,z} & -\frac{\mathrm{Ke}}{m_e}B_{0,y} \\ 0 & 0 & 0 & 0 & 0 & -\frac{\mathrm{Ke}}{m_e}B_{0,z} & 0 & \frac{\mathrm{Ke}}{m_e}B_{0,x} \\ 0 & 0 & 0 & 0 & 0 & \frac{\mathrm{Ke}}{m_e}B_{0,y} & -\frac{\mathrm{Ke}}{m_e}B_{0,x} & 0 \\ 0 & 0 & 0 & 0 & 0 & 0 & 0 & 0 \\ 0 & 0 & 0 & 0 & 0 & 0 & 0 & 0 \\ 0 & 0 & -\frac{c^2\mathrm{Ke}}{a_{ref}^2}n_{0,ion} & 0 & 0 & \frac{c^2\mathrm{Ke}}{a_{ref}^2}n_{0,e} & 0 & 0 \\ 0 & 0 & 0 & -\frac{c^2\mathrm{Ke}}{a_{ref}^2}n_{0,ion} & 0 & 0 & \frac{c^2\mathrm{Ke}}{a_{ref}^2}n_{0,e} & 0 \\ 0 & 0 & 0 & 0 & -\frac{c^2\mathrm{Ke}}{a_{ref}^2}n_{0,ion} & 0 & 0 & \frac{c^2\mathrm{Ke}}{a_{ref}^2}n_{0,e} \\ 0 & 0 & 0 & 0 & 0 & 0 & 0 & 0 \\ 0 & 0 & 0 & 0 & 0 & 0 & 0 & 0 \\ 0 & 0 & 0 & 0 & 0 & 0 & 0 & 0 \end{bmatrix}, \tag{A.28}$$

$$\mathcal{S}^{*(9-16)} = \begin{bmatrix} 0 & 0 & 0 & 0 & 0 & 0 & 0 & 0 \\ 0 & 0 & 0 & 0 & 0 & 0 & 0 & 0 \\ 0 & 0 & \frac{\mathrm{Ke}}{m_{ion}} & 0 & 0 & 0 & 0 & 0 \\ 0 & 0 & 0 & \frac{\mathrm{Ke}}{m_{ion}} & 0 & 0 & 0 & 0 \\ 0 & 0 & 0 & 0 & \frac{\mathrm{Ke}}{m_{ion}} & 0 & 0 & 0 \\ 0 & 0 & -\frac{\mathrm{Ke}}{m_e} & 0 & 0 & 0 & 0 & 0 \\ 0 & 0 & 0 & -\frac{\mathrm{Ke}}{m_e} & 0 & 0 & 0 & 0 \\ 0 & 0 & 0 & 0 & -\frac{\mathrm{Ke}}{m_e} & 0 & 0 & 0 \\ 0 & 0 & 0 & 0 & 0 & 0 & 0 & 0 \\ 0 & 0 & 0 & 0 & 0 & 0 & 0 & 0 \\ 0 & 0 & 0 & 0 & 0 & 0 & 0 & 0 \\ 0 & 0 & 0 & 0 & 0 & 0 & 0 & 0 \\ 0 & 0 & 0 & 0 & 0 & 0 & 0 & 0 \\ 0 & 0 & 0 & 0 & 0 & 0 & 0 & 0 \\ 0 & 0 & 0 & 0 & 0 & 0 & 0 & 0 \\ 0 & 0 & 0 & 0 & 0 & 0 & 0 & 0 \end{bmatrix}. \tag{A.29}$$

A.4.2 Eigen Analysis

The perturbative primitive solution state $\mathbf{W}^*$ is substituted in Equation (A.26) using

$$\mathbf{W}^* = \tilde{\mathbf{W}} \exp\left[i\left(\bar{\omega}\bar{t}^* + \bar{\alpha}\bar{x}^* + \bar{\beta}\bar{y}^*\right)\right] \tag{A.30}$$

and neglecting the z-direction derivative in order to make a two-dimensional approximation, the following eigen equation is obtained

$$\left(i\bar{\omega}\mathbf{I} + i\bar{\alpha}\mathcal{A}^* + i\bar{\beta}\mathcal{B}^* - \mathcal{S}^*\right)\tilde{\mathbf{W}} = \mathbf{0}. \tag{A.31}$$

It should be noted that all the above quantities are non-dimensional according to the following:

$$\bar{\omega} = \frac{\omega}{\nu}, \quad \bar{t} = t\nu, \quad \bar{x} = x\frac{\nu}{a_{ref}}, \quad \bar{\alpha} = \alpha\frac{a_{ref}}{\nu}, \quad \bar{\beta} = \beta\frac{a_{ref}}{\nu}. \tag{A.32}$$

Again, the bars are dropped for simplicity. The conversion for the α and β values of wave number should be noted.

A number of simplifications are made which include assuming equal pressures $p_{0,ion} = p_{0,e}$, which is perfectly reasonable for an equilibrium plasma. Also, $\rho_{0,e} = (m_e/m_{ion})\rho_{0,ion}$ is assumed, which means that the fluid has the same background number density, $n_0 = n_{0,ion} = n_{0,e}$. Finally, it is assumed that the background magnetic field is aligned with the x-direction, $\mathbf{B}_0 = (B_0, 0, 0)$. Therefore, the following eigen matrix is obtained:

$$A^{(1-8)} = \begin{bmatrix}
i\omega & 0 & i\alpha n_0 & i\beta n_0 & 0 & 0 & 0 & 0 \\
0 & i\omega & 0 & 0 & 0 & i\alpha n_0 & i\beta n_0 & 0 \\
0 & 0 & i\omega & 0 & 0 & 0 & 0 & 0 \\
0 & 0 & 0 & i\omega & -\frac{\mathrm{Ke}}{m_{ion}}B_0 & 0 & 0 & 0 \\
0 & 0 & 0 & \frac{\mathrm{Ke}}{m_{ion}}B_0 & i\omega & 0 & 0 & 0 \\
0 & 0 & 0 & 0 & 0 & i\omega & 0 & 0 \\
0 & 0 & 0 & 0 & 0 & 0 & i\omega & \frac{\mathrm{Ke}}{m_e}B_0 \\
0 & 0 & 0 & 0 & 0 & 0 & -\frac{\mathrm{Ke}}{m_e}B_0 & i\omega \\
0 & 0 & i\frac{5}{3}\alpha p_0 & i\frac{5}{3}\beta p_0 & 0 & 0 & 0 & 0 \\
0 & 0 & 0 & 0 & 0 & i\frac{5}{3}\alpha p_0 & i\frac{5}{3}\beta p_0 & 0 \\
0 & 0 & \frac{c^2\mathrm{Ke}}{a_{ref}^2}n_0 & 0 & 0 & -\frac{c^2\mathrm{Ke}}{a_{ref}^2}n_0 & 0 & 0 \\
0 & 0 & 0 & \frac{c^2\mathrm{Ke}}{a_{ref}^2}n_0 & 0 & 0 & -\frac{c^2\mathrm{Ke}}{a_{ref}^2}n_0 & 0 \\
0 & 0 & 0 & 0 & \frac{c^2\mathrm{Ke}}{a_{ref}^2}n_0 & 0 & 0 & -\frac{c^2\mathrm{Ke}}{a_{ref}^2}n_0 \\
0 & 0 & 0 & 0 & 0 & 0 & 0 & 0 \\
0 & 0 & 0 & 0 & 0 & 0 & 0 & 0 \\
0 & 0 & 0 & 0 & 0 & 0 & 0 & 0
\end{bmatrix}, \tag{A.33}$$

$$A^{(9-16)} = \begin{bmatrix} 0 & 0 & 0 & 0 & 0 & 0 & 0 & 0 \\ 0 & 0 & 0 & 0 & 0 & 0 & 0 & 0 \\ \frac{i\alpha}{n_0 m_{ion}} & 0 & -\frac{\mathrm{Ke}}{m_{ion}} & 0 & 0 & 0 & 0 & 0 \\ \frac{i\beta}{n_0 m_{ion}} & 0 & 0 & -\frac{\mathrm{Ke}}{m_{ion}} & 0 & 0 & 0 & 0 \\ 0 & 0 & 0 & 0 & -\frac{\mathrm{Ke}}{m_{ion}} & 0 & 0 & 0 \\ 0 & \frac{i\alpha}{n_0 m_e} & \frac{\mathrm{Ke}}{m_e} & 0 & 0 & 0 & 0 & 0 \\ 0 & \frac{i\beta}{n_0 m_e} & 0 & \frac{\mathrm{Ke}}{m_e} & 0 & 0 & 0 & 0 \\ 0 & 0 & 0 & 0 & \frac{\mathrm{Ke}}{m_e} & 0 & 0 & 0 \\ i\omega & 0 & 0 & 0 & 0 & 0 & 0 & 0 \\ 0 & i\omega & 0 & 0 & 0 & 0 & 0 & 0 \\ 0 & 0 & i\omega & 0 & 0 & 0 & 0 & -i\beta\frac{c^2}{a_{ref}^2} \\ 0 & 0 & 0 & i\omega & 0 & 0 & 0 & i\alpha\frac{c^2}{a_{ref}^2} \\ 0 & 0 & 0 & 0 & i\omega & i\beta\frac{c^2}{a_{ref}^2} & -i\alpha\frac{c^2}{a_{ref}^2} & 0 \\ 0 & 0 & 0 & 0 & i\beta & i\omega & 0 & 0 \\ 0 & 0 & 0 & 0 & -i\alpha & 0 & i\omega & 0 \\ 0 & 0 & -i\beta & i\alpha & 0 & 0 & 0 & i\omega \end{bmatrix}, \quad \text{(A.34)}$$

where $\mathbf{A}\hat{\mathbf{W}} = 0$

A.5 Numerical Values

The following values were used to determine the constants and reference values:

$$\begin{aligned} e &= 1.602189246 \times 10^{-19}\mathrm{C}, & \gamma &= \tfrac{5}{3}, \\ c &= 299792458\tfrac{\mathrm{m}}{\mathrm{s}}, & m_{ref} &= m_{ion} = 1.6736 \times 10^{-27}\mathrm{kg}, \\ \mu_0 &= 0.000001256637\tfrac{\mathrm{m\ kg}}{\mathrm{s^2 A^2}}, & n_{ref} &= n_0 = 7.31955 \times 10^{23}\tfrac{1}{\mathrm{m^3}}, \\ & & p_{ref} &= p_0 = 101325\mathrm{Pa}. \end{aligned} \quad \text{(A.35)}$$

The typical collision frequency is calculated from the ion-electron collision frequency based on the coulomb collision as follows [103, 123]:

$$\nu_{e,ion} = \frac{4\sqrt{2\pi}e_\circ^4}{3k^{\frac{3}{2}}} n_{ion} Z_e^2 Z_{ion}^2 \ln\Lambda \left(\frac{m_e + m_{ion}}{m_e m_{ion}}\right)^{\frac{1}{2}} \left(\frac{m_e + m_{ion}}{m_e T_{ion} + m_{ion} T_e}\right)^{\frac{3}{2}}, \quad \text{(A.36)}$$

where $e_\circ$ is the elementary charge constant in cgs and Z_e, Z_{ion} is the charge number for the electrons and ions respectively. This is just -1, and 1. This equation is in cgs units. Also,

$$\ln\Lambda = 23 + \frac{3}{2}\ln\left(\frac{T_e}{10^6}\right) - \frac{1}{2}\ln\left(\frac{n_e}{10^{12}}\right) \quad \text{(A.37)}$$

where this equation is in SI. The typical collision frequency is determined by using the following conversions to CGS from SI:

$$\begin{array}{rcl@{\qquad}rcl} & \textbf{CGS} & & & \textbf{SI} & \\ e_0 &=& e_{0,SI} * 2.9979 \times 10^9 \, \frac{\text{statC}}{\text{C}}, & e_{0,SI} &=& 1.602189246 \times 10^{-19}\text{C}, \\ k &=& k_{SI} * 1.0 \times 10^7 \, \frac{\text{erg}}{\text{J}}, & k_{SI} &=& 1.380658 \times 10^{-23} \frac{\text{J}}{\text{K}}, \\ n_0 &=& n_{0,SI} * 10^{-6} \, \frac{\text{m}^3}{\text{cm}^3}, & n_{0,SI} &=& 7.31955 \times 10^{23} \, \frac{1}{\text{m}^3}, \\ m_e &=& m_{e,SI} * 1.0 \times 10^3 \, \frac{\text{g}}{\text{kg}}, & m_{e,SI} &=& 9.1093897 \times 10^{-31}\text{kg}, \\ m_I &=& m_{I,SI} * 1.0 \times 10^3 \, \frac{\text{g}}{\text{kg}}, & m_{I,SI} &=& 1.6736 \times 10^{-27}\text{kg}. \end{array} \tag{A.38}$$

Next the following substitutions are made in order to recover known results:

$$p_0 = \frac{3 n_0 m_e v_{ae}^2}{5}, \quad n_0 = \omega_{pe}^2 \left(\frac{\epsilon_0 m_e}{e^2} \right), \quad B_0 = \omega_{ci} \frac{m_{ion}}{e}, \quad m_{ion} = \frac{\omega_{ce}}{\omega_{ci}} m_e. \tag{A.39}$$

The determinant of matrix **A** is taken to obtain the dispersion equation. The equation is far too long to include. One way of simplifying this equation even further is to take specific cases. For instance, the high and low frequency plasma limits are taken.

A.5.1 R-mode, L-mode and Alfvén Waves

First the case for waves propagating parallel to the background magnetic field will be examined. Note that the magnetic field is aligned in the x-direction only. This simplification is accomplished by setting $\beta = 0$ and $\alpha = k$ as the wave number for waves in the x-direction. The equation simplifies to

$$\begin{gathered} \left({\omega_{pe}}^2 \omega_{ci} \omega^2 - \omega_{ci} \omega^3 \omega_{ce} + \omega_{ci} k^2 \omega c^2 \omega_{ce} + \omega_{ci} \omega_{ce}{}^2 \omega^2 - \omega_{ci} k^2 \omega_{ce}{}^2 c^2 \right. \\ \left. + \omega_{ce} k^2 \omega^2 c^2 - \omega^4 \omega_{ce} + {\omega_{pe}}^2 \omega_{ce} \omega^2 - k^2 \omega c^2 \omega_{ce}{}^2 + \omega^3 \omega_{ce}{}^2 \right) \\ \left({\omega_{pe}}^2 \omega_{ci} \omega^2 + \omega_{ci} \omega^3 \omega_{ce} - \omega_{ci} k^2 \omega c^2 \omega_{ce} + \omega_{ci} \omega_{ce}{}^2 \omega^2 - \omega_{ci} k^2 \omega_{ce}{}^2 c^2 \right. \\ \left. + \omega_{ce} k^2 \omega^2 c^2 - \omega^4 \omega_{ce} + {\omega_{pe}}^2 \omega_{ce} \omega^2 + k^2 \omega c^2 \omega_{ce}{}^2 - \omega^3 \omega_{ce}{}^2 \right) \\ \left(-{\omega_{pe}}^2 \omega_{ci} \omega^2 + 2 {\omega_{pe}}^2 \omega_{ci} k^2 {v_{ae}}^2 - {\omega_{pe}}^2 \omega_{ce} \omega^2 \right. \\ \left. - \omega_{ci} k^2 {v_{ae}}^2 \omega^2 + \omega_{ci} k^4 {v_{ae}}^4 + \omega^4 \omega_{ce} - \omega_{ce} k^2 {v_{ae}}^2 \omega^2 \right) = 0. \end{gathered} \tag{A.40}$$

A short time interval is assumed, otherwise known as the high frequency limit where ion frequencies are negligible, $\omega_{ci} = 0$, then the following relation holds:

$$\begin{gathered} \left(k^2 \omega c^2 - \omega^3 + {\omega_{pe}}^2 \omega - c^2 k^2 \omega_{ce} + \omega^2 \omega_{ce} \right) \left(k^2 \omega c^2 - \omega^3 + {\omega_{pe}}^2 \omega + c^2 k^2 \omega_{ce} - \omega^2 \omega_{ce} \right) \\ \left({\omega_{pe}}^2 - \omega^2 + k^2 {v_{ae}}^2 \right) = 0. \end{gathered} \tag{A.41}$$

By inspection it can be seen that there are three factors resulting in three relations which are

$$\omega^2 = v_{ac}^2 k^2 + \omega_{pe}^2 \tag{A.42}$$

which is the electron plasma wave, and

$$\omega^2 = c^2k^2 + \frac{\omega\omega_{pe}^2}{\omega + \omega_{ce}} \tag{A.43}$$

and

$$\omega^2 = c^2k^2 + \frac{\omega\omega_{pe}^2}{\omega - \omega_{ce}} \tag{A.44}$$

which is the high frequency L-mode and R-mode plasma waves respectively. These match Loverich's results [133], which in turn match expected results from Chen [210]. In the course of the investigations of the eigen systems of this model, the non dimensional versions of the L-mode and R-mode equations were derived. They are provided here for reference:

$$\omega^3 \pm \frac{\mathrm{Ke}B_0}{m_e}\omega^2 - \left(\frac{c^2}{a_{ref}^2}k^2 + \frac{n_{ref}n_0c^2\mu_0e^2}{m_{ref}m_e\nu^2}\right)\omega \mp \frac{c^2\mathrm{Ke}B_0}{a_{ref}^2m_e}k^2 = 0. \tag{A.45}$$

The non dimensional version of the Electron plasma wave is

$$\omega^2 = \frac{5}{3}\frac{p_{ref}\gamma p_0}{n_{ref}m_{ref}n_0m_ea_{ref}^2}k^2 + \frac{n_0n_{ref}c^2\mu_0e^2}{m_e\nu^2m_{ref}}. \tag{A.46}$$

When $\omega \ll \omega_{ci} \ll \omega_{ce}$, this is the low frequency limit. The last factor in Equation (A.40) becomes

$$\omega^2 = v_{ae}^2k^2 + v_{ae}^2k^2\left(\frac{\omega_{pe}^2}{v_{ae}^2k^2 + \omega_{pe}^2}\right). \tag{A.47}$$

Taking the other two factors in Equation (A.40), the Alfvén wave becomes

$$\omega^2 = c^2k^2\frac{\omega_{ce}\omega_{ci}}{\omega_{pe}^2}. \tag{A.48}$$

The Alfvén speed is defined as $v_{al}^2 = c^2\left(\omega_{ci}/\omega_{pe}\right)^2$. The non-dimensional version of the low frequency electron plasma wave and the Alfvén wave are respectively

$$\omega^2 = \frac{5}{3}\frac{p_{ref}\gamma p_0}{m_{ref}m_ea_{ref}^2}k^2\left(\frac{1}{n_{ref}n_0} + \frac{c^2\mu_0e^2}{\frac{5}{3}\frac{p_{ref}\gamma p_0\nu^2}{n_{ref}n_0a_{ref}^2}k^2 + n_0n_{ref}c^2\mu_0e^2}\right), \tag{A.49}$$

$$\omega^2 = \frac{B_0^2\gamma p_{ref}}{a_{ref}^2m_{ref}m_{ion}n_0n_{ref}}k^2. \tag{A.50}$$

A.5.2 X-mode, O-mode and Magnetosonic Waves

Now $\alpha = 0$ and $\beta = k$ is examined to find relations for the waves travelling perpendicular to the background magnetic field. Again $\omega_{ci} = 0$ is set for the high frequency limit to get

$$\begin{gathered}\left({\omega_{pe}}^2 + c^2k^2 - \omega^2\right)\\ \left(-\omega^2{\omega_{ce}}^2 + k^2{\omega_{ce}}^2c^2 - k^2\omega^2c^2 + c^2k^2{\omega_{pe}}^2 - 2{\omega_{pe}}^2\omega^2\right.\\ \left.+{\omega_{pe}}^4 - k^2{v_{ae}}^2\omega^2 + {\omega_{pe}}^2k^2{v_{ae}}^2 + \omega^4 + k^4{v_{ae}}^2c^2\right) = 0.\end{gathered} \tag{A.51}$$

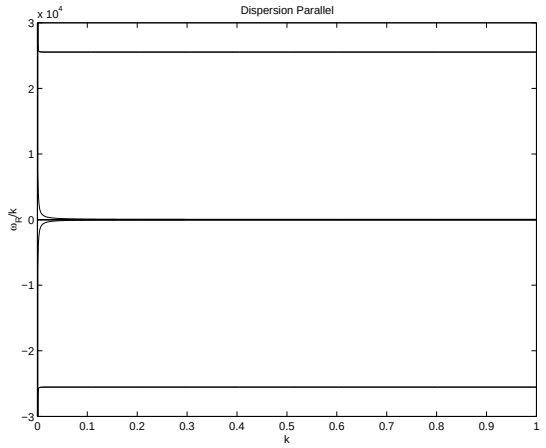

Figure A.1: Large scale dispersion analysis for the parallel direction

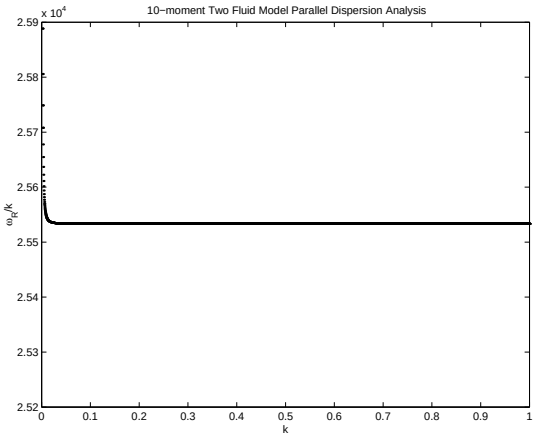

Figure A.2: Positive, large magnitude L and R-mode plasma waves for the parallel direction

The first factor in this equation is the ordinary or the O-mode,

$$\omega^2 = c^2k^2 + \omega_{pe}^2. \tag{A.52}$$

The second factor is the X-mode which can be given by

$$\omega^2 = c^2k^2 + \omega_{pe}^2\left(\frac{\omega^2 - \omega_{pe}^2}{\omega^2 - \omega_{ce}^2}\right) + \omega_{pe}^2\left(\frac{\omega^2 - c^2k^2}{\omega^2 - \omega_{ce}^2}\right) \tag{A.53}$$

if $v_{ae} \ll c$ which is quite valid. The magnetosonic wave can be obtained by a power expansion on the dispersion relation.

A.6 Results of Dispersion Analysis

The characteristic equation is derived by taking the determinant of matrix **A** (Matrix (A.33)-(A.34)) and numerically solving the resultant equations for temporal frequency ω for various values of the spatial wave number k. To make the analysis easier to understand and conform to results presented in Section A.5.1 and A.5.2 the analysis is split into two sections for parallel and perpendicular wave propagation.

A.6.1 Parallel Dispersion Analysis

The values first considered is $\beta = 0$ and $\alpha = k$ to obtain the following dispersion plot Figure A.1 for ω_R/k vs. k (or wavespeed versus spatial wavenumber). Note that there is no imaginary

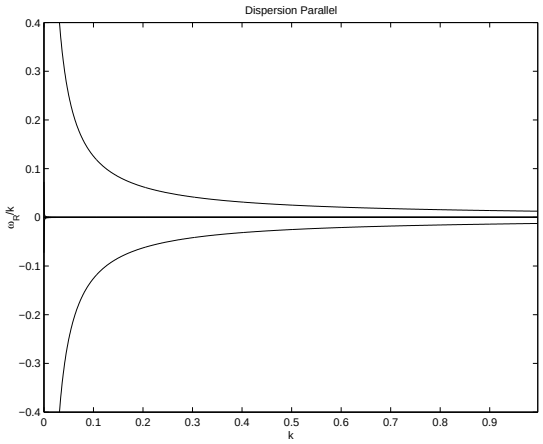

Figure A.3: Small magnitude L and R-mode plasma waves for the parallel direction

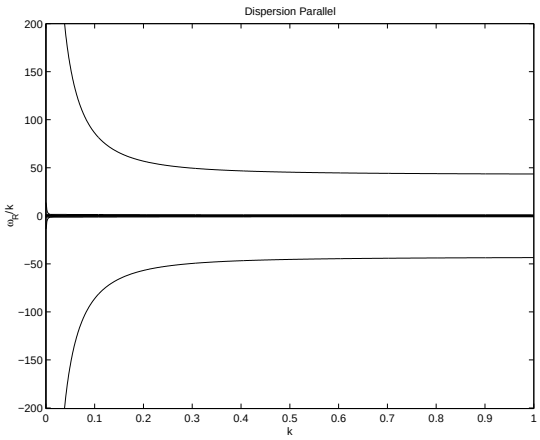

Figure A.4: Electron plasma waves for the parallel direction

eigenvalues for the regime being studied, and so there is no damping. All waves except for two, and the four zero waves (associated with purely perpendicular waves) go to infinite values of ω_R/k for small values of k. This means that near uniform physical variations will disperse much faster than more rapidly varying solutions of large values of k. In fact, for very large spatial wavelength disturbances, the wave interaction associated with that disturbance must propagate instantaneously.

There are four main wave regimes expressed in this analysis. The largest magnitude for wavespeed ω_R/k is the L and R-mode plasma waves. These waves consist of six waves. The L and R-mode waves are unique in the sense that they contain both the highest magnitude waves along with one of the smallest magnitude waves. Four of the waves (two positive and two negative) are of order 10^4 for large values of k. The waves have the same absolute value. The positive, large magnitude L and R-mode wave is shown in Figure A.2. The smallest magnitude L and R-mode plasma wave is of order 10^{-2} for large values of k and can be seen in Figure A.3.

The next regime is where the electron plasma wave exists. For large values of k, the magnitude is of order 10. The dispersion analysis can be seen in Figure A.4.

The next regime is for the Acoustic and Alfvén waves of order 1 for large values of k. The Figure A.5 shows the Alfvén waves along with the small magnitude L and R-mode waves. As can be seen in the figure, the Alfvén waves do not go off to infinity for small values of k but approach $\omega_R/k = 1.41$. The Figure A.6 is a close up view of the Alfvén mode.

The final regime is for the ion plasma frequency. This mode can be seen in Figure A.7 and is

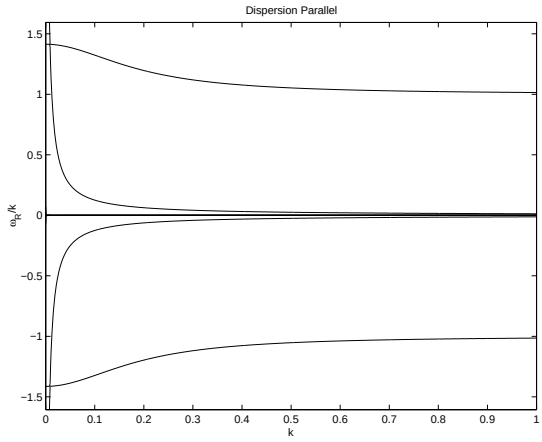

Figure A.5: Alfvén mode waves along with small magnitude L and R-mode waves for the parallel direction

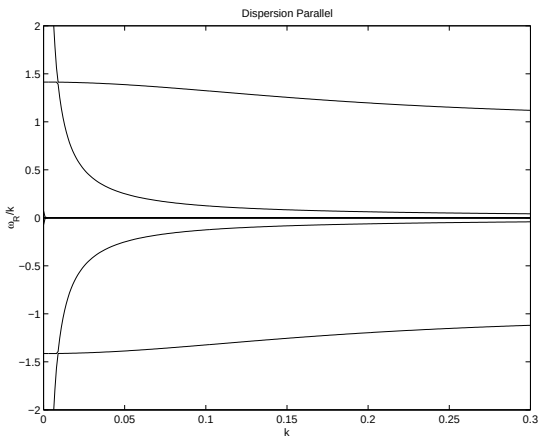

Figure A.6: Alfvén mode waves along with small magnitude L and R-mode waves for the parallel direction, close up

of order 10^{-5} for large values of k. This mode does not show up in Shumlak and Loverich's analysis and is a result of keeping the ion frequencies in the analysis.

A.6.2 Perpendicular Dispersion Analysis

The dispersion plot for the perpendicular case, $\alpha = 0$ and $\beta = k$ can be seen in Figure A.8. For the perpendicular direction, there are three main regimes with a total of six modes or waves. All the waves in the perpendicular direction go to infinite values of wavespeed, ω_R/k, for small values of spatial wavenumber k. The largest magnitude modes are the O and X-modes, totalling four waves with the same absolute value of order 10^5 for large values of k (one positive, and one negative O-mode, and one positive and one negative X-mode). The X-mode waves, similar to the L and R-mode waves of the parallel direction, have both large and small magnitude waves. Figure A.9 shows the positive O-mode and large positive magnitude X-mode waves.

The next regime is the small magnitude X-mode waves. Figure A.10 and A.11 shows these waves which are of order 10^3 for rapidly varying spatial solutions or large values of k.

The final mode is associated with the magnetosonic wave. This is the Acoustic/Alfvén wave in the parallel direction. As can be seen in Figure A.12, the waves are of order 1 for large values of k. In the non-dimensional formulation, 1 is representative of the acoustic velocity, which for large values of k, the magnetoacoustic wave approaches exactly. This is as expected as acoustic waves propagate in the real world in all directions at the same rate.

A.6.3 Infinite Wavespeeds

The infinite wavespeeds associated with pure plasma waves for small values of k was found to be due to the electron plasma frequency. This can be seen best when examining the analytical solution for the electron plasma wave Equation (A.42) when the equation is divided by k and then looking at the $k = 0$ case. However, it should be noted that the analytical solutions were derived with several simplyfying assuptions and do not tell the whole story [33].

This infinite wavespeed is well documented to exist [32, 211] and there are two reasons why this can exist in a physical model. First, the physical variations represented by these large wavelength waves are associated with small gradients. These small gradient at large distances do not effect much of a change in the solution state [33]. Second, the wavespeed is a phase velocity and it is well known that an unterminated wave can have phase velocities that are larger than the group velocity, which is associated with propagations of disturbances [32, 212]. Further, it can be shown that the group velocity becomes very small for large phase velocities in the case of the electron plasma, such that

$$v_{g,pe} = \frac{d\omega}{dk} = \frac{k}{\omega} v_{ac} = \frac{v_{ac}}{v_\phi}, \tag{A.54}$$

where $v_\phi = \omega/k$. It can be seen that as the phase velocity v_ϕ becomes larger, $v_{g,pe} \approx 0$.

A.7 Discrete Dispersion Analysis of the 5-Moment Collisionless Two Fluid Model

A dispersion analysis on the discrete system of equations for the 5-moment two-fluid model is undertaken. This is to understand where numerical difficulties may arise. The analysis proceeds in a similar manner to the non-dimensional dispersion analysis, but with the discretized form of the governing equations along with elastic collisions. In order to discretize the governing equations, the numerical scheme of this thesis is implemented to first-order. The procedure is identical to that described in Section 4.4.1. Equation 4.31 can be rearranged to give

$$\mathbf{I}\left(\tilde{\mathbf{U}}_j^{n+1} - \tilde{\mathbf{U}}_j^n\right) = \frac{\Delta t}{\Delta x_j}\left(\frac{1}{2}\right)\left[\mathbf{B}\tilde{\mathbf{U}}_{j-1}^n + \mathbf{C}\tilde{\mathbf{U}}_j^n + \mathbf{D}\tilde{\mathbf{U}}_{j+1}^n\right] + \Delta t \mathbf{E}\tilde{\mathbf{U}}_j^n, \tag{A.55}$$

where

$$\mathbf{B} = \mathbf{F}' + \frac{1}{a_{ref}}\mathbf{A}^T\mathbf{I}, \qquad \mathbf{C} = -2\frac{1}{a_{ref}}\mathbf{A}^T\mathbf{I}, \qquad \mathbf{D} = -\mathbf{F}' + \frac{1}{a_{ref}}\mathbf{A}^T\mathbf{I} \tag{A.56}$$

$$\mathbf{E}^{(1-6)} = \begin{bmatrix} 0 & 0 & 0 & 0 & 0 & 0 \\ 0 & 0 & 0 & 0 & 0 & 0 \\ 0 & 0 & 0 & \mathrm{Ke}\,\frac{B_{0,z}}{m_{ion}} & -\mathrm{Ke}\,\frac{B_{0,y}}{m_{ion}} & 0 \\ 0 & 0 & \mathrm{Ke}\,\frac{B_{0,z}}{m_{ion}} & 0 & -\mathrm{Ke}\,\frac{B_{0,x}}{m_{ion}} & 0 \\ 0 & 0 & \mathrm{Ke}\,\frac{B_{0,y}}{m_{ion}} & -\mathrm{Ke}\,\frac{B_{0,x}}{m_{ion}} & 0 & 0 \\ 0 & 0 & 0 & 0 & 0 & 0 \\ 0 & 0 & 0 & 0 & 0 & -\mathrm{Ke}\,\frac{B_{0,z}}{m_e} \\ 0 & 0 & 0 & 0 & 0 & -\mathrm{Ke}\,\frac{B_{0,y}}{m_e} \\ 0 & 0 & 0 & 0 & 0 & 0 \\ 0 & 0 & 0 & 0 & 0 & 0 \\ 0 & 0 & 0 & 0 & 0 & 0 \\ 0 & 0 & 0 & 0 & 0 & 0 \\ 0 & 0 & 0 & 0 & 0 & 0 \\ 0 & 0 & -\frac{\mathrm{Ke}}{m_{ion}}\,\frac{c^2}{a_{ref}^2} & 0 & 0 & \frac{\mathrm{Ke}}{m_e}\,\frac{c^2}{a_{ref}^2} \\ 0 & 0 & 0 & -\frac{\mathrm{Ke}}{m_{ion}}\,\frac{c^2}{a_{ref}^2} & 0 & 0 \\ 0 & 0 & 0 & 0 & -\frac{\mathrm{Ke}}{m_{ion}}\,\frac{c^2}{a_{ref}^2} & 0 \end{bmatrix} \tag{A.57}$$

$$\mathbf{E}^{(7-16)} = \begin{bmatrix} 0 & 0 & 0 & 0 & 0 & 0 & 0 & 0 & 0 & 0 \\ 0 & 0 & 0 & 0 & 0 & 0 & 0 & 0 & 0 & 0 \\ 0 & 0 & 0 & 0 & 0 & 0 & 0 & \mathrm{Ke}\,n_{ion,0} & 0 & 0 \\ 0 & 0 & 0 & 0 & 0 & 0 & 0 & 0 & \mathrm{Ke}\,n_{ion,0} & 0 \\ 0 & 0 & 0 & 0 & 0 & 0 & 0 & 0 & 0 & \mathrm{Ke}\,n_{ion,0} \\ -\mathrm{Ke}\,\frac{B_{0,z}}{m_e} & \mathrm{Ke}\,\frac{B_{0,y}}{m_e} & 0 & 0 & 0 & 0 & 0 & -\mathrm{Ke}\,n_{e,0} & 0 & 0 \\ 0 & \mathrm{Ke}\,\frac{B_{0,x}}{m_e} & 0 & 0 & 0 & 0 & 0 & 0 & -\mathrm{Ke}\,n_{e,0} & 0 \\ \mathrm{Ke}\,\frac{B_{0,x}}{m_e} & 0 & 0 & 0 & 0 & 0 & 0 & 0 & 0 & -\mathrm{Ke}\,n_{e,0} \\ 0 & 0 & 0 & 0 & 0 & 0 & 0 & 0 & 0 & 0 \\ 0 & 0 & 0 & 0 & 0 & 0 & 0 & 0 & 0 & 0 \\ 0 & 0 & 0 & 0 & 0 & 0 & 0 & 0 & 0 & 0 \\ 0 & 0 & 0 & 0 & 0 & 0 & 0 & 0 & 0 & 0 \\ 0 & 0 & 0 & 0 & 0 & 0 & 0 & 0 & 0 & 0 \\ 0 & 0 & 0 & 0 & 0 & 0 & 0 & 0 & 0 & 0 \\ \frac{\mathrm{Ke}}{m_e}\,\frac{c^2}{a_{ref}^2} & 0 & 0 & 0 & 0 & 0 & 0 & 0 & 0 & 0 \\ 0 & \frac{\mathrm{Ke}}{m_e}\,\frac{c^2}{a_{ref}^2} & 0 & 0 & 0 & 0 & 0 & 0 & 0 & 0 \end{bmatrix} \tag{A.58}$$

and

$$\mathbf{F}' = \begin{bmatrix}
0 & 0 & \frac{1}{m_{ion}} & 0 & 0 & 0 & 0 & 0 & 0 & 0 & 0 & 0 & 0 & 0 & 0 & 0 \\
0 & 0 & 0 & 0 & 0 & \frac{1}{m_e} & 0 & 0 & 0 & 0 & 0 & 0 & 0 & 0 & 0 & 0 \\
0 & 0 & 0 & 0 & 0 & 0 & 0 & 0 & (\gamma-1) & 0 & 0 & 0 & 0 & 0 & 0 & 0 \\
0 & 0 & 0 & 0 & 0 & 0 & 0 & 0 & 0 & 0 & 0 & 0 & 0 & 0 & 0 & 0 \\
0 & 0 & 0 & 0 & 0 & 0 & 0 & 0 & 0 & 0 & 0 & 0 & 0 & 0 & 0 & 0 \\
0 & 0 & 0 & 0 & 0 & 0 & 0 & 0 & 0 & (\gamma-1) & 0 & 0 & 0 & 0 & 0 & 0 \\
0 & 0 & 0 & 0 & 0 & 0 & 0 & 0 & 0 & 0 & 0 & 0 & 0 & 0 & 0 & 0 \\
0 & 0 & 0 & 0 & 0 & 0 & 0 & 0 & 0 & 0 & 0 & 0 & 0 & 0 & 0 & 0 \\
0 & 0 & \frac{\gamma}{\gamma-1}\frac{p_{ion,0}}{n_{ion,0}m_{ion}} & 0 & 0 & 0 & 0 & 0 & 0 & 0 & 0 & 0 & 0 & 0 & 0 & 0 \\
0 & 0 & 0 & 0 & 0 & \frac{\gamma}{\gamma-1}\frac{p_{e,0}}{n_{e,0}m_e} & 0 & 0 & 0 & 0 & 0 & 0 & 0 & 0 & 0 & 0 \\
0 & 0 & 0 & 0 & 0 & 0 & 0 & 0 & 0 & 0 & 0 & 0 & 0 & 0 & 0 & 0 \\
0 & 0 & 0 & 0 & 0 & 0 & 0 & 0 & 0 & 0 & 0 & 0 & 0 & 0 & 0 & -1 \\
0 & 0 & 0 & 0 & 0 & 0 & 0 & 0 & 0 & 0 & 0 & 0 & 0 & 0 & 1 & 0 \\
0 & 0 & 0 & 0 & 0 & 0 & 0 & 0 & 0 & 0 & 0 & 0 & 0 & 0 & 0 & 0 \\
0 & 0 & 0 & 0 & 0 & 0 & 0 & 0 & 0 & 0 & 0 & 0 & \frac{c^2}{a_{ref}^2} & 0 & 0 & 0 \\
0 & 0 & 0 & 0 & 0 & 0 & 0 & 0 & 0 & 0 & 0 & -\frac{c^2}{a_{ref}^2} & 0 & 0 & 0 & 0
\end{bmatrix}. \tag{A.59}$$

The substitution for $\tilde{\mathbf{U}}$ is made using

$$\tilde{\mathbf{U}}_j^n = Z^n \exp\left[i\left(jk\Delta x\right)\right]\hat{\mathbf{U}} \tag{A.60}$$

to arrive at the eigen equation

$$\mathbf{A}\left(Z-1\right) = \frac{\Delta t}{\Delta x}\frac{1}{2}\left(\mathbf{B}\mathrm{e}^{-ik\Delta x} + \mathbf{C} + \mathbf{D}\mathrm{e}^{ik\Delta x}\right) + \Delta t\mathbf{E}. \tag{A.61}$$

All elements are substituted for numerical values. The collision frequency is calculated using a coulomb collision model [103, 123]. Suitable Δx and Δt values are determined through the CFL number such that

$$\mathrm{CFL} = \frac{\Delta t}{\Delta x}(u+a). \tag{A.62}$$

A.8 Results of Dispersion Analysis

The characteristic equation is derived from taking the determinant of Equation (A.55) the resultant equations are numerically solved for the complex variable Z for various values of the spatial wave number k. The complex variable Z is defined by

$$Z = \left(\exp\left[i\,\omega\Delta t\right]\right) = e^{\omega_I}\left(\cos\omega_R + i\sin\omega_R\right), \tag{A.63}$$

where ω_R and ω_I are the real and imaginary parts of ω, respectively. The following relations are used in order to determine ω_R and ω_I:

$$\omega_R = \arctan \frac{\text{Imag}(Z)}{\text{Real}(Z)}, \qquad \omega_I = \ln \frac{\text{Real}(Z)}{\cos \omega_R}, \tag{A.64}$$

with the following definition for CFL:

$$\Delta x = \Delta t \frac{(a_{ref})}{CFL}. \tag{A.65}$$

There is also a theoretical maximum value for the spatial wavenumber defined by

$$k_{max} = \frac{\pi}{\Delta x}, \tag{A.66}$$

however, plots do not have to be plotted up to this maximum value.

The system of equations was solved in matrix form as an eigenvalue problem defined by

$$\mathbf{I}Z = \mathbf{I} + \frac{\Delta t}{\Delta x}\frac{1}{2}\left(\mathbf{B}\mathrm{e}^{-ik\Delta x} + \mathbf{C} + \mathbf{D}\mathrm{e}^{ik\Delta x}\right) + \Delta t\mathbf{E}. \tag{A.67}$$

where the right hand side is the eigen matrix being solved for the eigenvalues Z. The following figures are for CFL = 0.1 with Δx varying from 0.1 to 0.0001 in orders of magnitude. The solution from the analytic dispersion analysis is also included for comparison. In Figure A.13, the phase speed is plotted against spatial wave number for various values of Δx. As the spatial resolution increases, the phase speeds better follow the behaviour of the analytic solution. Figure A.14 shows the acoustic level scale showing the same behaviour. All waves exhibited this behaviour.

Figure A.15 shows the behaviour of the imaginary component of ω associated with the stability of the various eigenmodes. The plot is made for $\Delta x = 0.001$ and for values of CFL ranging from 0.1 to 0.0001. It can be seen that there are unstable growth modes (Associated with positive values of ω_I) up till when CFL=0.0001, at which point all eigenvalues become stable. However, these small CFL and Δx values are associated with very small time steps and high computational costs.

A.9 Implicit Discrete Dispersion Analysis

Proceeding as in Chapter 4 an implicit method is used to discretize the equations. A dispersion analysis is performed using the same procedure as in Section A.8, but with Equation 4.32 to obtain

$$\begin{gathered}\mathbf{U}_a\left(\tilde{\mathbf{U}}_j^{n+1} - \tilde{\mathbf{U}}_j^{n}\right) = \\ \frac{\Delta t}{\Delta x_j}\left(\frac{1}{2}\right)\left[\mathbf{F}_a\left(\tilde{\mathbf{U}}_{j-1}^{n+1} - \tilde{\mathbf{U}}_{j+1}^{n+1}\right) + \mathbf{A}^T\mathbf{U}_a\left(\tilde{\mathbf{U}}_{j-1}^{n+1} - 2\tilde{\mathbf{U}}_j^{n+1} + \tilde{\mathbf{U}}_{j+1}^{n+1}\right)\right] + \Delta t\mathbf{S}_a\tilde{\mathbf{U}}_j^{n+1},\end{gathered} \tag{A.68}$$

where $\mathbf{U}_a = \mathbf{I}$. Also,

$$\mathbf{F}_a = \begin{bmatrix}
0 & 0 & \frac{1}{m_{ion}} & 0 & 0 & 0 & 0 & 0 & 0 & 0 & 0 & 0 & 0 & 0 & 0 & 0 \\
0 & 0 & 0 & 0 & 0 & \frac{1}{m_e} & 0 & 0 & 0 & 0 & 0 & 0 & 0 & 0 & 0 & 0 \\
0 & 0 & 0 & 0 & 0 & 0 & 0 & 0 & (\gamma-1) & 0 & 0 & 0 & 0 & 0 & 0 & 0 \\
0 & 0 & 0 & 0 & 0 & 0 & 0 & 0 & 0 & 0 & 0 & 0 & 0 & 0 & 0 & 0 \\
0 & 0 & 0 & 0 & 0 & 0 & 0 & 0 & 0 & 0 & 0 & 0 & 0 & 0 & 0 & 0 \\
0 & 0 & 0 & 0 & 0 & 0 & 0 & 0 & 0 & (\gamma-1) & 0 & 0 & 0 & 0 & 0 & 0 \\
0 & 0 & 0 & 0 & 0 & 0 & 0 & 0 & 0 & 0 & 0 & 0 & 0 & 0 & 0 & 0 \\
0 & 0 & 0 & 0 & 0 & 0 & 0 & 0 & 0 & 0 & 0 & 0 & 0 & 0 & 0 & 0 \\
0 & 0 & \frac{\gamma}{\gamma-1}\frac{p_{ion,0}}{n_{ion,0}m_{ion}} & 0 & 0 & 0 & 0 & 0 & 0 & 0 & 0 & 0 & 0 & 0 & 0 & 0 \\
0 & 0 & 0 & 0 & 0 & \frac{\gamma}{\gamma-1}\frac{p_{e,0}}{n_{e,0}m_e} & 0 & 0 & 0 & 0 & 0 & 0 & 0 & 0 & 0 & 0 \\
0 & 0 & 0 & 0 & 0 & 0 & 0 & 0 & 0 & 0 & 0 & 0 & 0 & 0 & 0 & 0 \\
0 & 0 & 0 & 0 & 0 & 0 & 0 & 0 & 0 & 0 & 0 & 0 & 0 & 0 & 0 & -1 \\
0 & 0 & 0 & 0 & 0 & 0 & 0 & 0 & 0 & 0 & 0 & 0 & 0 & 0 & 1 & 0 \\
0 & 0 & 0 & 0 & 0 & 0 & 0 & 0 & 0 & 0 & 0 & 0 & 0 & 0 & 0 & 0 \\
0 & 0 & 0 & 0 & 0 & 0 & 0 & 0 & 0 & 0 & 0 & 0 & \frac{c^2}{a_{ref}^2} & 0 & 0 & 0 \\
0 & 0 & 0 & 0 & 0 & 0 & 0 & 0 & 0 & 0 & 0 & -\frac{c^2}{a_{ref}^2} & 0 & 0 & 0 & 0
\end{bmatrix}, \tag{A.69}$$

$$\mathbf{S}_a^{(1-6)} = \begin{bmatrix}
0 & 0 & 0 & 0 & 0 & 0 \\
0 & 0 & 0 & 0 & 0 & 0 \\
0 & 0 & 0 & \mathrm{Ke}\,\frac{B_{0,z}}{m_{ion}} & -\mathrm{Ke}\,\frac{B_{0,y}}{m_{ion}} & 0 \\
0 & 0 & \mathrm{Ke}\,\frac{B_{0,z}}{m_{ion}} & 0 & -\mathrm{Ke}\,\frac{B_{0,x}}{m_{ion}} & 0 \\
0 & 0 & \mathrm{Ke}\,\frac{B_{0,y}}{m_{ion}} & -\mathrm{Ke}\,\frac{B_{0,x}}{m_{ion}} & 0 & 0 \\
0 & 0 & 0 & 0 & 0 & 0 \\
0 & 0 & 0 & 0 & 0 & -\mathrm{Ke}\,\frac{B_{0,z}}{m_e} \\
0 & 0 & 0 & 0 & 0 & -\mathrm{Ke}\,\frac{B_{0,y}}{m_e} \\
0 & 0 & 0 & 0 & 0 & 0 \\
0 & 0 & 0 & 0 & 0 & 0 \\
0 & 0 & 0 & 0 & 0 & 0 \\
0 & 0 & 0 & 0 & 0 & 0 \\
0 & 0 & 0 & 0 & 0 & 0 \\
0 & 0 & -\frac{\mathrm{Ke}}{m_{ion}}\frac{c^2}{a_{ref}^2} & 0 & 0 & \frac{\mathrm{Ke}}{m_e}\frac{c^2}{a_{ref}^2} \\
0 & 0 & 0 & -\frac{\mathrm{Ke}}{m_{ion}}\frac{c^2}{a_{ref}^2} & 0 & 0 \\
0 & 0 & 0 & 0 & -\frac{\mathrm{Ke}}{m_{ion}}\frac{c^2}{a_{ref}^2} & 0
\end{bmatrix}, \tag{A.70}$$

and

$$\mathbf{S}_a^{(7-16)} = \begin{bmatrix} 0 & 0 & 0 & 0 & 0 & 0 & 0 & 0 & 0 & 0 \\ 0 & 0 & 0 & 0 & 0 & 0 & 0 & 0 & 0 & 0 \\ 0 & 0 & 0 & 0 & 0 & 0 & 0 & \mathrm{Ke}\, n_{ion,0} & 0 & 0 \\ 0 & 0 & 0 & 0 & 0 & 0 & 0 & 0 & \mathrm{Ke}\, n_{ion,0} & 0 \\ 0 & 0 & 0 & 0 & 0 & 0 & 0 & 0 & 0 & \mathrm{Ke}\, n_{ion,0} \\ -\mathrm{Ke}\, \frac{B_{0,z}}{m_e} & \mathrm{Ke}\, \frac{B_{0,y}}{m_e} & 0 & 0 & 0 & 0 & 0 & -\mathrm{Ke}\, n_{e,0} & 0 & 0 \\ 0 & \mathrm{Ke}\, \frac{B_{0,x}}{m_e} & 0 & 0 & 0 & 0 & 0 & 0 & -\mathrm{Ke}\, n_{e,0} & 0 \\ \mathrm{Ke}\, \frac{B_{0,x}}{m_e} & 0 & 0 & 0 & 0 & 0 & 0 & 0 & 0 & -\mathrm{Ke}\, n_{e,0} \\ 0 & 0 & 0 & 0 & 0 & 0 & 0 & 0 & 0 & 0 \\ 0 & 0 & 0 & 0 & 0 & 0 & 0 & 0 & 0 & 0 \\ 0 & 0 & 0 & 0 & 0 & 0 & 0 & 0 & 0 & 0 \\ 0 & 0 & 0 & 0 & 0 & 0 & 0 & 0 & 0 & 0 \\ 0 & 0 & 0 & 0 & 0 & 0 & 0 & 0 & 0 & 0 \\ 0 & 0 & 0 & 0 & 0 & 0 & 0 & 0 & 0 & 0 \\ \frac{\mathrm{Ke}}{m_e}\, \frac{c^2}{a_{ref}^2} & 0 & 0 & 0 & 0 & 0 & 0 & 0 & 0 & 0 \\ 0 & \frac{\mathrm{Ke}}{m_e}\, \frac{c^2}{a_{ref}^2} & 0 & 0 & 0 & 0 & 0 & 0 & 0 & 0 \end{bmatrix}. \quad \text{(A.71)}$$

Then making the substitution of Equation (4.35) in Equation (A.68) and rearranging in eigen problem form gives

$$\mathbf{I}Z = \left[\mathbf{U}_a - \frac{\Delta t}{\Delta x_j}\left(\frac{1}{2}\right)\left[\mathbf{F}_a\left(e^{-i\,k\Delta x} - e^{i\,k\Delta x}\right) + \mathbf{A}^T\mathbf{U}_a\left(e^{-i\,k\Delta x} - 2 + e^{i\,k\Delta x}\right)\right] + \Delta t\mathbf{S}_a\right]^{-1}\mathbf{U}_a \quad \text{(A.72)}$$

which is then solved for Z. Then Z is deconstructed as in Section A.8.

A.10 Results of Implicit Dispersion Analysis

The system of equations was solved for $\Delta x = 0.1$ and CFL's ranging from 1.0 to 0.001. This was to show that there is stability even at course grid sizes and high CFL numbers. As can be seen from Figure A.16 and A.17, it is indeed unconditionally stable, however, from Figure A.18 it can be seen that at these course grid sizes and CFL's the phase speed behaviour is not very accurate. To show that accurate behaviour can be recovered, the Δx value was reduced to 0.001 and Figures A.19 and A.20 were obtained that shows the solutions approach analytic values as the CFL value decreases and that the scheme is still stable.

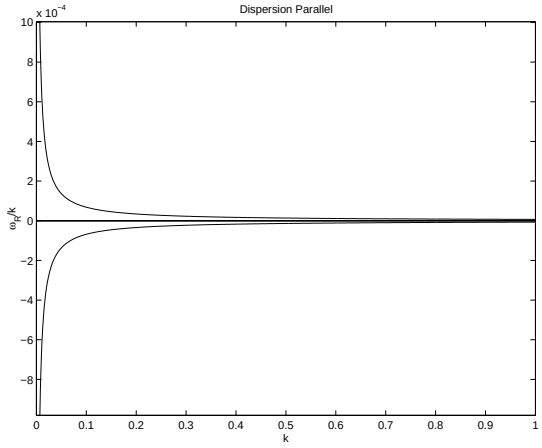

Figure A.7: Ion plasma waves for the parallel direction

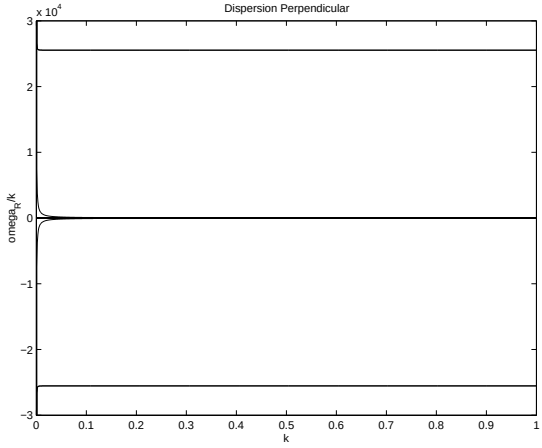

Figure A.8: Dispersion analysis for the perpendicular direction

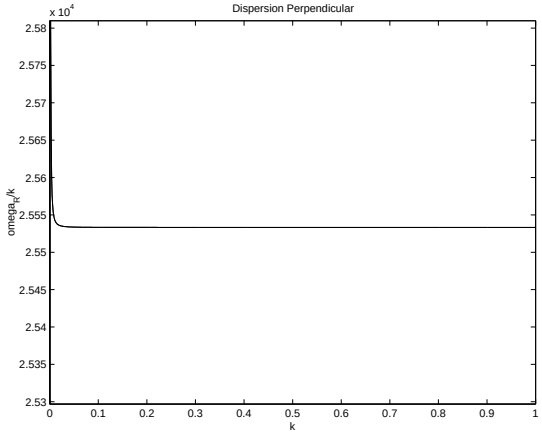

Figure A.9: Positive O-mode and large magnitude positive X-mode for the perpendicular direction

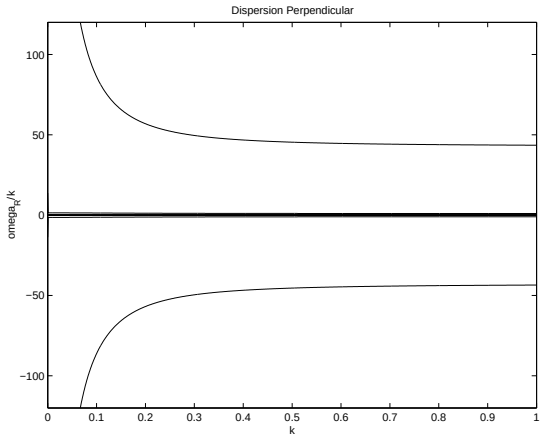

Figure A.10: Small magnitude X-mode for the perpendicular direction

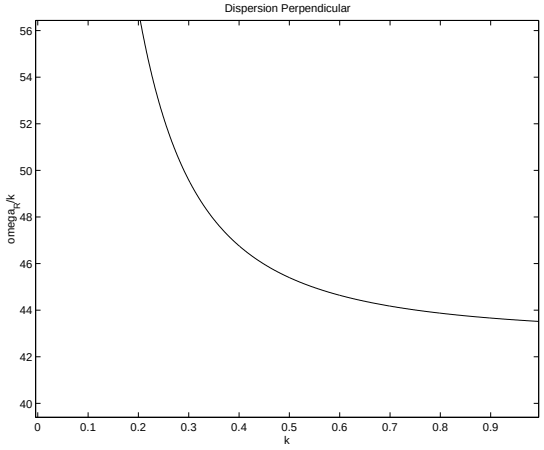

Figure A.11: Small magnitude positive X-mode for the perpendicular direction

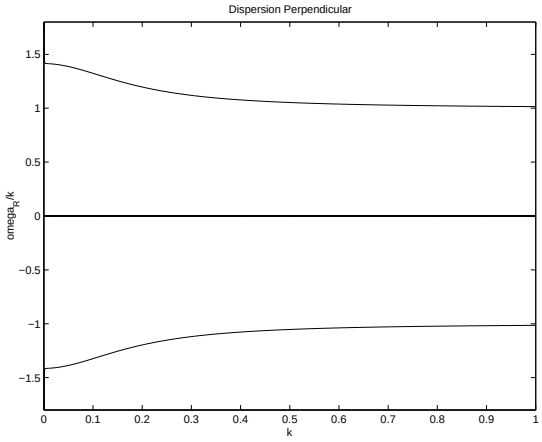

Figure A.12: Magnetosonic wave for the perpendicular direction

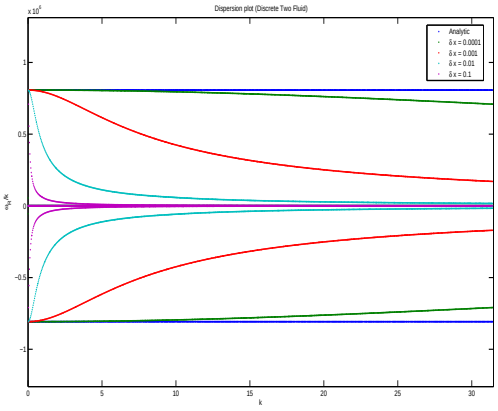

Figure A.13: Large scale dispersion analysis for the discrete two fluid system for various values of Δx compared to the analytic solution. CFL = 0.1

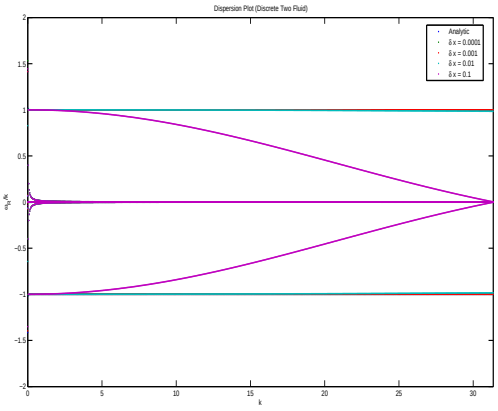

Figure A.14: Dispersion analysis for the discrete two fluid system for various values of Δx compared to the analytic solution. CFL = 0.1, acoustic

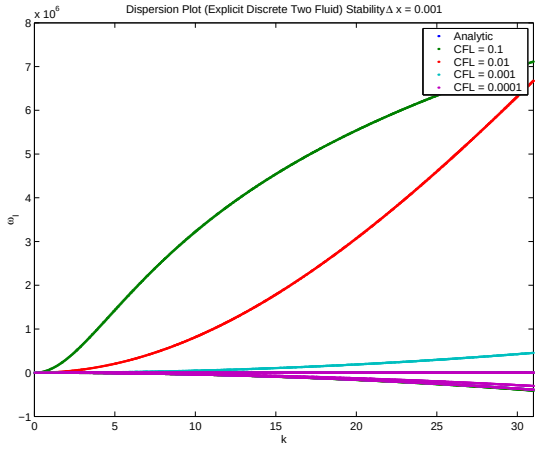

Figure A.15: Large scale dispersion analysis for the discrete two fluid system for various values of CFL for $\Delta x = 0.001$. Stability plot ω_I vs. k

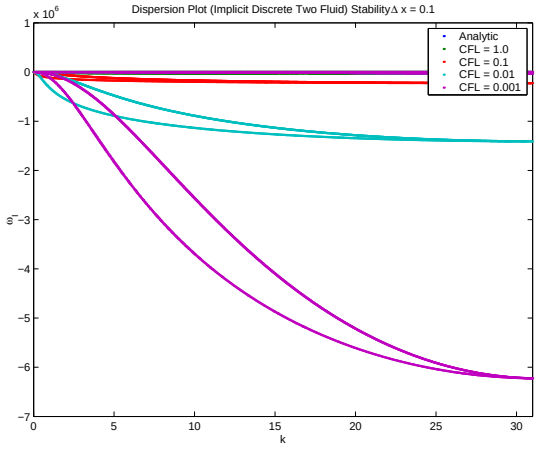

Figure A.16: Large scale dispersion analysis for the implicit discrete two fluid system for various values of CFL compared to the analytic solution for stability. $\Delta x = 0.1$

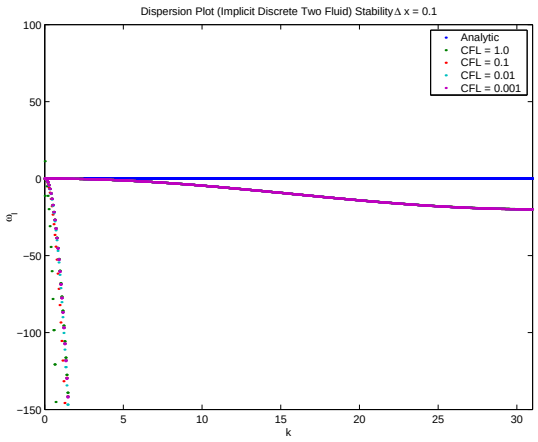

Figure A.17: Large scale dispersion analysis for the implicit discrete two fluid system for various values of CFL compared to the analytic solution for stability. $\Delta x = 0.1$

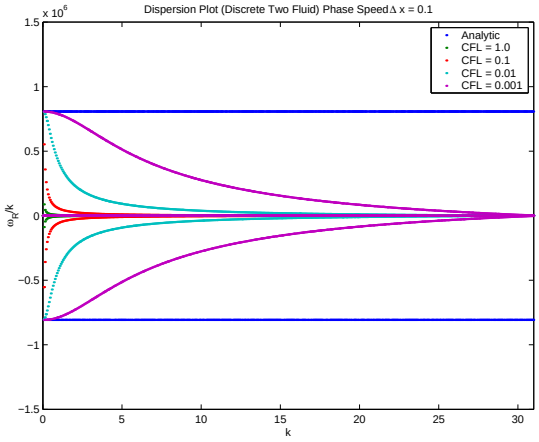

Figure A.18: Large scale dispersion analysis for the implicit discrete two fluid system for various values of CFL compared to the analytic solution for phase speed. $\Delta x = 0.1$

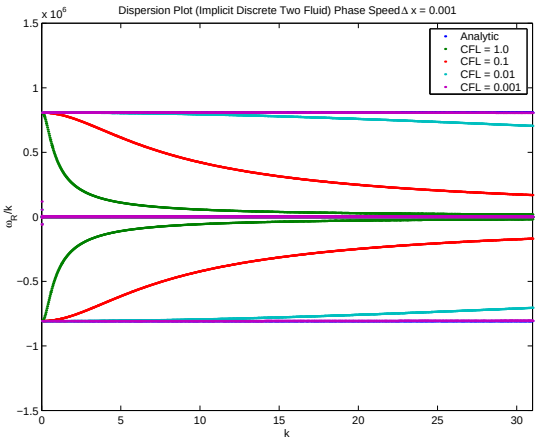

Figure A.19: Large scale dispersion analysis for the implicit discrete two fluid system for various values of CFL compared to the analytic solution for phase speed. $\Delta x = 0.001$

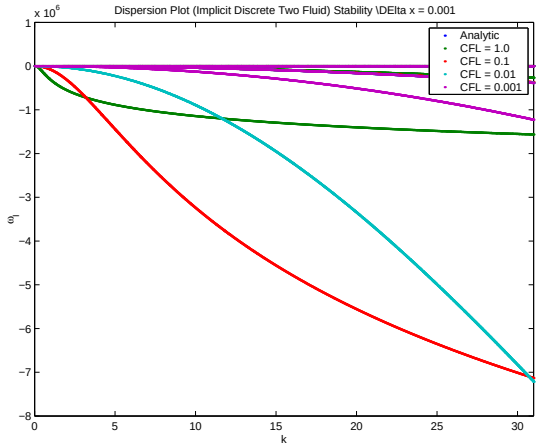

Figure A.20: Large scale dispersion analysis for the implicit discrete two fluid system for various values of CFL compared to the analytic solution for stability. $\Delta x = 0.001$

Appendix B

Additional Derivations Related to the Numerical Solution Scheme

B.1 Overview

This section contains extra derivations used to develop the numerical solution procedure utilized in this thesis. The HLLE approximate numerical Riemann solver and the banded tridiagonal matrix for the implicit 1D scheme of Chapter 5 is derived.

B.2 Harten-Lax-van Leer-Einfeldt (HLLE) Flux Function

In order to determine the numerical flux in Equations (5.6), the interface flux between the two adjacent computational cells is required. To determine this middle state flux, the interface is treated as a one-dimensional Riemann initial value problem assuming a short time interval allowing the source terms to be neglected. The approximate Riemann solver of Harten-Lax-van Leer-Einfeldt (HLLE) [132] is used.

The HLLE approximate Riemann solver is derived by solving for the fluxes around a control volume centered on the interface of the two cells (or rather at the interface for the Riemann initial value problem) and a control volume where one side is coincident with the interface (see Figures B.1 and B.2). The control volume in Figure B.1 is considered and the one-dimensional integral form of the conservation equation, Equations (5.2), are taken and integrated around

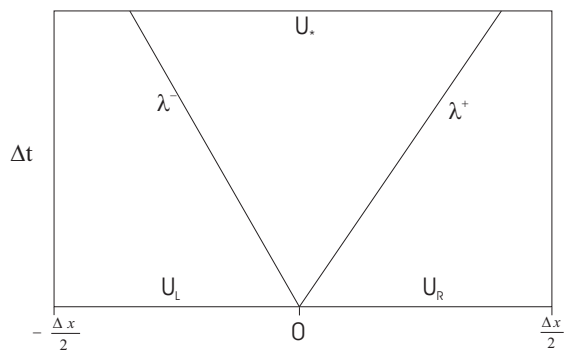

Figure B.1: Control volume centered on x=0 interface

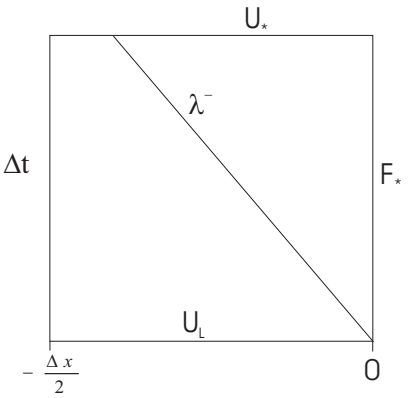

Figure B.2: Control volume on left side of interface

the control volume to get

$$0 = \mathbf{U_L}\frac{\Delta x}{2} + \mathbf{U_R}\frac{\Delta x}{2} - \mathbf{F_R}\Delta t - \mathbf{U_R}\left(\frac{\Delta x}{2} - \lambda^+\Delta t\right) - \mathbf{U}_*\lambda^+\Delta t \\ +\mathbf{U}_*\lambda^-\Delta t - \mathbf{U_L}\left(\frac{\Delta x}{2} + \lambda^-\Delta t\right) + \mathbf{F_L}\Delta t \tag{B.1}$$

where $\mathbf{U_L}$ and $\mathbf{U_R}$ are the left and right solution states, $\mathbf{F_L}$ and $\mathbf{F_R}$ are the left and right fluxes. The largest and smallest signal velocities are λ^+ and λ^- respectively. The intermediate state $\mathbf{U}_*$ is sought. Rearranging for $\mathbf{U}_*$ gives

$$\mathbf{U}_* = \frac{\lambda^+\mathbf{U_R} - \lambda^-\mathbf{U_L}}{\lambda^+ - \lambda^-} - \frac{(\mathbf{F_R} - \mathbf{F_L})}{\lambda^+ - \lambda^-}. \tag{B.2}$$

This gives the solution for $\mathbf{U}_*$ and now the volume of Figure B.2 is considered and integrated around to determine the flux at the interface such that

$$0 = \mathbf{U_L}\frac{\Delta x}{2} - \mathbf{F}_*\Delta t + \mathbf{U}_*\lambda^-\Delta t - \mathbf{U_L}\left(\frac{\Delta x}{2} + \lambda^-\Delta t\right) + \mathbf{F_L}\Delta t. \tag{B.3}$$

Rearranging and substituting for $\mathbf{U}_*$ from Equation (B.2) above results in

$$\mathbf{F}_* = \frac{\lambda^+\mathbf{F_L} - \lambda^-\mathbf{F_R}}{\lambda^+ - \lambda^-} + \frac{\lambda^+\lambda^-}{\lambda^+ - \lambda^-}\left(\mathbf{U_R} - \mathbf{U_L}\right). \tag{B.4}$$

This is the HLLE flux function and is used if the value of $x/t = 0$ lies within the region defined by the fast and slow signal velocities according to

$$\mathbf{F} = \begin{cases} \mathbf{F_L} & \text{for } \left(\frac{x}{t}\right) < \lambda^-, \\ \mathbf{F}_* & \text{for } \lambda^- \le \left(\frac{x}{t}\right) \le \lambda^+, \\ \mathbf{F_R} & \text{for } \left(\frac{x}{t}\right) > \lambda^+. \end{cases} \tag{B.5}$$

B.3 Implicit Banded Tridiagonal Matrix System

In order to derive the banded tridiagonal matrix system used in the dual time formulation for the numerical scheme in Chapter 5, the implicit Euler time marching method along with a HLLE type flux function was used for the first-order numerical scheme along with piecewise constant spatial reconstruction. A first-order scheme can be used for the left hand side matrix because the dual time formulation is used to iterate to a higher-order solution. The interface flux terms for the implicit Euler equation, Equation 4.30, are linearized as so that

$$\begin{aligned}\mathcal{F}^{n+1}_{i+\frac{1}{2}} = \mathcal{F}^{n}_{i+\frac{1}{2}} &+ \frac{\partial \mathcal{F}^{n}_{i+\frac{1}{2}}}{\partial \mathbf{U_L}} \frac{\partial \mathbf{U_L}}{\partial \mathbf{U}_i} \frac{\partial \mathbf{U}_i}{\partial t}\Delta t + \frac{\partial \mathcal{F}^{n}_{i+\frac{1}{2}}}{\partial \mathbf{U_R}} \frac{\partial \mathbf{U_R}}{\partial \mathbf{U}_i} \frac{\partial \mathbf{U}_i}{\partial t}\Delta t \\ &+ \frac{\partial \mathcal{F}^{n}_{i+\frac{1}{2}}}{\partial \mathbf{U_L}} \frac{\partial \mathbf{U_L}}{\partial \mathbf{U}_{i+1}} \frac{\partial \mathbf{U}_{i+1}}{\partial t}\Delta t + \frac{\partial \mathcal{F}^{n}_{i+\frac{1}{2}}}{\partial \mathbf{U_R}} \frac{\partial \mathbf{U_R}}{\partial \mathbf{U}_{i+1}} \frac{\partial \mathbf{U}_{i+1}}{\partial t}\Delta t,\end{aligned} \tag{B.6}$$

$$\begin{aligned}\mathcal{F}^{n+1}_{i-\frac{1}{2}} = \mathcal{F}^{n}_{i-\frac{1}{2}} &+ \frac{\partial \mathcal{F}^{n}_{i-\frac{1}{2}}}{\partial \mathbf{U_L}} \frac{\partial \mathbf{U_L}}{\partial \mathbf{U}_{i-1}} \frac{\partial \mathbf{U}_{i-1}}{\partial t}\Delta t + \frac{\partial \mathcal{F}^{n}_{i-\frac{1}{2}}}{\partial \mathbf{U_R}} \frac{\partial \mathbf{U_R}}{\partial \mathbf{U}_{i-1}} \frac{\partial \mathbf{U}_{i-1}}{\partial t}\Delta t \\ &+ \frac{\partial \mathcal{F}^{n}_{i-\frac{1}{2}}}{\partial \mathbf{U_L}} \frac{\partial \mathbf{U_L}}{\partial \mathbf{U}_{i}} \frac{\partial \mathbf{U}_{i}}{\partial t}\Delta t + \frac{\partial \mathcal{F}^{n}_{i-\frac{1}{2}}}{\partial \mathbf{U_R}} \frac{\partial \mathbf{U_R}}{\partial \mathbf{U}_{i}} \frac{\partial \mathbf{U}_{i}}{\partial t}\Delta t.\end{aligned} \tag{B.7}$$

Note that for piecewise constant reconstruction, the left and right states are just the cell centered values of the left or right cells of the interface. Therefore the linearized terms simplify to

$$\mathcal{F}^{n+1}_{i+\frac{1}{2}} = \mathcal{F}^{n}_{i+\frac{1}{2}} + \frac{\partial \mathcal{F}^{n}_{i+\frac{1}{2}}}{\partial \mathbf{U}_i} \frac{\partial \mathbf{U}_i}{\partial t}\Delta t + \frac{\partial \mathcal{F}^{n}_{i+\frac{1}{2}}}{\partial \mathbf{U}_{i+1}} \frac{\partial \mathbf{U}_{i+1}}{\partial t}\Delta t, \tag{B.8}$$

$$\mathcal{F}^{n+1}_{i-\frac{1}{2}} = \mathcal{F}^{n}_{i-\frac{1}{2}} + \frac{\partial \mathcal{F}^{n}_{i-\frac{1}{2}}}{\partial \mathbf{U}_{i-1}} \frac{\partial \mathbf{U}_{i-1}}{\partial t}\Delta t + \frac{\partial \mathcal{F}^{n}_{i-\frac{1}{2}}}{\partial \mathbf{U}_i} \frac{\partial \mathbf{U}_i}{\partial t}\Delta t. \tag{B.9}$$

Further, by discretizing the time derivative it can be shown that

$$\mathcal{F}^{n+1}_{i+\frac{1}{2}} = \mathcal{F}^{n}_{i+\frac{1}{2}} + \frac{\partial \mathcal{F}^{n}_{i+\frac{1}{2}}}{\partial \mathbf{U}_i} \Delta \mathbf{U}^n_i + \frac{\partial \mathcal{F}^{n}_{i+\frac{1}{2}}}{\partial \mathbf{U}_{i+1}} \Delta \mathbf{U}^n_{i+1}, \tag{B.10}$$

$$\mathcal{F}^{n+1}_{i-\frac{1}{2}} = \mathcal{F}^{n}_{i-\frac{1}{2}} + \frac{\partial \mathcal{F}^{n}_{i-\frac{1}{2}}}{\partial \mathbf{U}_{i-1}} \Delta \mathbf{U}^n_{i-1} + \frac{\partial \mathcal{F}^{n}_{i-\frac{1}{2}}}{\partial \mathbf{U}_i} \Delta \mathbf{U}^n_{i}. \tag{B.11}$$

Using the HLLE scheme, Equations B.5 and B.4, results in

$$\mathcal{F}_{i+\frac{1}{2}} = \begin{cases} \mathbf{F}_i & \text{for } \left(\frac{x}{t}\right) < \lambda^- \\ \mathbf{F}_{*i+\frac{1}{2}} & \text{for } \lambda^- \le \left(\frac{x}{t}\right) \le \lambda^+ \\ \mathbf{F}_{i+1} & \text{for } \left(\frac{x}{t}\right) > \lambda^+ \end{cases}, \qquad \mathcal{F}_{i-\frac{1}{2}} = \begin{cases} \mathbf{F}_{i-1} & \text{for } \left(\frac{x}{t}\right) < \lambda^- \\ \mathbf{F}_{*i-\frac{1}{2}} & \text{for } \lambda^- \le \left(\frac{x}{t}\right) \le \lambda^+ \\ \mathbf{F}_{i} & \text{for } \left(\frac{x}{t}\right) > \lambda^+ \end{cases}, \tag{B.12}$$

and

$$\mathbf{F}_{*i+\frac{1}{2}} = \frac{\lambda^+ \mathbf{F}_i - \lambda^- \mathbf{F}_{i+1}}{\lambda^+ - \lambda^-} + \frac{\lambda^+ \lambda^-}{\lambda^+ - \lambda^-} \left(\mathbf{U}_{i+1} - \mathbf{U}_i\right), \tag{B.13}$$

$$\mathbf{F}_{*i-\frac{1}{2}} = \frac{\lambda^+ \mathbf{F}_{i-1} - \lambda^- \mathbf{F}_i}{\lambda^+ - \lambda^-} + \frac{\lambda^+ \lambda^-}{\lambda^+ - \lambda^-} \left(\mathbf{U}_{i} - \mathbf{U}_{i-1}\right). \tag{B.14}$$

This means that when forming the matrices for the implicit method, it can be written such that

$$\left(\mathbf{I}+\frac{\Delta t}{\Delta x}\frac{\partial \mathcal{F}^n_{i+\frac{1}{2}}}{\partial \mathbf{U}_i}-\frac{\Delta t}{\Delta x}\frac{\partial \mathcal{F}^n_{i-\frac{1}{2}}}{\partial \mathbf{U}_i}-\Delta t\left.\frac{\partial \mathbf{S}}{\partial \mathbf{U}}\right|^n_i\right)\Delta\mathbf{U}^n_i+\frac{\Delta t}{\Delta x}\left(\frac{\partial \mathcal{F}^n_{i+\frac{1}{2}}}{\partial \mathbf{U}_{i+1}}\Delta\mathbf{U}^n_{i+1}-\frac{\partial \mathcal{F}^n_{i-\frac{1}{2}}}{\partial \mathbf{U}_{i-1}}\Delta\mathbf{U}^n_{i-1}\right)$$
$$=-\frac{\Delta t}{\Delta x}\left(\mathcal{F}^n_{i+\frac{1}{2}}-\mathcal{F}^n_{i-\frac{1}{2}}\right)+\Delta t\mathbf{S}^n_i. \tag{B.15}$$

The terms on the left hand side form a tridiagonal matrix where the flux Jacobian terms are determined as follows. Each flux Jacobian term has three cases:

$$\frac{\partial \mathcal{F}^n_{i+\frac{1}{2}}}{\partial \mathbf{U}_{i+1}}=\begin{cases}\mathbf{0} & \text{for } \left(\frac{x}{t}\right)<\lambda^-,\\ -\left(\frac{\lambda^-}{\lambda^+-\lambda^-}\left.\frac{\partial \mathbf{F}}{\partial \mathbf{U}}\right|^n_{i+1}-\frac{\lambda^+\lambda^-}{\lambda^+-\lambda^-}\mathbf{I}\right) & \text{for } \lambda^-\le\left(\frac{x}{t}\right)\le\lambda^+,\\ \left.\frac{\partial \mathbf{F}}{\partial \mathbf{U}}\right|^n_{i+1} & \text{for } \left(\frac{x}{t}\right)>\lambda^+,\end{cases} \tag{B.16}$$

$$\frac{\partial \mathcal{F}^n_{i+\frac{1}{2}}}{\partial \mathbf{U}_{i}}=\begin{cases}\left.\frac{\partial \mathbf{F}}{\partial \mathbf{U}}\right|^n_{i} & \text{for } \left(\frac{x}{t}\right)<\lambda^-,\\ \left(\frac{\lambda^+}{\lambda^+-\lambda^-}\left.\frac{\partial \mathbf{F}}{\partial \mathbf{U}}\right|^n_{i}-\frac{\lambda^+\lambda^-}{\lambda^+-\lambda^-}\mathbf{I}\right) & \text{for } \lambda^-\le\left(\frac{x}{t}\right)\le\lambda^+,\\ \mathbf{0} & \text{for } \left(\frac{x}{t}\right)>\lambda^+,\end{cases} \tag{B.17}$$

and

$$\frac{\partial \mathcal{F}^n_{i-\frac{1}{2}}}{\partial \mathbf{U}_{i}}=\begin{cases}\mathbf{0} & \text{for } \left(\frac{x}{t}\right)<\lambda^-,\\ -\left(\frac{\lambda^-}{\lambda^+-\lambda^-}\left.\frac{\partial \mathbf{F}}{\partial \mathbf{U}}\right|^n_{i}-\frac{\lambda^+\lambda^-}{\lambda^+-\lambda^-}\mathbf{I}\right) & \text{for } \lambda^-\le\left(\frac{x}{t}\right)\le\lambda^+,\\ \left.\frac{\partial \mathbf{F}}{\partial \mathbf{U}}\right|^n_{i} & \text{for } \left(\frac{x}{t}\right)>\lambda^+,\end{cases} \tag{B.18}$$

$$\frac{\partial \mathcal{F}^n_{i-\frac{1}{2}}}{\partial \mathbf{U}_{i-1}}=\begin{cases}\left.\frac{\partial \mathbf{F}}{\partial \mathbf{U}}\right|^n_{i-1} & \text{for } \left(\frac{x}{t}\right)<\lambda^-,\\ \left(\frac{\lambda^+}{\lambda^+-\lambda^-}\left.\frac{\partial \mathbf{F}}{\partial \mathbf{U}}\right|^n_{i-1}-\frac{\lambda^+\lambda^-}{\lambda^+-\lambda^-}\mathbf{I}\right) & \text{for } \lambda^-\le\left(\frac{x}{t}\right)\le\lambda^+,\\ \mathbf{0} & \text{for } \left(\frac{x}{t}\right)>\lambda^+.\end{cases} \tag{B.19}$$

It should be noted that the solution to the Maxwell's equation is taken to be the left state since the $x/t=0$ line lies on a stationary characteristic and so could be either. The scheme solves the HLLE flux function, and therefore the flux Jacobians separately for each of the species and Maxwell's equations at every step, so the combined flux Jacobian will be composed of three blocks down the diagonal of the matrix. This is because the fluxes are not coupled to any of the other equations so can therefore be calculated individually before forming the matrix. Because of the lack of cross coupling, these blocks lie on the diagonal of the matrix for the entire system. This characteristic may be used later to speed up the matrix inversion.

Appendix C

GLM Maxwell's Equations Eigenstructure and Numerical Flux Function Derivations

C.1 Overview

This section contains a complete eigenstructure for the GLM Maxwell's equations. There is also a comparison between the HLLE flux function and the Godunov exact flux function for the GLM Maxwell's equations. The Maxwell's equations with and without divergence cleaning will be presented.

C.2 Eigenstructure of the Non-GLM Maxwell's Equations

This section lists useful matricies and vectors for the Maxwell's equations without divergence cleaning. The equations for Faraday's Law and Ampere's Law can be rearranged into the following weak conservative form in 1D:

$$\frac{\partial \mathrm{U}}{\partial t} + \frac{\partial \mathrm{F}}{\partial x} = \mathrm{S}, \tag{C.1}$$

where

$$\mathrm{U} = \begin{bmatrix} B_x \\ B_y \\ B_z \\ D_x \\ D_y \\ D_z \end{bmatrix}. \qquad \mathrm{V} = \begin{bmatrix} B_x \\ B_y \\ B_z \\ E_x \\ E_y \\ E_z \end{bmatrix}. \qquad \mathrm{F} = \begin{bmatrix} 0 \\ -E_z \\ E_y \\ 0 \\ H_z \\ -H_y \end{bmatrix}, \qquad \mathrm{S} = \begin{bmatrix} 0 \\ 0 \\ 0 \\ -j_x \\ -j_y \\ -j_z \end{bmatrix}. \tag{C.2}$$

Taking the hyperbolic part and rearranging for the primitive variables results in

$$\frac{\partial \mathrm{U}}{\partial \mathrm{V}}\frac{\partial \mathrm{V}}{\partial t} + \frac{\partial \mathrm{F}}{\partial \mathrm{V}}\frac{\partial \mathrm{V}}{\partial x} = \mathbf{0}, \qquad \frac{\partial \mathrm{V}}{\partial t} + \mathcal{A}\frac{\partial \mathrm{V}}{\partial x} = \mathbf{0}, \tag{C.3}$$

where

$$\mathcal{A} = \frac{\partial \mathrm{V}}{\partial \mathrm{U}}\frac{\partial \mathrm{F}}{\partial \mathrm{V}} = \begin{bmatrix} 0 & 0 & 0 & 0 & 0 & 0 \\ 0 & 0 & 0 & 0 & 0 & -1 \\ 0 & 0 & 0 & 0 & 1 & 0 \\ 0 & 0 & 0 & 0 & 0 & 0 \\ 0 & 0 & \frac{1}{\varepsilon_0\mu_0} & 0 & 0 & 0 \\ 0 & -\frac{1}{\varepsilon_0\mu_0} & 0 & 0 & & \end{bmatrix}. \tag{C.4}$$

The right eigenvectors are arranged in columns as follows:

$$\mathbf{R} = \begin{bmatrix} 0 & 0 & 0 & 1 & 0 & 0 \\ \sqrt{\frac{\mu_0}{\varepsilon_0}} & 0 & 0 & 0 & -\sqrt{\frac{\mu_0}{\varepsilon_0}} & 0 \\ 0 & -\sqrt{\frac{\mu_0}{\varepsilon_0}} & 0 & 0 & 0 & \sqrt{\frac{\mu_0}{\varepsilon_0}} \\ 0 & 0 & 1 & 0 & 0 & 0 \\ 0 & 1 & 0 & 0 & 0 & 1 \\ 1 & 0 & 0 & 0 & 1 & 0 \end{bmatrix}, \tag{C.5}$$

and are associated with the eigenvalues in order,

$$(-c, -c, 0, 0, c, c). \tag{C.6}$$

The left eigenvector matrix, $\mathbf{R^{-1}}$, is

$$\mathbf{L} = \mathbf{R^{-1}} = \begin{bmatrix} 0 & 1/2\sqrt{\frac{\varepsilon_0}{\mu_0}} & 0 & 0 & 0 & 1/2 \\ 0 & 0 & -1/2\sqrt{\frac{\varepsilon_0}{\mu_0}} & 0 & 1/2 & 0 \\ 0 & 0 & 0 & 1 & 0 & 0 \\ 1 & 0 & 0 & 0 & 0 & 0 \\ 0 & -1/2\sqrt{\frac{\varepsilon_0}{\mu_0}} & 0 & 0 & 0 & 1/2 \\ 0 & 0 & 1/2\sqrt{\frac{\varepsilon_0}{\mu_0}} & 0 & 1/2 & 0 \end{bmatrix} \tag{C.7}$$

where the rows are the left eigen vectors arranged in the same order. Characteristic variables obtained from $\mathbf{L}_{glm,p}\mathbf{W}_{glm} = \mathbf{L}_{glm,c}\mathbf{U}_{glm} =$ are

$$\left[\frac{1}{2}\left(\varepsilon_0 E_z + \sqrt{\frac{\varepsilon_0}{\mu_0}}B_y\right), \frac{1}{2}\left(\varepsilon_0 E_y - \sqrt{\frac{\varepsilon_0}{\mu_0}}B_z\right), \varepsilon_0 E_x, B_x, \frac{1}{2}\left(\varepsilon_0 E_z - \sqrt{\frac{\varepsilon_0}{\mu_0}}B_y\right), \frac{1}{2}\left(\varepsilon_0 E_y + \sqrt{\frac{\varepsilon_0}{\mu_0}}B_z\right)\right]. \tag{C.8}$$

The method of characteristics state that the characteristic variables are constant along the characteristic lines with slopes of the eigenvalues (for the linear Maxwell's equations). Figure 6.1 represents an interface between two regions i and o with two intermediate states in the middle separated by the stationary characteristic which represents the x-direction (normal) electric and magnetic fields. An interesting note about the stationary state is that it is associated with changes in E_x and B_x, however, the flux does not change across the state because it is stationary. This can be seen when taking the 1D, line integral form of the hyperbolic conservation laws

$$\oint (\mathbf{U}dx - \mathbf{F}dt) = 0 \tag{C.9}$$

and integrating it counter-clockwise around the control volume integral around the stationary state as seen in Figure C.1 such that

$$\mathbf{U}_1\frac{dx}{2} + \mathbf{U}_2\frac{dx}{2} - \mathbf{F}_2 dt - \mathbf{U}_2\frac{dx}{2} - \mathbf{U}_1\frac{dx}{2} + \mathbf{F}_1 dt = 0 \tag{C.10}$$

or

$$\mathbf{F}_1 = \mathbf{F}_2. \tag{C.11}$$

More generally for linearized waves,

$$\Delta\mathbf{F} = a\Delta\mathbf{U} \tag{C.12}$$

where a is the velocity of the characteristic wave splitting the control volume. Since the characteristic only affects E_x and B_x, the other variables will remain continuous across the interface. Each variable can be solved as follows where $E_{1,y} = E_{2,y} = E_y$, $E_{1,z} = E_{2,z} = E_z$, $B_{1,y} = B_{2,y} = B_y$ and $B_{1,z} = B_{2,z} = B_z$ and

$$(E_z + cB_y) = (E_{o,z} + cB_{o,y}), \tag{C.13}$$

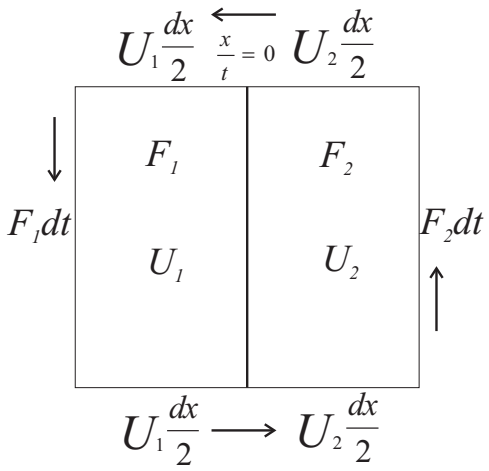

Figure C.1: Finite Volume around stationary state

$$(E_z - cB_y) = (E_{i,z} - cB_{i,y}), \tag{C.14}$$

where E_z and B_y was solved for by adding and subtracting Equations (C.13) and (C.14) as an example. Repeating the above calculations results in

$$\begin{array}{rclcrcl} B_y &=& \frac{1}{2}\left((B_{i,y}+B_{o,y})+\frac{1}{c}(E_{o,z}-E_{i,z})\right), & & B_{1,x} &=& B_{i,x}, \\ B_z &=& \frac{1}{2}\left((B_{i,z}+B_{o,z})+\frac{1}{c}(E_{i,y}-E_{o,y})\right), & \text{and} & B_{2,x} &=& B_{o,x}, \\ E_y &=& \frac{1}{2}\left(c(B_{i,z}-B_{o,z})+(E_{i,y}+E_{o,y})\right), & & E_{1,x} &=& E_{i,x}, \\ E_z &=& \frac{1}{2}\left(c(B_{o,y}-B_{i,y})+(E_{i,z}+E_{o,z})\right), & & E_{2,x} &=& E_{o,x}, \end{array} \tag{C.15}$$

noting that it does not matter which side you take for E_x and B_x at the interface $x/t = 0$ due to the stationary state.

C.3 Eigenstructure of GLM Maxwell's Equations

The eigenstructure of the GLM Maxwell's equation is now presented. The equations in Section 3.8.4 can be arranged into the weak conservative form in 1D, Equation (C.1), where

$$\mathrm{U} = \begin{bmatrix} B_x \\ B_y \\ B_z \\ D_x \\ D_y \\ D_z \\ \Psi \\ \Phi \end{bmatrix}, \qquad \mathrm{V} = \begin{bmatrix} B_x \\ B_y \\ B_z \\ E_x \\ E_y \\ E_z \\ \Psi \\ \Phi \end{bmatrix}, \qquad \mathrm{F} = \begin{bmatrix} \Psi \\ -E_z \\ E_y \\ \frac{\Phi}{\mu_0} \\ H_z \\ -H_y \\ {c_h}^2 B_x \\ \chi^2 E_x \end{bmatrix}, \qquad \mathrm{S} = \begin{bmatrix} 0 \\ 0 \\ 0 \\ -j_x \\ -j_y \\ -j_z \\ -\frac{{c_h}^2 \Psi}{{c_p}^2} \\ \frac{\rho_q \chi^2}{\epsilon_0} \end{bmatrix}. \tag{C.16}$$

Taking the hyperbolic part and rearranging to get the coefficient matrices as before, produces

$$\mathcal{A} = \frac{\partial \mathrm{V}}{\partial \mathrm{U}} \frac{\partial \mathrm{F}}{\partial \mathrm{V}} = \begin{bmatrix} 0 & 0 & 0 & 0 & 0 & 0 & 1 & 0 \\ 0 & 0 & 0 & 0 & 0 & -1 & 0 & 0 \\ 0 & 0 & 0 & 0 & 1 & 0 & 0 & 0 \\ 0 & 0 & 0 & 0 & 0 & 0 & 0 & \frac{1}{\epsilon_0 \mu_0} \\ 0 & 0 & \frac{1}{\epsilon_0 \mu} & 0 & 0 & 0 & 0 & 0 \\ 0 & -\frac{1}{\epsilon_0 \mu_0} & 0 & 0 & 0 & 0 & 0 & 0 \\ {c_h}^2 & 0 & 0 & 0 & 0 & 0 & 0 & 0 \\ 0 & 0 & 0 & \chi^2 & 0 & 0 & 0 & 0 \end{bmatrix}. \tag{C.17}$$

Also there are a few other Jacobians of interest including

$$\frac{\partial \mathrm{F}}{\partial \mathrm{U}} = \begin{bmatrix} 0 & 0 & 0 & 0 & 0 & 0 & 1 & 0 \\ 0 & 0 & 0 & 0 & 0 & -\frac{1}{\epsilon_0} & 0 & 0 \\ 0 & 0 & 0 & 0 & \frac{1}{\epsilon_0} & 0 & 0 & 0 \\ 0 & 0 & 0 & 0 & 0 & 0 & 0 & \frac{1}{\mu_0} \\ 0 & 0 & \frac{1}{\mu_0} & 0 & 0 & 0 & 0 & 0 \\ 0 & -\frac{1}{\mu_0} & 0 & 0 & 0 & 0 & 0 & 0 \\ {c_h}^2 & 0 & 0 & 0 & 0 & 0 & 0 & 0 \\ 0 & 0 & 0 & \frac{\chi^2}{\epsilon_0} & 0 & 0 & 0 & 0 \end{bmatrix} \tag{C.18}$$

and

$$\frac{\partial \mathrm{S}}{\partial \mathrm{U}} = \begin{bmatrix} 0 & 0 & 0 & 0 & 0 & 0 & 0 & 0 \\ 0 & 0 & 0 & 0 & 0 & 0 & 0 & 0 \\ 0 & 0 & 0 & 0 & 0 & 0 & 0 & 0 \\ 0 & 0 & 0 & 0 & 0 & 0 & 0 & 0 \\ 0 & 0 & 0 & 0 & 0 & 0 & 0 & 0 \\ 0 & 0 & 0 & 0 & 0 & 0 & 0 & 0 \\ 0 & 0 & 0 & 0 & 0 & 0 & -\frac{{c_h}^2}{{c_p}^2} & 0 \\ 0 & 0 & 0 & 0 & 0 & 0 & 0 & 0 \end{bmatrix}. \tag{C.19}$$

Note that $1/(\epsilon_0 \mu_0) = c^2$, where c is the speed of light.

The eigen problem of matrix (C.17) is solved to obtain the following eigenvalues and right eigenvectors:

$$c_h, \qquad [1,0,0,0,0,0,c_h,0], \tag{C.20}$$

$$-c_h, \qquad [1,0,0,0,0,0,-c_h,0], \tag{C.21}$$

$$\frac{\chi}{\sqrt{\epsilon_0\mu_0}}, \qquad [0,0,0,\frac{1}{\chi\sqrt{\epsilon_0\mu_0}},0,0,0,1], \tag{C.22}$$

$$-\frac{\chi}{\sqrt{\epsilon_0\mu_0}}, \qquad [0,0,0,-\frac{1}{\chi\sqrt{\epsilon_0\mu_0}},0,0,0,1], \tag{C.23}$$

$$\frac{1}{\sqrt{\epsilon_0\mu_0}}, \qquad [0,0,1,0,\frac{1}{\sqrt{\epsilon_0\mu_0}},0,0,0],[0,1,0,0,0,-\frac{1}{\sqrt{\epsilon_0\mu_0}},0,0], \tag{C.24}$$

$$-\frac{1}{\sqrt{\epsilon_0\mu_0}}, \qquad [0,0,1,0,-\frac{1}{\sqrt{\epsilon_0\mu_0}},0,0,0],[0,1,0,0,0,\frac{1}{\sqrt{\epsilon_0\mu_0}},0,0]. \tag{C.25}$$

Therefore the eigenvalues are

$$\left[\begin{array}{cccccccc} -\chi c, & -c_h, & -c, & -c, & c, & c, & c_h, & \chi c \end{array}\right], \tag{C.26}$$

and the right eigenvector matrix is

$$\mathrm{R} = \left[\begin{array}{cccccccc} 0 & 1 & 0 & 0 & 0 & 0 & 1 & 0 \\ 0 & 0 & 0 & 1 & 0 & 1 & 0 & 0 \\ 0 & 0 & 1 & 0 & 1 & 0 & 0 & 0 \\ -\frac{1}{\chi\sqrt{\epsilon_0\mu_0}} & 0 & 0 & 0 & 0 & 0 & 0 & \frac{1}{\chi\sqrt{\epsilon_0\mu_0}} \\ 0 & 0 & -\frac{1}{\sqrt{\epsilon_0\mu_0}} & 0 & \frac{1}{\sqrt{\epsilon_0\mu_0}} & 0 & 0 & 0 \\ 0 & 0 & 0 & \frac{1}{\sqrt{\epsilon_0\mu_0}} & 0 & -\frac{1}{\sqrt{\epsilon_0\mu_0}} & 0 & 0 \\ 0 & -c_h & 0 & 0 & 0 & 0 & c_h & 0 \\ 1 & 0 & 0 & 0 & 0 & 0 & 0 & 1 \end{array}\right] \tag{C.27}$$

with a left eigenvector matrix

$$\mathrm{L} = \begin{bmatrix} 0 & 0 & 0 & -\frac{1}{2}\chi\sqrt{\epsilon_0\mu_0} & 0 & 0 & 0 & \frac{1}{2} \\ \frac{1}{2} & 0 & 0 & 0 & 0 & 0 & -\frac{1}{2}\frac{1}{c_h} & 0 \\ 0 & 0 & \frac{1}{2} & 0 & -\frac{1}{2}\sqrt{\epsilon_0\mu_0} & 0 & 0 & 0 \\ 0 & \frac{1}{2} & 0 & 0 & 0 & \frac{1}{2}\sqrt{\epsilon_0\mu_0} & 0 & 0 \\ 0 & 0 & \frac{1}{2} & 0 & \frac{1}{2}\sqrt{\epsilon_0\mu_0} & 0 & 0 & 0 \\ 0 & \frac{1}{2} & 0 & 0 & 0 & -\frac{1}{2}\sqrt{\epsilon_0\mu_0} & 0 & 0 \\ \frac{1}{2} & 0 & 0 & 0 & 0 & 0 & \frac{1}{2}\frac{1}{c_h} & 0 \\ 0 & 0 & 0 & \frac{1}{2}\chi\sqrt{\epsilon_0\mu_0} & 0 & 0 & 0 & \frac{1}{2} \end{bmatrix}. \tag{C.28}$$

Adding the Lagrange multiplier to the Maxwell's equations creates two new waves with signal velocities c_h and χc that advect Ψ and Φ as seen above. Also, the waves associated with B_x and E_x are no longer stationary as in the original Maxwell's equations. The left and right eigenmatrices are scaled and normalized, to arrive at the GLM eigenvectors

$$\mathbf{R}_{glm,c} = \begin{bmatrix} 0 & 1 & 0 & 0 & 0 & 0 & 1 & 0 \\ 0 & 0 & \sqrt{\frac{\mu_0}{\varepsilon_0}} & 0 & -\sqrt{\frac{\mu_0}{\varepsilon_0}} & 0 & 0 & 0 \\ 0 & 0 & 0 & -\sqrt{\frac{\mu_0}{\varepsilon_0}} & 0 & \sqrt{\frac{\mu_0}{\varepsilon_0}} & 0 & 0 \\ 1 & 0 & 0 & 0 & 0 & 0 & 0 & 1 \\ 0 & 0 & 0 & 1 & 0 & 1 & 0 & 0 \\ 0 & 0 & 1 & 0 & 1 & 0 & 0 & 0 \\ 0 & -c_h & 0 & 0 & 0 & 0 & c_h & 0 \\ -\chi\sqrt{\frac{\mu_0}{\varepsilon_0}} & 0 & 0 & 0 & 0 & 0 & 0 & \chi\sqrt{\frac{\mu_0}{\varepsilon_0}} \end{bmatrix}, \tag{C.29}$$

$$\mathbf{L}_{glm,c} = \begin{bmatrix} 0 & 0 & 0 & \frac{1}{2} & 0 & 0 & 0 & -\frac{1}{2}\chi^{-1}\sqrt{\frac{\varepsilon_0}{\mu_0}} \\ \frac{1}{2} & 0 & 0 & 0 & 0 & 0 & -\frac{1}{2}{c_h}^{-1} & 0 \\ 0 & \frac{1}{2}\sqrt{\frac{\varepsilon_0}{\mu_0}} & 0 & 0 & 0 & \frac{1}{2} & 0 & 0 \\ 0 & 0 & -\frac{1}{2}\sqrt{\frac{\varepsilon_0}{\mu_0}} & 0 & \frac{1}{2} & 0 & 0 & 0 \\ 0 & -\frac{1}{2}\sqrt{\frac{\varepsilon_0}{\mu_0}} & 0 & 0 & 0 & \frac{1}{2} & 0 & 0 \\ 0 & 0 & \frac{1}{2}\sqrt{\frac{\varepsilon_0}{\mu_0}} & 0 & \frac{1}{2} & 0 & 0 & 0 \\ \frac{1}{2} & 0 & 0 & 0 & 0 & 0 & \frac{1}{2}{c_h}^{-1} & 0 \\ 0 & 0 & 0 & \frac{1}{2} & 0 & 0 & 0 & \frac{1}{2}\chi^{-1}\sqrt{\frac{\varepsilon_0}{\mu_0}} \end{bmatrix}, \tag{C.30}$$

and

$$\mathbf{L}_{glm,p} = \begin{bmatrix} 0 & 0 & 0 & \frac{1}{2}\varepsilon_0 & 0 & 0 & 0 & -\frac{1}{2}\sqrt{\frac{\varepsilon_0}{\mu_0}}\chi^{-1} \\ \frac{1}{2} & 0 & 0 & 0 & 0 & 0 & -\frac{1}{2}{c_h}^{-1} & 0 \\ 0 & \frac{1}{2}\sqrt{\frac{\varepsilon_0}{\mu_0}} & 0 & 0 & 0 & \frac{1}{2}\varepsilon_0 & 0 & 0 \\ 0 & 0 & -\frac{1}{2}\sqrt{\frac{\varepsilon_0}{\mu_0}} & 0 & \frac{1}{2}\varepsilon_0 & 0 & 0 & 0 \\ 0 & -\frac{1}{2}\sqrt{\frac{\varepsilon_0}{\mu_0}} & 0 & 0 & 0 & \frac{1}{2}\varepsilon_0 & 0 & 0 \\ 0 & 0 & \frac{1}{2}\sqrt{\frac{\varepsilon_0}{\mu_0}} & 0 & \frac{1}{2}\varepsilon_0 & 0 & 0 & 0 \\ \frac{1}{2} & 0 & 0 & 0 & 0 & 0 & \frac{1}{2}{c_h}^{-1} & 0 \\ 0 & 0 & 0 & \frac{1}{2}\varepsilon_0 & 0 & 0 & 0 & \frac{1}{2}\sqrt{\frac{\varepsilon_0}{\mu_0}}\chi^{-1} \end{bmatrix} \tag{C.31}$$

which are the right conservative, left conservative, and left primitive eigenvector matrices respectively. The characteristic variables are obtained by $\mathbf{L}_{glm,p}\mathbf{W}_{glm} = \mathbf{L}_{glm,c}\mathbf{U}_{glm} =$

$$\left[\left(\phi - \frac{\chi}{c}E_x\right), \left(B_x - \frac{\psi}{c_h}\right), \left(B_z - \frac{E_y}{c}\right), \left(B_y + \frac{E_z}{c}\right), \left(B_z + \frac{E_y}{c}\right), \left(B_y - \frac{E_z}{c}\right), \left(B_x + \frac{\psi}{c}\right), \left(\phi + \frac{\chi}{c}E_x\right)\right]. \tag{C.32}$$

The above characteristics can be used to find an intermediate state using the method of characteristics, as before, where the regions are split as in Figure 6.2 with an intermediate state in the middle formed by the Riemann problem. This time there is only one intermediate region (when $\chi = 1$ and $c_h = c$). Each variable can be solved for as follows:

$$\left(\phi - \frac{\chi}{c}E_x\right) = \left(\phi_o - \frac{\chi}{c}E_{o,x}\right), \tag{C.33}$$

$$\left(\phi + \frac{\chi}{c}E_x\right) = \left(\phi_i + \frac{\chi}{c}E_{i,x}\right), \tag{C.34}$$

where E_x and ϕ is solved for by adding and subtracting Equations (C.33) and (C.34) as an example. Repeating the above calculations gives

$$\begin{aligned}
B_x &= \tfrac{1}{2}\left((B_{i,x}+B_{o,x})+\tfrac{1}{c_h}(\psi_i-\psi_o)\right),\\
B_y &= \tfrac{1}{2}\left((B_{i,y}+B_{o,y})+\tfrac{1}{c}(E_{o,z}-E_{i,z})\right),\\
B_z &= \tfrac{1}{2}\left((B_{i,z}+B_{o,z})+\tfrac{1}{c}(E_{i,y}-E_{o,y})\right),\\
E_x &= \tfrac{1}{2}\left((E_{i,x}+E_{o,x})+\tfrac{c}{\chi}(\phi_i-\phi_o)\right),\\
E_y &= \tfrac{1}{2}\left(c(B_{i,z}-B_{o,z})+(E_{i,y}+E_{o,y})\right),\\
E_z &= \tfrac{1}{2}\left(c(B_{o,y}-B_{i,y})+(E_{o,z}+E_{i,z})\right),\\
\psi &= \tfrac{1}{2}\left(c_h(B_{i,x}-B_{o,x})+(\psi_i+\psi_o)\right),\\
\phi &= \tfrac{1}{2}\left(\tfrac{\chi}{c}(E_{i,x}-E_{o,x})+\phi_o+\phi_i\right),
\end{aligned} \tag{C.35}$$

for all the variables.

Comparing the eigen matrices and eigenvalues, we can see that it is easy to arrive at the non-GLM eigenstructure by simply setting the GLM coefficients to zero. In this way it is possible to move from the GLM to the non-GLM Maxwell's equations.

C.4 Godunov Numerical Flux for Maxwell's Equations without Divergence Cleaning

When the flux is linear, it is possible to solve the exact flux. The Riemann problem at the cell interface is the initial value problem of the form

$$\frac{\partial \mathbf{U}}{\partial t}+\mathcal{C}\frac{\partial \mathbf{U}}{\partial x}=\mathbf{0}, \tag{C.36}$$

$$\mathbf{U}(x,0)=\begin{cases}\mathbf{U}_l & \text{for} \quad x<0,\\ \mathbf{U}_r & \text{for} \quad x>0,\end{cases} \tag{C.37}$$

in one-dimension. Here, $\mathcal{C}$ is equal to $\frac{\partial \mathbf{F}}{\partial \mathbf{U}}$. The method of characteristics is used to solve the IVP. There are three characteristics in this system separating 4 states:

$$\mathbf{U}_l, \mathbf{U}_1, \mathbf{U}_2, \mathbf{U}_r. \tag{C.38}$$

The intermediate states can be found by

$$\mathbf{U}_1=\mathbf{U}_l+\Sigma_{i=1}^{2}\alpha_i\mathbf{r}^i=\mathbf{U}_r-\Sigma_{i=0}^{3}\alpha_{6-i}\mathbf{r}^{6-i}, \tag{C.39}$$

$$\mathbf{U}_2=\mathbf{U}_l+\Sigma_{i=1}^{4}\alpha_i\mathbf{r}^i=\mathbf{U}_r-\Sigma_{i=0}^{1}\alpha_{6-i}\mathbf{r}^{6-i}, \tag{C.40}$$

where

$$\alpha_i = \mathbf{l}_i(\mathbf{U}_r - \mathbf{U}_l). \tag{C.41}$$

The flux is thus

$$\mathbf{F} = \mathcal{C}\mathbf{U}_1 = \mathcal{C}\mathbf{U}_2, \tag{C.42}$$

for the 1D case. It should be noted that whatever the values that $\mathbf{U}_1$ or $\mathbf{U}_2$ take, when operated on by $\mathcal{C}$, the term associated with B_x and E_x will always be zero.

C.5 HLLE Numerical Flux for Maxwell's Equations without Divergence Cleaning

The HLLE flux is determined by integrating around the linear (or linearized) Riemann problem control volume, as in Figure B.1, and results in the following for the intermediate state:

$$0 = \mathbf{U_L}\frac{\Delta x}{2} - \mathbf{F}_*\Delta t + \mathbf{U}_*\lambda^-\Delta t - \mathbf{U_L}\left(\frac{\Delta x}{2} + \lambda^-\Delta t\right) + \mathbf{F_L}\Delta t. \tag{C.43}$$

Applying the same integration for flux and substituting in for the intermediate state above, the intermediate flux is

$$\mathbf{F}_* = \frac{\lambda^+\mathbf{F_L} - \lambda^-\mathbf{F_R}}{\lambda^+ - \lambda^-} + \frac{\lambda^+\lambda^-}{\lambda^+ - \lambda^-}\left(\mathbf{U_R} - \mathbf{U_L}\right). \tag{C.44}$$

As can be seen from above, using $\mathbf{F}_*$ does not guarantee that the x-direction fluxes are zero. In fact there will be a flux if there is a change in the x-direction magnetic field B_x.

For example, taking just the x-direction magnetic field equation for B_x the following is obtained

$$F_*(B_x) = \frac{\lambda^+F_L(B_x) - \lambda^-F_R(B_x)}{\lambda^+ - \lambda^-} + \frac{\lambda^+\lambda^-}{\lambda^+ - \lambda^-}\left(U_R(B_x) - U_L(B_x)\right), \tag{C.45}$$

where, $F(B_x) = 0$ for any solution state. Thus,

$$F_*(B_x) = \frac{\lambda^+\lambda^-}{\lambda^+ - \lambda^-}\left(B_{x,r} - B_{x,l}\right), \tag{C.46}$$

and likewise for E_x

$$F_*(E_x) = \frac{\lambda^+\lambda^-}{\lambda^+ - \lambda^-}\left(E_{x,r} - E_{x,l}\right). \tag{C.47}$$

When comparing the Godunov and HLLE fluxes, only the B_x and E_x terms are different as above.

C.6 HLLE and Godunov Exact Numerical Fluxes for the GLM Maxwell's Equations

Repeating the above process for the GLM equations and keeping the eigenvalues all equal to $\pm c$, both the HLLE and Godunov fluxes are equivalent as it should be. Obviously the difference between the HLLE and Godunov flux for the regular Maxwell's equations comes from the fact that there is a third, stationary wave, which is associated with the B_x and E_x wave.

It is interesting to note that even though the only term in the flux for the B_x and E_x (or D_x) equations is in terms of ψ or ϕ, the flux is actually a function of B_x and E_x as well as ψ, and ϕ. The terms are listed below, noting that it is equal for both HLLE and Godunov flux functions:

$$F^*(B_x) = \frac{1}{2}\left(\psi_l + \psi_r - cB_{r,x} + cB_{l,x}\right), \tag{C.48}$$

$$F^*(D_x) = \frac{1}{2}\left(\psi_l + \psi_r - cD_{r,x} + cD_{l,x}\right). \tag{C.49}$$

C.7 Exact Numerical Flux Function

Because the Maxwell's equations have a stationary wave pattern, the intermediate flux is always used. Therefore, an analytical solution for the exact flux can be derived. This actually reduces both computation and round off errors, which can be very large with the GLM equations. Below are the analytic exact flux functions for the regular and GLM Maxwell's equations:

$$\mathbf{F}_{x,MF} = \begin{bmatrix} 0 \\ \frac{1}{2}\left(c\left(B_{l,y} - B_{r,y}\right) - E_{l,z} - E_{r,z}\right) \\ \frac{1}{2}\left(c\left(B_{l,z} - B_{rz}\right) + E_{l,y} + E_{r,y}\right) \\ 0 \\ \frac{1}{2}\left(H_{l,z} + H_{r,z} + \sqrt{\frac{\varepsilon_0}{\mu_0}}\left(E_{l,y} - E_{r,y}\right)\right) \\ -\frac{1}{2}\left(H_{l,y} + H_{r,y} + \sqrt{\frac{\varepsilon_0}{\mu_0}}\left(E_{r,z} - E_{l,z}\right)\right) \end{bmatrix}, \tag{C.50}$$

$$\mathbf{F}_{x,GLM} = \begin{bmatrix} \frac{1}{2}\left(\psi_l + \psi_r - B_{r,x}\, c_h + B_{l,x}\, c_h\right) \\ \frac{1}{2}\left(c\left(B_{l,y} - B_{r,y}\right) - E_{l,z} - E_{r,z}\right) \\ \frac{1}{2}\left(c\left(B_{l,z} - B_{r,z}\right) + E_{l,y} + E_{r,y}\right) \\ \frac{1}{2}\left(\frac{1}{\mu_0}\left(\phi_l + \phi_r\right) + \sqrt{\frac{\varepsilon_0}{\mu_0}}\chi\left(E_{l,x} - E_{r,x}\right)\right) \\ \frac{1}{2}\left(H_{l,z} + H_{r,z} + \sqrt{\frac{\varepsilon_0}{\mu_0}}\left(E_{l,y} - E_{r,y}\right)\right) \\ -\frac{1}{2}\left(H_{l,y} + H_{r,y} + \sqrt{\frac{\varepsilon_0}{\mu_0}}\left(E_{r,z} - E_{l,z}\right)\right) \\ \frac{1}{2}c_h\left(c_h B_{l,x} + c_h B_{r,x} - \psi_r + \psi_l\right) \\ \frac{1}{2}\chi\left(\chi E_{l,x} + \chi E_{r,x} - c\,\phi_r + c\,\phi_l\right) \end{bmatrix}, \tag{C.51}$$

which are the non-GLM (MF) and GLM fluxes respectively. As before, setting the GLM coefficients and constants to 0 will result in shutting off the associated divergence cleaning algorithm. Setting ψ, c_h, ϕ, and χ all to 0 will reduce the GLM equations to the non-GLM Maxwell's equations.

References

[1] William Crochot. Schematic of magnetosphere. Illustration NASA Website, November 2007.

[2] M. A. Shay, J. F. Drake, B. N. Rogers, and R. E. Denton. Alfvénic collisionless magnetic reconnection and the hall term. *Journal of Geophysical Research: Space Physics*, 106(A3):3759–3772, 2001.

[3] P. L. Pritchett. Geospace environment modeling magnetic reconnection challenge: Simulations with a full particle electromagnetic code. *Journal of Geophysical Research*, 106(A3):3783–3798, 2001.

[4] H. Schmitz and R. Grauer. Kinetic Vlasov simulations of collisionless magnetic reconnection. *Physics of Plasmas*, 13(9):092309, 2006.

[5] M. Rieke, T. Trost, and R. Grauer. Coupled Vlasov and two-fluid codes on GPUs. *Journal of Computational Physics*, 283:436 – 452, 2015.

[6] E. A. Johnson. *Gaussian-Moment Relaxation Closures for Verifiable Numerical Simulation of Fast Magnetic Reconnection in Plasma*. PhD thesis, University of Wisconsin-Madison, 2011.

[7] E. A. Johnson and J. A. Rossmanith. Ten-moment two-fluid plasma model agrees well with PIC/Vlasov in GEM problem. In *Proceedings of the 13th International Conference on Hyperbolic Problems, Windsor, Ontario, Canada, June 9–11*, 2010.

[8] E. A. Johnson and J. A. Rossmanith. Two-fluid 20-moment simulation of fast magnetic reconnection. Presentation, SIAM Conference on Computational Science and Engineering, February 2013.

[9] T. Corke, E. Jumper, M. Post, D. Orlov, and T. McLaughlin. Application of weakly ionized plasmas as wing flow control devices. Paper 2002-0350, AIAA, 2002.

[10] M. L. Post and T. Corke. Separation control on high angle of attack airfoil using plasma actuators. Paper 2003-1024, AIAA, 2003.

[11] J. S. Shang and S. T. Surzhikov. Magneto-Fluid-Dynamics interaction for hypersonic flow control. Paper 2004-0508, AIAA, January 2004.

[12] Y. B. Suzen, P. G. Huang, J. D. Jacob, and D. E. Ashpis. Numerical simulations of plasma based flow control applications. Paper 2005-4633, AIAA, June 2005.

[13] D. Giordano. Hypersonic-flow governing equations with electromagnetic fields. Paper 2002-2165, AIAA, May 2002.

[14] S. O. Macheret, M. N. Shneider, and R. B. Miles. Magnetohydrodynamic and electrohydrodynamic control of hypersonic flows of weakly ionized plasmas. *AIAA*, 42(7):1378–1387, 2004.

[15] R. W. MacCormack. Evaluation of the low magnetic Reynolds approximation for aerodynamics flow calculations. Paper 2005-4780, AIAA, June 2005.

[16] D. D'Ambrosio and D. Giordano. A numerical method for two-dimensional hypersonic fully coupled electromagnetic fluid dynamics. Paper 2005-5374, AIAA, June 2005.

[17] G. Seller, M. Capitelli, S. Longo, and I. Armenise. Numerical MHD of aircraft re-entry; fluid dynamic, electromagnetic and chemical effects. Paper 2005-5048, AIAA, June 2003.

[18] M. Martinez-Sanchez and J. E. Pollard. Spacecraft electric propulsion — an overview. *Journal of Propulsion and Power*, 14(5):688–699, 1998.

[19] J. R. Brophy and M. Noca. Electric propulsion for solar system exploration. *Journal of Propulsion and Power*, 14(5):700–707, 1998.

[20] G. Krülle, M. Auweter-Kurtz, and A. Sasoh. Technology and application aspects of applied field magnetoplasmadynamic propulsion. *Journal of Propulsion and Power*, 14(5):754–763, 1998.

[21] H. Bijiao, Z. Jianhua, and C. Guobiao. Numerical simulation of stationary plasma thruster plume. Paper 05-C4.P.04, IAF, October 2005.

[22] C. Chunpei and I. D. Boyd. 3D simulation of plume flows from a cluster of plasma thrusters. Paper 2005-4662, AIAA, June 2005.

[23] S. Elaskar, L. Maglione, O. Falcinelli, H. Brito, and J. Tamagno. Numerical simulation of MGD flows for plasma propulsion. Paper 06-C4.P.4.10, IAF, October 2005.

[24] K. Miura. Propellant management system for a microwave thruster in a MOST class spacecraft (BASc thesis), 2001.

[25] D. Shinohara, K. Noda, Y. Kajimura, and H. Nakashima. Numerical study of magneto plasma sail by using three-dimensional hybrid code. Paper 05-C4.6.07, IAF, October 2005.

[26] M. Auweter-Kurtz and H. Kurtz. High power plasma propulsion for in-space transportation. Paper 05-C3.5-C4.7.05, IAF, October 2005.

[27] J. Birn, J. F. Drake, M. A. Shay, B. N. Rogers, R. E. Denton, M. Hesse, M. Kuznetsova, Z. W. Ma, A. Bhattacharjee, A. Otto, and P. L. Pritchett. Geospace Environmental Modeling (GEM) magnetic reconnection challenge. *Journal of Geophysical Research*, 106:3715–3720, March 2001.

[28] R. Keppens, O. Porth, K. Galsgaard, J. T. Frederiksen, A. L. Restante, G. Lapenta, and C. Parnell. Resistive magnetohydrodynamic reconnection: Resolving long-term, chaotic dynamics. *Physics of Plasmas*, 20(9):092109+, 2013.

[29] J. A. Ratcliffe. *An introduction to the ionosphere and magnetosphere*. University Press Cambridge [Eng.], 1972.

[30] R.T. Merrill. *Our Magnetic Earth: The Science of Geomagnetism*. University of Chicago Press, 2010.

[31] National Research Council. *Severe Space Weather Events–Understanding Societal and Economic Impacts: A Workshop Report*. The National Academies Press, Washington, DC, 2008.

[32] G. W. Sutton and A. Sherman. *Engineering Magnetohydrodynamics*. McGraw-Hill, Toronto, 1965.

[33] F. F. Chen, editor. *Introduction to Plasma Physics*. Plenum Press, New York, 1977.

[34] T. I. Gombosi. Space plasma physics. Lecture notes.

[35] F. Y. Zhang and C. P. T. Groth. Theoretical analysis of VASIMR using a gyration-dominated anisotropic plasma model. Paper 233, CASI, November 2002.

[36] C. P. T. Groth, D. L. De Zeeuw, T. I. Gombosi, and K. G. Powell. Global three-dimensional MHD simulation of a space weather event: CME formation, interplanetary propagation, and and interaction with the magnetosphere. *Journal of Geophysical Research*, 105(A11):25,053–25,078, 2000.

[37] C. P. T. Groth, D. L. De Zeeuw, K. G. Powell, T. I. Gombosi, and Q. F. Stout. A parallel solution-adaptive scheme for ideal magnetohydrodynamics. Paper 99-3273, AIAA, June 1999.

[38] A. Otto. Geospace environment modeling (GEM) magnetic reconnection challenge: MHD and Hall MHD–constant and current dependent resistivity models. *Journal of Geophysical Research: Space Physics*, 106(A3):3751–3757, 2001.

[39] Dinshaw S. Balsara and Chi-Wang Shu. Monotonicity preserving weighted essentially non-oscillatory schemes with increasingly high order of accuracy. *Journal of Computational Physics*, 160(2):405 – 452, 2000.

[40] G. Tóth and D. Odstrčil. Comparison of some flux corrected transport and total variation diminishing numerical schemes for hydrodynamic and magnetohydrodynamic problems. *Journal of Computational Physics*, 128:82–100, 1996.

[41] Dongsu Ryu and TW Jones. Numerical magnetohydrodynamics in astrophysics: algorithm and tests for one-dimensional flow. *astro physics*, 1994.

[42] Jorge Balbás, Eitan Tadmor, and Cheng-Chin Wu. Non-oscillatory central schemes for one-and two-dimensional MHD equations: I. *Journal of Computational Physics*, 201(1):261–285, 2004.

[43] Guang-Shan Jiang and Cheng chin Wu. A high-order weno finite difference scheme for the equations of ideal magnetohydrodynamics. *Journal of Computational Physics*, 150(2):561 – 594, 1999.

[44] S. I. Pai. *Magnetogasdynamics and Plasma Dynamics*. Springer Verlag, Wien, 1962.

[45] D. D'Ambrosio and D. Giordano. Electromagnetic fluid dynamics for aerospace applications. Part I: Classification and critical review of physical models. Paper 2004-2165, AIAA, June 2004.

[46] H. Nishida, Y. Inatani, H. Ogawa, and I. Funaki. Propulsive characteristic analyze of magnetic sail. Technical Note ISAS RN 791, ISAS Research Note, 2005.

[47] K. Miura and C. P. T. Groth. Development of two-fluid magnetohydrodynamics model for non-equilibrium anisotropic plasma flows. Paper 2007-4373, AIAA, June 2007.

[48] T. Ohsawa. Development of an extended multi-fluid magnetohydrodynamic model for fully- and partially-ionized anisotropic plasmas. Master's thesis, University of Toronto, October 2005.

[49] A. V. Ilin, F. R. Chang Díaz, J. P. Squire, B. N. Briezman, and M. D. Carter. Particle simulations of plasma heating in VASIMR. Paper 2000-3753, AIAA, July 2000.

[50] P. L. Pritchett, F. V. Coroniti, and V. K. Decyk. Three-dimensional stability of thin quasi-neutral current sheets. *Journal of Geophysical Research: Space Physics*, 101(A12):27413–27429, 1996.

[51] C. K. Birdsall and A. B. Landon. *Plasma Physics Via Computer Simulation*. Adam Hilger Press, New York, 1991.

[52] G. A. Bird. *Molecular Gas Dynamics and the Direct Simulation of Gas Flows*. Clarendon Press, Oxford, 1994.

[53] K. S. Breuer, E. S. Piekos, and D. A. Gonzales. Dsmc simulations of continuum flows. Paper 95-2088, AIAA, June 1995.

[54] Masha M. Kuznetsova, Michael Hesse, and Dan Winske. Collisionless reconnection supported by nongyrotropic pressure effects in hybrid and particle simulations. *Journal of Geophysical Research: Space Physics*, 106(A3):3799–3810, 2001.

[55] R. Asahi, I. Funaki, K. Fujita, H Nishida, H. Tamakawa, and H. Ogawa. Performance evaluation of a magneto plasma sail. in proceedings of ISSS-7, March 2005.

[56] D. V. Gaitonde. High-Order solution procedure for Three-Dimensional nonideal magnetogasdynamics. *AIAA Journal*, 39(11):2111–2120, 2001.

[57] D. D'Ambrosio and D. Giordano. Electromagnetic fluid dynamics for aerospace applications. Part II: Numerical simulations using different physical models. Paper 2004-2362, AIAA, June 2004.

[58] I. D. Boyd and J. T. Yim. Modeling of the near field plume of a Hall thruster. *Journal of Applied Physics*, 95:4575–4584, May 2004.

[59] J. S. Shang. Recent research in magneto-aerodynamics. *Progress in Aerospace Sciences*, 37:1–20, 2001.

[60] J. S. Shang. Shared knowledge in computational fluid dynamics, electromagnetics, and magneto-aerodynamics. *Progress in Aerospace Sciences*, 38:449–467, 2002.

[61] M. S. Konstantinov, V. A. Obukhov, V. G. Petukhov, G. A. Popov, and G. G. Tchernobelsky. Spacecraft station-keeping in the molniya orbit using electric propulsion. Paper 05-C1.1.01, IAF, October 2005.

[62] U. Shumlak and J. Loverich. Approximate Riemann solver for the two-fluid plasma model. *Journal of Computational Physics*, 187:620–638, 2003.

[63] John Loverich, Ammar Hakim, and Uri Shumlak. A discontinuous galerkin method for ideal two-fluid plasma equations. *Communications in Computational Physics*, 9(02):240–268, 2011.

[64] A. Hakim, J. Loverich, and U. Shumlak. A high resolution wave propagation scheme for ideal two-fluid plasma equations. *Journal of Computational Physics*, 219:418–442, 2006.

[65] A. Hakim. Extended MHD modelling with the ten-moment equations. *Journal of Fusion Energy*, 27:36–43, 2008.

[66] J. Loverich, S. C. D. Zhou, K. Beckwith, M. Kundrapu, M. Loh, S. Mahalingam, P. Stoltz, and A. Hakim. Nautilus: A tool for modeling fluid plasmas. Paper 2013-1185, AIAA, January 2013.

[67] J. Du. *Simulation of Magnetohydrodynamic Multiphase Flow*. PhD thesis, State University of New York at Stony Brook, 2007.

[68] C. P. Escoubet, A. Masson, H. Laakso, and M. L. Goldstein. Recent highlights from Cluster, the first 3-D magnetospheric mission. *Annales Geophysicae*, 33(10):1221–1235, 2015.

[69] J. Burch. The Magnetospheric Multiscale Mission. In *40th COSPAR Scientific Assembly*, volume 40 of *COSPAR Meeting*, 2014.

[70] Michael Hesse, Joachim Birn, and Masha Kuznetsova. Collisionless magnetic reconnection: Electron processes and transport modeling. *Journal of Geophysical Research*, 106(A3):3721–3735, 2001.

[71] Joachim Birn and Michael Hesse. Geospace environment modeling (GEM) magnetic reconnection challenge: Resistive tearing, anisotropic pressure and Hall effects. *Journal of Geophysical Research: Space Physics*, 106(A3):3737–3750, 2001.

[72] Z. W. Ma and A. Bhattacharjee. Hall magnetohydrodynamic reconnection: The geospace environment modeling challenge. *Journal of Geophysical Research*, 106(A3):3773–3782, 2001.

[73] Chang Liu and Kun Xu. A unified gas kinetic scheme for continuum and rarefied flows v: Multiscale and multi-component plasma transport. *Communications in Computational Physics*, 22(5):11751223, 2017.

[74] P. Song, T. I. Gombosi, and A. J. Ridley. Three-fluid Ohm's law. *Journal of Geophysical Research: Space Physics*, 106(A5):8149–8156, 2001.

[75] Holger Schmitz and Rainer Grauer. Darwin-Vlasov simulations of magnetised plasmas. *J. Comput. Physics*, 214(2):738–756, 2006.

[76] Dirk Helbing. Traffic and related self-driven many-particle systems. *Rev. Mod. Phys.*, 73:1067–1141, Dec 2001.

[77] N. Bellomo, M. Delitala, and V. Coscia. On the mathematical theory of vehicular traffic flow I: Fluid dynamic and kinetic modelling. *Mathematical Models and Methods in Applied Sciences*, 12(12):1801–1843, 2002.

[78] J. Binney and S. Tremaine. *Galactic Dynamics: (Second Edition)*. Princeton Series in Astrophysics. Princeton University Press, 2011.

[79] T. I. Gombosi. *Gaskinetic Theory*. Cambridge University Press, Cambridge, 1994.

[80] H. Grad. On the kinetic theory of rarefied gases. *Communications on Pure and Applied Mathematics*, 2:331–407, 1949.

[81] C. Cercignani, R. Illner, and M. Pulvirenti. *The Mathematical Theory of Dilute Gases*. Springer-Verlag, New York, 1994.

[82] N. N. Bogoliubov. Kinetic equations. *Journal of Physics USSR*, 10(3):265–274, 1946.

[83] Harold Grad. Principles of the kinetic theory of gases. In *Thermodynamik der Gase/Thermodynamics of Gases*, pages 205–294. Springer, 1958.

[84] C. D. Levermore. Moment closure hierarchies for kinetic theories. *Journal of Statistical Physics*, 83:1021–1065, 1996.

[85] C. P. T. Groth. Numerical modeling of non-equilibrium micron-scale flows using the Gaussian moment closure. In *Proceedings of the Eighth Annual Conference of the CFD Society of Canada, Montreal, Canada, June 11–13, 2000*, volume 1, pages 481–486. CFD Society of Canada, 2000.

[86] S. L. Brown, P. L. Roe, and C. P. T. Groth. Numerical solution of a 10-moment model for nonequilibrium gasdynamics. Paper 95-1677, AIAA, June 1995.

[87] J. C. Maxwell. On the dynamical theory of gases. *Philosophical Transactions of the Royal Society of London*, 157:49–88, 1867.

[88] L. H. Holway. *Approximation Procedures for Kinetic Theory*. PhD thesis, Harvard University, 1963.

[89] L. H. Holway. Temperature overshoots in shock waves. *Physics of Fluids*, 8(10):1905–1906, 1965.

[90] L. H. Holway. The effect of collisional models upon shock wave structure. In C. L. Brundin, editor, *Rarefied Gas Dynamics*, volume I, pages 759–784, New York, 1967. Academic Press.

[91] C. P. T. Groth and J. G. McDonald. Towards physically-realizable and hyperbolic moment closures for kinetic theory. *Continuum Mechanics and Thermodynamics*, 21(6):467–493, 2009.

[92] C. D. Levermore and William J. Morokoff. The Gaussian moment closure for gas dynamics. *SIAM Journal on Applied Mathematics*, 59(1):72–96, 1999.

[93] J. G. McDonald and C. P. T. Groth. Numerical modeling of micron-scale flows using the Gaussian moment closure. Paper 2005-5035, AIAA, June 2005.

[94] J. G. McDonald, J. S. Sachdev, and C. P. T. Groth. Gaussian moment closure for the modelling of continuum and micron-scale flows with moving boundaries. Paper, ICCFD, July 2006.

[95] J. G. McDonald and C. P. T. Groth. Extended fluid-dynamic model for micron-scale flows based on Gaussian moment closure. *46th AIAA Aerospace Sciences Meeting and Exhibit*, pages 7–10, 2008.

[96] J. G. McDonald. *Extended Fluid-Dynamic Modelling for Numerical Solution of Micro-Scale Flows*. PhD thesis, University of Toronto, 2011.

[97] J. G. McDonald, J. S. Sachdev, and C. P. T. Groth. Application of Gaussian moment closure to microscale flows with moving embedded boundaries. *AIAA Journal*, 52(9):1839–1857, 2014.

[98] C. Hirsch. *Numerical Computation of Internal and External Flows, Volume 2, Computational Methods for Inviscid and Viscous Flows*. John Wiley & Sons, Toronto, 1990.

[99] P. L. Bhatnagar, E. P. Gross, and M. Krook. A model for collision processes in gases. I. small amplitude processes in charged and neutral one-component systems. *Physical Review*, 94(3):511–525, 1954.

[100] James Clerk Maxwell. A dynamical theory of the electromagnetic field. *Philosophical Transactions of the Royal Society of London*, 155:459–513, 1865.

[101] O. Heaviside. *Electromagnetic Theory*. Number v. 3. Cosimo Classics, 2008.

[102] J. M. Burgers. *Flow Equations for Composite Gases*. Academic Press, New York, 1969.

[103] V. H. Hansteen and E. Leer. Coronal heating, densities, and temperatures and solar wind acceleration. *Journal of Geophysical Research*, 100(A11):21577–21593, 1995.

[104] T. E. Holzer. Interaction of the solar wind with the neutral component of the interstellar gas. *Geophysical Research Letters*, 77:5407–5431, 1972.

[105] H. W. Ripken and H. J. Fahr. Modification of the local interstellar gas properties in the heliospheric interface. *Annual Review of Astronomy and Astrophysics*, 122:181–192, 1983.

[106] T. Ohsawa. Higher-order moment closures for partially ionized plasmas. Research Assessment Committee Report, UTIAS, April 2004.

[107] F. J. de Heer, M. R. C. McDowell, and R. W. Wagenaar. Numerical study of the dispersion relation for e - -H scattering. *Journal of Physics B: Atomic and Molecular Physics*, 10(10):1945, 1977.

[108] Victor Franco and Brian K. Thomas. Elastic and inelastic scattering of protons by hydrogen atoms. *Phys. Rev. A*, 4:945–954, Sep 1971.

[109] F. J. de Heer, R. H. J. Jansen, and W. van der Kaay. Total cross sections for electron scattering by Ne, Ar, Kr and Xe. *Journal of Physics B: Atomic and Molecular Physics*, 12(6):979, 1979.

[110] W. H. Cramer. Elastic and inelastic scattering of low-velocity ions: Ne+ in A, A+ in Ne, and A+ in A. *Journal of Chemical Physics*, 30(3):641–642, 1959.

[111] A. V. Phelps, C. H. Greene, and J. P. Burke Jr. Collision cross sections for argon atoms with argon atoms for energies from 0.01 eV to 10 keV. *Journal of Physics B: Atomic and Molecular Physics*, 33(16):2965, 2000.

[112] H. R. Baum and T. M. Fang. Kinetic equations for a chemically reacting plasma. *Physics of Fluids*, 15(10):1771–1777, 1972.

[113] Martin I. Hoffert and Hwachii Lien. Quasi-one-dimensional, nonequilibrium gas dynamics of partially ionized two-temperature argon. *Physics of Fluids*, 10(8):1769–1777, 1967.

[114] T. T. Scholz and H. R. J. Walters. Collisional rates and cooling within atomic hydrogen plasmas. *Astrophysical Journal*, 380:302–306, October 1991.

[115] H.J. Fahr. Towards a better understanding of a hydrodynamic plasma-gas coupling by charge exchange processes. *Astrophysics and Space Science*, 284:1035–1054, 2002.

[116] W. L. Fite, A. C. H. Smith, and R. F. Stebbings. Charge transfer in collisions involving symmetric and asymmetric resonance. *Proceedings of the Royal Society of London A*, 268(1335):527–536, 1962.

[117] C. D. Munz, P. Omnes, R. Schneider, E. Sonnendrücker, and U. Voβ. Divergence correction techniques for Maxwell solvers based on a hyperbolic model. *Journal of Computational Physics*, 161:484–511, 2000.

[118] A. Dedner, F. Kemm, D. Kröner, C. D. Munz, T. Schnitzer, and M. Wesenberg. Hyperbolic divergence cleaning for the MHD equations. *Journal of Computational Physics*, 175:645–673, 2002.

[119] A. Bruce Langdon. On enforcing Gauss' law in electromagnetic particle-in-cell codes. *Computer Physics Communications*, 70(3):447 – 450, 1992.

[120] P.J. Mardahl and J.P. Verboncoeur. Charge conservation in electromagnetic PIC codes; spectral comparison of Boris/DADI and Langdon-Marder methods. *Computer Physics Communications*, 106(3):219 – 229, 1997.

[121] C. P. T. Groth, P. L. Roe, T. I. Gombosi, and S. L. Brown. On the nonstationary wave structure of a 35-moment closure for rarefied gas dynamics. Paper 95-2312, AIAA, June 1995.

[122] J. A. Hittinger. *Foundations for the Generalization of the Godunov Method to Hyperbolic Systems with Stiff Relaxation Source Terms*. PhD thesis, University of Michigan, 2000.

[123] K. Miura. Development of an extended magnetohydrodynamic model for anisotropic plasmas. Master's thesis, University of Toronto Institute for Aerospace Studies, 2004.

[124] J. M. Weiss and W. A. Smith. Preconditioning applied to variable and constant density flows. *AIAA Journal*, 33(11):2050–2057, 1995.

[125] H. Nishikawa, P. L. Roe, Y. Suzuki, and B. van Leer. A general theory of local preconditioning and its application to the 2d ideal MHD equations. Paper 2003-3704, AIAA, June 2003.

[126] E. Turkel. Review of preconditioning methods for fluid dynamics. *Applied Numerical Mathematics*, 12(1):257 – 284, 1993.

[127] Wei Peng, Guo Ping Chen, and Lang Li. Low-speed preconditioning for ausm+-up scheme. In *Applied Mechanics and Materials III*, volume 723 of *Applied Mechanics and Materials*, pages 224–228. Trans Tech Publications, 3 2015.

[128] F. Giroux and J. McDonald. A low-mach-number preconditioner for the ten-moment, gaussian moment closure of gas dynamics. In *Proceedings of the 26th Annual Conference of the Computational Fluid Dynamics Society of Canada, June 18-20, 2017*. CFD Society of Canada, 2017.

[129] H. Lomax, T. Pulliam, and D. Zingg. *Fundamentals of Computaional Fluid Dynamics*. Springer, Berlin, 2001.

[130] T. Wuilbaut and H. Deconinck. Improving monotonicity of the 2nd order backwards difference time integration scheme by temporal limiting. Paper 5th International Conference on Computational Fluid Dynamics, ICCFD, July 2008.

[131] S. A. Northrup. *A Parallel Implicit Adaptive Mesh Refinement Algorithm for Predicting Unsteady Fully-Compressible Reactive Flows*. PhD thesis, University of Toronto, 2014.

[132] B. Einfeldt. On Godunov-type methods for gas dynamics. *SIAM Journal on Numerical Analysis*, 25:294–318, 1988.

[133] J. Loverich. *A Finite Volume Algorithm for the Two-Fluid Plasma System in One Dimension*. PhD thesis, University of Washington, 2003.

[134] M. Torrilhon. Non-uniform convergence of finite volume schemes for Riemann problems of ideal magnetohydrodynamics. *Journal of Computational Physics*, 192:73–74, 2003.

[135] S. K. Godunov. Finite-difference method for numerical computations of discontinuous solutions of the equations of fluid dynamics. *Matematicheskii Sbornik*, 47:271–306, 1959.

[136] T. J. Barth. Recent developments in high order k-exact reconstruction on unstructured meshes. Paper 93-0668, AIAA, January 1993.

[137] S. Venkateswaran and C. L. Merkle. Dual time stepping and preconditioning for unsteady computations. Paper 95–0078, AIAA, January 1995.

[138] T. J. Barth and D. C. Jespersen. The design and application of upwind schemes on unstructured meshes. Paper 89-0366, AIAA, January 1989.

[139] P. L. Roe. Characteristic-based schemes for the Euler equations. *Annual Review of Fluid Mechanics*, 18:337–365, 1986.

[140] J. W. Eastwood R. W. Hockney. *Computer Simulation Using Particles*. Institute of Physics Publishing, Bristol, 1988.

[141] M. Brio and C. C. Wu. An upwind differencing scheme for the equations of ideal magnetohydrodynamics. *Journal of Computational Physics*, 75:400–422, 1988.

[142] P. J. Roache. Code verification by the method of manufactured solutions. *ASME Journal of Fluids Engineering*, 124:4–10, 2002.

[143] P. J. Roache. *Verification and Validation in Computational Science and Engineering*. Hermosa Publisher, Albuquerque, NM, 1998.

[144] K. Salari and P. Knupp. Code verification by the method of manufactured solutions. Report SAND2000–1444, Sandia, June 2000.

[145] K. G. Powell. An approximate Riemann solver for magnetohydrodynamics (that works in more than one dimension). Report 94-24, ICASE, July 1994.

[146] Y. Suzuki and B. van Leer. An extension of the upwind moment scheme to systems of 1-D nonlinear hyperbolic-relaxation equations. In *Proceedings of the 15th Annual Conference of the CFD Society of Canada, Toronto, Canada, May 27–31, 2007*. CFD Society of Canada, 2007.

[147] C. P. T. Groth and S. A. Northrup. Parallel implicit adaptive mesh refinement scheme for body-fitted multi-block mesh. Paper 2005-5333, AIAA, June 2005.

[148] S. A. Northrup. A parallel adaptive-mesh refinement scheme for predicting laminar diffusion flames. Master's thesis, University of Toronto, 2004.

[149] S. A. Northrup and C. P. T. Groth. Solution of laminar diffusion flames using a parallel adaptive mesh refinement algorithm. Paper 2005–0547, AIAA, January 2005.

[150] X. Gao and C. P. T. Groth. A parallel adaptive mesh refinement algorithm for predicting turbulent non-premixed combusting flows. *International Journal of Computational Fluid Dynamics*, 20(5):349–357, 2006.

[151] X. Gao. *A Parallel Solution-Adaptive Method for Turbulent Non-Premixed Combusting Flows*. PhD thesis, University of Toronto, August 2008.

[152] X. Gao and C. P. T. Groth. A parallel solution-adaptive method for three-dimensional turbulent non-premixed combusting flows. *Journal of Computational Physics*, 229(5):3250–3275, 2010.

[153] X. Gao, S. A. Northrup, and C. P. T. Groth. Parallel solution-adaptive method for two-dimensional non-premixed combusting flows. *Progress in Computational Fluid Dynamics*, 11(2):76–95, 2011.

[154] M. R. J. Charest, C. P. T. Groth, and Ö. L. Gülder. A computational framework for predicting laminar reactive flows with soot formation. *Combustion Theory and Modelling*, 14(6):793–825, 2010.

[155] M. R. J. Charest, H. I. Joo, C. P. T. Groth, and Ö. L. Gülder. Experimental and numerical study of soot formation in laminar ethylene diffusion flames at elevated pressures from 10 to 35 atm. *Proceedings of the Combustion Institute*, 33:549–557, 2011.

[156] M. R. J. Charest, C. P. T. Groth, and Ö. L. Gülder. Effects of gravity and pressure on laminar co-flow methane-air diffusion flames at pressures from 1 to 60 atmospheres. *Combustion and Flame*, 158(5):860–875, 2011.

[157] M. R. J. Charest, C. P. T. Groth, and Ö. L. Gülder. Solution of the equation of radiative transfer using a Newton-Krylov approach and adaptive mesh refinement. *Journal of Computational Physics*, 231:3023–3040, 2012.

[158] J. S. Sachdev, C. P. T. Groth, and J. J. Gottlieb. A parallel solution-adaptive scheme for predicting multi-phase core flows in solid propellant rocket motors. *International Journal of Computational Fluid Dynamics*, 19(2):159–177, 2005.

[159] J. S. Sachdev, C. P. T. Groth, and J. J. Gottlieb. Parallel AMR scheme for turbulent multi-phase rocket motor core flows. Paper 2005-5334, AIAA, June 2005.

[160] Barry F. Smith, Petter E. Bjørstad, and William D. Gropp. *Domain Decomposition: Parallel Multilevel Methods for Elliptic Partial Differential Equations*. Cambridge University Press, New York, NY, USA, 1996.

[161] M. J. Aftomis, M. J. Berger, and S. M. Murman. Applications of space-filling curves to cartesian methods for CFD. Paper 2004-1232, AIAA, January 2004.

[162] J.S. Sachdev, C.P.T. Groth, and J.J. Gottlieb. A parallel solution-adaptive scheme for predicting multi-phase core flows in solid propellant rocket motors. *International Journal of Computational Fluid Dynamics*, 19(2):157–175, 2005.

[163] W. Gropp, E. Lusk, and A. Skjellum. *Using MPI*. MIT Press, Cambridge, Massachussets, 1999.

[164] R. W. MacCormack. The effect of viscosity in hypervelocity impact cratering. Paper 69-354, AIAA, January 1969.

[165] Y. Saad and M. H. Schultz. GMRES: A generalized minimal residual algorithm for solving nonsymmetric linear equations. *SIAM Journal for Scientific and Statistical Computing*, 7(3):856–869, 1986.

[166] Y. Saad. *Iterative Methods for Sparse Linear Systems*. PWS Publishing Company, Boston, 1996.

[167] Y. Saad. *Iterative Methods for Sparse Linear Systems*. Society for Industrial and Applied Mathematics, Philadelphia, PA, USA, 2nd edition, 2003.

[168] D. A. Knoll and D. E. Keyes. Jacobian-free Newton-Krylov methods: A survey of approaches and applications. *Journal of Computational Physics*, 193:357–397, 2004.

[169] H. A. Schwarz. Gesammelte mathematische abhandlungen. In *Vierteljahrsschrift der Naturforschenden Gesellschaft in Zürich*, volume 15, pages 272–286, 1870.

[170] E. J. Nielsen, W. K. Anderson, R. W. Walters, and D. E. Keyes. Application of Newton-Krylov methodology to a three-dimensional unstructured Euler code. Paper 95-1733-CP, AIAA, June 1995.

[171] H. Luo, J. D. Baum, and R. Löhner. A fast, matrix-free implicit method for compressible flows on unstructured grids. *Journal of Computational Physics*, 146:664–690, 1998.

[172] A. Jameson. Time dependent calculations using multigrid, with applications to unsteady flows past airfoils and wings. Paper 1991-1596, AIAA, June 1991.

[173] L. Dubuc, F. Cantariti, M. Woodgate, B. Gribben, K. J. Badcock, and B. E. Richards. Solution of the unsteady Euler equations using an implicit dual-time method. *AIAA Journal*, 36(8):1417–1424, August 1998.

[174] W. A. Mulder and B. van Leer. Experiments with implicit upwind methods for the Euler equations. *Journal of Computational Physics*, 59:232–246, 1985.

[175] W. J. Coirier. *An Adaptively-Refined, Cartesian, Cell-Based Scheme for the Euler and Navier-Stokes Equations*. PhD thesis, University of Michigan, 1994.

[176] W. J. Coirier and K. G. Powell. An accuracy assessment of Cartesian-mesh approaches for the Euler equations. *Journal of Computational Physics*, 117:121–131, 1995.

[177] E. R. Priest. *Solar Magneto-Hydrodynamics*. Reidel Publishing, Boston, 1982.

[178] John Jackson. *Classical electrodynamics*. Wiley, New York, 1999.

[179] B. R. Tensuda, J. G. McDonald, and C. P. T. Groth. Numerical solution of a maximum-entropy-based 14-moment closure for multi-dimensional flows. In H.X Zhang, X.G. Deng, and Z.L. Fans, editors, *Proceedings of the Eighth International Conference on Computational Fluid Dynamics, ICCFD8, Chengdu, China, July 14–18, 2014*, pages 1491–1507, 2014.

[180] B. R. Tensuda. Interpolative hyperbolic realizable moment closures for non-equilibrium flows with heat transfer. Master's thesis, University of Toronto, October 2015.

[181] B. R. Tensuda, J. G. McDonald, and C. P. T. Groth. Application of a maximum-entropy-based 14-moment closure for multi-dimensional non-equilibrium flows. Paper 2015-3420, AIAA, June 2015.

[182] E. G. Harris. On a plasma sheath separating regions of oppositely directed magnetic field. *Il Nuovo Cimento (1955-1965)*, 23(1):115–121, 1962.

[183] M.C. Kelley and R.A. Heelis. *The Earth's Ionosphere: Plasma Physics and Electrodynamics*. International geophysics series. Academic Press, 1989.

[184] M. Echim, R. Maggiolo, J. De Keyser, T.L. Zhang, G. Voitcu, S. Barabash, and R. Lundin. Comparative investigation of the terrestrial and venusian magnetopause: Kinetic modeling and experimental observations by Cluster and Venus Express. *Planetary and Space Science*, 59(10):1028 – 1038, 2011.

[185] Division on Engineering National Research Council, Solar Physical Sciences, Space Studies Board, and Space Physics Survey Committee. *The Sun to the Earth – and Beyond: A Decadal Research Strategy in Solar and Space Physics*. National Academies Press, 2003.

[186] P. M. E. Décréau, P. Fergeau, V. Krasnoselskikh, E. Le Guirriec, M. Lévêque, Ph. Martin, O. Randriamboarison, J. L. Rauch, F. X. Sené, H. C. Séran, J. G. Trotignon, P. Canu, N. Cornilleau, H. de Féraudy, H. Alleyne, K. Yearby, P. B. Mögensen, G. Gustafsson, M. André, D. C. Gurnett, F. Darrouzet, J. Lemaire, C. C. Harvey, P. Travnicek, and Whisper experimenters. Early results from the Whisper instrument on Cluster: an overview. *Annales Geophysicae*, 19(10/12):1241–1258, 2001.

[187] A. Runov, R. Nakamura, W. Baumjohann, R. A. Treumann, T. L. Zhang, M. Volwerk, Z. Vörös, A. Balogh, K.-H. Glaßmeier, B. Klecker, H. Rème, and L. Kistler. Current sheet structure near magnetic x-line observed by Cluster. *Geophysical Research Letters*, 30(11), 2003.

[188] Michael Hesse, Karl Schindler, Joachim Birn, and Masha Kuznetsova. The diffusion region in collisionless magnetic reconnection. In *The 40th annual meeting of the division of plasma physics of the american physical society*, volume 6, pages 1781–1795, 1999.

[189] Paolo Ricci, Giovanni Lapenta, and J. U. Brackbill. GEM reconnection challenge: Implicit kinetic simulations with the physical mass ratio. *Geophysical Research Letters*, 29(23):3–1–3–4, 2002.

[190] E. A. Johnson and J. A. Rossmanith. Simulation of fast magnetic reconnection using a two-fluid model of collisionless pair plasma without anomalous resistivity. In *Proceedings of the 19th Annual Wisconsin Space Conference*, 2009.

[191] A. Ishizawa and N. Nakajima. Turbulence driven magnetic reconnection causing long-wavelength magnetic islands. *Physics of Plasmas*, 17(7), 2010.

[192] M. J. Berger. Adaptive mesh refinement for hyperbolic partial differential equations. *Journal of Computational Physics*, 53:484–512, 1984.

[193] S. A. Northrup and C. P. T. Groth. Parallel implicit adaptive mesh refinement algorithm for solution of laminar combusting flows. 14th Annual Conference of the CFD Society of Canada, Kingston, Ontario, Canada, July 16–18, 2006, July 2006.

[194] S. A. Northrup and C. P. T. Groth. Prediction of unsteady laminar flames using a parallel implicit adaptive mesh refinement algorithm. In *Proceedings of the U. S. National Combustion Meeting, Ann Arbor, Michigan, U.S.A., May 17–20, 2009*, page paper 23H3, 2009.

[195] M. R. J. Charest, C. P. T. Groth, and Ö. L. Gülder. Parallel solution adaptive method for prediction of sooting laminar diffusion flames. In *Proceedings of the Combustion Institute Canadian Section Spring Technical Meeting*, Université de Montréal, Québec, May 11–13 2009.

[196] M. R. J. Charest, C. P. T. Groth, and Ö. L. Gülder. Numerical prediction of sooting laminar diffusion flames using adaptive mesh refinement. In *Proceedings of the 6th U.S. National Combustion Meeting*, Ann Arbor, Michigan, May 17–20 2009. Paper 23H4.

[197] M. K. Hryniewicki, C. P. T. Groth, and J. J. Gottlieb. Parallel implicit anisotropic block-based adaptive mesh refinement finite-volume scheme for the study of fully resolved oblique shock wave reflections. *Shock Waves*, 25(4):371–386, 2015.

[198] C. P. T. Groth M. J. Williamschen. Parallel anisotropic block-based adaptive mesh refinement algorithm for three-dimensional flows. In *21st AIAA Computational Fluid Dynamics Conference*, pages 1–22, 2013.

[199] L. Freret and C. P. T. Groth. Anisotropic non-uniform block-based adaptive mesh refinement for three-dimensional inviscid and viscous flows. In *22nd AIAA Computational Fluid Dynamics Conference*, page 2613, 2015.

[200] K. G. Powell, P. L. Roe, T. J. Linde, T. I. Gombosi, and D. L. De Zeeuw. A solution-adaptive upwind scheme for ideal magnetohydrodynamics. *Journal of Computational Physics*, 154:284–309, 1999.

[201] N. M. Narechania, L. Freret, and C. P. T. Groth. Block-based anisotropic AMR with a posteriori adjoint-based error estimation for three-dimensional inviscid and viscous flows. Paper 2017-4113, AIAA, June 2017.

[202] C. N. Ngigi, L. Freret, and C. P. T. Groth. Comparison of h-and p-derived output-based error estimates for directing anisotropic adaptive mesh refinement in three-dimensional inviscid flows. Paper 2018-0829, AIAA, January 2018.

[203] R. W. Ziemer. Experimental investigation in magneto-aerodynamics. *ARS Journal*, 29:642–647, Sept. 1959.

[204] A. Knapp, M. Fertig, D. Haag, G. Herdrich, and M. Auweter-Kurtz. Investigation of the interaction between a magnetic probe body and argon plasma. Paper 2007–4133, AIAA, June 2007.

[205] M. Kawamura, A. Matsuda, H. Katsurayama, H. Otsu, D. Konigorski, S. Sato, and T. Abe. Experimental study on drag enhancement in electrodynamic heat shield for a blunt body in a weakly ionized plasma flow. Paper 2007–3889, AIAA, June 2007.

[206] R. W. MacCormack. Numerical simulation of aerodynamic flow within a strong magnetic field with hall current and ion slip. Paper 2007-4370, AIAA, June 2007.

[207] J. Poggie and D. V. Gaitonde. Magnetic control of flow past a blunt body: Numerical validation and exploration. *Physics of Fluids*, 14(5):1720–1731, May 2002.

[208] T. Fujino, S. Kondo, and M. Ishikawa. Preliminary analysis of electric power extraction by MHD technology in reentry flight. Paper 2007–4248, AIAA, June 2007.

[209] O. U. Kahn and K. A. Hoffmann. Numerical investigation of decomposed full magneto-fluid-dynamics equations. Paper 2008–1068, AIAA, January 2008.

[210] F. F. Chen, editor. *Introduction to Plasma Physics and Controlled Fusion*. Plenum Press, New York, 1984.

[211] P. A. Sturrock. *Plasma Physics : An Introduction to the Theory of Astrophysical, Geophysical & Laboratory Plasmas*. Cambridge, Cambridge, 1994.

[212] L. Brillouin. *Wave Propagation and Group Velocity*. Academic Press, New York, 1960.